THE DEVELOPMENT AND APPLICATION OF VARIOUS NOVEL SERS SUBSTRATES, BASED ON THE ORDERED ASSEMBLIES OF (CLOSELY PACKED) GOLD NANOPARTICLES, FOR RELIABLE DETECTION OF NANOPLASTICS IN WATER

AISHA BIBI

Doctor of Philosophy

Aston University

September 2024

Abstract

Micro- and nanoplastics have a harmful impact on human health with potential to damage organs. The harmful effects of the latter (i.e. nanoplastics) on human health are of particular concern because nanoplastics are smaller in size than microplastics, which makes the nanoplastics greater in surface area to volume. Consequently, nanoplastics have greater capacity to absorb persistent organic pollutants, ions, pathogens and other harmful contaminants present in the environment. The smaller size of nanoplastics also makes nanoplastic penetration through cell wall and tissue possible, therefore, nanoplastics pose more of a threat to human health as compared to microplastics. In order to get better knowledge about the occurrence, transport and toxicological impact of nanoplastics, there is a need to be able to reliably and accurately detect these tiny particles. Whilst in the near past an increase in the research on development of analytical techniques for detection of nanoplastics has been noticed, but in comparison to microplastics detection, there is a dearth in the analytical tools that can achieve reproducible and cost-effective detection of nanoplastics, with the existing technologies in a pre-mature phase of development. Of the existing analytical techniques, Surface-Enhanced Raman Scattering (SERS) has demonstrated great potential in the field, albeit there is still a lot of research required for developing SERS substrates suitable for nanoplastic detection.

To this end, the work presented in the thesis was carried out to develop low-cost SERS substrate based on gold nanoparticles, for the reliable detection of low concentrations of nanoplastics in water. Three different methodologies were devised and tested to form ordered assemblies of closely packed gold nanoparticles to be used as SERS substrates detecting low concentrations (of at least 1 μg/mL) of 50 nm and 100 nm pristine polystyrene nanoplastics in dH_2O. The reliability of the methodologies and subsequently the homogeneity of the prepared substrates was checked using the parameter coefficient of variation (CV%). The obtained CV% values lower than 15% proved the reliability of the substrates. Furthermore, the practicality of the developed substrates for detection of real world nanoplastics was demonstrated by detecting nanoplastics released from hot insulated cup and food preparation gloves. The methodologies and SERS substrates presented in this thesis overcome the state of the art, therefore contributing to the field of nanoplastic detection through the use of SERS.

Dedication

To my family - my late in-laws, Zubaida Bibi and Atta Ullah, who remain forever in our hearts; to my parents, Zarina Naseeb and Naseeb Ullah, for their unwavering belief in me; to my husband, Zia Ul Hassan, who has stood by me through every challenge with strength and support; and to my children, Abeera Zia, Shaan Ul Haq, and Inayah Hassan, whose love and encouragement have been my greatest motivation.

Acknowledgments

Firstly, I would like to express my sincere gratitude to my supervisor, Dr. Daniel Hill, for securing the H2020-MSCA-ITN funding for the MONPLAS project (Marie Skłodowska-Curie grant agreement No 860775), which made this research possible, and for serving as a guiding figure throughout my work. I aspire to become an expert proposal writer like him one day. I would like to thank my Associate Supervisor, Prof David J Webb, for always having an answer to all my photonics related questions, for always knowing what's wrong when the equipment "misbehaved" in the laboratory and for his great suggestions related to data analysis. His broad expertise and deep knowledge have always left me in awe and hoping to become as knowledgeable and kind as him someday. I would like to express my heartfelt gratitude towards Dr David Benton for his interest in my work and for the countless insightful discussions which led to ideas and gave me different perspective to my research. May I become as curious and helpful as him someday. I would also like to thank Dr Kirill Tokmakov and Ms Swaroopa Mucheli Sudhakar for being there whenever I needed help with countless things related to the laboratory and for being there to get equipment installed in my absence. I would also like to thank my counterpart at Aston University within the MONPLAS project, Atif for insightful discussions regarding our work and for being with me in this journey. What would I have done without my friends like family, who were always there to hear me out, give fabulous advice and be the best human beings possible – thank you my dearest friends/sisters Karina (also my office mate) and Arooj. A special thanks to Arooj for being there for me when I needed help the most, I wouldn't have been able to write this thesis without her moral support. A special thanks to Karina too for always being there for me and being my go-to person for advice and support. They are both very precious to me and this PhD journey would have been extremely difficult if not impossible without them.

I would like to express my utmost gratitude towards Dr Cuong Cao, who always welcomed me with an open heart to his laboratory and gave me the opportunity to not only use the state-of-the-art equipment available at Institute for Global Food Security (IGFS), but also work alongside great researchers (James Tate and Udit Pant) which led to a lot of excellent collaborative pieces of work. Every discussion I have ever had with Dr Cuong was filled with amazing ideas and advice for experimental work – he taught me a lot about the field. A special shout out to James Tate for his contributions in the experimental work of Chapter 4. I am extremely grateful to him for his "crazy" ideas, inspiring discussions and help without which this thesis wouldn't have turned out the way it has. A special thanks to Udit Pant too for all his valuable suggestions for experimental work, but particularly for

his help with the COMSOL modelling done within this thesis. I am extremely grateful for the friends (Girish, Shalini, Udit, James, Naomi, Sunny and Vinayak) I made at Belfast during my secondments there who were there with me through thick and thin.

I would like to thank Dr Christoph Kraft for hosting me at Leibniz Institute for Photonics Technologies, where I got to learn a lot about Raman and SERS under his guidance. I would also like to extend my gratitude towards Dr Dana Cialla May and Edo who were always having amazing ideas for experimental work related to SERS. During my secondments at IPHT I also made friends (Shiwani, Shrawan, Mohit, Nikhilesh, Miftah, Aarya, Nishitha and Hiya) who left a lifelong impact on me with their knowledge and kindness. I have had enlightening discussions related to Physics and Photonics with the entire lot of them for which I am grateful, but I would like to express my utmost gratitude for Shiwani who helped me develop my knowledge on instrumentation and Raman spectroscopy, she has always extended a helping hand for me throughout the PhD journey and I would not have been able to face its challenges without her help; I would like to thank her for being an amazing researcher and an even more amazing human being and a friend I can always count on.

I would like to thank all other colleagues within the MONPLAS project particularly collaborators from Aston University, IGFS and IPHT who I have had the pleasure to work with. I would also like to thank my childhood friend, Mamoona Mujtaba for always being a call away no matter what time of day or night it might be. Thank you believing in me even when I lose hope and for being there for me to give me motivational talks when I am feeling low (and of course there were many lows during this strenuous journey). I would also like to thank my friends all over the world, especially Mahmoud & Nada with lovely Omar and Alia; Jauwairia, Samreen, Aleena and Nida; Zain Umer with his lovely family and Jahanzaib who have always believed in me even when I doubt myself.

A special thank you to my parents, Zarina Naseeb and Naseeb Ullah, for instilling in me the courage to dream big and work hard, and to my lovely children, Abeera, Shaan, and Inayah, for their patience and pride in my work, which motivates me to contribute to a better future for them.

Lastly, my deepest thanks to my husband, Zia Ul Hassan, for being my unwavering rock and taking on all responsibilities while I pursued my PhD. Your belief in me and support made this journey possible.

Table of Content

List of Figures

List of Tables

Abbreviations

AAO	Anodic Aluminium Oxide
Ache	Acetylcholinesterase
AFM	Atomic Force Microscopy
Ag	Silver
Agnp	Silver Nanoparticle
Agnw	Silver Nanowires
ALF	Aluminium Foil
ALF@Aunp	Aluminium Foil With Gold Nanoparticles
ALF-HB	Hydrophobic Aluminium Foil
ALF-HB@Aunp	Hydrophobic Aluminium Foil With Gold Nanoparticles Drop Casted
ALF-IL	Aluminium Foil Having Islands Of Gold Nanoparticles
Aphtms	Aminophenyltrimethoxysilane
APTES	Aminopropyltriethoxysilane
APTMS	Aminopropyltrimethoxysilane
As	Arsenic
ATP	Aminothiophenol
ATR	Attenuated Total Reflection
A.U.	Arbitrary Unit
Au	Gold
Aunp	Gold Nanoparticles
Aunr	Gold Nanorods
Auns	Gold Nanostars
Aunu	Gold Nanourchins
BPA	Bisphenol A
BSA	Bovine Serum Albumin
CARS	Coherent Anti-Stokes Raman Scattering
CB[N]	Cucurbit Molecule Having N Glycouril Units
CCD	Charged Coupled Device
CL	Crosslinking
CPR	Continuous Plankton Recorder

CRS	Coherent Raman Scattering
CTAB	Cetyltrimethylammonium Bromide
Cu	Copper
CV	Coefficient Of Variation
Dh_2o	Deionised Water
DFH-4T	Diperfluorohexylguaterthiophene
EDX/EDS	Energy-Dispersive X-Ray Spectroscopy
EF	Enhancement Factor
EM	Electron Microscopy
EM-CCD	Electron-Multiplying Charged Coupled Device
FEM	Finite Element Method
FPR	Fibre Reinforced Polymers
FTIR	Fourier-Transform Infrared Spectroscopy
GUI	Graphical User Interface
$Haucl_4$	Tetrachloroauric Acid
HDPE	High Density Polyethylene
InGaAs	Indium Gallium Arsenide
IR	Infrared
Kcl	Potassium Chloride
KI	Potassium Iodide
LDPE	Low Density Polyethylene
LG	Liquid-Gas Interfsection
LLF	Laser Line Filter
Lob	Limit Of Blank
Lod	Limit Of Detection
MBA	Mecrcaptobenzoic Acid
$Mgso_4$	Magnesium Sulphate
ML	Machine Learning
MNP	Micro- and Nano-Plastics
MPTES	Mercaptopropyltriethoxysilane
MPTMS	Mercaptoproplytrimethoxysilane
Mt	Million Tonnes

$Na_3C_6H_5O_7$	Trisodium Citrate
Nacl	Sodium Chloride
Nai	Sodium Iodide
$Nano_3$	Sodium Nitrate
NCL	Non-Crosslinking
NDBS	Notch Dichroic Beam Splitter
NF	Notch Filter
$–NH_3$	Amine Group
Ni	Nickel
NIR	Near-Infrared
NMR	Nuclear Magnetic Resonance
NR	Nile Red
NWERS	Nanowell Raman Enhanced Substrate
$O–CH_3$	Ethoxy Group
–OH	Hydroxyl Group
PA	Polyamide
PAH	Polyacrylamide Hydrogel
Pd	Palladium
PDMS	Polydimethylsiloxane
PE	Polyethylene
PET	Polyethylene Terephthalate
PHB	Polyhydroxybutyrate
PMMA	Polymethyl Methacrylate
Pos	Point Of Site
PP	Polypropylene
Pph_3	Phosphorus Triphenyl
PS	Polystyrene
Pt	Platinum
PTC	Phase Transfer Catalyst
PUR	Polyurethanes
PVA	Polyvinyl Alcohol
PVC	Polyvinyl Chloride

PVD	Physical Vapor Deposition
PY-GC-MS	Pyrolysis Gas Chromatography Mass Spectrometry
R6G	Rhodamine 6G
S-ALF	Salinised Aluminium Foil Having A Monolayer Of Gold Nanoparticles
SB	Senate Bill
SD	Standard Deviation
SEM	Scanning Electron Microscopy
SERS	Surface Enhanced Raman Spectroscopy
SG	Soild-Gas Intersection
Si	Silicon
Sio_2	Silicon Dioxide
SL	Solid-Liquid Intersection
SNR	Signal To Noise Ratio
SORS	Spatially Offset Raman Spectroscopy
SPM	Scanning Probe Microscopy
SPR	Surface Plasmon Resonance
SRS	Stimulated Raman Scattering
SS	Stock Solution
T-CHO	Total Cholesterol
TED-GC-MS	Thermal Extraction Desorption Gas Chromatography Mass Spectrometry
TEM	Transmission Electron Microscopy
TG	Triglyceride
TNT	Trinitrotoluene
TOAB	Tetraoctylammonium Bromide
UMARS	Universal Multiple Angle Raman Spectroscopy
UV-Vis	Ultraviolet-Visible
WOS	Web Of Science
WWTP	Waste Water Treatment Plant
XPS	X-Ray Photoelectron Spectroscopy

Preface

This thesis documents work done on the detection of nanoplastics through the use of surface enhanced Raman spectroscopy (SERS). To this end, different SERS substrates were designed, prepared, characterized using Rhodamine 6G (R6G) dye, before being evaluated in their detection of nanoplastics, both for pristine commercial particles and for environmentally found ones. To understand the relevance and importance of the work presented, the first chapter of the thesis is dedicated to the background of micro and nano plastics, including the history of plastic development, production and use, and their formation from macro plastics.

Chapter One

Introduction

The English term "plastics" has its linguistic roots in Greek vocabulary, being traced to "plastikos" or "plastos," signifying "fit for moulding" or "moulded," respectively. This nomenclature is a direct reflection of plastic's intrinsic quality of malleability, affording it the capacity to undergo casting, compression, and extrusion processes to assume a diverse array of shapes and forms [1] and thus become ubiquitous in the modern world.

1.1 The history of plastics

The history of plastics, or hydrocarbon-based polymeric materials, can be traced back to circa 1600 BC when ancient Mesoamericans manipulated rubber, refined from latex – an emulsion of polymer microparticles in water, to create objects such as balls, figurines, and bands [2]. The production and use of plastics, hydrocarbon based polymeric materials within a subset of polymers, has since evolved until today where their use can be found in almost every aspect of life.

The contemporary modification of naturally plastic materials and their use dates to 1844 and Charles Goodyear 's innovative acquisition of an American patent for a natural rubber processing technique [3]. It involves heating the rubber in the presence of sulphur, a vulcanization process, to produce a product with the remarkable ability of retaining nearly all of the rubber’s original elasticity while concurrently enhancing its chemical resistance across a broader spectrum of temperatures [4]. The next breakthrough came in 1856, with the first patent to encompass the first man-made, or synthetic, plastic, denominated "Parkesine," a hardened form of nitrocellulose, and attributed to Alexander Parks [5], although it was not a commercial success. The first commercially successful manmade plastic however came in 1869 when John Wesley Hyatt, an American innovator, developed a procedure to organically process cloth, ivory dust, and shellac, thereby pioneering a polymer dubbed "celluloid", which was used to manufacture combs, billiard balls and cinema reels at affordable rates[6].

The era of modern plastics began in 1907 with the development of the first fully synthetic plastic, Leo Bakeland’s Bakelite, from fossil fuel derived phenol [7]. However, plastics did not gain popularity until the 1920s when substances, later termed as plasticizers, were discovered and added to them to easily vary their otherwise unremarkable and rigid properties according to their application – for a greater variety of plastics still. One of the

most important examples of this is the transformation of the rigid and brittle polyvinyl chloride (PVC) in 1926 to plasticized PVC, which is found in omnipresent in modern building and construction work [8]. Polyethylene (PE), the most widely used type of plastic today, is a variant of low density Polyethylene (LDPE) which itself was accidentally invented in 1933 by E.W. Fawcett and R.O. Gibson at Imperial Chemical Industries (ICI) Limited [9]. Thereafter acrylic nylon, polymer and polyethylene terephthalate (PET) were synthesised for the first time in 1935, 1936 and 1941 respectively [1].

In addition to plasticizers, nearly all plastic materials contain notable proportions of chemical additives for various purposes, including enhancing functionality (e.g., flame retardants and plasticizers), providing colour (via pigments), making cheaper (e.g. fillers such as calcium carbonate), and mechanical reinforcement the plastics (e.g., using glass fibres) [10,11]. Notably, these additives do not undergo polymerization with the plastic monomers and therefore, not being chemically bonded to the polymer have the potential to detach and enter the surrounding environment [11]. The subsequent section focusses on broad the classifications of plastics.

1.2 Classification of Plastics

Plastics can be broadly classified into two categories based on their origin: (a) natural, or non-synthetic, plastics; and (b) synthetic plastics. Natural plastics are derived from naturally occurring resources and can further be classified into two main categories: (i) plant-based and (ii) animal-based. The former, such as cellulose, rubber and starch, are derived from the stems, leaves, and seeds of plants, and typically contain polymers that can be processed to exhibit plastic-like characteristics. The latter, such as chitin and shellac, are derived from animal sources, primarily through extraction or processing specific constituents. Natural plastics often require minimal processing to extract or modify the naturally occurring polymers and can be put through simple chemical or mechanical treatments to enhance their properties or form them into usable shapes. Being conducive to biodegradability, and thus a diminished environmental impact, natural plastics serve as sustainable alternatives to their synthetic counterparts.

Synthetic plastics have traditionally been produced through a series of complex chemical processes from fossil fuels such as natural gas, or much more commonly, crude oil. Production from the latter consists of: distillation - the separation of heavy crude oil into lighter fractions; cracking - the generation of monomers from the hydrocarbon chains resulting from the distillation process; and polymerization - the linking of hydrocarbon monomers to form polymers [12]. While crude oil remains the primary source of carbon for the fabrication of synthetic plastics, a wide source of sustainable biomass sources,

including terpenes, vegetable fats and oils, food waste, bacteria, carbohydrates and lignin and cellulose [11] are also being used to produce a diverse range of others, collectively known as bioplastics. Although the discovery of bioplastics dates back to 1926, when Maurice Lemoigne first produced polyhydroxybutyrate (PHB) from bacteria like Bacillus megaterium, it wasn't until the 1970's oil crisis that the need for substitutes of petroleum-based products increased, marking a pivotal moment in the exploration of bioplastics as viable alternative synthetic plastics [12]. It is of note however that whilst the absence of a crude oil origin makes bioplastics more environmentally friendly they are not necessarily a more sustainable alternative in every scenario, but can have promising applications when managed properly, e.g. for single-use items like biodegradable bottles and packaging films [12,13]. As the properties of plastics depend upon the different monomers that they are made from, their structure and their formulation [1], subsequently synthetic plastics can be further classified as either thermoplastics or thermosets. Thermoplastics include the most commonly used plastics, such as PE, PVC, PET, polypropylene (PP) and polystyrene (PS). They are plastic polymer materials that become pliable or mouldable at certain elevated temperatures and solidify upon cooling, permitting repeated cycling of melting, reshaping, and solidification, for multiple reuses across diverse applications. Changes to the physical attributes of thermoplastics during the heating and cooling processes, occur without any alterations to their chemical bonds or structural configuration. Commonly used thermosets, or thermosetting plastics, include polyurethanes (PUR), unsaturated polyester, silicone, epoxy, melamine, phenolic, and acrylic resins. Unlike thermoplastics, however, they do undergo a chemical change upon heating, forming an irreversible three-dimensional network of bonds, instead of linear or branched chains, and so cannot be remelted once set, making their recycling challenging. Most fibre reinforced polymers (FRPs), where the strength of plastics is enhanced through addition of fibres, are based on fibres being added to thermosets, which creates further challenges for recycling [10]. Table 1.1 shows the most commonly used plastics, their types and applications.

Table 1.1: Plastics used and their applications

Polymer	Type	Applications
PET	Thermoplastic	Packaging of food and other retail items, beverage bottles, food photographic films, insulated clothing.
High density polyethylene (HDPE)	Thermoplastic	bottles containing milk, toiletries, detergent, and other cleaning products.
PVC	Thermoplastic	Pipes, hoses, cable insulation, window frames, raincoats, shower curtains
LDPE	Thermoplastic	bags, food and other packaging, plastic film
PP	Thermoplastic	packaging consumer products, transportation
PS	Thermoplastic	Packaging, food containers, CD cases
Polymethyl methacrylate (PMMA)	Thermoplastic	automotive lights, lenses for glasses, shatter-resistant panels for windows, skylights, signs and displays, LCD screens, bathtubs, furniture, acrylic nails
PUR	Thermosetting	foam products such as mattresses, pillows, insulation.
Polyester	Thermosetting	fishing nets, carpets, ropes, clothing, sportswear, air filters
Polyamides (PA)	Thermosetting	textiles, automotive industry, carpets, kitchen utensils, sportswear

1.3 Plastic Production

Since the early 1800's plastics have contributed towards the development of the society through their wide range of applications and usage in daily life. Subsequently plastic production has followed a rising trend with annual production increasing from 2 million tonnes (Mt) in 1950 to nearly 460 Mt in 2019, an average annual growth of nearly 10% (Figure 1.1a) [14,15], with the production in 2050 predicted to be quadruple that at 1480 Mt, of which more than 50% will be produced in Asia (Figure 1.1b) [16]. 1950 is considered the start of plastic mass production [10] even though plastic products were produced and used extensively in World War II both as a result of the shortage of other materials and because of the diverse properties that they offer, due to the lack of data prior to that year.

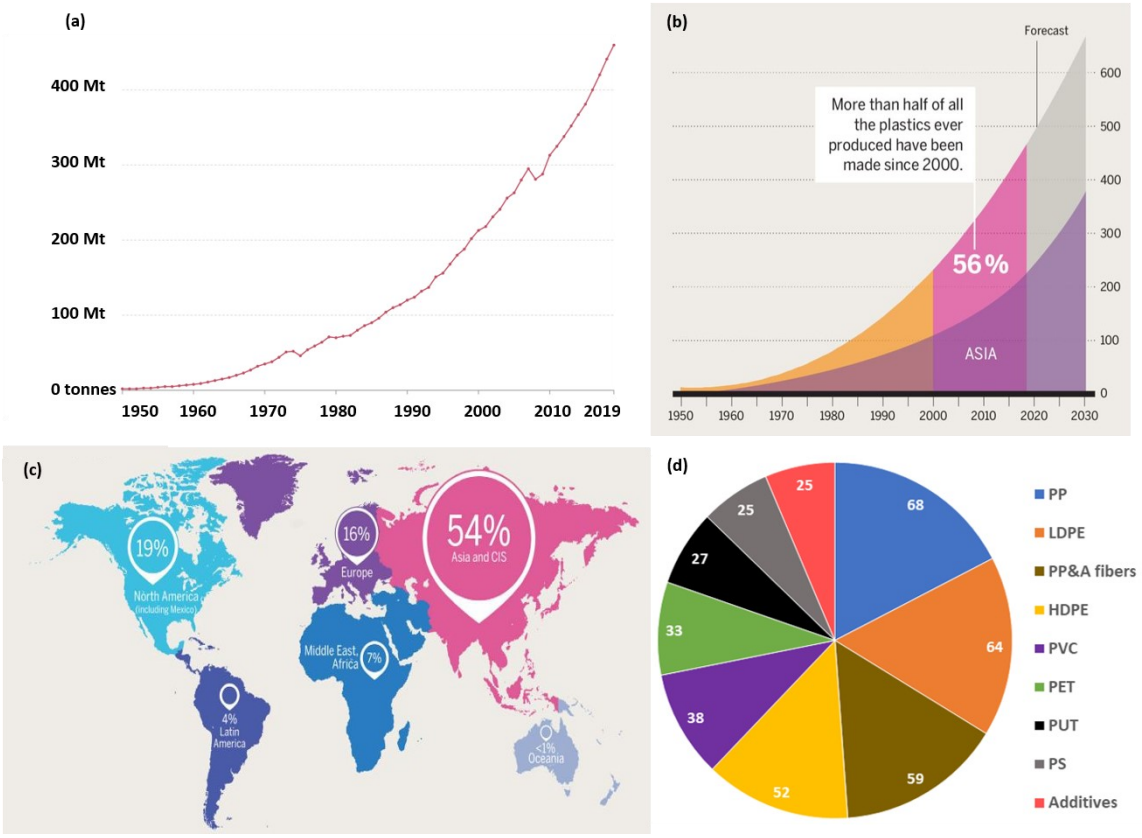

Figure 1.1: (a) Global annual production of plastics in million tonnes from 1950 to 2019 [15] (b) Production of plastics globally vs production of plastics in Asia (in million tonnes) with projections up to 2050 [16] (c) Region-wise global production of plastics as per 2019 [16] (d) Global plastic produced in Mt distributed by polymer type for the year 2015 [17].

The estimated cumulative global production of plastics in 1950 was between 4 to 8 Mt [18] by 1950, which since rose to a staggering 9540Mt by 2019 [19] of which more than half was produced just in the previous 19 years (Figure 1.1b) [16]. Between 1950 and 2019, a drop in annual global production has only taken place three times (Figure 1.1a), 1975 and 1980, corresponding to the global oil crisis, and 2008 resulting from the worldwide financial crisis which also produced similar decreases in production of various other resources [10],

[15]. Post 2019, the only other downward trend occurred in 2020 due to the pandemic of COVID19, with global plastic production falling from 368Mt to 367Mt [20].

In regard to the regional distribution of plastic production, Asia and the Commonwealth of Independent States, or CIS (which includes Armenia, Azerbaijan, Belarus, Kazakhstan, Kirghizstan, Moldavia, Uzbekistan, Russia, Tajikistan, Turkmenistan, Ukraine) together has the largest share at 54%, followed by North America (USA, Canada and Mexico) and Europe at 19% and 16%, respectively. Africa and the Middle East, and then Latin America contributed the least with rates of 7% and 4% respectively [16]. Within the 54% share of Asia and CIS, the leading contribution within Asia comes from China at 32%, making it the largest global producer and consumer of plastics [20-22], fundamentally due to its rapid 20th century industrial development [23]. Globally, by polymer type, the plastic most produced in 2015 was PP, closely followed by LDPE, as seen in Figure 1.1d [17]. The production rate of different plastic types is directly associated with their usage. It is of note that certain countries are endeavouring to produce last plastic, as of 2021 Japan and European countries were among the few that produced less plastic compared to 2017, with reductions of 1% and 4%, respectively (Table 1.2). The same table shows that production share percentages for North America, Latin America and Asia (excluding China, Japan, and the CIS) remained consistent across the two years [22].

Table 1.2: Region wise distribution of plastic production as a percentage of global production, for the years 2017 and 2021 [22].

Region	**2017 (%)**	**2021 (%)**
China	29	32
Japan	4	3
CIS	2	3
Asia (remaining countries)	17	17
EU	19	15
Middle East & Africa	7	8
North America	18	18
Latin America	4	4

With the production of plastics derived from fossil fuels still growing, the world will have ever more plastic [10] and so it is of interest to see how plastics are used (section 1.4) and what is their fate once they have fulfilled their intended purposes (section 1.5).

1.4 Plastic use

Plastics are used widely in various aspects of modern life due to desirable properties such as versatility, durability, flexibility, impermeability and cost-effectiveness, and the way they are used can be classified into two groups: (a) commercial use and (b) regular use. Commercial use refers to the use of plastics by industries for commercial purposes,

whereas regular use refers to the daily use of plastics by people all over the world. Since their discovery, for many years plastics were used in the majority for commercial purposes by large industries, but over the years excessive use of plastics has become common in every household.

As seen in the previous section, PP and PE are the prevalent plastics primarily due to their low production cost, flexibility, light weight, impermeability and their adaptability for a diverse array of product applications [1], in food packaging, household items, shopping bags, plastic wrap, door frames, and construction materials [24]. Figure 1.2a [25] shows that in 2015 the dominant use of plastics in Mt was seen by packaging industry at 42% [26], which since increased in 2021 by 2% [22], thereafter the building and construction industry, which primarily uses PVC [27], at 19% [25], although this had dropped by 1% in 2021 [22]. The third placed textile industry consumes nearly all synthetic fibre production, primarily for the production of clothing, but also for a variety of other items such as carpets, upholstery, and household textiles [28]. Other industries of use include transportation, electrical and electronic equipment, machine parts, consumer products as well as medical equipment and supplies, making plastics ubiquitous [25].

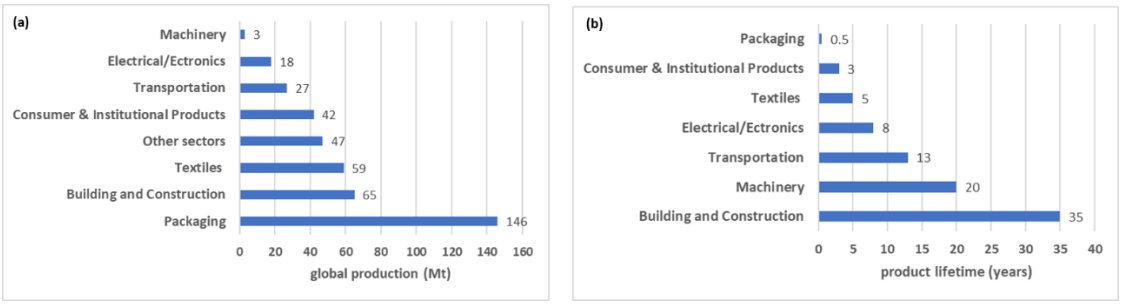

Figure 1.2: (a) Global production rate (Mt) allocated by industrial sector according to 2015 [25] (b) mean product lifetime (years) of various plastic products [29].

With regards to the mean lifetime of the plastics used in those industrial sectors (see Figure 1.2b), measured as time from manufacture to disposal, in 2015 packaging had the shortest mean product lifetime [29], although it was seen to be the largest user and thus the largest waste producing sector. Every year, the average European discards 172.2 kilos of packaging waste, and with 19.5% being plastic that equates to 34.5 kilos of plastic packaging per capita per annum [30]. However, it should be noted that the mass of plastic waste generated is not directly the mass produced, it also depends on polymer type and the lifespan of the final product. For example, although the building and construction sector is the second largest producer of plastic products (65 Mt in 2015), because their mean product lifetime of 35 years is the highest of all sectors (Figure 1.2a and b), it

produces less waste over a short period compared to others [25,29]. Further discussion on plastic waste is presented in the next subsection.

1.5 Plastic Waste

With approximately 40% of all plastics products discarded within one month the fate of plastic at the end of its useful life is a growing source of concern [31]. In terms of waste produced nationally a study from 2016 shows that the United States of America generated the most waste in total and per capita [32] whilst the United Kingdom, Russia and Germany also generate a considerable amount of plastic waste per capita per annum (Figure 1.3). However, in reality it is some of the world's largest corporations amongst others, who are responsible for the majority of the litter with over half of the plastics used in consumer products, primarily in the form of disposable packaging [16]. They include oil companies such as ExxonMobil, Chevron, Shell, and Total; chemical companies such as DowDuPont, BASF, SABIC, and Formosa Plastics; well-known consumer goods conglomerates Procter & Gamble (P&G), Unilever, Nestlé, Coca-Cola, and PepsiCo; and waste management leaders such as SUEZ and Veolia.

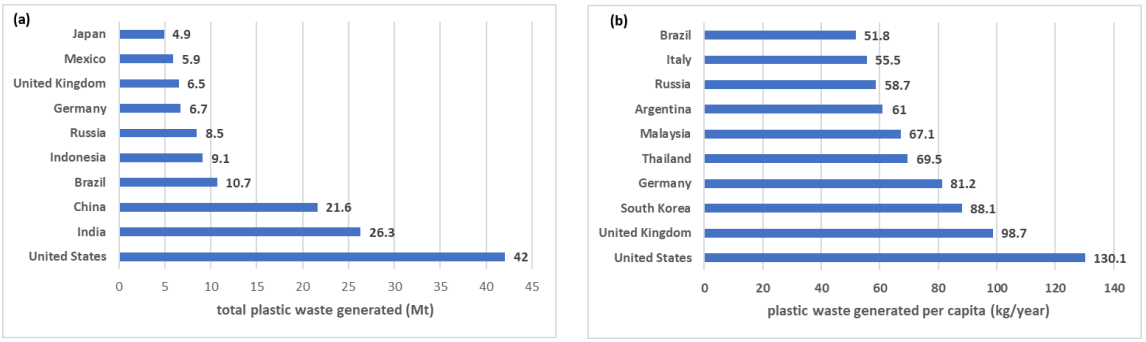

Figure 1.3: (a) Total plastic waste generated (Mt) by the top 10 countries (b) plastic waste generated per capita (kg/year) for the top 10 countries [32].

Therefore in order to get an idea of the top polluters around the world, the Plastic Soup Foundation (Netherlands) collected and analysed data from World Clean-up Day 2020 [32] (Figure 1.4a) which shows that CocaCola is the largest plastic polluter with 19,826 pieces of plastic from its products found in 39 different countries [32]. According to another international study, Break Free from Plastics Audit 2020 [33], Coca-Cola products were the most likely to end up in the environment due to Coca-Cola's decision in 1978 to switch from its iconic glass bottles to single use PET bottles. The same report also recognised Coca Cola, PepsiCo, and Nestlé as the top three global polluters. The remaining brands named by the audit as the world's top polluters are also major multinationals that produce not only food, beverages, or household items, but also their packaging [16,33]. The

situation of plastic waste is bleak as according to UN, every year the Earth is additionally burdened by approximately 300 million tonnes [34].

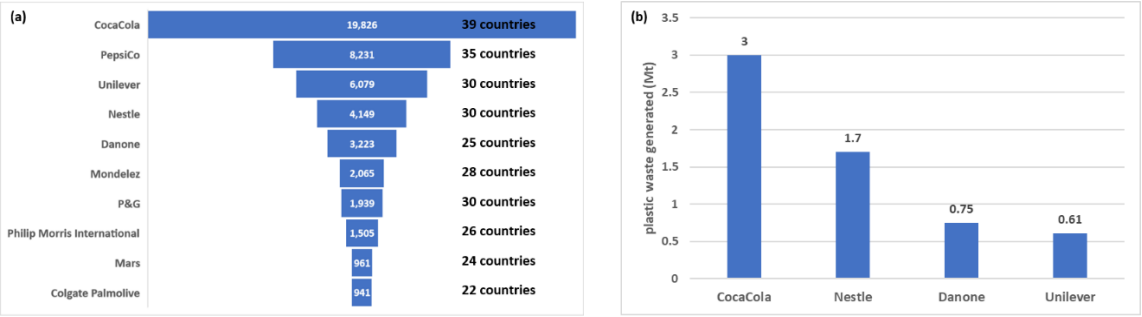

Figure 1.4: (a) Number of plastic pieces collected of waste from products of international brands with the corresponding number of countries the waste was found in [32] (b) Plastic waste produced by a few international brands in million tonnes [16].

The quantitative findings presented on plastic waste frequently raises the question: What is the global framework for managing generated waste? Figure 1.5a shows how different methods for managing global plastic waste have evolved since 1950 and whilst it is clear that prior to 1980 it was neither incinerated or recycled, those methods of handling the waste have since increased by 0.7 percent annually [26]. The same figure shows that as of 2015 almost 55% of global plastic waste was discarded, 25% was incinerated, and only the remaining 20% was recycled [35]. Recycling can be done by one of two ways: (a) Mechanical recycling (shredding, cleaning, and re-compounding) (b) chemical recycling (depolymerizing and repolymerizing).

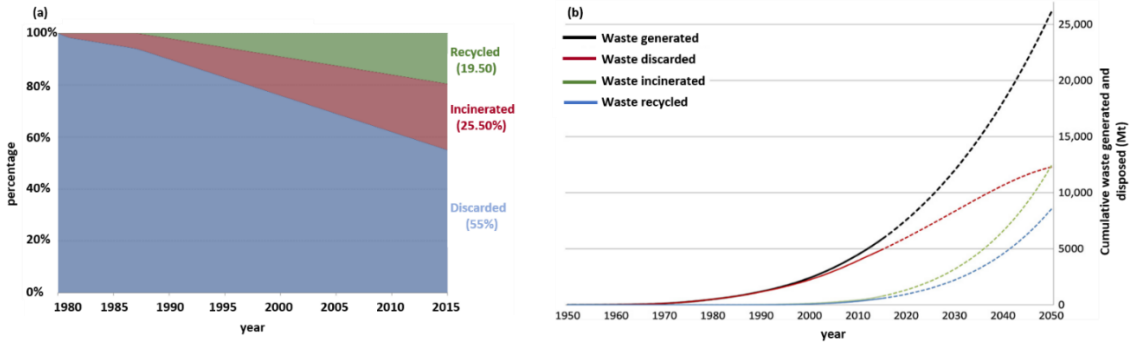

Figure 1.5: (a) Fate of global plastic waste according to disposal method from 1980 to 2015 [35] (b) Fate of cumulative plastic waste generated and disposed of globally from 1950 to 2015 with projections up to 2050 [26].

Out of the two, the latter is more expensive but produces higher-value material. Recycling and reuse helps the environment by reducing primary production, and therefore extraction of unsustainable fossil fuels, and the avoidance of landfilling plastic waste, replacing for greater environmental benefits [36]. Without recycling or reuse the only way to remove non-biodegradable plastic waste from the environment is through thermal destruction, typically through incineration, with or without energy recovery, with all the environmental and health effects [10] that it has. The final waste management option, discarding, can

take the form of managed landfills, unmanaged dumps, or release into the natural environment. This is also the eventual fate of all plastics as they cannot be recycled nor reused indefinitely [37].

Figure 1.5b shows the cumulative waste in Mt disposed of through the three different methods since 1950 along with simple extrapolations up to 2050 (represented by dashed lines) based on historical trends. From those extrapolations for cumulative waste disposal rates can be determined year on year, which by 2050 will probably have increased to 50% and 44% for incineration and recycling rates, respectively, and the discarding of plastic waste reduced to a mere 6% [26]. Clearly however, even if incineration and recycling of plastics results in a reduction in the amount of plastic discarded in the environment every year, there is no denying the environmental pollution caused by plastic waster already discarded. Furthermore, the discarded macro plastics upon degradation can lead to an additional type of pollution, potentially worse, in the form of micro and nanoplastics (MNPs).

1.6 Micro and Nano Plastics (MNPs)

Recent research has shown that the presence of MNPs is having adverse effects on the ecosystem and everything within it [38]. The following sub-sections will focus on: (i) the origins of MNPs including the challenges associated with having a standard definition of MNPs and the different types of MNPs based on their origin; (ii) a brief description of how MNPs enter the environment and the human food chain; (iii) the impact MNPs have on the environment, human beings and other living beings; (iv) the importance of the detection of MNPs followed by a brief description of the different analytical techniques used to identify them and a comparison of them.

1.6.1 The origin of MNPs

Scientific observations of small plastic debris using continuous plankton recorder (CPR) surveys in bodies of water date to the 1960s, but the first evidence of sea borne plastic debris was reported in 1972, in the western Sargasso Sea [39,40]. Thereafter, plastic debris was reported in the North-Western Atlantic Ocean [41] and South Atlantic Ocean [42], and inside animals [43]. Investigations into the source of the plastic debris revealed that macroplastics discarded in the environment when exposed to atmospheric agents such as sunlight and ocean waves, results in photo-oxidation and abrasion deteriorating the material into the smaller plastic debris [44]. Another mechanism identified for the breakdown of macroplastics into plastic debris is their biodegradation by microorganisms in the environment [45]. Prior to 2004, and Thompson et al. [46] introducing the term

“microplastic” (<0.5cm) for the first time, no universally accepted terms existed to describe these tiny plastic particles, instead being commonly referred to as "plastic pellets" [42] and "plastic particles" [41,43]. Since then further size classification has taken place by L. Lebreton et al. [47]: with megaplastic (>50 cm), macroplastic (5-50 cm), mesoplastic (0.5-5 cm) and microplastic (<0.5 cm). Further sub-classifications then followed with large microplastics (1-5 mm) [48], small microplastics (0.3-1 mm) [49], and nanoplastics (<0.3mm) [50]. The size-based definition of nanoplastics has since changed, but no standard definition has been reached. This is because whilst most researchers use the conventional definition of nanoparticles, recognised in the ISO standard [51,52] as having dimensions ranging from 1 to 100 nm in all three directions [53-55] (and thus microplastics are larger than 100nm but smaller than 5mm), many define them as being of less than 1 micron (and thus a higher lower limit for microplastics), which confusingly is also the ISO standard for nanoplastics. Further controversy then lies in a sub-division of microplastics based on their origin or source, being either primary or secondary. Some define primary microplastics as those being produced intentionally for commercial applications, such as within the form of microbeads [56], cosmetics and nurdles [57], whilst secondary microplastics result from the degradation of larger plastic products once they are in the environment [58]. Other definitions of primary microplastics includes one that also adds microplastics that are directly released into the environment from the use of products that bear them, such as through tyre abrasion and laundering of synthetic garments [59] and another goes beyond that to also include microplastics that are generated from spills of products such as paints during the production of any product, whilst the microplastics resulting from the peeling and flaking of paints are secondary microplastics [60]

1.6.2 Introduction to the Environment

There are many different routes through which MNPs enter the environment (Figure 1.6).

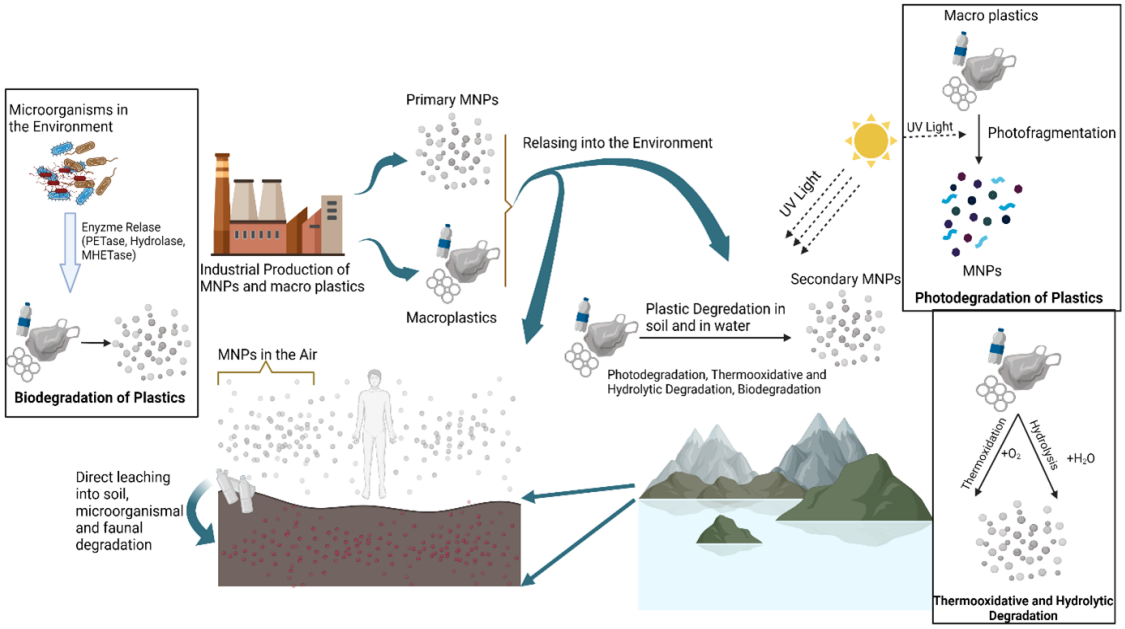

Figure 1.6: Various pathways for the introduction of MNPs into the environment [61].

They can enter soil through landfill leaching, and agricultural practices and products, whilst many microplastics enter the aquatic environment from waste water treatment plants (WWTPs) [62-65]. Micro/nano beads, which are present in personal care products [66] like facial cleansers [67], often find their way into wastewater systems upon the use of these personal care items and despite their management at WWTPs, every day approximately 8 trillion of them are released from them into the aquatic environment just in the United States alone [54]. Within the soil microplastics can be consumed by organisms such as earthworms whose digestion can lead to their breaking down into smaller MNPs, another pathway for their entry into the environment [68]. MNPs that make their way into the air, water, and soil via these various routes can enter living beings via ingestion, inhalation and dermal contact [69]. For ingestion, aquatic organisms may consume microplastics while filter-feeding or mistaking them for food, accumulating in their gut before translocating to redistribute in other tissues and systems of [70,71]. Therefore although only mussels and clams are eaten whole, and therefore also their guts [72], MNPs can enter the human food chain from all aquatic species if consumed directly or indirectly by humans. Another potential source for MNPs to enter the human food chain is through the ingestion of organisms that have inhaled airborne MNPs whereupon they accumulate in their tissues. In addition to the ingestion of MNP bearing organisms, edible items such as honey [73], beer [74] and salt [75] are common sources for MNP ingestion, as are exposed meats or other food products, whilst it can also take place indirectly through the release of MNPs from food packages and containers [76]. Humans can also be exposed to MNPs directly through the inhalation of airborne MNPs arising from

atmospheric fallout, wave action in aquatic environments or the application of wastewater treatment sludge on agricultural land. Dermal contact specifically takes place through the use of care products [66,77]. Summarizing, MNPs are found throughout the ecosystem, including freshwater [48], saltwater [78], ice cores [79], soil [80], air [77], plants [81], various organisms [82], and even the human body [44].

1.6.3 Harmful Effects of MNPs

The preceding sub-section illustrated how MNPs enter the ecosystem and the human food chain, and within this sub-section a comprehensive understanding of the full extent of their impact on the environment and living organisms is provided through considering their toxicity and associated harmful effects. For their potential impact on human health, experiments have taken place where mice were exposed to MNPs, within which they were found to accumulate in vital organs such as the liver, kidney, and gut [83]. Furthermore, energy and lipid metabolism indicators suggested prejudicial consequences, there was a significant reduction in total cholesterol (T-CHO) and triglyceride (TG) levels and lipid droplets were detected in the liver, suggesting that MNPs can cause lipid metabolism problems and liver inflammation in mice. Compared to controls, mice exposed to PS microplastics were also found to have less intestinal mucus and significant changes in the richness and diversity of their gut bacteria [84,85]. Results obtained from other animal models demonstrated that exposure to MNPs can lead to other adverse effects, including oxidative stress [86], diminished cell viability [87], neurotoxicity [88], genotoxicity [89], heightened reactive oxygen species (ROS) [90], inflammation [91], endocrine disruption [92], and reduced reproductive capacity [93]. The manifestation of these toxicities is influenced by several interacting factors, such as the MNPs' disruptive, penetrating, absorbing, and endocytosis capabilities [94], whilst the diverse ways in which MNPs enter and interact with cells and tissues also plays a crucial role [95,96], their size being key, with smaller particles exhibiting greater harm than larger ones [97,98].

Nonetheless, although nanoplastics are small enough to cross cell-wall boundaries and damage cell nuclei [99], the primary concern for MNP toxicity frequently arises from the molecules and metals they can transport, which are thus considered the primary toxins [100-102]. Among these primary toxins are a variety of environmental pollutants such as polycyclic aromatic hydrocarbons, pesticides, chlorinated biphenyls, and heavy metals such as cadmium, zinc, nickel, and lead once in the human body they can be released to accumulate in the tissues, causing harm to health [103,104]. Furthermore, biological contaminants such as algae, fungi, bacteria, viruses, and other microorganisms can also attach to the MNPs in the environment to cause damage to human health, including

through diseases such as viral infections, gastrointestinal disorders, asthma, migraines, or dermatitis, and in the most serious cases, chronic pathologies such as heart disease or osteoarthritis [105] can be cause by the 'bio-corona' of the MNPs. Moreover antibiotics may bind to the surface of MNPs and upon entering the human body potentially favour the emergence of antibiotic resistance with drastic impacts for the human race, whilst dispersants and preservatives used to suspend plastic particles may contribute to observed toxicological effects [86]. In addition to the adsorption of contaminants, additives used to improve the properties of plastics during their manufacture, such as plasticizers, flame retardants, stabilisers, and antioxidants, are known to leach into the environment, particularly during the formation of MNPs. Some of these plasticizers and additives are linked to the induction of endocrine disruption, with Bisphenol A (BPA), a widely used additive in plastic manufacturing, being one such example, with numerous studies showing its potential to cause a variety of diseases, including breast cancer, infertility, and cardiovascular [106]. It should be noted however that the nature and quantity of the aforementioned compounds adsorbed onto and/or leached out from MNPs are dependent upon the physical and chemical properties of the MNPs, the prevailing environmental conditions, and the intermolecular forces established between the components and the plastic particles [107]. Nevertheless, it is evident that human exposure to MNPs is inevitable, subjecting individuals to equal risks from the adverse effects linked to ingested MNPs, the contaminants adsorbed by them, and the additives leached from these particles.

1.6.4 MNP Analysis

Given the presence of MNPs in the environment and human food chain and subsequently the impact of these particles on human health, it is clear why the omnipresence of MNPs has been recognized as a huge threat to the ecosystem and all life forms within it. This had led to the commitment of numerous stakeholders to their proper management and thus regulatory measures [108] including global legislative measures such as the Microbead-Free Waters Act of 2015 in the USA [109] which has restricted or banned the production and use of primary MNPs such as microbeads, Senate Bill (S.B.) 1422 of 2018 [110] requiring the California State Water Resources Control Board to develop testing methods for the control of microplastics release in drinking water, S.B. 1263 of 2018 [111] requiring the California Ocean Protection Council to implement strategies to mitigate microplastics pollution in the marine ecosystems, and Commission Regulation (EU) 2023/2055 - The Microplastics Restriction of 2023 [112] restricting the production of synthetic polymer microparticles on their own or intentional addition of such particles to

other products. However, to enforce such regulatory measures and legislations, there is a need for standardized analytical techniques for MNPs, with current procedures, compared to those for microplastic analysis being also laborious and challenging. The analysis of MNP samples in all matrices can be broadly categorised into two steps: sampling and identification (Figure 1.7). While the identification step aligns with the focus of this thesis and will be explored in greater detail, a cursory overview of the sampling step will also be provided to offer a comprehensive understanding as the methods used within the former are often determined by those used within the latter, which are typically matrix dependent.

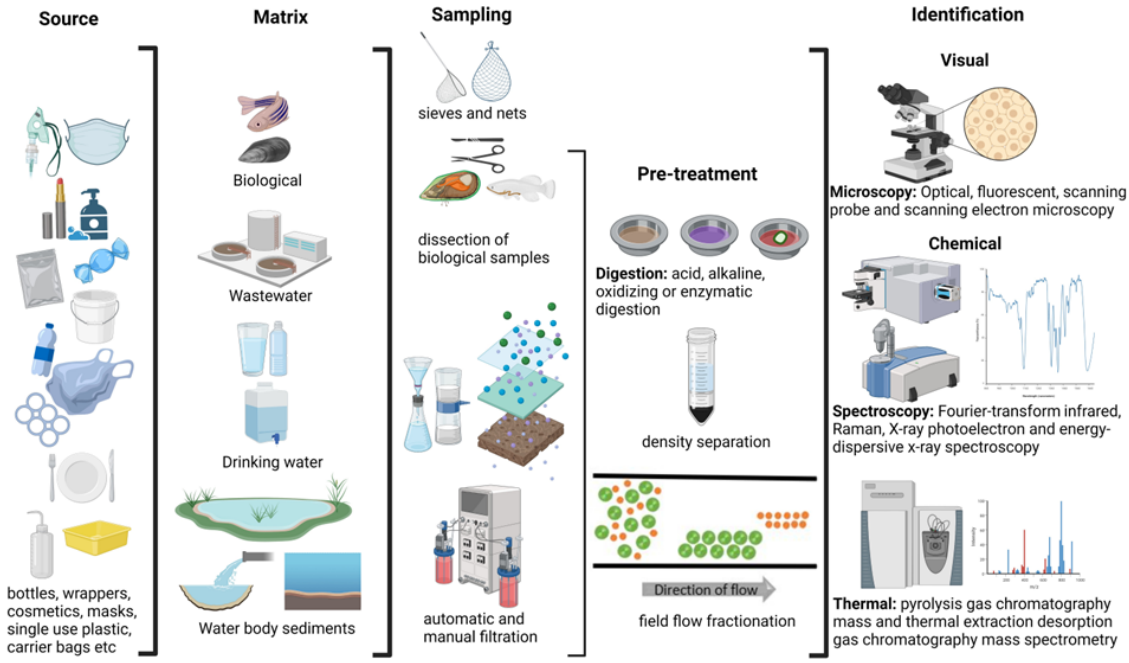

Figure 1.7: Overview of MNP analysis process consisting of sampling and identification [61].

1.6.4.1 MNP Identification

The detection, identification and enumeration of MNPs in matrix samples are intricate tasks due to their diverse shapes, sizes, and colours, being difficult, if not impossible, to achieve by a single analytical technique with combination of two or more usually employed [113]. Those techniques can be broadly classified based on the information they provide, falling into two categories: visual identification and chemical identification. The time consuming chemical analysis of MNPs is typically performed following a visual analysis, often with an optical microscope, to aid in the identification of smaller and less conspicuous MNPs, serving as a discriminative step to identify potential MNPs from other particles [61]. This reduces the risk of false-positive identifications and thus provides more accurate data on the number and type of MNPs.

1.6.4.2 Visual Identification

Large microplastics, whose sizes range from 1 to 5 mm, are typically visible to the naked eye whilst an optical microscope becomes a necessity for viewing smaller microplastics between 0.3 to 1 mm. Through the use of either techniques they can be distinguished from non-plastic materials by characteristics such as morphology, colour, and light transmission properties, however simply relying on these characteristics can be misleading, resulting in false positive and/or negative instances and thus overestimation or underestimation of the amount of microplastics in a sample [114]. Other visual identification techniques are also used, especially for smaller particles, and Figure 1.8 shows a bibliometric analysis of the Web of Science's (WOS) database (from the early 1970's until mid-2023) for literature published on the visible detection of MNPs. It includes the microscopy techniques of stereo or dissecting microscopy, fluorescence microscopy, transmission electron microscopy (TEM), scanning electron microscopy (SEM), atomic force microscopy (AFM), dark field, and hyperspectral imaging techniques. The number of publications per year for the visual identification of MNPs, both for review and research articles, can be seen in Figure 1.8a, whereas Figure 1.8b lists the ten countries that have published the most research in that area and Figure 1.8c depicts the distribution of publications in a map chart.

(a)

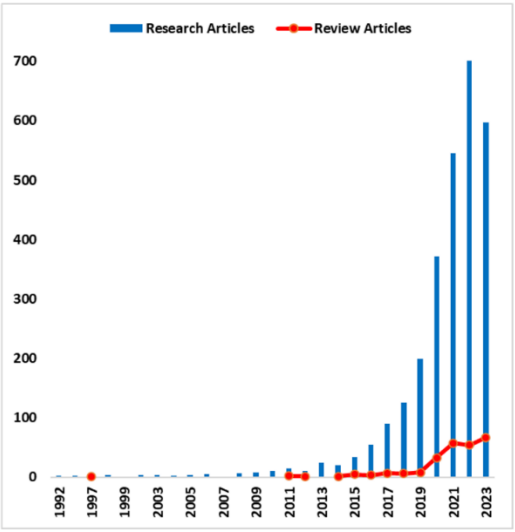

(b)

County	No. of Publications
China	951
USA	360
Germany	247
India	199
England	193
Italy	189
Spain	147
Canada	139
Australia	135
France	119

(c)

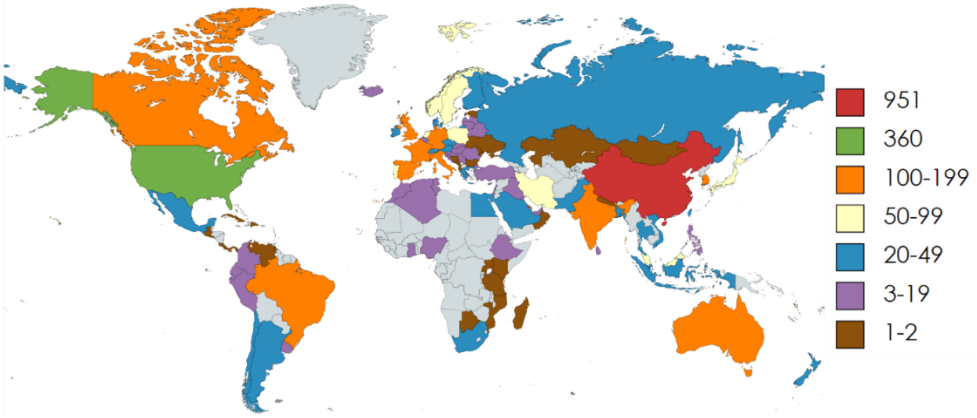

Figure 1.8: Bibliometric analysis done on publications in WOS from 1970 until 2023 on the visible analysis of MNPs: (a) number of articles published annually, (b) the 10 counties that have published the most research, (c) map chart showing the worldwide distribution of research done in the field.

Typically, microscopy based techniques for visual identification of MNPs fall within the following four groups: (a) optical microscopy [115,116], (b) fluorescence microscopy [117,118], (c) scanning probe microscopy (SPM) [119,120], and (d) electron microscopy (EM) [121,122]. Optical microscopy magnifies the visible light image of an object, thereby making detection of microplastics and its structural properties possible, however, the diffraction limit makes it ineffectual for detecting sub-micron microplastics and thus nanoplastics**.** Fluorescence microscopy, although also restricted by the diffraction limit, has been reported [123] to successfully detect much smaller particles (down to sub-micron range) due to the emission from the dyed particles. Nevertheless, chemical additives and/or environmental contaminants within MNPs may also exhibit fluorescent properties and so fluorescence microscopy can lead to an overestimation [61]. Unlike the previous two techniques, SPM and EM are not optical techniques and so are not diffraction limited;

therefore they have the potential to detect nanoplastics, with the former technique having the ability to provide very detailed morphological information for MNPs [121]. That with said both require highly expensive equipment that must be operated by specially trained and skilled personnel, making them expensive techniques. In general, although the aforementioned visual techniques are used for the detection of MNPs, they cannot provide the necessary information on their chemical composition to identify them and they can provide misleading information due to the limited, commonly morphological, information they can provide. Techniques that provide the necessary chemical identification of MNPs will be covered in the following subsection.

1.6.4.3 Chemical Identification

Visual techniques can identify impurities within samples extracted from 'real world' matrices, that remain following even optimal sample preparation, as MNPs. The avoidance of this type-I error is the fundamental reason for coupling visual identification (for morphological and quantitative information) with chemical identification (for plastic type and chemical properties), with the most commonly used analytical techniques for the latter broadly classified into: (i) thermal techniques and (ii) spectroscopic techniques. These techniques are discussed in detail in the subsequent subsections; with spectroscopic techniques more so as they are more relevant to this thesis. Figure 1.9 shows a bibliometric analysis done using the Web of Science's (WOS) database from the early 1970's till date, for literature published on the chemical identification of MNPs whose techniques include Fourier-transform infrared spectroscopy (FTIR), Raman spectroscopy, X-ray photoelectron spectroscopy (XPS), energy-dispersive x-ray spectroscopy (EDX/EDS), Nuclear Magnetic Resonance (NMR), photoluminescence spectroscopy, and mass spectrometry.

(a)

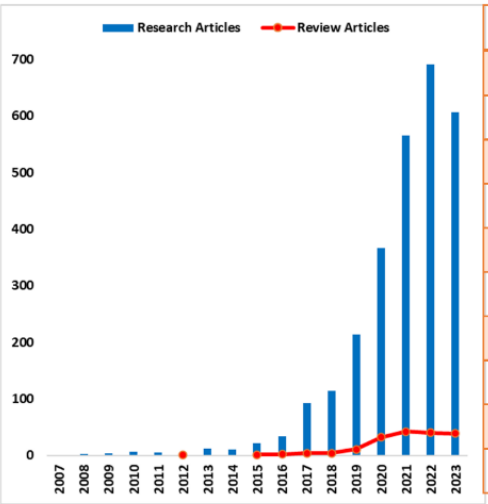

(b)

County	No. of Publications
China	668
USA	298
Germnay	271
Italy	233
India	222
Spain	157
England	137
Australia	132
France	126
South Korea	122

(c)

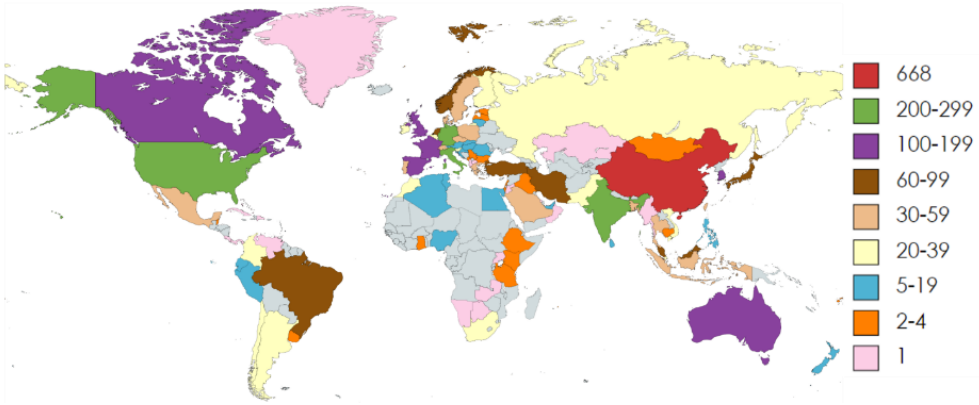

Figure 1.9: Bibliometric analysis done on publications in WOS from 1970 until 2023 on the chemical analysis of MNPs: (a) number of articles published annually, (b) the 10 counties that have published the most research, (c) map chart showing the worldwide distribution of research done in the field.

1.6.4.4 Thermal Techniques

In thermo-analytical techniques, a bulk sample is heated in an inert environment to high temperatures to examine decomposition patterns and by-products, allowing the chemical composition of the analyte to be determined. As the physical and chemical characteristics of polymers are dependent on their thermal stability [124] thermal techniques are therefore often used as a complementary technique to spectroscopic methods for a thorough analysis of MNPs, especially for less soluble MNPs and additives that are difficult to dissolve, remove, or hydrolyze [125]. The selectivity they offer makes them suitable for examining mixtures of diverse MNPs and thus highly appropriate for analysing complex environmental samples [126]. In contrast to spectroscopic techniques, which are primarily used for polymer identification, thermo-analytical techniques provide both qualitative and mass-based quantitative information [127], which is complementary to the quantitative and

morphological information from visual identification techniques that have limitations when converting particle count data to mass due to the highly variable morphology of microplastics that necessitate strong approximations when calculating shape and density. However, thermo-analytical techniques do not provide spatial resolution for allow for further analysis due to their destructive nature. Nevertheless, the popularity of these techniques for MNP analysis continues to grow due to the valuable information they offer on mass and concentration, and also particularly because of the lower limits of detection that they offer for nanoplastics compared to spectroscopic techniques [128]. Pyrolysis (PY) gas chromatography (GC) mass spectrometry (MS) (or PY-GC-MS) [129,130] and thermal extraction desorption (TED) gas chromatography (GC) mass spectrometry (MS) (or TED-GC-MS) [131,132] are both commonly used variants that share a very similar working principle whose thermally degraded sample fragments are separated by gas chromatography and characterized by mass spectrometry [133]. In comparison to TED-GC-MS, Py-GC-MS offers greater sensitivity, enabling analysis of lower quantities of nanoplastics [134], but it is only suitable for simple matrices, whereas TED-GC-MS also works fine with complex matrices, even for those with organic and inorganic contaminants without any sample preparation [126]. Whilst PY-GC-MS and TED-GC-MS are both particularly attractive for bulk samples; the former is restricted by the size of the pyrolyzer making it unsuitable for large quantities of samples. Furthermore, whilst the thermal techniques provide data of analyzed plastic samples on a weight basis, their destructive nature results in quantitative information such as the number, size and shape of the analyzed particles being lost, although this can be avoided by first putting the sample through a visual analysis (see subsection 1.6.4.2). Finally, a significant drawback of the thermal techniques is their reliance on high-maintenance expensive equipment that necessitates specially trained and skilled personnel to operate them, rendering these techniques very costly and with most not being operable at Point of Site [113].

1.6.4.5 Spectroscopic Techniques

Spectroscopy is the wavelength-dependent study of the interaction of light with matter, and its ability to provide atomic and molecular identification allows for the chemical characterization of samples, and thus is largely used for the analysis of MNPs. To date the different types of spectroscopic techniques used for MNP detection are FTIR [135,136], Raman spectroscopy [137,138], XPS [67], [139], EDX [118], [140], and photoluminescence spectroscopy [141,142]. This thesis focusses on vibrational spectroscopy techniques, such as FTIR, but mostly Raman spectroscopy and its variant SERS, which are typically used in conjunction with optical microscopy as an integrated

approach for the chemical analysis of MNPs [143,144]. FTIR and Raman spectroscopy are complementary techniques that provide chemical analysis of MNP, either through a change in dipole moment or a change in polarizability, respectively. Both however have a sized based limit of detection for MNPs given the due minimum spatial feature resolution of each, which is 10 μm and 1 μm respectively, that has led researchers to combine them with electron microscopy, although with inevitable elevated analysis costs.

FTIR spectroscopy consists of two steps: (i) the irradiation of a sample over a broad range of infra-red frequencies and, (ii) the Fourier transform of the obtained interferograms; following these steps a characteristic fingerprint spectra corresponding to specific molecular vibrations is obtained [145,145]. Three distinct modes of operation are commonly used for the FTIR analysis of microplastics: transmission [146,147], reflection [148,149], and attenuated total reflection (ATR) [150,151] with the choice of mode used determined by the specific physical properties of the microplastics within a sample. Although FTIR in transmission and reflection modes of operation provides resolution of just 10 μm; ATR-FTIR spectroscopy the significantly higher numerical aperture of ATR-FTIR objectives have led to it successfully identifying nanoplastics present in facial scrubs; although the sample was of a few milligrams [67], [152].

In Raman spectroscopy, samples are irradiated with a monochromatic laser source of a wavelength typically between 500 nm – 800 nm. Vibrational, rotational, and other low-frequency interactions between the light and its molecules and atoms cause shifts in the wavelength of the backscattered light from that of the incident laser light, with the detectable shifts forming a substance-specific spectra [153]. Given that MNPs, like other substances, have unique Raman spectra, this technique can quickly identify them by comparing measured spectra to that of well-established libraries of reference spectra. Raman spectroscopy has been used in conjunction with confocality and to identify plastic particles of various sizes, including those smaller than the spatial resolution limit of conventional Raman spectroscopy of 1 μm [154]. The better resolution from confocal systems is attributed its specificity in providing signal from a particular point of the sample at a specific depth rather than an averaged signal, therefore supressing unwanted signal (noise) originating from the background [155].

Raman spectroscopy has many advantages over FTIR spectroscopy. Firstly, spectral analysis for FTIR can only be undertaken on dry sample due to significant water absorption by near-infrared light, whilst Raman requires minimum or no sample preparation (except for those with impurities that may be highly fluorescent). Secondly, unlike FTIR spectroscopy, the spectral intensities of Raman spectroscopy are proportional to the amount of sample, making it suitable for quantitative analysis. Nevertheless, Raman

spectroscopy has its own limitations, the most important being an inherently low-intensity signal and susceptibility to auto-fluorescence [156]. Additionally, Raman spectra are less sensitive to compositional changes, which is disadvantageous when the environmental impact on a sample needs to be studied [157]. To overcome the issues of low intensity, as well as to resolve particles of 1 μm or less in size, researchers have begun to use SERS, for greater sensitivity and improved resolution limits compared to Raman [158]. Chapter 2, where the state of art for Raman and SERs is presented, shows that SERS is the most promising technique and thus the predominant technique used in the experimental work presented in this thesis. Although SERS is the most promising there are technological limitations for its characterisation of nanoplastics and given the 'dangers' posed by them work in the experimental chapters focuses on the development of SERS for nanoplastics detection.

The preceding discussion highlights the inherent strengths and limitations of each analytical technique. While there is evidence supporting the complementary nature of combining two or more techniques for enhanced MNP detection results, existing literature indicates a lack of standardization across various aspects of MNPs, including the processes for sampling, sample preparation and analysis [159]. As work to standardise definitions, classifications, MNP sampling, sample preparation, detection, and risk analysis advances, it contributes to a more nuanced understanding of the origin and nature of MNP pollution and its adverse impacts, laying the groundwork for effective mitigation strategies and future research.

1.7 Thesis Structure

The body of this thesis is composed of six chapters with the following general content. The first focusses on the overall introduction of the problem, whilst the second presents the detection techniques relevant to the experimental work presented in later chapters and the state of the art for those techniques for MNP detection. After which there are three experimental chapters, with each having its own brief, standalone literature review for a better understanding of the conceptualization behind the experimental design. The final chapter summarises the principal findings and their relevance from the three experimental chapters, before providing a perspective on where and how parts of this work could be continued and/or used to advance research elsewhere.

Despite having gained the attention of the research community due to its suspected higher risk (Chapter 1), bibliometric analysis of the last decade [38] still shows a lot less research has been done on the detection of NPs as compared to MPs" "This can be attributed to the challenges in detecting them through the use of current analytical technologies, with

Chapter 2 specifying where these lie for SERS analysis, the most promising technique, and thus the focus of experimental work in Chapters 3-5. The specific content of each is thus:

Chapter one, 'Introduction', starts off with the history of plastics and their evolution over the time; it focuses on how mass production of plastics coupled with their improper discard has led to the dilemma of MNPs. Following the origin of MNPs and their introduction into the environment, the chapter continues with the toxicity of MNPs by such means, highlighting the adverse nature of the problem, following which the chapter focuses on its solution by detailing the MNP analysis process with a focus on the detection of MNP, particularly spectroscopic analytical techniques used for detection and identification of MNPs which concludes the first chapter.

Chapter two, 'Background', integrates the overall theoretical concepts involved in the analytical techniques of Raman spectroscopy and SERS with detailed discussion and critical evaluation of the state of the art in MNP detection using these two techniques. The section on theoretical concepts starts off with the working principle of Raman spectroscopy, following the reason behind the need for SERS, and subsequently its working principle. The advantages offered and limitations of Raman spectroscopy and SERS are also discussed to give a comprehensive background of each of the analytical techniques. The chapter details the different aspects that need to be considered for MNP detection through these techniques, with special focus on the different types of SERS substrates developed and utilised for MNP analysis over time.

Chapter three, 'Utilising salt-assisted aggregation of gold nanoparticles for detection of nanoplastics', is based on NaCl aggregation of AuNPs for detection of nanoplastics. The work presented in this chapter is the first ever instance of salt assisted aggregation of AuNPs for SERS based nanoplastic detection, unlike previous aggregation-based nanoplastic detection studies which used Ag nanoparticles (AgNPs) [160]. The developed methodology was also tested for nanoplastic detection in drinking water via spiking experiments.

Chapter four, 'Detection of nanoplastics through the use of surface enhanced Raman spectroscopy with controlled clustering of gold nanoparticles by forming hydrophobic SERS substrates', following the uncontrolled aggregation of AuNPs achieved via salt, better controlled and sophisticated controlled clustering of AuNPs was attempted through the use of hydrophobicity. It describes how the surface of aluminium foil (ALF) can be modified to form a hydrophobic layer which can then be used to cluster AuNPs in a more organised manner resulting in a more homogeneous SERS substrate as compared to the previous approach of salt aggregation of AuNPs.

Chapter five, 'Detection of nanoplastics through the use of surface enhanced Raman spectroscopy (SERS) substrates with islands of gold nanoparticles (AuNPs) formed with cucurbit[5]uril (CB[5])' focuses on the development on a unique SERS substrate. The methodology developed in this chapter is much more sophisticated than both the salt-assisted aggregation and hydrophobic clustering of AuNPs as it relies on surface functionalisation of ALF to systematically introduce a layer of AuNPs onto the ALF. The AuNP aggregates like islands formed due to CB[5] attach onto ALF via the layer of AuNPs.

Chapter six, 'Summary and Future Work' compares and contrasts all the major findings of thesis with those found elsewhere in literature, therefore highlighting the importance and impact of the work presented with the thesis. The highlights are followed by a brief dive into potential future work which concludes the monograph.

Chapter Two

Background

2.1 Theory of Raman based techniques

As seen in the previous chapter over the years various analytical techniques have been used for the detection, identification and quantification of MNPs. In this section, theoretical concepts of those analytical techniques relevant to the work carried out during the PhD, Raman and SERS, are briefly described to help develop a basic understanding of their working principles and parameters that require consideration when using them for MNP analysis.

2.1.1 Raman Spectroscopy

Raman spectroscopy is a non-destructive technique that provides in-depth information on the molecular composition and structure of an analysed substance [161], or analyte, through the analysis of light scattered from its chemical bonds. Usually, when high-intensity light scatters from matter, it does with the same energy, and thus frequency and wavelength, as the incident light, and is known as elastic or Rayleigh scattering. However, some of the light, 1 in 10^6-10^8 photons, does so with a different energy, undergoing what is known as inelastic, or Raman scattering. The inelastic effect arises from an exchange of energy between incident photons and molecules within the scattering medium of the analyte, with the scattered light resulting in either a lower or higher energy or frequency (and thus a lower or higher wavelength), than the incident light, being known as Stokes or anti-Stokes Raman scattering, respectively (Figure 2.1a). The change in energy is associated with the vibrational energy levels of the electronic ground state for the molecules within the scattering media, and thus the observed Raman shifts provide a measure of the types and quantities of molecular vibrational energies, and thus a characterization of the sample. As only molecules whose vibrational energies are above the ground state prior to irradiation, which is less densely populated, can give rise to anti-Stokes scattering, it is of comparatively lower intensity and thus it is the Stokes scattering that is usually observed in Raman spectroscopy (Figure 2.1b) [162]. With Raman scattering dependent on virtual states, all bond energies can be observed largely independent of the excitation wavelength making it a very powerful technique.

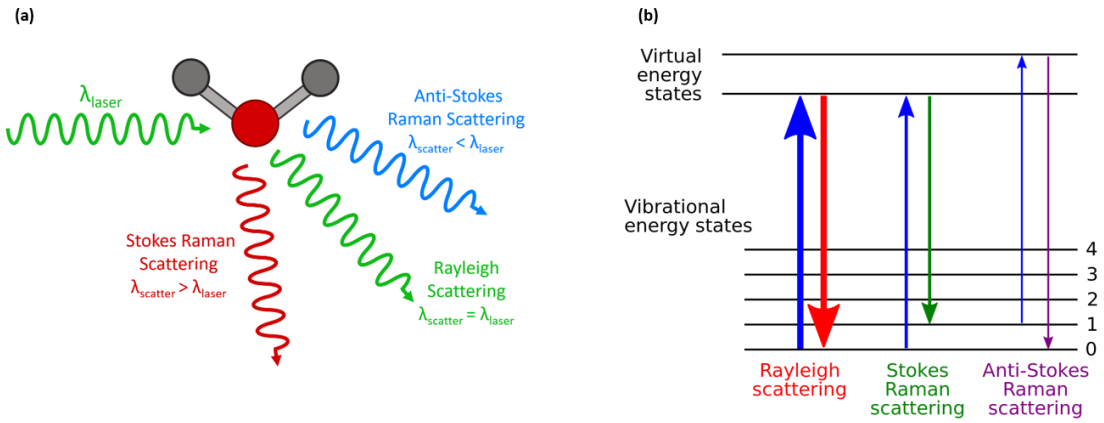

Figure 2.1: (a) The fundamental working principle of Raman scattering (b) A basic Jablonski diagram of the Rayleigh and Raman scattering processes.

For smaller sizes of analyte, or particles, these can be characterized through combining Raman spectroscopy with an optical microscope, thus being known as micro-Raman spectroscopy or μ-Raman spectroscopy. The optical microscope in μ-Raman spectroscopy results in high magnification visualisation of a sample and thus the maximum collection of light to characterize microscopic samples, or microscopic sections of larger samples [163,164]. Additionally, spatially resolved Raman spectra from μ-Raman spectroscopy can be used to create chemical images of samples to enable the visualization of its molecular variations at micron scales [165]. Furthermore, the combination of a Raman spectrometer to an optical microscope with a spatial filter, commonly in the form of a pin-hole, results in a confocal Raman spectrometer, capable of high resolution chemical analysis of sub-microscopic samples or sub-microscopic sections of larger samples [166]. The confocal optics within a confocal Raman spectrometer allows for spatial filtering of the analysis volume within a sample, providing high resolution along both the lateral (x-y) and axial (z) axes [166,167]. Subsequently, confocal Raman spectroscopy provides the highest degree of spatial resolution, allowing for chemical analysis of samples along their depth, and thus suitable for the analysis of layered sub-microscopic or sub-microscopic sections of samples [167].

Four different geometries can be used in Raman spectroscopy, chosen on the basis of the application and sample to be characterised, and are known as: Backscattering [155,157,168]; Transmission [169-171]; Spatially offset Raman spectroscopy (SORS) [172-174]; Universal Multiple Angle Raman Spectroscopy (UMARS) [175-177]. Transmission geometry is suitable for thin or non-highly absorbing samples as the illumination of sample and collection of Raman signal is done from opposing sides of the sample, thus allowing for the probing of the entire thickness of a sample, making it a popular choice when representative analysis of the bulk of a sample needs to be done

[178]. For diffraction-limited spot sizes Backscattering offers better spatial resolution, however, it cannot provide a detailed analysis of layered samples. SORS can provide that however as it introduces an offset when collecting the scattered signal with respect to the illumination, with increments in the collection offset increasing the intensity of the Raman signal of the inner layer compared to the outer layer [176]. Finally, UMARS is used to analyse samples embedded deep within highly scattering media as the collection direction is independent of the direction of illumination [176]. Thus, although traditionally the first two geometries were usually used, SORS and UMARS have become more and more popular recently.

For all Raman spectroscopy geometries, the consideration of laser stability, line width, power and wavelength are crucial. The first two parameters determine spectral resolution, with a poor one corresponding to broadened spectra and the inability to resolve peaks for analysis. Thereafter, the choice of laser power and wavelength determines Raman signal intensity, being linearly dependent on laser power but also inversely proportional to the fourth power of the excitation wavelength which leads to a low intensity (see drawback i). This dependence on wavelength leads, where possible, to shorter wavelengths within the visible or even UV range being chosen over the near-infrared (NIR) or infrared (IR) region. Where possible, because samples that produce fluorescence (see drawback ii) and photo-degradation that can obscure Raman spectral peaks do so more at lower wavelengths due to electronic excitation within molecules. With low intensities requiring signal integration and therefore long measurement times (see drawback iii) accumulated irradiation can damage samples (see drawback iv). Thereafter this choice is further convoluted given that there is a significant decrease in quantum efficiency for typical detectors at NIR and IR wavelengths that necessitates the use of considerably more expensive indium gallium arsenide (InGaAs) detectors [155].

(i) **Low Intensity:** As aforementioned, being inversely proportional to the fourth power of the wavelength, a Raman signal is of extremely low intensity that with said a lower frequency source is often used to resolve Raman signals as fluorescence diminishes at longer wavelengths [170].

(ii) **Fluorescence:** When the energy of an incident photon, and thus laser source, is nearly equal to the transition energy between two electronic states an electron can transition to a higher electronic state instead of a virtual state, that upon relaxation to the lower energy state results in broadband fluorescence which can mask the much lower intensity and narrower Raman signals [179].

(iii) **Slow Measurements:** With its low intensity, a long integration time is typically required to increase the signal to noise ratio (SNR) of the Raman signal to a

detectable level. This particularly true when Raman spectroscopy is used for single-particle analysis [121].

(iv) **Destructive:** Although Raman Spectroscopy is inherently a non-destructive technique it does involve focusing high-power lasers over a small area for long durations, which can result in damaging samples of a biological and polymeric nature [180].

With the majority of the drawbacks deriving from the low-intensity signal, various improvements and enhancements in optical sources and detectors over the years has resulted in an improvement of the SNR for Raman spectra, however, these there are limited particularly for small samples. For such samples, certain variants of Raman spectroscopy have been adopted [137,181,182,183], with the one of most relevance to this project being the only one discussed hereafter, surface-enhanced Raman scattering (SERS).

2.1.2 SERS

SERS was first identified in 1974 by M. Fleischmann and his colleagues when signal enhancement was observed for Raman scattering measurements of pyridine adsorbed on a rough silver electrode [184], although it was initially attributed to just an increased surface area due to the protrusions of its roughened surface [185]. In 1977, two groups, comprising of Jeanmaire and Van Duyne [186], and Albrecht and Creighton [187], independently identified this phenomenon and reported enhancement factors (EFs) of 10^5 – 10^6, with the latter group correctly attributing it to plasmon excitation [185]. Since then, enhancement factors (EF) of up to 10^{14} have been observed [188,189], although values of only 10^5 – 10^8 are usually observed for entire SERS substrates [190,191].

It was Moskovits [192] who successfully identified that the enhancement was specifically due to the enhanced electric fields arising from the localized surface plasmons generated by the nanostructured metals. Surface Plasmons, predicted by R. Ritchie in 1957, are coherent delocalized electron oscillations that exist at any interface between two materials where the real part of the dielectric function changes sign across the interface, typically a metal-dielectric interface, such as a metal sheet in air. The charge motion in a surface plasmon always creates electromagnetic fields outside (as well as inside) the metal, with the two forming a total excitation, either as a surface plasmon polariton at a planar interface, or a localized surface plasmon for the closed surface of a small particle. Under resonant conditions those excitations become surface plasmon resonances, or SPR (Figure 2.2a), and local surface plasmon resonances, or LSPR (Figure 2.2b), respectively., with the latter arising when the SPR is confined to a particle size comparable

to the wavelength of incident light, causing the free electrons of the particle to collectively oscillate [193].

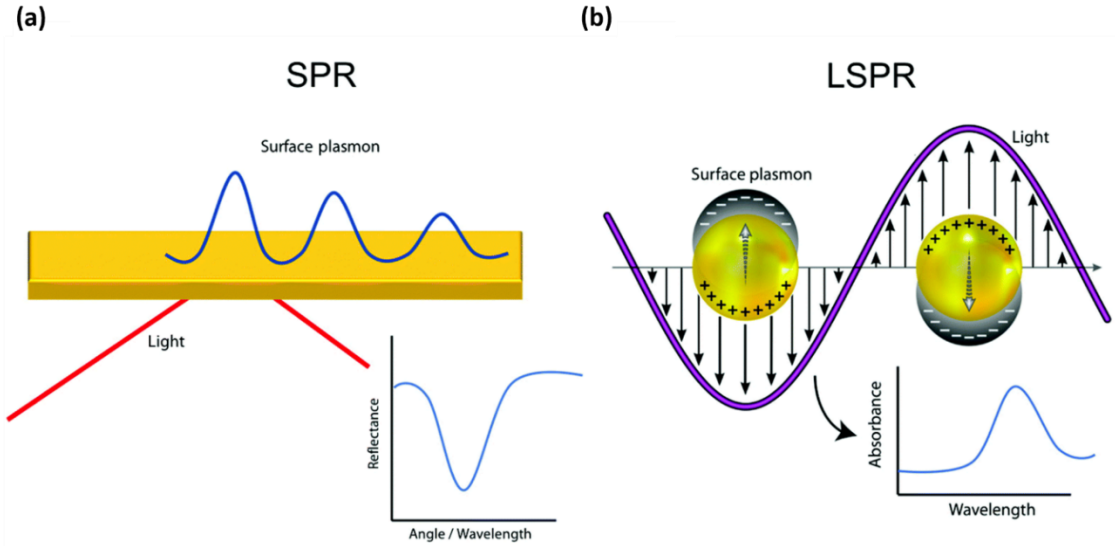

Figure 2.210: (a) Generation of a SPR when a metallic film is excited under resonant conditions by photons (b) Generation of LSPR when a metallic nanoparticle is under resonant conditions by photons.

For LSPR, where there is no travelling wave, it specifically occurs in metallic structures, such as metal particles, that have a lateral size that is less than half the wavelength of its excitation source [194], leading to an enhancement of the electric field around them and thus enabling SERS (Figure 2.3) which is described hereafter.

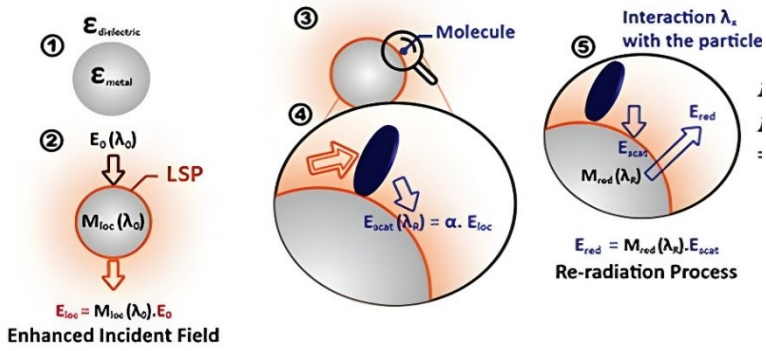

Figure 2.3: The SERS mechanism

The metallic nanostructures, which are surrounded by a dielectric material (1), are usually fabricated from the nobel metals of gold (Au), silver (Ag), copper (Cu), platinum (Pt) and palladium (Pd) as their plasmon resonance frequencies fall within the visible to NIR range and so Raman modes within them can be excited by light in those wavelength ranges. Thereafter the metallic nanoparticle is excited by an incident electromagnetic field or appropriate wavelength, creating a local electric field around it (2), and when an analyte molecule enters its vicinity, the local electric field polarises the molecule resulting in

Raman scattering (3&4). The Raman scattered signal then interacts with the nanoparticle itself, in what is termed the re-radiation process (5), resulting in the enhancement of the Raman signal. The overall enhancement observed is a combination of the electromagnetic (EM) enhancement, due to the excitation of plasmons in the metal nanoparticle, and the chemical (CH) enhancement, which is associated with the capability of analyte molecules to transfer electrons to/from the metal particles.

Although SERS can be achieved using a single nanoparticle; for practical use, elaborate substrates comprising of periodic arrays of metallic nanoparticles separated by nano-metre sized gaps are typically used due to the strong electromagnetic coupling between the adjacent metallic nanostructures that create localized plasmon modes [185] within the gaps, known as ´hot spots'. These 'SERS substrates' can provide an EF equal to 10^5 – 10^6 [195], [196], [197], with a broadening of the plasmon resonance peak due to coupling between adjacent nanostructures increasing the possibility of the resonance covering the Raman peak along with the excitation wavelength [198]. As its name suggests, the enhancement factor (EF) is a parameter used to quantify the enhancement of the Raman signal in the presence of metallic nanostructures, defined as the ratio of SERS to Raman measured intensities for an analyte and thus [199]:

$$EF = \frac{I_{SERS}}{I_{Raman}}$$

where:

I_{SERS} – the intensity of SERS signal for the selected peak.

I_{Raman} – the intensity of Raman signal for the same peak.

That with said, various formulas can be found in the literature to get the best practical estimation of EF, with one of the most commonly used one being the following [199,200]:

$$EF = \frac{I_{SERS}/N_{SERS}}{I_{Raman}/N_{Raman}}$$

where:

I_{SERS} – the intensity of SERS signal for the selected peak.

N_{SERS} – the number of analyte particles contributing to I_{SERS}.

I_{Raman} – the intensity of Raman signal for the same peak.

N_{Raman} – the number of analyte particles contributing to I_{Raman}.

With the EF of a substrate being a very important factor in SERS analysis the parameters which it depends upon, for a given wavelength, are detailed hereafter, being for the periodic array of nanostructures or particles, (A) the metal they are fabricated from, (B) the gap between adjacent nanoparticles and (C) their geometry:

(A) Given the cost of Pt and Pd, Au, Ag and Cu are usually used for the nanostructures, with Ag being the most popular as it offers higher enhancement, lower cost and ease of synthesis [190,201,202]. That with said Ag is easily oxidized due to oxygen and water vapour present in the atmosphere [203] leading to reduced lifetime and reproducibility, making stabilization of Ag nanostructures critical at such small dimensions [202]. Au is therefore also often used instead, especially at wavelengths longer than 600-650 nm where it has a comparable enhancement, having a lower enhancement below 600nm due to lossy plasmon resonance from lower absorption [190].

(B) Significant near-field interaction is found between adjacent nanostructures when the gap between them is not greater than half their width or diameter [198,204], with the enhancement increasing as the gap becomes smaller, in accordance with classical electromagnetics that predicts an inverse relationship between the gap and plasmonic enhancements [185,205]. This holds down to 1 nm whereupon quantum effects from electron tunnelling can occur affecting the plasmon energies, resulting in a reduced electromagnetic field and lower enhancement [185]. Fundamentally, for uniform maximum enhancement, precise control of the gap between adjacent nanostructures within the sub-10 nm regime is required, which is currently not possible through existing nano-fabrication methods [204].

(C) Larger nanostructures have a larger number of available electrons and thus enhancement [206], but only up until the length scale of the excitation wavelength, whereafter the SERS effect starts to diminish due to the excitation of nonradiative modes. Conversely, for smaller nanostructures, the effective conductivity and light scattering properties required for effective SERS enhancement reduce [207]. Finally, as well as the size and gap between them the enhancement is also dependent on the shape of nanostructures [204]. Non spherical or anisotroptic nanostructures, such as rods, hexagonal, cubical, star shape etc, are beneficial as they offer more intense near-fields at the sharp edges [208].

Given the above critical parameters the successful design and fabrication of substrates for SERS is a particularly formidable challenge. Whilst the design of SERS substrates is contingent upon the specific analyte under consideration, the methodologies for fabricating SERS substrates can be broadly classified into two categories: (i) top-down lithography and (ii) bottom-up synthesis. The former consists of the reduction of bulk metals to metallic nanostructures through the application of lithographic techniques [209], resulting in substrates with reproducible and uniform structures and thus a highly reproducible SERS signal. That with said, the use of sophisticated and expensive equipment for those techniques makes the substrates economically impractical for routine

real-world applications. Bottom-up synthesis however produces much more cost-effective SERS substrates as it relies solely on chemical processes rather than high-cost specialized equipment and highly trained operators. That with said its substrates have considerable move variability compared to the structural homogeneity of those fabricated through the top-down approach, which is attributed to the inherent challenges associated with exercising precise control over the chemical reactions that govern substrate formation. Despite this limitation, bottom-up synthesised substrates are widely used, particularly in applications where qualitative detection takes precedence over quantitative due to their low cost [210,211].

SERS substrates may be categorized alternatively based on their structural attributes, giving rise to three broad categories: (i) suspensions of metallic nanostructures, (ii) immobilized metallic nanostructures on substrates and (iii) metallic nanostructures fabricated or grown on a substrate [212]. To date the first typically has challenges for reproducible quantitative measurements due to the difficulties in controlling the number of enhancement nanoparticles within the vicinity of each analyte molecule [213]. The latter two have generally consisted of planar substrates that offer both a limited concentration of hotspots due to a single plane of surfaces only being available, and not true compatibility with 'in flow' analytical systems due to being located beyond several diffusion lengths of the flow of analyte in microfluidic systems [214]. In contrast, the latter two categories also include 3D substrates with their inherent large surface areas that can be exploited to increase the number of hotspots and sites for analyte adsorption leading to increased SERS enhancements and thus sensitivity [215].

For all types of SERS substrates, their application can be classified as either label-free or label-based SERS. Label-free SERS is a direct method that relies solely on the probability of analyte molecules being in proximity of hotspots in order to take advantage of the SERS enhancement. Label-based SERS methods however are indirect methods that utilise binding agents or SERS tags consisting of Raman reporting molecules which selectively bind analyte to the substrate. Unlike label-free SERS, this method helps target the analyte to the hotspots thereby increasing the sensitivity and repeatability. That with said, although the absence of a binding agent in the label-free method makes it less efficient it does the advantage of being simple, cost efficient and free of interfering signal from the binding agent or SERS tag [216,217]. The choice between label-free or label-based SERS method therefore depends on whether there is an appropriate binding agent for the analyte and the binding efficiency of the analyte to that agent.

In summary, through increasing the Raman signal to enable the detection and analysis of analytes that would have been otherwise difficult, if not impossible, to detect, SERS has

proven to be very useful, although the following key considerations must be made for its use:

Substrate Preparation: For quantitative analysis uniform and reproducible enhancement is required and thus a uniform SERS substrate that can be reproduced. Production of such substrates is challenging, costly and time-consuming, requiring the use of ultra-pure reagents to avoid contamination that would otherwise affect the properties of the substrate produced, essentially changing the SERS enhancement and making it non-uniform [218].

Proximity of analyte: For SERS measurements, the analyte molecule needs to be in close contact with the substrate, which is difficult when the sample is solid-state as opposed to liquid [218].

2.2 State of art in Raman analysis of MNPs

In this section, the state of art in MNP detection by techniques relevant to this thesis will be discussed in two parts – first through the use of Raman spectroscopy and then through SERS, with each having separate segments on microplastic detection and nanoplastic detection. With Raman most commonly used for the detection of microplastics as opposed to nanoplastics, most of sub-section 2.2.1. is based on the former, as well as describing the limitations in general for Raman spectroscopy before focussing on the challenges for its application to microplastic detection. The MNP detection through SERS in sub-section 2.2.2. includes a special focus on nanoplastic detection with greater understanding of it provided through a detailed explanation of the various SERS substrates used for detection of MNPs and their limitations.

2.2.1 Detection of MNPs through the use of Raman spectroscopy

2.2.1.1 Microplastic Detection using Raman Spectroscopy

As discussed in section 1.6.4, Raman spectroscopy is one of the most commonly used techniques for detecting MNPs with conventional Raman spectroscopy detecting microplastics greater than 10 µm, µ-Raman spectroscopy for microplastics down 1 µm and confocal Raman spectroscopy for nanoplastics as small as 300 nm [219-221]. Through Raman MNPs have been detected and identified in various matrices, including, but not limited to, drinking water [137], seawater [222], freshwater [223], wastewater [224], sediment [225], soil [226], plants [227], aquatic organisms [228], honey [229], salt [230], food [231], wine [232], cosmetics [233], human semen [234], human breastmilk [235], human blood [236], amniotic fluid [237]. This demonstrates its capability for application, which is due not least to its continuous development and advancements over time. That

with said, its application to MNP analysis has three drawbacks: (A) fluorescence, (B) low signal intensity and (C) long overall analysis times due to the presence of other matter in samples requiring pre-selection of particles for Raman measurements and the shear volumes of samples.

(A): Fluorescence observed in MNP samples emanates either from the inherent composition of MNPs, impurities such as organic/inorganic material, colouring agents etc that might have attached to the MNPs at some later stage or from the filters employed to separate them from their matrix. Its presence in Raman signals leads to an elevated baseline that, in severe instances, completely masks the spectral peaks of interest [238] and so many different practices are used to reduce or completely get rid of it when analysing MNP samples. Specifically when arising from additional impurities, pre-treatment through the use of acid [239], alkaline [240], oxidative [129] or enzymatic agents [241] is undertaken to remove as much of the impurities as possible to minimize the fluorescence signal, whilst avoiding the degradation of the MNP sample. For example, previously, the International Council for Exploration of Sea (ICES) recommended the use of nitric acid as a digestion agent for the impurities of MNP samples, however various studies subsequently showed significant plastic degradation leading to MNP underestimation in Raman measurements [240,242]. Subsequently, Enders et al. [242] in partnership with the ICES formulated a new protocol based on 30% KOH:NaClO as the official method for cleaning MNP samples. Nevertheless occasionally, despite rigorous pre-treatment, fluorescence can remain, which is attributed to the presence of a strong colouring agent. Photo bleaching, whereby the sample is exposed to high intensity laser light until the agent degrades, is usually applied to get rid of it, although that is limited by time constraints and the high probability of damaging the sample due to the long exposure times to the light [238]. In an alternative approach, Zhao et al. [243] applied an automated algorithm, based on a modified multi-polynomial fitting method [244], to spectral data in order to remove the fluorescence signal to reveal the underlying Raman peaks. Ghosal et al. [228] were the first to develop a graphical user interface (GUI) based on the algorithm proposed by Zhao et al. [243] and through applying it demonstrate the recovery of Raman spectra of five different types of microplastic samples. Whilst the use of such algorithms is an efficient method to extract Raman spectra from broadband fluorescence signal, a meticulous selection of filters employed to separate MNPs from the matrix is also necessary to minimise fluorescence emanating from those. A study of performance comparison between six different commercial filters commonly used for μ-Raman spectroscopy with custom made polycarbonate filters coated with three different metals showed that the most efficient substrate for MNP analysis was the custom-made polycarbonate filter coated with aluminium. It offers prominent advantages over others: (i)

minimum fluorescence and (ii) optimum contrast between the filter and sample making automated particle detection easier [231].

(B): Low Raman signal intensity can be tackled in some instances by extending the integration time, this however, as well as increasing measurement time also introduces the risk of sample burning or laser-induced degradation due to prolonged exposure [238]. A more promising solution, by improving the signal to noise ratio (SNR) in Raman measurements, has arisen from the development of improved detectors such as electron-multiplying charged coupled device (EM-CCD) detectors over conventional charged coupled device (CCD) detectors. This is because they have the capability to amplify the gain up to 1000 times for the same magnitude of SNR but for shorter integration times and subsequently there has been an increased use of EM-CCD detectors for fast Raman mapping and imaging applications, including for MNP detection and analysis [245-247]. Specifically Dieing and Hollricher demonstrated the Raman imaging of microplastics within a glass slide covered with PMMA microplastics and contamination [247] through using a EM-CCD detector with one tenth the integration time of a standard CCD detector. A radical alternative to 'enhancing' the low intensity of the Raman signal involves abandoning conventional Raman scattering, i.e. spontaneous Raman scattering, in favour of nonlinear Raman scattering, stimulated Raman scattering (SRS), coherent anti-Stokes Raman scattering (CARS) and coherent Raman scattering (CRS). However, despite offering a high SNR, nonlinear techniques for microplastic detection have only been sporadically used, such as SRS [181], CARS [154] and CRS [248,249] because they require expensive equipment and skilled personnel, and are out of the scope for this thesis. Besides the aforementioned non-linear scattering methods, SERS, a commonly used analytical technique for detection and analysis of MNPs (a detailed discussion is presented in the following section) provides a better SNR without the additional complexities associated with non-linear Raman scattering as it is based on spontaneous Raman scattering.

(C): Filtered samples often contain non microplastics which can slow down the whole analysis process as it can be difficult to determine through microscopy which particles are probably microplastics and thus should be characterised through Raman spectroscopy. An innovative strategy to enable fast but precise analysis of microplastics actually introduces fluorescence to more easily identify them through microscopy [250-254], doing so through the use of a fluorescent dye that almost exclusively colourises the microplastics. The concept originated from the analysis of surface water samples as they bear microbiota that can be mistaken for microplastics under the microscope, although they do not undergo colourisation by fluorescent dyes [50], and Shim et al. [250] were the first to using Nile Red (NR) to stain laboratory-controlled and field samples. It should be

noted however, that although the staining method reduces the probability of missing the detection and subsequent quantification of microplastics it does however hinder microplastic detection as lipids and organic natural organic contaminants within the sample are also dyed, moreover greatly weathered microplastics do not stain properly. That with said, dyed contaminants can be avoided through appropriate pre-treatment methods, although the challenges associated with dying weathered microplastics are more difficult. A study of five different dyes, Oil red EGN, Eosin B, Rose Bengal, Hostasol Yello 3G and NR, has demonstrated that NR is the best amongst them in terms of adsorption and fluorescence intensity [251] when staining microplastics. Erni-Cassola et al. [252] detected NR stained microplastics across the size range of 20 μm to 338 μm through fluorescence microscopy before verifying their identity with μ-Raman spectroscopy. The combination of imaging and Raman spectra confirmed that only the microplastics were fluorescing, and the same study also explored the potential of using fluorescence staining to perform high-throughput detection of microplastics, with the samples being appropriate for chemical analysis through Raman spectroscopy. The fluorescence dye staining of microplastics doesn't usually produce sufficient fluorescence as to mask Raman spectral features of microplastics as NR is usually used, due to its efficiency in dying microplastics, in small amounts [251]. That with said where the fluorescence signal is so high that it impedes the acquisition of Raman spectra, a short duration of photo-bleaching has been reported to help [252]. The shear volumes of samples from environmental matrices to be analysed and the necessary time to do so has led to the development of automated analysis, either in the form of complete mapping of each point of the filter containing a sample or a pre-scanning. The former is precise but comes at the cost of being time consuming, whilst Elert et al. [255] has used microscopic sorting and quick Raman mapping collectively as a pre-scanning step. The microscopic sorting helped find the areas containing microplastics to narrow down the mapping area whilst the quick Raman mapping was done to form a spectral image of each particle detected during the microscopic pre-scan. Thereafter higher resolution Raman spectra was taken for particles of interest making the process more time-efficient than mapping of the entire filter [255]. Various studies have demonstrated the advantage of utilizing different image analysis software to help reduce the time taken to perform comprehensive Raman mapping for microplastic samples [137,256].

An important aspect of identifying environmental MNP samples by matching measured Raman spectra to those from reference libraries, particularly through automated identification, is that their weathering and the presence of additives from commercial plastic production may prevent a 100% match as reference spectra are of pristine plastics. In some cases, the variation in the spectra is so high that automated routines will fail to

identify the plastic particles. An example is that of Lenz et al. in [257] who demonstrated that exposure of PVC to photo-degradation resulted in the disappearance of Raman peaks typical of PVC at 693 cm^{-1} and 637cm^{-1} as well as the addition of extra peaks at 1139 cm^{-1} and 1540 cm^{-1} and thus did not match successfully to PVC library reference spectra. Consequently a need was recognised for the addition of spectra for plastics at various states of degradation within spectral libraries, particularly for environmental samples [238]. Furthermore, spectra for the typical impurities found in MNP samples extracted from environmental matrices have been successfully added to Raman reference spectral libraries, with their use show to increase the matching score [257]. Machine learning (ML) is increasingly used to achieve automated Raman routines and a portable Raman device equipped with a ML algorithm was reported to distinguish and classify various microplastics collected from marine water with a selectivity of 98.82%; demonstrating the efficiency of ML in MNP analysis [258].

2.2.1.2 Nanoplastic Detection using Raman Spectroscopy

As stated at the beginning of section 2.2.1.1 μ-Raman spectroscopy and confocal Raman spectroscopy have also demonstrated, in a few instances, the detection of nanoplastics. For example, a correlative approach based on SEM and μ-Raman spectroscopy successfully detected PS beads of diameter 200 nm in diverse matrices such as distilled water, sea salt and human amniotic fluids with detection limits of $2x10^{-3}$ μg/L, 20 μg/L and 200 μg/L, respectively [237]. Luo et al. demonstrated the release of MNPs into the environment from the burning of face masks through using Raman imaging to successfully detect MNPs in the residuals of burnt masks [259]. In another study confocal Raman spectroscopy was used to identify nanoplastics, specifically PS particles of 600nm, 300 nm and 100 nm diameter. Whilst those of the first two sizes were detected on a glass slide, the smallest were instead placed on a gold coated glass slide for detection also through SEM [219] and thus the spectral analysis for the 100nm nanoplastics was in all likelihood surface-enhanced Raman spectroscopy (SERS). The recognition of false positive and false negative features in the Raman mapping of the PS nanoplastics [219] from the intensities of a characteristic Raman peak, due to low intensity Raman signal, however led to follow-up studies [260,261] to develop an algorithm to take images at multiple characteristic peaks rather than one [260]. In this way the precision of the Raman map was increased, and afterwards a further improvement was made by advancing the algorithm to combine the multi-images of the various characteristic peaks to be mapped simultaneous into a single image through using colour off-setting got a higher SNR [261]. The aforementioned studies also demonstrated the efficiency of the developed

methods by applying them to real world MNP samples obtained from car paint-polishing dust [260] and toner ingredients of a laser printer [261].

In summary, Raman spectroscopy has found widespread application in microplastic detection; however, its efficacy has been consistently hindered by inherent limitations that have presented challenges for the detection of microplastics in environmental samples. Moreover, confocal Raman spectroscopy, whether employed individually or in conjunction with other techniques, has demonstrated success in detecting nanoplastics, the subsequent section elucidates on how an advanced Raman spectroscopy variant, that is surface-enhanced Raman spectroscopy, has emerged as a superior alternative for MNP detection [262].

2.2.2 Detection of MNPs through the use of SERS

2.2.2.1 Microplastic Detection using SERS

Compared to microplastics for nanoplastics it is typically more challenging to obtain comprehensive physicochemical information such as chemical composition, concentration, abundance, and morphology. The improved sensitivity, higher SNR and greater spatial resolution offered by SERS over μ-Raman spectroscopy and confocal Raman spectroscopy makes it the better analytical technical to address that challenge though [263].

Xu et al. were among the first to report the detection of single particle microplastics through the use of SERS by using commercial substrates of gold coated inverted pyramids by Klarite [264], specifically for PS (1 μm, 2 μm, and 5 μm diameter) and PMMA (2 μm, and 5 μm diameter) microspheres. The SERS enhancement was proven through comparing the Raman signal intensity from microplastics on Klarite substrates to that from microplastics on silicon wafers, being greater for the former [265]. Elsewhere a flexible and highly reproducible SERS substrate based on AuNP doped filter paper was used to detect 10 μm, 15 μm and 20 μm PET microplastics and also microplastics found in tap and pond water [266], with the filter paper preventing the AuNPs from aggregation, leaching and degradation. In another study [267], 1 μm, 2 μm, and 5 μm diameter PS, and 1 μm, and 2 μm PMMA microspheres were detected through SERS using substrates formed by sputtering gold onto a V-shaped anodic aluminium oxide (AAO) membrane made up of 2D-array of inverted cone-shaped nanopores which were then used to also detect microplastics in rainwater. The same authors also compared substrates when the gold was deposited through magnetron sputtering and when they were prepared by ion sputtering, showing a higher EF for those prepared by the former technique which was attributed to the formation of nanotopography with a higher density of hotspots.

Although SERS substrates used for MNP detection are usually gold or gold nanoparticle coated, other noble metals have been used, typically Ag. For example, commercial PE and PP microplastics nearly 10 μm in diameter were detected in pure water and sea water through the use of colloidal AgNPs to enhance the Raman signal [160], with the maximum SERS enhancement achieved by optimising their aggregation through control of the concentration of the aggregation agent (NaCl) and the sample. Similarly, other salts have been used as aggregating agents for AgNPs, such as magnesium sulphate ($MgSO_4$) for 1 μm PS [268] or potassium iodide (KI) for 1 μm and 2 μm of PS microplastics [269]. That with said, the SERS signal for all samples did not vary much as the microplastics are too large for the AgNPs aggregating around them to form many hotspots. In comparison to nanoplastics, microplastics have lower specific surface area and thus provide less contact with metallic nanoparticles [270,271], and consequently, lower SERS signal, making the use of colloidal nanoparticles unsuitable for efficient microplastic detection [160,268,269].

SERS substrates that are neither based on continuous thin films or colloidal nanoparticles have also been used to detect microplastics. For example Yin et al. successfully developed and then employed a AuNP decorated sponge for the SERS detection of microplastics (PS, PET, PE, PVE, PP and polycarbonate) generated from grinding of macro-plastics [272] and thus of random sizes within the range 80 μm – 150 μm. The use of a sponge as the skeleton for forming a SERS substrate has multifaceted advantages. One is that the large number of pores offer a 3D framework and thus lots of lots of sites for AuNPs and therefore hotspots, whilst another is that the pores can filter out water and smaller particles from the sample matrix with the bowl-shaped pores perfect for trapping microplastics. Finally, the variation of the pore size allows for both tuning the size of microplastics trapped as well as the interparticle gap and therefore the size of the hotspot. The prepared SERS substrates were used to detect microplastics in water from five different matrices, namely seawater, rainwater, river water, snow and tap water. The process used to produce the substrates was found to be reproducible with SERS experiments carried out over nine individually prepared substrates having a less than 10% standard deviation, whilst results led the authors to hypothesise that the limit of detection can be lowered indefinitely if a sufficient volume of sample is available. Another unique, flexible and ultra-thin SERS substrate fabricated from gold mesh was used within a wearable SERS sensor [273] that used an external laser source to detect microplastics, particularly PE microbeads of a 1 –10 μm diameter, in addition to two other real-word applications. The creation of the gold mesh is a low-cost four-step process: (i) preparation of aqueous solution of polyvinyl alcohol (PVA), (ii) preparation of nanofibers using PVA, (iii) formation of PVA mesh by intertwining the nanofibers (iv) coating the PVA nanomesh with gold.

Although section 2.2.2.2. shows that SERS is much more popular for the detection of nanoplastics, it has clearly been seen to be used for qualitative and quantitative analysis of microplastics and gives better a performance for detection than by standalone standard Raman spectroscopy.

2.2.2.2 Nanoplastic Detection using SERS

As reported in section 2.2.2.1 as well as for detecting microplastics Xu et al. [265] used the same (Klarite) substrates to detect nanoplastics, in particular, PS and PMMA spheres with diameters of 360 nm and 500 nm. In that published work the Raman signal for 500 nm PS spheres on silicon wafer was seen to be much lower in intensity compared to that of the (SERS) signal for 360 nm PS spheres on Klarite. It was also reported that there was a 2 orders of magnitude lower EF for PMMA particles than for PS, being hypothesised as to be due to the PMMA particles' low Raman cross section and sensitivity to the SERS substrate. Furthermore, the difference in the SERS signal for same sized particles and their subsequent imaging also showed that the highest signal is obtained in the pits of the inverted pyramid, which are clearly the hotspots of the substrate, this was further substantiated through numerical simulations. Finally, the study also employed the use of the Klarite substrate for the detection of ambient atmospheric MNPs collected within samples from the roof of a university building in Shanghai with spectra indicating the presence of PET and PS.

Typically colloids of Ag and Au nanoparticles, that are prone to agglomeration in the presence of an electrolyte solution resulting in the generation of a great number of hotspots, are used as SERS substrates for the detection of nanoplastics [274,275], with their most attractive feature being the simplicity of the process. As an example Lv et al. detected 100 nm and 500 nm of self-synthesised [276] PS spherical nanoplastic beads through the use of NaCl aggregated Ag colloids that were previously seen to be used for also detecting microplastics in section 2.2.2.1 [160]. The publication showed that for both sample matrices, pure water and sea water, the maximum SERS signal for nanoplastics was achieved for an optimum concentration of NaCl being 0.25 mol/L and equal volumes ratio of PS solution to colloidal solution with the concentration of salt already present in the sea water insufficient to further aggregate the AgNPs. The work also showed that although the SERS intensities for 500nm sized PS nanoplastics in both matrix samples are maximum at a concentration of 0.08 mg/ml, the SERS intensity for 100 nm PS reaches a maximum at 0.80 mg/ml for pure water samples whilst it continues to increase up to 1.60 mg/ml for sea water samples, although the authors did not provide any explanation for this. Another study based on aggregation of AgNPs, but using $MgSO_4$ [268], successfully detected PS nanoplastics with an average diameter of 53 nm. However, it gave uneven

SERS enhancement and poor reproducibility, which is a common problem faced due to uncontrolled/inhomogeneous hotspot regions and is predominantly a drawback of SERS substrates prepared using the bottom-up approach. The same study highlighted another drawback of this approach, due to the limited lateral resolution of the technique individual SERS spectra may contain contributions from multiple nanoplastics. Another study that used AgNPs [269] and a salt to aggregate them, this time potassium iodide (KI), was capable of detecting and quantifying 50 nm, 100 nm, 200 nm and 500 nm PS nanoplastics. The method was validated for real-world applications through achieving recovery rates between 87.5% – 110% for lake water samples with spiked nanoplastics of the sizes above. Compared to other coagulants used elsewhere for the aggregation of AgNPs KI provides an additional benefit, serving as a cleaner by dislodging impurities present on the nanoparticles [160,268].

Other nanoplastic SERS studies have used non colloidal nanoparticle substrates, such as the two sets of glass slides with coatings of different sized AuNPs that were used to detect 161 nm and 33 nm sized PS nanoplastics and PET particles with an average of 62nm [277]. Its 14nm and 46nm sized AuNPs were prepared using the Turkevich method [278] and a slightly modified Brown method [279], respectively. Within that study the detection of 161 nm and 33 nm PS was successful for both types of substrates, however, PET nanoplastics smaller than 62 nm were not detected for either type demonstrating that suitability of a SERS substrate is also dependent upon the plastic type within a sample. The same study showed a higher EF achieved for the larger AuNPs which is attributed to the nanoparticle's ability to scatter light and the presence of electrons on its surface. Additionally, particles smaller than a specific size threshold exhibit surface interactions primarily governed by electronic scattering mechanisms, leading to a reduction in the re-radiated electromagnetic energy and subsequently diminishing the overall SERS signal [280].

In MNP detection, some samples require prior filtration necessitating an additional processing step of transferring the sample from a filter onto the SERS substrate. While this step can be tedious and time consuming, especially for samples containing small particles, a far greater concern is that of sample loss due the embedment of tiny particles from samples within the filter [263]. To address this Jeon et al. developed a flexible SERS substrate, which also serves as a filter, by vacuum filtering synthesised Au nanorods (AuNRs) and Ag nanowires (AgNWs) on to regenerated cellulose (RC) hydrogel films [281] before both were used to detect PS nanoplastics with diameters of 84 nm, 44 nm and 630 nm. A performance comparison of the two substrates showed a superior one by the AgNWs which was postulated as being due to the higher plasmonic effect offered by

Ag compared to Au [282,283]. Another study based on SERS substrates formed through simple filtration of AgNWs onto filter paper showed the successful detection of trace quantities of PS particles with diameters between 50 nm – 1000 nm [284]. The practicality of the prepared substrates was then demonstrated by using them to detect nanoplastics in water from a seafood market. In a non-film based approach Lee and Fang developed and used a SERS substrate based on Au NanoUrchins (AuNUs) with an average diameter of 50 nm to demonstrate single particle detection for PS nanobeads of 600 nm diameter by mixing and drying the two solutions of nanoplastics and AuNUs [285]. In a more exotic approach still Chang et al. reported the development of a unique nanowell Raman enhanced substrate (NWERS) by sputtering Ag onto the surface of a crystal formed by the interfacial assembly of silicon dioxide (SiO_2) nanospheres. The prepared substrate was used to detect individual PS nanoplastics of 200 nm, 500 nm and 800 nm in diameter and demonstrate its capability for real-world samples by recovering PS nanoplastics in spiked samples of bottled water, tap water and river water [286]. In previous sub-sections it has been seen that SERS is better suited than Raman spectroscopy for nanoplastic detection because the size of the particles is ideal for the location and sizes of hotspots. Likewise given the larger size of microplastics, there is only a small and almost negligible increase in signal size for their detection through SERS rather than Raman spectroscopy compared to that seen for nanoplastics. Specifically, this due to either the microplastics not ‘sitting’ in the hotspot region for solid SERS substrates or because the nanoparticles don’t sufficiently cover the larger plastic microplastic in the case of colloidal SERS substrates.

2.3 Research Gap

The comprehensive discussion on the introduction of MNPs to the environment in combination with the comparison of the impact of microplastics versus nanoplastics discussed in Chapter 1 clearly showed an immediate need for greater understanding of the latter’s distribution, concentration and toxicity to assess their suspected significant risk. Section 1.6.4 of the same chapter established the need for analytical techniques that could provide this information, with SERs being predominantly the most appropriate to do so, although it has some technological limitations that were explored within a comprehensive review of the state of the art in the SERS detection of nanoplastics in this Chapter. Specifically, it showed that although a variety of SERS substrates developed successfully detected nanoplastics, there is still a clear need for the development of cost-effective and simple methodologies for the reproducible fabrication of homogeneous and stable low-cost SERS substrates capable of detecting ultra-low concentrations of small nanoplastics.

The experimental work presented in this monograph is a contribution to developing such SERS substrates and does so through the development of three simple methodologies based on the use of gold nanoparticles (AuNPs) for cost-effective detection of 50 nm and 100 nm polystyrene (PS) nanoplastics. The practical applicability of each of the developed methodologies was also demonstrated by utilising it for the detection of nanoplastics released in real-world samples.

Chapter Three

Salt-assisted aggregation of gold nanoparticles for the SERS detection of nanoplastics.

3.1 Introduction

Ever since the discovery of SERS its application in detection and sensing has been enabled through the use of substrates based on different shaped nanostructures formed from noble metals, particularly silver (Ag) and gold (Au), due to their SERS enhancement and absence of Raman active modes [287,288]. Ag provides a much higher SERS enhancement than Au [289], however the latter is more commonly used due to its greater biocompatibility, lower cytotoxicity and chemical stability in ambient conditions (Ag even oxidises easily in air) [290,291]. Therefore, it is spherical gold nanoparticles, which are also easy and cost effective to synthesise [292,293] as well as functionalise [294-297] and hereafter referred to as AuNPs, that are the focus for SERS substrate development in this thesis. Their optical properties, including plasmonic enhancement which is of interest for SERS, can be tuned by varying their size, shape, aggregation state, and the composition and dielectric constant of their surrounding medium, as these strongly affect how much light they scatter [298]. In general, the unique optical properties of AuNPs render them as valuable nanostructures for extensive applications in imaging [299], sensing [300], and targeted drug delivery [301].

3.1.1 Synthesis of AuNPs

The Turkevich, Frens and Brust-Schriffin methods are those primarily used to chemically synthesize AuNPs, stable in aqueous solution for extended periods of time [302], and covering a range of diameters from 2 nm to 250 nm, with their functionalities depending on their size and surface chemistries.

3.1.1.1 The Turkevich Method

The Turkevich method essentially a reduction method, is the method most commonly used [278] given its simplicity and compatibility with large-scale production, and the long-term stability of its synthesised particles. It (Figure 3.1a) consists of tetrachloroauric acid ($HAuCl_4$) being dissolved in deionized water (dH_2O) to form a gold(III) chloride solution which upon being heated to boiling under constant stirring then has trisodium citrate ($Na_3C_6H_5O_7$) added to reduce the Au^{3+} ions to Au^0 for the nucleation of gold atoms that act as seeds for further growth to form AuNPs (Figure 3.1b). During AuNP synthesis, the

solution undergoes a visible colour change from yellow to wine red upon the formation of colloidal gold nanoparticles with diameters ranging between 10 nm to 20 nm, with the colour depending on the size and shape of the particles due to surface plasmon resonance. The size, shape and optical properties of the synthesised AuNPs in water [303] can be tuned through varying the amount of trisodium citrate used during the synthesis process.

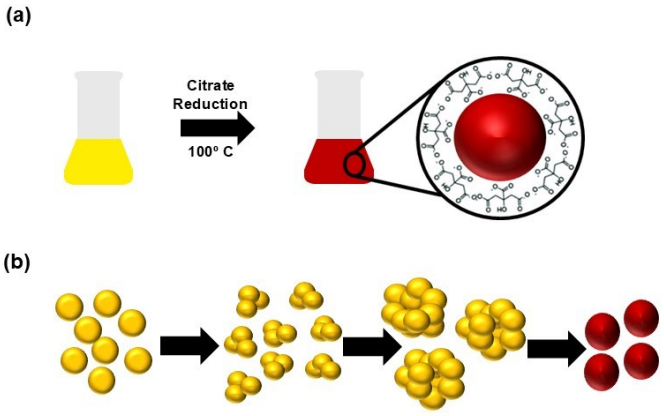

Figure 3.11: (a) A schematic of the steps involved in the citrate reduction Turkevich method through the use of gold salt (HAuCl4); (b) A schematic illustrating how the citrate reduction results in the nucleation of gold atoms that act as seeds for further growth to form gold nanoparticles.

Each nanoparticle within the colloidal AuNPs is surrounded by a strong negative charge which keeps interparticle separated via electrostatic repulsion [278]. That with said the use of trisodium citrate as a reducing agent has the additional benefit of passivating the surface of AuNPs through the chemisorption and/or physisorption of citrate ions resulting in loose citrate ions and preventing their aggregation [304]. Moreover, those loose citrate ions can be displaced in the presence of desirable ligands, such as DNA, proteins, thiols, etc, thus functionalising the AuNPs which makes them ideal for sensing applications [304], [305].

3.1.1.2 The Frens Method

The Frens method, which closely resembles the Turkevich method, was developed to produce larger AuNPs, and also in water. It does so through adjusting the concentration of the reducing agent relative to the gold precursor, or the stoichiometric ratio of gold precursors to trisodium citrate, for precise tuning of nanoparticle dimensions [306]. It typically yields AuNPs with diameters from 10 nm to 30 nm, although nanoparticles up to 100 nm in size have also been reported [303], [307].

3.1.1.3 The Brust-Schiffrin Method

The Brust-Schiffrin method (Figure 3.2) employs a two-phase system to synthesize, under ambient conditions and without the need for heating, alkanethiol-functionalized AuNPs in an organic phase (toluene), in contrast to those produced in the aqueous phase by the

Turkevich and Frens methods [308]. Specifically, the phase transfer catalyst (PTC) of tetraoctylammonium bromide (TOAB) changes the phase of $HAuCl_4$ dissolved in dH_2O into toluene and the subsequent addition of dodecanethiol to this organic phase results in the reduction of Au^{3+} to Au^{1+}. Following this reduction step, the main reducing agent, an aqueous solution of sodium borohydride, is brought into contact with the organic phase resulting in further reduction of gold ions (Au^{1+} and the remaining Au^{3+} to Au^0) and the formation of AuNPs as indicated by a colour change [308].

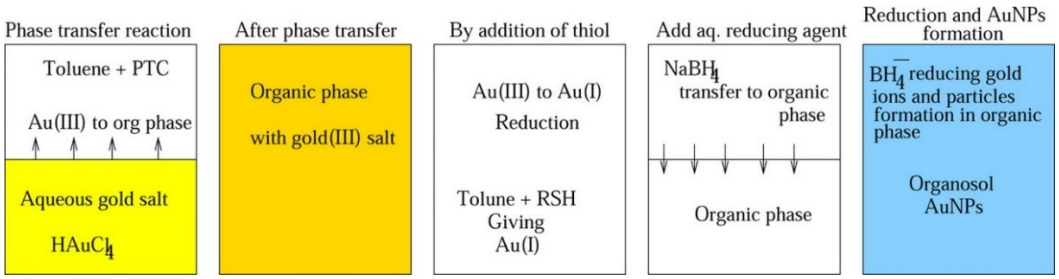

Figure 3.2: A schematic diagram of the main steps in the Brust-Schriffin method for the synthesis of alkanethiol capped gold nanoparticles [308].

The strong interaction between alkanethiols and the nanoparticle surface leads to effective passivation [308], [309], [310], [311] making the AuNPs highly stable. Similar to the Frens method, the size of the AuNPs synthesized can be controlled by adjusting the ratio of alkanethiol to gold precursors [312], although it can produce significantly smaller AuNPs than the other two methods, with diameters as small as 2 nm.

3.2 Stabilization of gold nanoparticles

Gold nanoparticles (AuNPs) are stabilized during the synthesis process. Based on the synthesis process and the stabilizing agent used the resulting stabilization can either be electrostatic stabilization, steric stabilization or electrosteric stabilization.

3.2.1 Electrostatic Stabilization

Ionic groups in liquids surrounding AuNPs have a tendency to attach to their surface to form charged nanoparticles that attract equal but opposite charges in their vicinity and thus a double charge layer around each nanoparticle which is overall electrically neutral (Figure 3.3). The electrostatic stabilization, which is formed due to ionic groups and so cannot be achieved in an electrolyte sensitive media [313], depends on the pH of the colloidal, its concentration and storage temperature [314], and prevents aggregation [313].

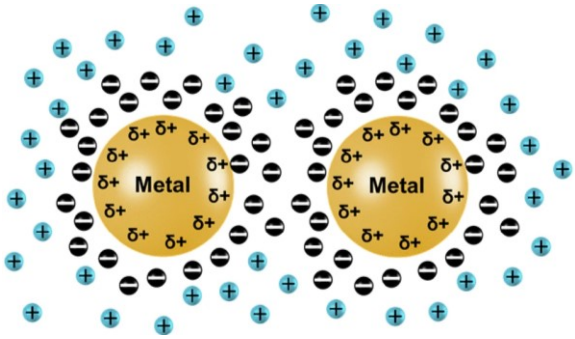

Figure 3.3: A pictorial representation of the double charge layer around each AuNP resulting in electrostatic stabilization and therefore no aggregation [315].

3.2.2 Steric Stabilization

Stabilizing agents surrounding nanoparticles during the synthesis process include functional groups, such as hydroxyl groups, surfactants and polymers, that adsorb onto the AuNP surface reducing interparticle contact and thus aggregation [313] through steric stabilization (Figure 3.4), rendering the colloidal stable [316], [317]. Unlike aggregates formed within an electrostatically stabilized AuNP colloidal, those formed from steric stabilized AuNPs are reversible because the steric stabilization can be switched on and off by a stimuli, such as temperature, pH, light, polarity or magnetic fields [318], [319], [320].

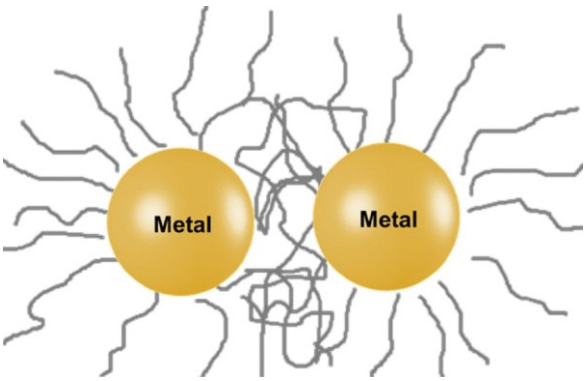

Figure 3.4: A pictorial representation of the steric stabilization between two AuNPs generated by the stabilizing agent surrounding each nanoparticle [315].

3.2.3 Electrosteric Stabilization

Electrostatic stabilization (Figure 3.5), a combination of electrostatic and steric stabilization, results when polyelectrolyte, a polymer with both positive and negative charge, is used as a surfactant. Being ionic it provides electrostatic repulsion, whilst its long chains and polar head groups contribute steric repulsion, consequently stabilizing the AuNP colloidal [321].

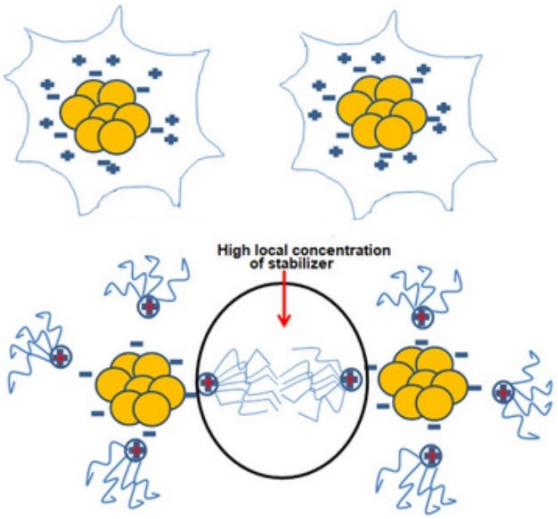

Figure 3.5: A pictorial representation of the combination of electrostatic and steric stabilization in electrosteric stabilization [313].

3.3 Aggregation of gold nanoparticles

Having discussed the stability of AuNPs, a desirable property for many applications including SERS detection, it is worth mentioning that aggregation of AuNPs is not always bad, in fact intentional aggregation of AuNPs is carried out sometimes especially for optical detection including SERS detection as explained in section 3.3.1. The aggregation of AuNPs occurs only after the repulsion forces surrounding the nanoparticles have been disturbed, such as the electrostatic ones for citrate capped AuNPs synthesized through either the Turkevich and Frens methods, or the steric ones in the case of the thiol capped AuNPs synthesized via the Brust-Schriffin method. Furthermore, aggregation of AuNPs occurs through van der Waals attractive forces [322] via two primary mechanisms: (i) crosslinking (CL) aggregation and (ii) non-crosslinking (NCL) aggregation.

(i) In CL aggregation, AuNPs aggregate through the formation of specific chemical or biological bridges (crosslinks) between individual nanoparticles [322]. The CL aggregation of AuNPs occurs in presence of crosslinker molecules that have a couple of binding sites which link two AuNPs to each other. CL aggregation is when binding forces such as, electrostatic interaction, metal–ligand coordination, etc overcome the electrostatic and/or steric interparticle repulsive forces resulting in aggregation of the AuNPs [323], [324].

(ii) NCL aggregation [322], through AuNPs capability to link without forming an actual bond, is driven by changes in their surrounding environment that disrupt the stability of the colloidal system such as ionic strength [38], pH [325], or the presence of organic molecules [326]. For example, citrate capped AuNPs, that

are stabilized through electrostatic repulsion forces from the surrounding citrate ions, undergo aggregation upon the addition of NaCl as the positive charged salt ions neutralize the negatively charged citrate ions [327].

3.3.1 Aggregation of Gold Nanoparticles for Optical Detection

The use of gold nanoparticles (AuNPs) for the detection of trace analytes is highly favoured due to their tunable, morphology-dependent optical properties, high stability against oxidation, ease of synthesis, cost-effectiveness, and versatility in surface modification [294], [295], [296]. While AuNPs in their colloidal form are extensively employed for SERS detection (owing to the plasmonic enhancement offered by these nanoparticles), aggregated nanoparticles are often preferred for detecting trace analytes that remain undetectable with colloidal AuNPs alone. Importantly, the above mentioned favourable properties of colloidal AuNPs are preserved when they are aggregated, however this holds true only to a certain degree of aggregation prior to losing the plasmonic properties altogether [298], [328]. Therefore, extreme care needs to be taken while carrying out aggregation of AuNPs in order to not lose their plasmonic properties [329]. Therefore, AuNP aggregation is sometimes deliberately induced to enable detection of trace analytes through the use of surface-enhanced Raman spectroscopy (SERS).

For SERS applications, the stability of AuNPs is sometimes deliberately disrupted by adding aggregating agents to induce aggregation forming AuNP clusters, which significantly increase the overall size of the nanoparticle assemblies and generate "hot spots"—regions of intense electromagnetic fields between closely spaced nanoparticles [330]. These hot spots are critical to the substantial enhancement of the SERS signal, enabling the sensitive detection of even trace amounts of analytes [331]. Schwartzberg et al. [332] and Hadano et al. [333] demonstrated the detection of R6G concentrations down to 0.1 μM and 0.2 μM through aggregated AuNPs and colloidal AuNPs, respectively.

AuNPs aggregates are often used for biomolecular detection, including biomedical screening, and they have been used to do so through SERS for the detection of ultra-low concentrations of biological analytes such as bovine serum albumin (BSA), hemoglobin and catalase [331], [334]. Their potential for field based, or Point of Site (PoS) identification of environmental pollutants was demonstrated through the SERS detection of 0.38 μg/L of a pesticide (‘thiram) through the use of a controlled aggregation of AuNPs enclosed within a polyacrylamide hydrogel (PAH), or PAH-AuNPs, with the PAH responsible for controlling and stabilizing the AuNP aggregates [335]. Furthermore, organophosphate pesticides were detected via SERS through the use of a athiocholine-induced aggregation of organometallic osmium carbonyl covered AuNPs and the inhibitory properties of

glyphosate on acetylcholinesterase (AChE) and its effect on thiocholine [336]. Elsewhere, highly sensitive and selective SERS detection of trinitrotoluene (TNT) was demonstrated through the formation of a Meisenheimer complex from the TNT induced aggregation of AuNPs functionalized with cysteine, at an ultra-low concentration of 2 pM and against other nitro based compounds [337].

In addition to its application in SERS-based detection, which enables chemical identification and the detection of trace analytes, gold nanoparticle (AuNP) aggregation is also commonly employed for rapid, convenient and cost-effective colorimetric detection [338]. This approach utilizes the optical properties of AuNPs, where aggregation induces a visible colour change, allowing for simple and efficient analyte detection by the naked eye without the need for sophisticated equipment [339]. Subsequently they are used in either PoS/at home [340] detection by the naked eye [339] for rapid, convenient and cost-effective qualitative tests [338] or by an ultraviolet-visible (UV-Vis) absorption spectrophotometer for a quantitative result [341]. Colorimetric analysis has been used for detection of analytes such as DNA [342], [343], dopamine [344], cocaine [345] and heavy metal ions [346], [347], [348], [348], [349]. Whilst colorimetric analysis based on the aggregation of AuNPs is commonly used for the rapid detection of analytes in screening, it lacks the chemical identification, and thus high selectivity of SERS for identifying potential cross-reactivities [350]. Therefore, some researchers have integrated both, in a 'dual mode', to achieve rapid screening with precise chemical identification. Dual mode detection has been applied for the successful detection of ultra-low concentrations of various harmful chemicals, ions and toxins such as arsenic (III) (As^{3+}) [351], ochratoxin A [352], chlorpyrifos [353] and nickel(II) (Ni(II)) [354].

Table 3.1Table 3.1 summarizes the studies that have been done to detect low concentrations of various analytes through the use of aggregated AuNPs with SERS, colorimetric analysis and combination of both.

Table 3.1: A comprehensive summary of the studies using AuNP aggregation in SERS detection, colorimetric analysis and a combined approach of both for the identification of a wide range of analytes, including biological substances found within the human body and toxic chemicals *with subsequent limit of detections (LoDs) achieved*.

Detection Mechanism	Aggregation Mechanism	Analyte	LoD	Reference
SERS	NCL	R6G	0.2 μM	[332]
	NCL	R6G	0.1 μM	[333]
	NCL	Bovine serum albumin (BSA)	150 pM	[331]
	NCL	BSA Hemoglobin Catalase	50 nM 1 pM 10 nM	[334]
	NCL	Thiram	0.38 μg/L	[335]
	CL	organophosphate pesticides	0.1 ppb	[336]
	NCL	Trinitrotoluene	2 pM	[337]
	NCL	100 nm PS	1 ppm	[38]
Colorimetric	CL	DNA	-	[342]
	CL	DNA	1 pM	[343]
	CL	Dopamine	2 nM	[344]
	NCL	Cocaine	50–500 μM	[345]
	NCL	Hg^{2+} in tap water Hg^{2+} in bottled water Hg^{2+} in saline Hg^{2+} in sea water	2 ppb 2 ppb 13 ppb 10 ppb	[346]
	CL	Pb^{2+}	30 nM	[347]
	NCL	Ni^{2+} Zn^{2+}	-	[348]
	NCL	Hg^{2+} Ag^{+}	0.1 μM 0.1 μM	[349]
	CL	Hg^{2+}	0.275 nM	[355]
	CL	Hg^{2+}	71 ppb	[355]
SERS[1] and Colorimetric[2]	CL	As^{3+}	0.14 ppb[1] 0.11 ppb[2]	[351]
	NCL	ochratoxin A	0.017 μg/kg [1] 0.039 μg/kg [2]	[352]
	NCL	chlorpyrifos	0.009 ppm	[353]
	CL	Ni(II)	0.5 ppm [1] 5 ppm [2]	[354]
	NCL	Melamine	0.089 mg/L [1] 0.60 mg/L [2]	[356]

3.4 Aims and Objectives

In line with the approaches described in the previous section to detect low concentrations of thiram using a salt aggregation of AuNPs and given the challenges in detecting NPs including their small size and thereby very low SERS signal intensity, the experimental work reported in subsequent sections of this Chapter aimed to use sodium chloride (NaCl) salt as an aggregating agent to aggregate AuNPs for nanoplastic detection through the use of SERS. The main experimental objectives of this chapter are thus:

1. A thorough study of the aggregation of AuNPs by varying volumes of NaCl.
2. The determination of the efficiency of NaCl as an aggregating agent for nanoplastic detection through undertaking a complete concentration study using pristine nanoplastics in deionised water.
3. Validation of the results of the concentration study by comparing them to that of pristine nanoplastics in drinking water, i.e. “spiking experiments”.

3.5 Materials and Methods

3.5.1 Chemicals and Reagents

Sodium citrate tribasic dehydrate (HOC(COONa) $(CH_2COONa)_2 \cdot aq$), gold (III) chloride trihydrate ($HAuCl_4 \cdot 3H_2O$, 99.9%) and sodium chloride (NaCl) were purchased from Sigma Aldrich (UK). TEM carbon coated copper grids were purchased from Agar Scientific (UK). 1 cm x 1 cm silicon (Si) filters having a pore size of 1 µm were purchased from ThermoFisher Scientific (UK). Aqueous suspensions of 2.5% solids polystyrene (PS) nanoplastic latex beads of 50 nm diameter and 10% solids polystyrene nanoplastic latex beads of 100 nm with a density of 1.05 g/cm^3 were purchased from Sigma Aldrich (UK). Deionised water (dH_2O) having resistivity of 18.2 MΩ.cm was obtained from the PureLab Chorus water purification system of Veolia Water Technologies (UK). Drinking water was collected from the drinking cooler at Institute for Global Food Security (Belfast, UK).

3.5.2 Numerical Simulations

Numerical simulations were carried out to calculate the theoretical enhancement factor (EF). For this purpose, the wave optics physics module within COMSOL Multiphysics was used to perform near-field simulations through the finite element method (FEM). To simulate gold nanoparticle (AuNP) aggregation around a PS nanoplastic, the geometry shown in Figure 3.6 was made in the software. Within the simulations (Figure 3.6) the substrates were represented by a 100 nm PS sphere, representing the pristine nanoplastis

used in the experiments, surrounded by 10 nm diameter spheres, to represent the aggregated AuNPs. The aggregation of the AuNPs was simulated by having the 10 nm AuNP spheres being closely packed around the 100 nm PS nanoplastic sphere and in one layer, under the assumption that except for high spatial localization in 3D geometries, the hotspot of the closely placed nanoparticles is of the same order as that for clusters of nanoparticles [357]. The SERS enhancement factor (EF) is equated to the electromagnetic enhancement factor (G), calculated from Equation 3.1 [358], as its chemical enhancement component is orders of magnitude weaker and thus negligible [359].

$$G = |E_{loc}(\omega_0)/E_0(\omega_0)|^4 \qquad (3.1)$$

where:

E_{loc} – the localised electric field.

E_0 – the incident electric field.

ω_0 – the incident wave frequency.

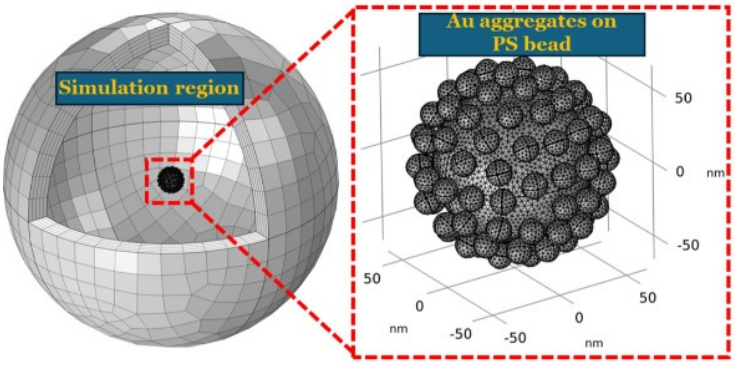

Figure 3.6: Simulation region for the numerical model created in COMSOL MultiPhysics software with the inset showing 100 nm PS nanoplastic sphere surrounded by 10 nm gold nanoparticles to simulate AuNP aggregation.

3.5.3 Gold Nanoparticle synthesis

Au nanoparticles (AuNPs) were synthesised using the Turkevich method [278], albeit with some minor adjustments. Briefly, 1 mM $HAuCl_4$ is dissolved in 50 mL of dH_2O and heated on a hotplate at a constant temperature of 90ºC with slow but continuous stirring until it boils. Upon reflux, the solution is subjected to vigorous stirring and 5 mL of 1% sodium citrate solution is quickly added to the boiling solution. The solution is then vigorously stirred until its colour changed from pale-yellow to transparent to greyish black and finally wine-red, which is an indicator of the citrate reduction of gold ions, upon which it is

removed from the heat to allow the colloidal AuNPs to cool naturally to room temperature whilst continuously stirring. The entire synthesis process involves reduction, nucleation, growth and stabilization with the first and last two triggered by sodium citrate, which behaves as reducing as well as stabilizing agent. The synthesised AuNPs was stored at 4 °C for subsequent experiments.

3.5.4 Gold Nanoparticle Characterisation

The successful synthesis AuNPs was confirmed by measuring their absorbance with ultra-violet visible (UV-vis) spectrophotometer. the diameter of the AuNPs and their concentration via equation 3.2 and 3.3 [360].

$$r = \frac{A_{max}}{A_{450}} \qquad (3.2)$$

where:

r – ratio.

A_{max} – the highest absorbance value in the UV-vis spectrum.

A_{450} – the value of absorbance at 450 nm in the UV-vis spectrum.

The value of r when matched with data table found in the Table S-2 of [360] provides the theoretically calculated diameter of the AuNPs.

$$c = \frac{A_{450}}{\varepsilon_{450}} \qquad (3.3)$$

where:

c – concentration of AuNPs (in M).

ε_{450} – molar decadic extinction coefficient (in M^{-1}) at 450 nm (obtained from Table S-3 of [360] for the theoretical diameter calculated using the ratio found in equation 3.2).

A_{450} – the value of absorbance at 450 nm wavelength in the UV-vis absorption curve.

In addition to the above, the morphology of the AuNPs was visualized with transmission electron microscopy (TEM).

3.5.5 Determining Appropriate Volume of Salt Solution

1% sodium chloride (NaCl) solution was prepared in deionised water (dH_2O) by dissolving 10 mg of NaCl per mL of dH_2O. In order to aggregate the AuNPs sufficiently without losing their plasmonic properties, 60 µL to 400 µL of the prepared 1% NaCl solution, with an increment of 20 µL for each measurement, was added to cuvette containing 950 µL synthesised colloidal AuNPs and 50 µL of dH_2O and UV-vis measurements were carried out on this mixture. The 50 µL of dH_2O was added as a substitute for the nanoplastic

solution which was not added with a concern for effecting the aggregation of the AuNPs as the purpose of these UV-vis measurements was to find out the best volume of 1% NaCl that aggregates the AuNPs such that maximum absorbance is achieved at the excitation wavelength (785 nm) used for the experiments. It is worth mentioning that fresh AuNPs and dH_2O mixture was used for each measurement instead of adding 20 µL of NaCl solution to the same mixture after each measurement. As seen in Figure 3.9a the maximum absorbance at 785 nm was found for 340 µL of the 1% NaCl solution.

3.5.6 Preparation of Nanoplastic Solutions

The commercially available 2.5% (i.e. 25 mg/mL) and 10% (i.e. 100 mg/mL) solids aqueous solution of the 50 nm and 100 nm PS nanoplastics were used to prepare 0.5, 1, 5, 20, 50, 80 and 100 µg/mL suspensions of the nanoplastics by adding appropriate volumes of dH_2O to dilute the purchased stock solutions.

3.5.7 Methodology for Detecting Nanoplastics

Figure 3.7 shows an illustration of the experimental methodology adopted to detect nanoplastics through the use of SERS with aggregated AuNPs. 170 µL of the 1% NaCl solution was added to a mixture of 25 µL of the prepared nanoplastic suspension (Section 3.3.6) and 475 µL of AuNPs. The addition of the NaCl solution caused immediate aggregation of the AuNPs which was visible with naked eye in the form of a color change from wine red to bluish purple. The solution is immediately vacuum filtered onto the Si filters, followed by an immediate vacuum filtration of 2 µL of dH_2O to avoid further aggregation of AuNPs and by extension the loss of plasmonic properties of the AuNP aggregates is avoided. Subsequently, SERS measurements were carried out on the filter containing the aggregated AuNPs and nanoplastics. The calibration curve for each sized nanoplastic was plotted by taking an average of the SERS signal intensity at the diagnostic peak for the various concentrations with the standard deviation denoted through error bars. The diagnostic peak was selected from the Raman spectrum taken from a PS pellet with all the characteristic peaks marked and compared to those found in the literature.

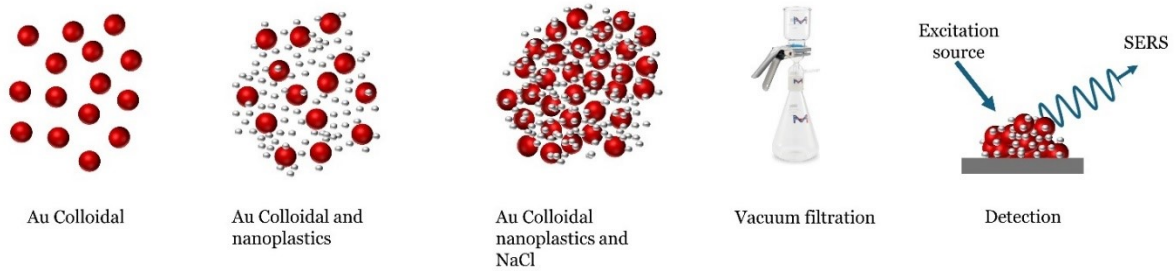

Figure 3.7: An illustration of the experimental methodology used for detecting nanoplastics through the use of SERS with aggregated AuNPs.

3.5.8 Detection of Nanoplastics Spiked in Drinking Water

Following the concentration study on nanoplastic suspensions prepared in laboratory grade water (dH_2O), the validation of the methodology for 'real world-like' samples was tested by spiking experiments carried out on drinking water. The spiking experiments were done for 20, 50, 80 µg/mL of 100 nm PS nanoplastics prepared in water taken from drinking cooler at Institute for Global Food Security (IGFS) Belfast, UK. The recovery percentage was calculated for the spiked drinking water in comparison to those detected in dH_2O.

3.5.9 Analysis Instrumentation

Ultraviolet-visible (UV-vis) absorption spectroscopy measurements were performed using an Agilent Technologies (USA) Cary 60 spectrophotometer. Transmission electron microscopy (TEM) measurements were performed using a Jeol JEM 1400 Plus model, operated at 200 kV, provided by Thermo Fisher Scientific (UK). Vacuum filtration was carried out using a filtration pump by Davidson & Hardy Ltd (UK). Raman and SERS measurements were carried out using a Thermo Fisher Scientific (UK) DXR2 Raman microscope operated with an excitation laser light at 785 nm and 20mW. An objective lens of 50x magnification with a numerical aperture of 0.75 was used in the microscope. The DXR2 spectrometer can provide spectra in the range of 200 to 3000 cm^{-1} with a spectral resolution of 4 cm^{-1}. All the spectra presented and discussed in this work were subjected to a baseline correction and spectra were taken for an integration time of 3 s with each measurement being an average of 3 acquisitions.

3.6 Results and Discussion

3.6.1 Numerical Simulations

The numerical simulation carried out using COMSOL Multiphysics (Figure 3.8) calculated the maximum value of EF (EF_{max}) as $10^{6.7}$ (Figure 3.8b), but the surface plasmon resonance (SPR) of the nanoparticles is dependent upon their size and shape therefore affecting the hotspots and subsequently the EF_{max} that can be achieved experimentally [357]. The numerical model presented could be used as a generic approach to model clustering and agglomeration of metallic nanoparticles for SERS applications.

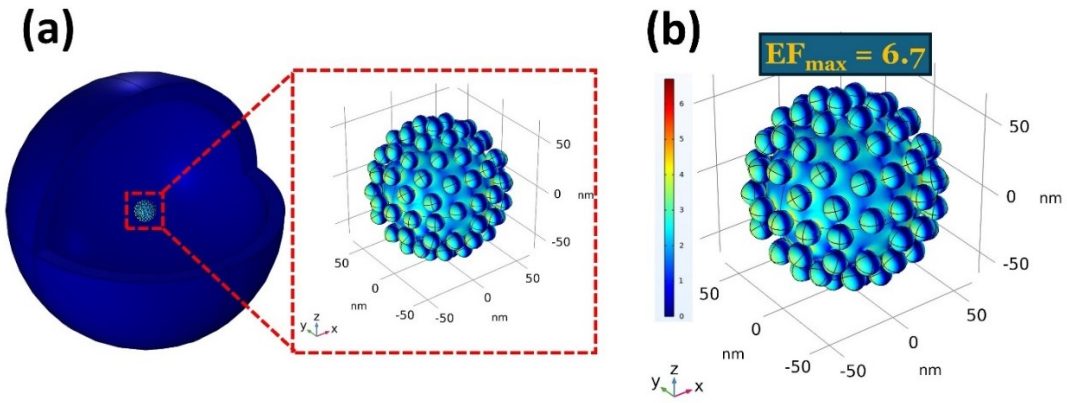

Figure 3.8: (a) A finite element method numerical simulation of AuNPs surrounding a 100 nm PS nanoplastic, showing the entire simulation region with the inset focusing on the mesh used for the nanoplastic and surrounded by AuNPs after the simulation is run (b) the AuNPs surrounding PS nanoplastic with the maximum enhancement factor indicated.

3.6.2 Gold Nanoparticle Characterisation

The synthesis of stable Au nanoparticles is confirmed by a single narrow maximum at 520 nm (λ_{max}) in their absorbance spectrum (Figure 3.9a) [361], with the ratio calculated as 1.54 (using Equation 3.2) resulting in an estimation of 10 nm as the nanoparticle diameter [362]. The concentration (c) of the synthesised AuNPs is determined from Equation 3.3 [362], using ε_{450} = 6.15E+07 M^{-1} for particles of that diameter, to be 0.16 nM. The morphology of the Au nanoparticles can be seen in TEM images (Figure 3.9b) to be that as fairly spherical and having a diameter that varies just by a few nanometres.

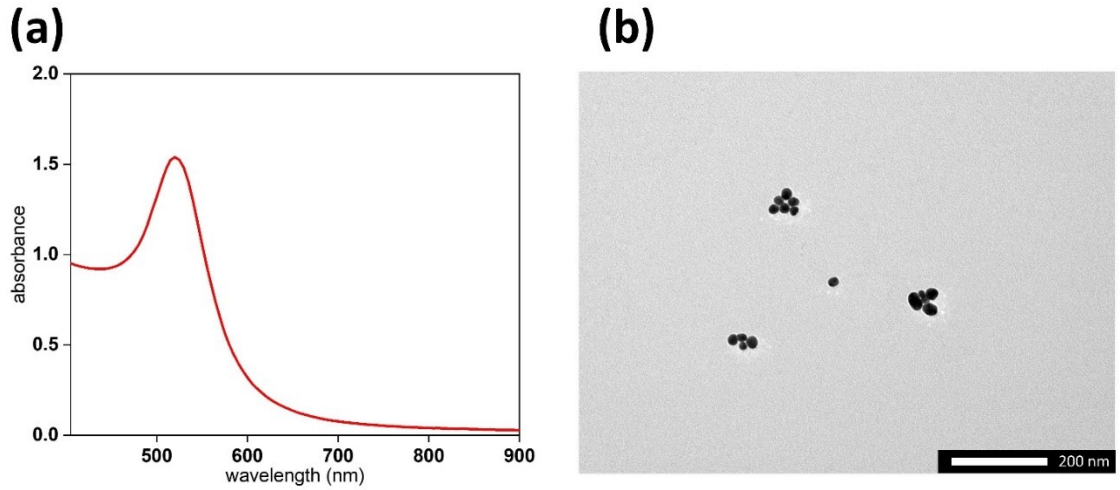

Figure 3.9: (a) UV-vis absorbance spectrum for the synthesised colloidal AuNPs having maximum absorbance of 1.51 at the plasmon resonance of 520 nm (b) TEM image of colloidal Au nanoparticles showing a fairly spherical morphology.

3.6.3 Characterisation of Aggregated Gold Nanoparticles

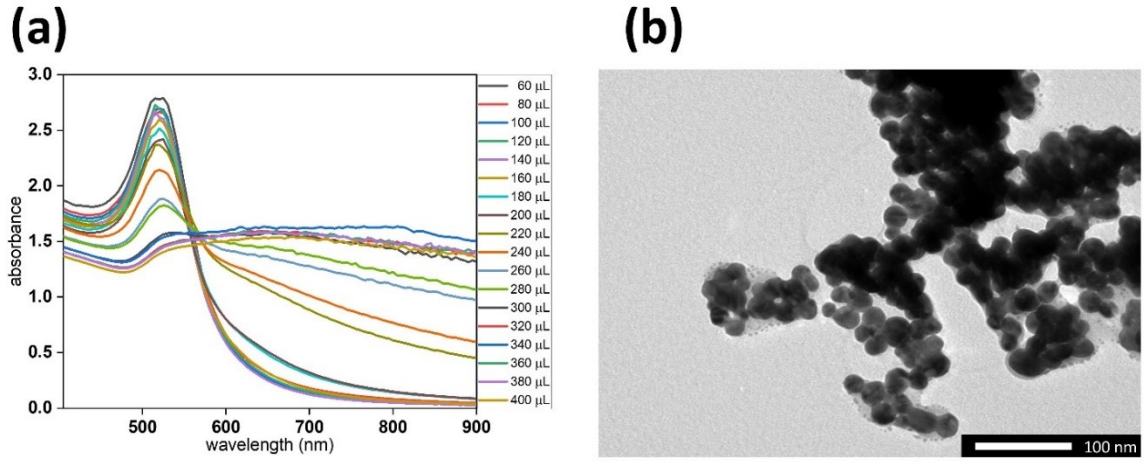

Figure 3.10: a) UV-vis absorbance spectroscopy curves for agglomerated Au nanoparticles formed through the addition of varying volumes of 1% NaCl to a 1ml colloid of gold (b) TEM image of aggregated AuNPs within saltwater.

UV-vis absorbance spectroscopic measurements of 95 µL AuNPs and 50 µL dH_2O with the varying additional volumes of a 1% NaCl solution showed a broadening and red shift in the absorbance peak of the colloidal nanoparticles due to multiple scattering from the formed AuNP clusters (Figure 3.10a). TEM images of the aggregated nanoparticles show them in clusters (Figure 3.10b), held together by van der Waals forces, thereby forming lots of hotspots [363] through plasmon interaction between the aggregated nanoparticles [364].

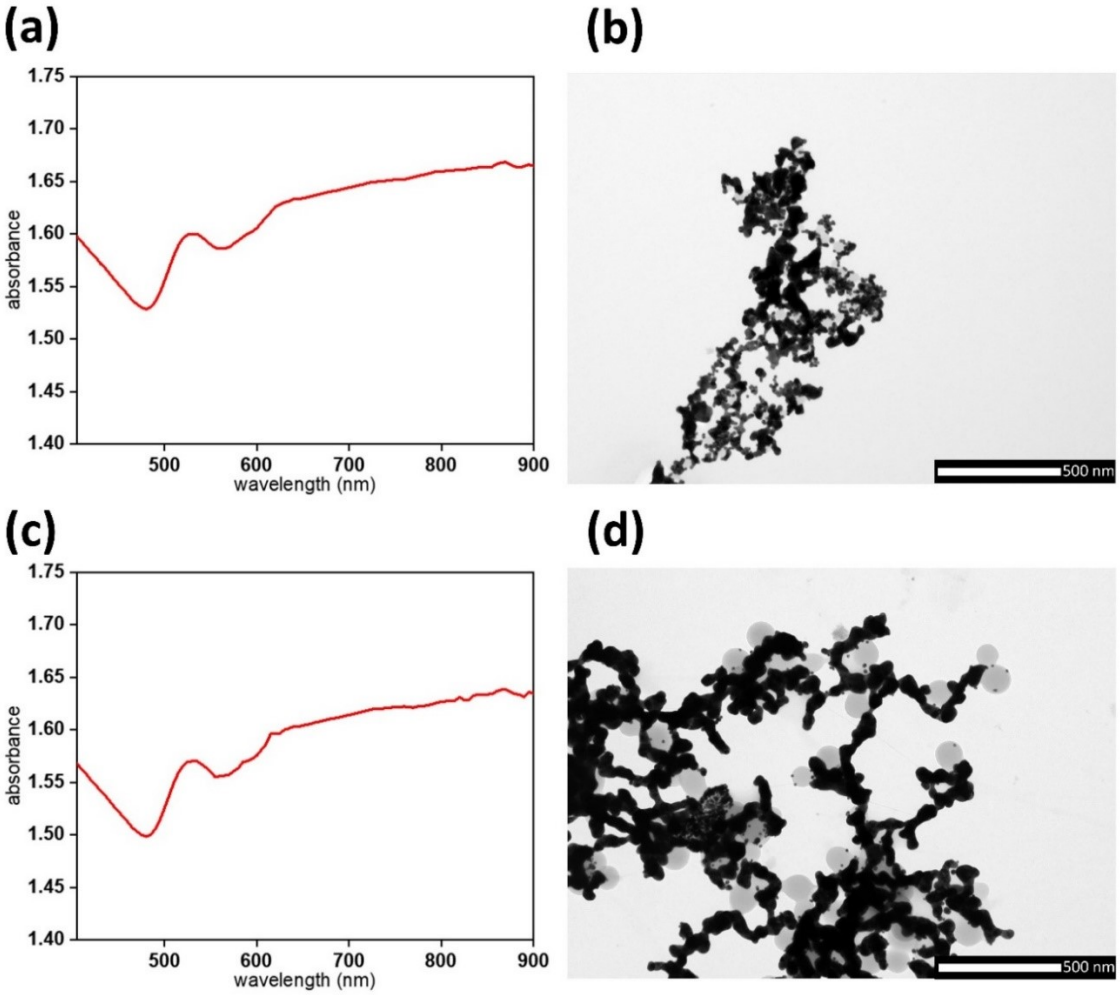

Figure 3.11: a) UV-vis absorbance spectroscopy curves of 50 nm PS nanoplastics surrounded by aggregated AuNPs (b) TEM image of 50 nm PS nanoplastics surrounded by aggregated AuNPs (c) UV-vis absorbance spectroscopy curves of 100 nm PS nanoplastics surrounded by aggregated AuNPs (d) TEM image of 50 nm PS nanoplastics surrounded by aggregated AuNPs

Optical absorption spectra for aggregated AuNPs surrounding the nanoplastics, formed from the addition of 170 µL of 1% NaCl (in dH_2O) to 475 µL AuNPs and 25 µL solutions of nanoplastics (in dH_2O), show no significant difference compared to their analogue without nanoplastics (Figure 3.10a) for either 50 nm (Figure 3.11a) or 100 nm (Figure 3.11c) diameter PS nanoplastics. As the presence of the nanoplastics does not affect the optical properties of the aggregated AuNPs, they do not affect the aggregation process itself either [365]. Instead, the TEM images (Figure 3.11 b and d) of the 50 nm and 100 nm PS nanoplastics surrounded by aggregated AuNPs shows that the aggregation process brings them closer together, trapping them between the aggregated nanoparticles, and improving the SERS enhancement, as explained in the Section 3.4.4.

3.6.4 SERS Detection of Nanoplastics

Figure 3.12 shows the Raman spectrum of a PS pellet which was carried out to determine the with all the characteristic peaks of PS marked on the spectrum. The experimentally measured characteristic peaks, at approximately 618 cm^{-1}, 795 cm^{-1}, 1000 cm^{-1}, 1030 cm^{-1}, 1154 cm^{-1}, 1447 cm^{-1}, 1581 cm^{-1}, and 1601 cm^{-1}, were then compared with those found in the literature for complete peak assignment as seen in Table 3.2. The most prominent peak for PS found at approximately 1000 cm^{-1} was selected as the diagnostic peak of interest for the subsequent concentration study.

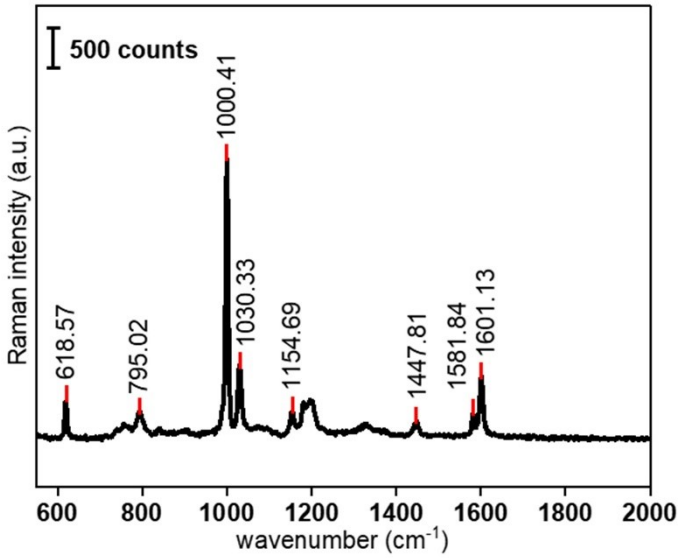

Figure 3.12: A Raman spectral analysis for a PS pellet with the most prominent peaks indicated for subsequent comparison with those reported in the literature that are associated with characteristic bands and thus the selection of the most appropriate diagnostic peak for a concentration study of 50 nm and 100 nm PS nanoplastics.

Table 3.2: Experimentally measured characteristic peaks for polystyrene listed against values found in the literature and their band assignment.

Raman shift according to the experiment (cm^{-1})	Raman shift according to the literature (cm^{-1})	Peak assignment	Ref
618.57	621	Ring deformation mode	[366]
795.02	795	C-H out-of-plane deformation	[366]
1000.41	1001	Ring breathing mode	[366]
1030.33	1031	C-H in-plane deformation	[366]
1154.69	1155	C-C stretching	[366]
1447.81	1450	CH_2 scissoring	[366]
1581.84	1583	C=C stretching	[366]
1601.13	1602	Ring-skeletal stretching	[366]

SERS spectra for various concentrations (0.5, 1, 5, 20, 50, 80 and 100 µg/mL) of 50 nm and 100 nm PS spherical nanoplastics within aggregated AuNPs can be seen in Figure 3.13 a and b, respectively. Whilst the comparable intensity of SERS signals for the different sized nanoplastics at all concentrations (Figure 3.13 a and b) may be due to the AuNPs bringing the nanoplastics closer to each other during aggregation, making size somewhat irrelevant, another cause is more likely. The 50 nm PS nanoplastics [367] are amine modified by their manufacturer which increases the likelihood of their attachment to the AuNPs [368] and thus entering hotspot regions for an increased SERS signal that is comparable to unmodified 100 nm PS nanoplastics among AuNP aggregations. For nanoplastics of both sizes, ultra-low concentrations of 0.5 µg/mL were successfully detected, proving the efficiency of the used methodology.

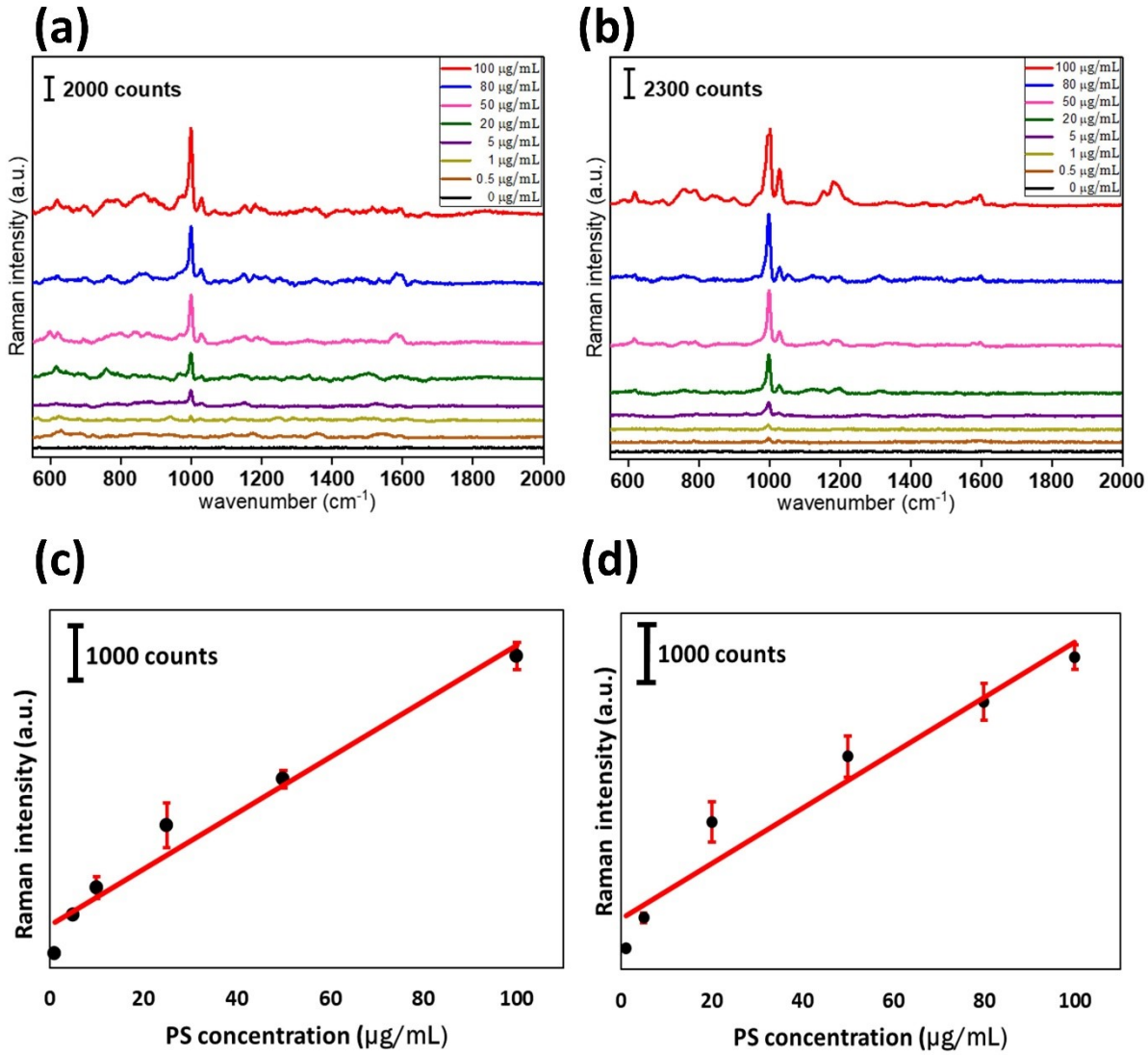

Figure 3.13: (a) Concentration dependent SERS spectra for 50 nm polystyrene nanoplastics in dH_2O (b) Concentration dependent SERS spectra for 100 nm polystyrene nanoplastics in dH_2O (c) Calibration curve for the SERs signal of various concentrations of the diagnostic peak at 1000 cm^-

[1] for 50 nm polystyrene nanoplastic (d) Calibration curve for the SERs signal from various concentrations of the diagnostic peak at 1000 cm^{-1} for 100 nm polystyrene nanoplastic

Figure 3.13 c and d illustrates the change in intensity across various concentrations for the selected diagnostic peak at 1000 cm^{-1} for 50 nm and 100 nm PS nanoplastics, respectively, with error bars corresponding to the three different measurements being taken for each concentration. Although the calibration curves of PS concentration vs Raman intensity (Figure 3.13 c and d) from the linear regression lines fit well through the intensity data, having R^2 values of 0.96 (for 50 nm PS nanoplastics) and 0.94 (for 100 nm PS nanoplastics), but a more of logarithmic trend is clearly visible particularly for the lower concentrations of 50 nm and 100 nm PS nanoplastics. A similar trend has been seen in SERS detection of nanoplastic through potassium iodide (KI) induced aggregation of AgNPs [269]. Although no particular reason was explained in the mentioned study, we believe it is because in lower concentrations all the nanoplastics are surrounded by much more clusters of the metallic nanoparticles as compared to those seen by nanoplastics in higher concentrations, therefore the lower concentrations of nanaoplastic get higher plasmonic enhancements resulting in such a trend.

3.6.5 Detection of Nanoplastics Spiked in Drinking Water

Figure 3.14 shows the SERS signal intensity at 1000 cm^{-1} for 20, 50 and 80 µg/mL of 100 nm nanoplastic samples prepared in dH_2O (black) and in drinking water (orange).

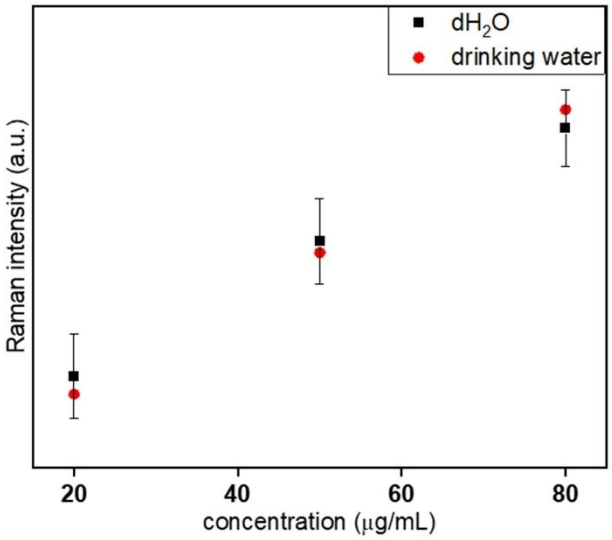

Figure 3.14: SERS intensity at the characteristic peak of 1003 cm^{-1} from substrates prepared using 20, 50 and 80 µg/mL concentrations of 100 nm PS nanoplastics in dH_2O and in drinking water in the salt induced gold nanoparticle agglomeration-based methodology from section 3.2.

Table 3.3 presents Figure 3.14 in a tabular form and also includes the recovery rates for the intensities from the drinking water-based substrates signals over those from the substrates prepared using dH_2O.

Table 3.3: SERS intensity at 1000 cm^{-1} as a function of the concentration of 100 nm polystyrene nanoplastics in dH2O and drinking water that were used to prepare the substrates. Also shown for each concentration is the recovery rates for the intensities of the drinking water-based substrate signals over those from the substrates prepared using dH_2O.

Concentration (µg/mL)	dH_2O	Drinking water	Recovery rate%
20	2493	2347	94.1
50	3587	3497	97.5
80	4504	4658	103.4

As seen in Table 3.3, from the lowest concentration to the highest the range of the recovery rate of 95.2% and 104.5% is well within the acceptable (±20%) [65] and preferred range (±10%) [66] overall confirming the reliability and repeatability of the methodology for detecting nanoplastics in real world samples.

3.7 Conclusions

This Chapter reports on the development of a unique methodology, that is both simple and efficient and is based on filtering salt induced aggregations of AuNPs surrounding the nanoplastics, that enabled the cost-effective SERS detection of 50 nm and 100 nm PS nanoplastics, with the main findings being the following:

- Addition of salt to AuNPs aggregates them resulting in a broadening and redshift of the UV-vis absorption spectroscopic spectrum of the AuNPs.
- Addition of nanoplastics to AuNPs has no effect on either the optical properties of the AuNPs or the aggregation of the AuNPs.
- Aggregation of AuNPs around nanoplastics results in formation of hotspots that increase the plasmonic enhancement as compared to colloidal AuNPs, therefore enabling detection of nanoplastics as low as 0.5 µg/mL.

Whilst the SERS detection of nanoplastic through the use of salt aggregation of AuNPs. was successful, the process to do so it is not controllable as it relies on the removal of the stability of the AuNPs and the aggregation is dependent upon the diffusion of the salt in the AuNP colloidal which is uncontrolled.

Therefore, a methodology was sought that was more controllable and with AuNP not being made unstable, so that the SERS signal would be repeatable and sustainable across each substrate produced and from substrate to substrate. To this end it was hypothesised that the wettability of a solid surface could be modified to form a homogenous hydrophobic layer that when AuNPs were drop cast on it they would undergo a highly controlled and homogenous clustering capable of such a SERS signal. Detailed explanations, including the adopted methodology and the results achieved for SERS detection of nanoplastics is presented in Chapter Four.

Chapter Four

Detection of nanoplastics through the use of surface enhanced Raman spectroscopy with controlled clustering of gold nanoparticles by forming hydrophobic SERS substrates.

The work presented in this chapter was done in collaboration with a colleague, James Tate, from Queen's University Belfast. He particularly did the characterisation of the SERS substrate using the Rhodamine 6G (sections 4.4.2-4.4.4).

4.1 Introduction

The wetting properties of a surface can be exploited ingeniously to develop SERS substrates that do not require typically used complicated time-consuming pre-treatments and expensive. Therefore, subsections 4.1.1 – 4.1.4 will concentrate on concepts and models related to wettability of a surface.

4.1.1 Wettability of a surface

The wettability of any solid surface is defined as the capacity of a liquid droplet to sustain contact with it and can be represented by the angle that forms at the three-phase contact of a solid (S), liquid (L) and gas (G), or contact angle of wetting, θ_c, which is also known as the liquid contact angle [369], [370].

4.1.1.1 Young's Equation

Equation 4.1, illustrated in Figure 4.1, is known as Young's equation, and is derived from the liquid-gas (LG), solid-liquid (SL) and solid-gas (SG) intersections forming a contact angle of wetting, θ_c [371].

$$\cos\theta_c = \frac{\gamma_{SG}-\gamma_{SL}}{\gamma_{LG}} \quad (4.1)$$

where:

θ_c – is the solvent contact angle.

γ_{SG} – is the surface free energy or surface tension of the solid.

γ_{SL} – is the interfacial tension between the solid and liquid.

γ_{LG} – is the surface tension of the liquid.

Young's equation (equation 4.1) includes a linear relationship between the solid surface energy and the cosine of the solvent contact angle, thus solids with high surface energies exhibit lower contact angles, while those with low surface energies display higher contact angles [371], [372]. A low surface energy means that the solid is not capable of forming strong bonds and so it is not energetically favourable for a liquid to break bulk bonding to interact with it.

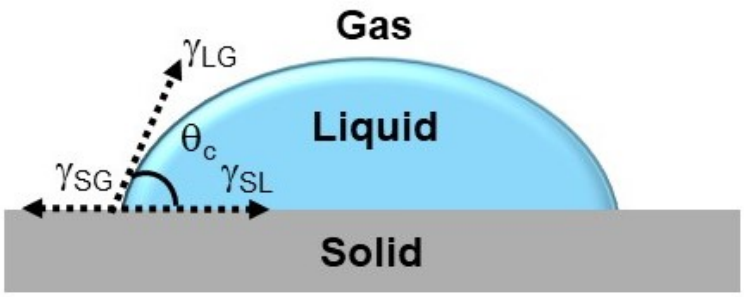

Figure 4.1: Illustration of Young's equation that represents the wettability of a surface in terms of its capacity to form a contact with the surface of a liquid, expressed as the contact angle (θ_c). The arrows indicate the direction of the forces i.e. the surface tension of the solid, the interfacial tension between the solid and liquid and the surface tension of the liquid, acting on the three-phase contact line of a droplet of liquid on a smooth solid surface within a gas.

Furthermore, a high surface tension liquid prefers to maintain bonds with itself rather than with a solid surface as indicated by the inverse relationship between the liquid surface tension and contact angle (equation 4.1). This can be seen with oils and non-polar solvents that have lower surface tensions compared to water, 20 – 35 mN/m and ~72 mN/m respectively, and thus have a greater tendency to collapse under the downward pressure of gravity, an indication of a lower contact angle [373], [374]. Summarising, a surface is classified as wetting when its θ_c is below 90°, and as non-wetting or anti-wetting when it exceeds 90° [5], with the specific terminology when the solvent is water being (Figure 4.2) hydrophilic where there is a strong affinity ($\theta_c < 90^o$), hydrophobic where there is a moderate affinity ($90^o \leq \theta_c \leq 150^o$) or super-hydrophobic ($\theta_c > 150^o$) [375].

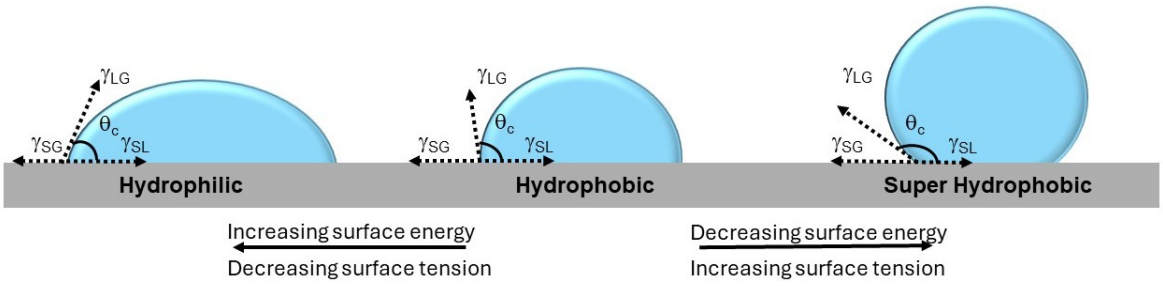

Figure 4.2: An illustration of Young's equation with the contact angles, and correspondingly the type of surface achieved for a water droplet, with identification of how changes in surface energy and surface tension effect the surface type.

Whilst Young's equation is effective for describing the wetness of ideal smooth surfaces, it has been extended to the Wenzel and Cassie-Baxter models in order to consider the effects of surface roughness and heterogeneity on contact angles, as most surfaces present some roughness [376].

4.1.1.2 The Wenzel Model

The Wenzel model, illustrated in Figure 4.3a and Equation 4.2, considers liquid penetrating rough surfaces whilst maintaining contact with the top and hollow parts of them forming Wenzel state. Specifically, it describes how the complete penetration of a solvent into the rough microstructure of a surface with a uniform topography, such as pores or regular columns, can amplify both anti-wetting ($\theta_c > 90°$) and wetting ($\theta_c < 90°$) through inclusion of an additional factor, the roughness ratio (r) [377].

$$\cos\theta_w = r\,\frac{\gamma_{SG} - \gamma_{SL}}{\gamma_{LG}} = r\cos\theta_c \qquad (4.2)$$

where:

θ_w – is the Wenzel apparent contact angle.

r – is the roughness factor (the ratio of the real surface area of the solid to the projected surface area).

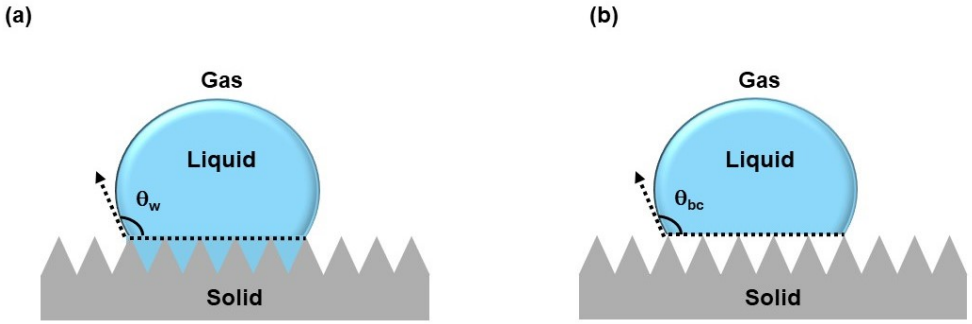

Figure 4.3: Illustration of (a) Wenzel and (b) Cassie-Baxter wetting models through the use of a single droplet on a rough solid surface.

4.1.1.3 The Cassie-Baxter Model

Should the contact angle become pinned at the surface asperities, rather than aligning with the underlying solid, given the roughness geometry and liquid surface tension, the Wenzel model no longer holds true. This led to the development of the Cassie-Baxter model (Figure 4.3b and equation 4.3) [378] where liquid droplets rest on heterogeneous surfaces, spanning the uppermost features of a rough substrate, while the grooves between these features are filled with other materials, such as air. According to Cassie-Baxter model for a rough surface with trapped air, the water droplet can contact both the solid and the air forming composite liquid-air and solid-liquid interfaces, with its wetting state still existing at higher contact angles compared to that in the Wenzel model [379].

$$\cos\theta_{bc} = \varphi_S\cos\theta_c + \left(1 - \varphi_S\right)\cos\theta_a \qquad (4.3)$$

where:

θ_{bc} – is the Cassie-Baxter apparent contact angle.

φ_S – is the fraction of the solid surface in contact with the liquid.

$(1 - \varphi_S)$ – is the fraction of air in contact with the liquid on a Cassie-Baxter surface.

θ_a – is the contact angle of the air portion.

The Cassie-Baxter state, typically observed on high surface energy substrates that would be wetting according to the Young's equation (also shown in Figure 4.2), can be induced through a multivalued topography. Such a topography is characteristic of surfaces where a line drawn from the base is likely to intersect solid features at least once, as in the case of mushroom-shaped protrusions where the rough valleys are interconnected with the surrounding atmosphere [380]. Air trapped within these valleys can generate negative Laplace pressure (the pressure difference between the droplet's interior and exterior), transforming the liquid-vapor interface from concave to convex and thus preventing liquid infiltration [381].

4.1.1.4 Contact Angle Hysteresis

Previously, in the Young, Wenzel, and Cassie-Baxter models a static contact angle has been considered, whereas contact angle hysteresis, where there is a dynamic adhesive interaction between a solvent droplet and the substrate, should also be considered (Figure 4.4). In such a consideration the tilting angle (β) is the difference between the receding contact angle (θ_r), representing solid-liquid adhesion, and the advancing contact angle (θ_a), representing solid-liquid cohesion [382], with a surface classified as slippery when $\beta < 5°$ or sticky when $\beta > 5°$ [383]. Due to the pinning of droplets on rough substrates, surfaces in the Wenzel model typically exhibit higher tilting angles compared to those in the Cassie-Baxter model, with the reduced adhesion in the Cassie-Baxter model resulting in slippery surfaces that repel liquids. This slippery, or liquid repellent, effect offered is traditionally referred to as the lotus effect [384] as the leaves of that plant have naturally, slippery and liquid repellent behaviour. A less prevalent phenomenon exists at the intermediate state between the Wenzel and Cassie-Baxter states, or the Cassie-impregnating wetting state, where a solvent can infiltrate the larger surface features but is prevented from penetrating finer nanoscale features where air pockets remain trapped [385], [386]. As a result, the Cassie-impregnating state produces surfaces with high

adhesion (β >5°) and high contact angles (>150°), and thus sticky liquid repelling surfaces, commonly referred to as the petal effect [386].

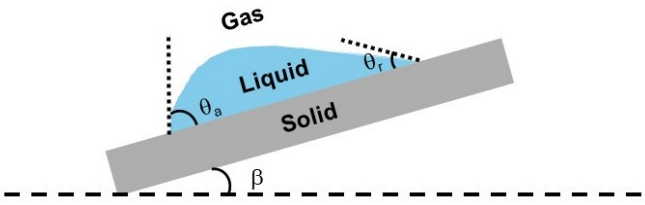

Figure 4.4: An illustration of contact angle hysteresis which considers the adhesiveness of a solvent droplet to a substrate when sliding over a tilted surface with θ_a, θ_r, and β representing the advancing contact angle, recending contact angle and tilting angle, respectively.

4.1.2 Wettability and surface enhanced Raman spectroscopy (SERS)

As the work within the Chapter considers the development of hydrophobic substrates based on aluminium foil (ALF-HB), the subsequent section section 4.1.2.1, concentrates on the state of the art in surface enhanced Raman spectroscopy (SERS) detection of various analytes through the use of hydrophobicity.

4.1.2.1 Use of hydrophobicity for surface enhanced Raman spectroscopy (SERS) applications

A droplet of liquid that contains a solvent and an analyte that pins to an adhesive hydrophilic surface undergoes heterogeneous drying, evaporating slowly at the contact point and faster at its edge, with the evaporation gradient directing it to flow towards the latter, leading to a non-uniform radial distribution of the analyte concentration, otherwise known as ‘coffee ring patterns’.

It is therefore hypothesised that by decreasing the wettability of a SERS substrate it would potentially increase the uniformity and stability of the Raman signal from the solvent and analyte introduced to it as a droplet [387]. Moreover, in reducing the diffusion rate of the analyte molecules [388], thus bringing the analyte molecules closer [389], the analyte would be concentrated over a smaller area consequently improving the detection limits, for the detection of trace quantities of analyte that would prove otherwise impossible. The most prevalent method for reducing the wettability of a SERS substrate is to modify its surface to become hydrophobic with the methods used to do so categorising the resulting substrates into natural, biomimetic and synthesised hydrophobic substrates.

For the former, the hydrophobicity observed in plants and insects, which arises from either micro-/nano-scale surface structures, a low surface energy coating, or a combination of

both [390], has gained interest for use in SERS detection due to its facile characteristics and low cost. Amongst these, Lotus leaves are the most superhydrophobic naturally occurring plant leaf, with contact angles >160º, due to their coating with a wax composed of a mixture of the non-polar long-chain fatty alcohols, nonacosanediols and nonacosan-10-ol [391], [392], [393]. Due to their super hydrophobicity the simple drop-casting of silver nanoparticles (AgNPs) onto Lotus leaves has reported to have been used to detect 1.2 μg/L of Paraquat [394]. Taro leaves, despite having a hydrophobicity 10% less than that of lotus leaves, have also been used for SERS detection, for example, a layer of Ag deposited onto a taro leaf through physical vapor deposition (PVD) was used to demonstrate a low limit of detection (LoD) of 10^{-8} M for Rhodamine 6G (R6G) [395]. Despite their high levels of hydrophobicity, their use for SERS detection is challenging as the pigment chlorophyll is found in all green leaves and its significant fluorescence typically obscures the Raman scattering peaks of interest in Raman measurements [395]. The chlorophyll can be easily decomposed however through direct exposure to intense ultraviolet (UV) radiation, but this process is time-consuming, and does not remove the Raman scattering peaks that it also produces that can obscure the signal from trace quantities of analytes [396]. As an alternative, given their lack of chlorophyll, rose petals, have been used to detect R6G at concentrations as low as 10^{-9} M in [397], whilst naturally occurring insect-based hydrophobic surfaces have also been used, such as the tapered nanopillars on cicada wings in the presence of AgNPs to detect difenoconazole down to 0.016 parts per million (ppm) [398]. Unfortunately, such naturally occurring surfaces don't have homogenous or reproducible structures and so their SERS signal is neither uniform across the same surface nor is its distribution identical from surface to the next. Moreover, their surfaces are prone to withering and dehydration, resulting in damage to the structure and a reduction in the hydrophobicity offered [399]. To overcome these challenges while still taking advantage of naturally occurring hydrophobic surfaces there has been an increase of interest in biomimetics [400].

Biomimetics, the imitation of biological processes or models, has been applied to techniques such as soft lithography, nanoimprinting or simply sputtering, through the use of naturally occurring materials as templates, to develop hierarchical micro-/nano-structures [400], [401], [402]. For example, a nanostructured polymer polydimethylsiloxane (PDMS) surface was produced in soft lithography through the use of a taro leaf as both template and stamp to pattern the deposited PDMS, with the layer of Ag deposited upon it leaving it hydrophobic and capable of detecting malachite green down to ultralow concentrations of 10^{-11} M [403]. That with said, as nanoscale feature loss can occur where the polymer might fail to penetrate, it is more suitable to use

nanoimprinting, where the natural hydrophobic surfaces are used as a template to pattern a thin film of resist with the nanoscale features and structures that once cured through heat or UV radiation becomes the stamp itself [404]. One such example of nanoimprinting, is the transfer of the uniformly distributed ridges and valleys on lettuce leaves, via a patterned and cured resist based stamp, into PDMS for a hydrophobic layer that through coverage by sputtered Ag was used to detect 4-mercaptobenzoic acid through SERS [401]. However, although nanoimprinting can reproduce nanoscale features more faithfully than soft lithography, defects in fabricated nanostructures have been reported due to contamination between the mask and the resist and from distortions upon removal of the template [405].

Finally, hydrophobic layers have been reported as synthesised without using any naturally occurring surface as a template or stamp. For example, wax was melted onto a patterned silicon wafer, resulting in a hydrophobic layer, that when covered with AuNPs was used to detect methyl parathion and melamine 10^{-9} M through SERS [406]. In another approach, a layer of PDMS that was spin coated onto filter paper demonstrated hydrophobic behaviour, and following the deposition of a layer of graphene oxide onto that and AuNPs grown on that layer, as a SERS substrate it enabled the detection of R6G concentrations as low as 10 nM [407]. Summing up, the surface modification of ubiquitous, low-cost materials, such as filter paper, silicon filters, glass slides, cotton etc, with yet again commonly available and inexpensive materials, such as wax, PDMS, lubricating liquids etc, has been widely reported to produce highly hydrophobic layers that can be subsequently used for the low-cost SERS detection of trace analytes.

Table 4.1, a comprehensive summary of SERS detection through the use of hydrophobic substrates, shows that such substrates have been reported for the detection of trace quantities of dyes [408] [409], and the chemicals used in antibiotics [410], fungicides [411], insecticides [412], herbicides [400] and pesticides [413]. Despite their efficiency however, aside from one example, hydrophobic SERS substrates have never been used for the detection of nanoplastics. Even then that one exception, where Li et al. detected 100 nm and 500 nm polystyrene (PS) nanoplastics, it had to be done with a centrifugally enriched solution of Ag nanoparticles and nanoplastics [414]. Furthermore, the process used to prepare the hydrophobic surface in the study was a time-consuming lengthy process requiring more than 12 hours before a droplet of the enriched solution could be added, to create a smaller spot than on a non-hydrophobic surface, to then demonstrate an increase in the SERS signal intensity and reproducibility of the substrate.

Type	Plasmonic structures	Hydrophobic layer	Contact Angle	Analyte	LoD	Ref
Natural	AgNP	Lotus leaf	149.1º	Paraquat	1.2 µg/L	[394]
	Ag layer via physical vapour deposition	Taro leaf	154º	R6G	$1x10^{-8}$ M	[395]
	Thermally deposited Ag film	Chitin film from Japanese giant silkworm	98.9º	Methylene blue	$1x10^{-9}$ M	[415]
	Ag	Cicada wings	115º	-	-	[416]
	Ag	Rose petal	158º	R6G	$1x10^{-9}$ M	[397]
	AgNPs	Cicada wings	-	difenoconazole	0.016 ppm	[398]
Biomimetic	Ag layer via sputtering	Biomimetic lettuce leaf using nanoimprinting	-	4-mercaptobenzoic acid	$1×10^{-9}$ M	[401]
	Ag nanofilm via sputtering	Biomimetic butterfly wing	-	Crystal violet	$1x10^{-9}$ M	[417]
	Ag layer	Biomimetic taro leaf using soft lithography	128º	Malachite green	$1x10^{-11}$ M	[403]
	AgNP coated filter paper	Biomimetic lotus leaf using PDMS	150.3º	R6G Thiram	$1x10^{-10}$ M 0.5ng /cm^2	[413]
	AuNPs	Biomimetic leaves using soft lithography	135º	Herbicides (TBZ and CZ)	$1x10^{-9}$ M	[400]
	AuNPs	Biomimetic beetle wings	123.8º	Methylene blue and carbendazim	$1x10^{-9}$ M	[418]
	Ag micro-islands covering graphene oxide	Magnetron sputtering and dip-coating used to replicate nanostructures on lotus leaf	-	Crystal violet	$5 × 10^{-10}$ M	[402]
	Ag	Biomimetic Cicada wings	119º	R6G melamine	1 ppm	[416]
Synthetic	Au nano-islands	Ivy like nanostructures of α, ω-diperfluorohexylquaterthiophene (DFH-4T) on polydimethylsiloxane (PDMS) modified using nitrogen plasma	146º	cholecalciferol	$1 x 10^{-10}$ M	[419]
	Cu nanowires covered with AgNPs	cetylpyridinium chloride coating on AgNPs	134º	R6G	10^{-11} M	[420]
	AgNPs	alkyl ketene dimer treated filter paper	114º	4-aminothiophenol, thiram and ferbam	$0.46 x 10^{-9}$ M	[411]
	Cu nanostructures grown from AuNPs	Cu nanostructures varying in size attached through polyethylene glycol	137º	R6G Tamoxifen	$10 x 10^{-9}$ M $1 x 10^{-3}$ M	[412]

	AuNPs on graphene oxide	Filter paper with layer of PDMS spin-coated	130º	R6G	10 x 10^{-9} M	[407]
	AuNPs	Wax covered silicon wafer	112.5º	methyl parathion and melamine	1 x 10^{-9} M	[406]
	AuNRs	Layer of silicone oil spin-coated and annealed onto glass slide	110º	ciprofloxacin and norfloxacin	0.01 ppm	[410]
	Aggregating AuNPs	Paper covered with spin-coated lubricating liquid	-	R6G Cytochrome C	4.3 × 10^{-10} M 3.90 × 10^{-8} M	[421]
	Au layer via ablation	stearic acid covered textured stainless-steel sheet	120.3º	R6G	1 x 10^{-14} M	[408]
	Ag layer via vacuum evaporation	Cotton sprayed with PDMS and nano silica	118.6º	p-aminothiophenol	1 x 10^{-11} M	[388]
	AuNPs	Teflon	-	Crystal violet	1 x 10^{-12} M	[409]
	AgNPs	Silicon wafer covered in methyltrichlorosilane-n-Hexane	143.71º	100 nm PS 500 nm PS	1 mg/mL 0.5 mg/L	[414]

Table 4.1: A comprehensive summary of SERS detection through the use of hydrophobic substrates studies, including details on the plasmonic structures used, the hydrophobic layers, resultant contact angles, analytes detected and the LoDs achieved.

4.2 Aims and Objectives

As explained in section 4.1, hydrophobic surfaces reduce the wettability, the capacity of droplets to sustain contact with a solid surface, of solutions prepared in water. Metallic surfaces are generally covered by a thin oxide layer, which exhibits inherent hydrophilicity and adhesion due to interactions between polar water molecules and surface metal cations, oxygen anions, and hydroxyl groups [422]. In the case of aluminium, this hydrophilicity, combined with its natural surface roughness, enhances its wettability, consistent with the Wenzel model [423]. This characteristic poses challenges for trace SERS detection, as analytes spread across the hydrophilic surface when drop-cast, leading to dilution of the target [407]. Furthermore, the formation of coffee ring patterns due to increased diffusion of analyte molecules on a hydrophilic surface can compromise the uniformity of the SERS signal across the surface [387]. Therefore, the work explained in the subsequent sections of the Chapter was done to utilise hydrophobicity by modifying the surface of aluminium foil (ALF) decreasing its wettability to help detect low concentrations of nanoplastics. The approach to utilise hydrophobicity was adopted as a

step-forward from the uncontrolled and completely randomised salt- assisted aggregation of AuNPs reported in Chapter Three. The main aim of the work presented in the subsequent sections was to achieve a more controlled clustering of AuNPs as compared to that achieved through salt-assisted aggregation and demonstrate its suitability for detection of low concentrations of nanoplastics.

In order to fulfil the aim of the Chapter following main objectives were formulated:

1. To reduce the wettability of ALF by modifying its surface to form hydrophobic aluminium foil (ALF-HB).
2. To monitor the variations in SERS signal over the surface of ALF-HB by carrying out complete characterisation through the use of Rhodamine 6G (R6G) dye.
3. To study the efficiency of the ALF-HB for in nanoplastic detection by doing a complete concentration study using pristine nanoplastics.
4. To study the efficiency of ALF-HB for environmental nanoplastics by trying to detect the release of nanoplastics from cups made of expanded polystyrene used for hot drinks.

4.3 Materials and Methods

4.3.1 Chemicals

Gold (III) chloride trihydrate ($HAuCl_4 \cdot 3H_2O$, 99.9%), sodium citrate tribasic dehydrate (HOC(COONa) $(CH_2COONa)_2 \cdot aq$), ethanol, potassium hydroxide (KOH), lauric acid ($C_{12}H_{24}O_2$) and red colour dye rhodamine 6G (R6G) were purchased from Sigma Aldrich (UK). Aqueous suspensions of 2.5 % and 10% solid polystyrene nanoplastic latex beads with 50 nm and 100 nm diameter respectively, and densities of 1.05 g/cm^3, were purchased from Sigma Aldrich (UK). 1x1 cm^2 silicon (Si) filters with pore size of 1 µm were purchased from Thermo Fisher Scientific (UK). Polystyrene insulation cups were bought online from Amazon (UK). Kitchen aluminium foil was purchased from a local store, Tesco Extra (Belfast, UK).

4.3.2 Analysis Instruments

Unless mentioned otherwise, all SERS measurements were carried out using a DXR2 Raman microscope (Thermo Fisher Scientific, UK) with a 532 nm laser operated at 10 mW, 10x magnification and an acquisition time of 5 s. Optical absorbance spectrophotometry measurements were carried out using a Cary 60 spectrophotometer (Agilent Technologies, USA). All scanning electron microscope images were taken with a

JSM-6500F SEM microscope (JEOL, Japan) at 15 kV. Spectral peaks were labelled using OMNICTM Series software and its inbuilt Atlμs function was used to carry out Raman mapping (Thermo Fisher Scientific, UK). All contact angle analysis was completed using a Theta optical tensiometer and its inbuilt OneAttension software (Biolin Scientific, England). All the spectra presented and discussed in this work were subjected to a baseline correction.

4.3.3 Theoretical Modelling

As the ALF-HB is based on the concept of bringing AuNPs and nanoplastics closer together in the form of clusters, theoretical modelling using the COMSOL MultiPhysics software was done to monitor the effect on the theoretical enhancement factor with changes on the interparticle distance. For this purpose, a geometry comprising of a spherical simulation region with three gold nanoparticles having a varying interparticle distance (from 1 nm to 10 nm with a step size of 1 nm) was simulated. The resultant EF were plotted against the varying interparticle distance.

4.3.4 Gold Nanoparticle (AuNPs) Synthesis

AuNPs were synthesised using the Turkevich method [278], with minor adjustments. 500 µl of 100 mM $HAuCl_4 \cdot 3H_2O$ was dissolved into 49.5 ml dH_2O and the solution heated under constant stirring until it reached boiling point upon which 5 ml of 1% $HOC(COONa)(CH_2\text{-}COONa)^2$ was quickly injected. Finally, the solution was slowly cooled under constant stirring for 30 min whilst the colour changed from a translucent yellow to a wine red. The synthesised AuNPs were then stored at 4 °C for subsequent experiments.

4.3.5 AuNP Characterisation

To verify that the AuNPs had been successfully synthesised, UV-vis absorption measurements of the colloid were taken, and the UV-vis absorption spectral data was used to determine the ratio r (Equation 4.4) to determine the diameter of the AuNPs which was further used to match the value to find ε_{450} from Table S-3 found in [362] to calculate the concentration of AuNPs from Equation 4.5 [362]:

$$r = \frac{A_{max}}{A_{450}} \tag{4.4}$$

$$c = \frac{A_{450}}{\varepsilon_{450}} \tag{4.5}$$

where:

r – the ratio of two absorbance

A_{max} – the maximum absorbance found in the UV-vis

A_{450} – the absorbance value at 450 nm

c – the concentration of the AuNPs

ε_{450} – the decadic extinction coefficient in M^{-1} at a wavelength of 450 nm obtained from Table S-3 of [360]

4.3.6 Synthesis of SERS substrate ALF-HB

The ALF was modified using an amended version of a method [424]. Briefly, a 3″ x 1″ piece of ALF was annealed through heating at 350°C on a hotplate until a mark previously made with a permanent marker disappears. Following the annealing, the ALF was etched by immersing it in 10 g/L of KOH in dH_2O for a few seconds until it frizzed. Subsequently, after being rinsed with ethanol and dH_2O, the ALF was immediately immersed in 20 g/L $C_{12}H_{24}O_2$ in ethanol for 30 mins for the hydrophobic coating. Finally, it was allowed to air dry to use for subsequent experiments as hydrophobic ALF (ALF-HB) (Figure 4.5).

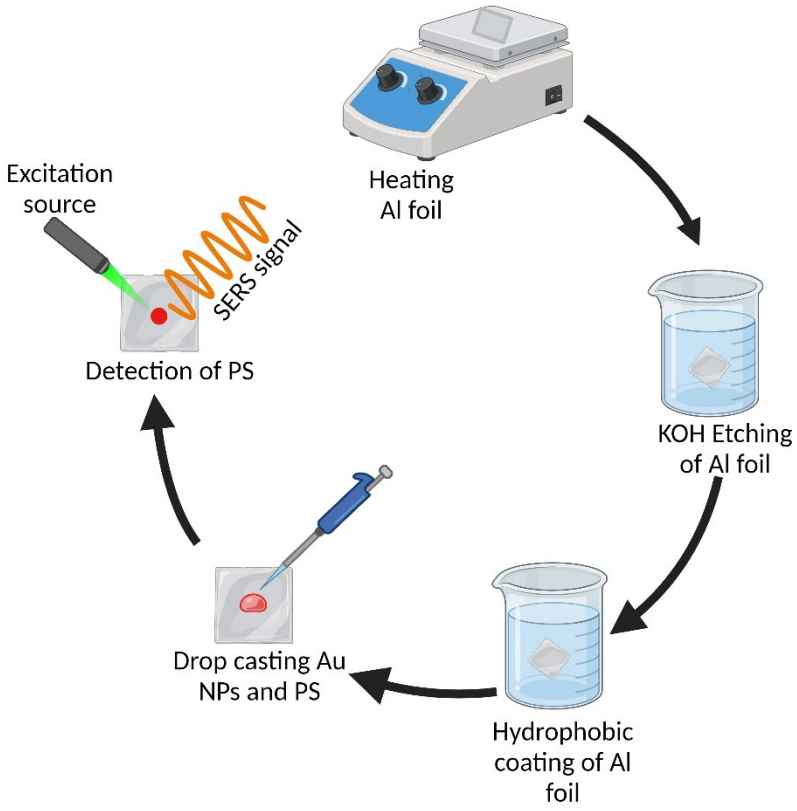

Figure 4.5: Illustration of the preparation of the SERS substrate based on hydrophobic aluminium foil (ALF-HB) which was used subsequently for SERS detection of nanoplastics.

4.3.7 Characterisation of ALF and ALF-HB

The ALF and ALF-HB covered with AuNPs, referred to as ALF@AuNPs and ALF-HB@AuNPs respectively for the remainder of this chapter, were characterised with images from scanning electron microscopy (SEM) to analyse the AuNP distribution for the two different types of foils. Following the SEM imagining, the contact angles offered by both the types of foils, ALF and ALF-HB, were measured using an optical tensiometer. A 10 µl water droplet was dispensed onto ALF and ALF-HB whilst an-built video camera within the optical tensiometer measured the right and left contact angle of the water on the foils 84 times over 30 s, with an average contact angle determined for each.

4.3.8 Preparation of R6G solutions

The molecular weight of R6G was 479.02 g/mol and so to prepare a 1 mM stock solution (SS) of R6G, 239.51 mg of R6G was added to 5 mL of dH_2O (graphpad molarity calculator was used for calculations). The various concentrations of R6G (10^{-11} to 10^{-5} M) for subsequent experiments were prepared by diluting the 1 mM stock solution with the required quantity of dH_2O.

4.3.9 SERS performance of ALF@AuNPs and ALF-HB@AuNPs

For a practical comparison of ALF@AuNPs and ALF-HB@AuNPs, and thus assess the impact of the differing wettability of ALF and ALF-HB on SERS performance, R6G, a well-characterized Raman dye [425] was employed. Specifically, 1 µL of the different concentrations of R6G were first deposited onto ALF and ALF-HB samples, before being allowed to partially dry for 30 s. Thereafter, 1 µL of AuNPs were added on top of the R6G and allowed to dry before SERS measurements were taken of the R6G on ALF@AuNPs and ALF-HB@AuNPs.

To determine the LoD of the SERS substrates, the peaks present in the spectra for R6G were identified and compared to those found in the literature to identify an appropriate diagnostic peak.

The LoD was then calculated using the following equations [426]:

$$LoD = LoB + 1.645\ (SD_{low\ concentration\ sample}) \quad (4.6)$$

$$LoB = mean_{blank} + 1.645\ (SD_{blank}) \quad (4.7)$$

where:

LoD – limit of detection

LoB – limit of the blank

SD – standard deviation

SD_{blank}, or the standard deviation of the blank signals, was determined by measuring a matrix blank, 10 times for a robust. The matrix blank consisted of depositing 1 µL of a negative control onto ALF, allowing it to evaporate partially for 30 s, adding 1 µL AuNPs on top and allowing the blank to dry before a SERS measurement was taken.

4.3.10 Calculating the reproducibility of ALF-HB@AuNPs

To determine the reproducibility of SERS enhancement across the surface of the ALF-HB@AuNPs substrate 1 µL of R6G (10^{-5} M) in dH_2O was first deposited onto ALF before being allowed to partially dry for 30 s. 1 µL of AuNPs (8.19 nM) was then dropped onto the R6G and allowed to dry before SERS measurements were taken across a 10 × 10 μm^2 area. From the map, collected with a 1 µm step size using the inbuilt AtlµS function in the OMNIC™ Series software, the percent of Coefficient of Variation (CV%) for the R6G's diagnostic peak was then determined through Equation 4.8

$$CV\% = \frac{standard\ deviation}{average}\ x\ 100 \qquad (4.8)$$

4.3.11 Preparation of nanoplastic suspensions

Suspensions of nanoplastics in dH_2O with various concentrations (1, 5, 25, 50, 100, 500 and 1000 µg/mL) were prepared by considering the purchased 2.5% (i.e. 25 mg/mL) and 10% (100mg/mL) solid suspensions of 50 nm and 100 nm PS respectively as SS.

4.3.12 SERS measurements of nanoplastics

SERS measurements of the different concentrations of nanoplastics, of either 50nm or 100nm, were taken after first adding 1 µL drops of prepared nanoplastic solutions onto the ALF-HB1 followed by 1 µL drop of synthesised AuNPs. All the SERS measurements were carried out using the DXR2 Raman microscope operated with 532 nm laser, at laser power of 10 mW, 50x magnification and an acquisition time of 3 s.

4.3.13 Detection of micro- and nanoplastics (MNPs) released from hot cups

Disposable hot insulated cups made out of expanded PS were used to detect disposable cup was first thoroughly rinsed with dH_2O at room temperature. Following the rinsing, the disposable cup was filled with 200ml of boiling dH_2O. To avoid possible contamination from surrounding air, the cup was covered with a clean piece of Al foil. The cup with the hot water was left sitting under a fume hood, with occasional stirring using a wooden

stirrer, for 15 minutes which is the duration on average taken to have a cup of hot beverage [427]. After 15 minutes, the water was vacuum filtered onto a Si filter. As the pore size of the filter was 1 μm, all the microplastics were expected to be collected onto the filter, leaving the nanoplastics behind in the filtered solution. The filtered solution, then containing only the nanoplastics, was enriched by centrifugation carried out at 10 ˚C and 1200 relative centrifugal force (rcf) for 25 mins. A 1μL drop from the enriched solution was then drop-casted onto the hydrophobic SERS substrate and allowed to dry, subsequently the SERS measurements for detecting nanoplastics were carried out. Furthermore, a 10x10 μm^2 region of the filter was selected and analysed for presence of microplastics using the particle analysis feature of the OMNIC software.

4.4 Results and Discussion

4.4.1 Numerical Simulation

The numerical simulation done to monitor the effect of variations in interparticle distance on the EF can be seen in Figure 4.6(a-j) with each image showing a visual representation of the electromagnetic field enhancement seen between the three AuNPs for each interparticle distance.

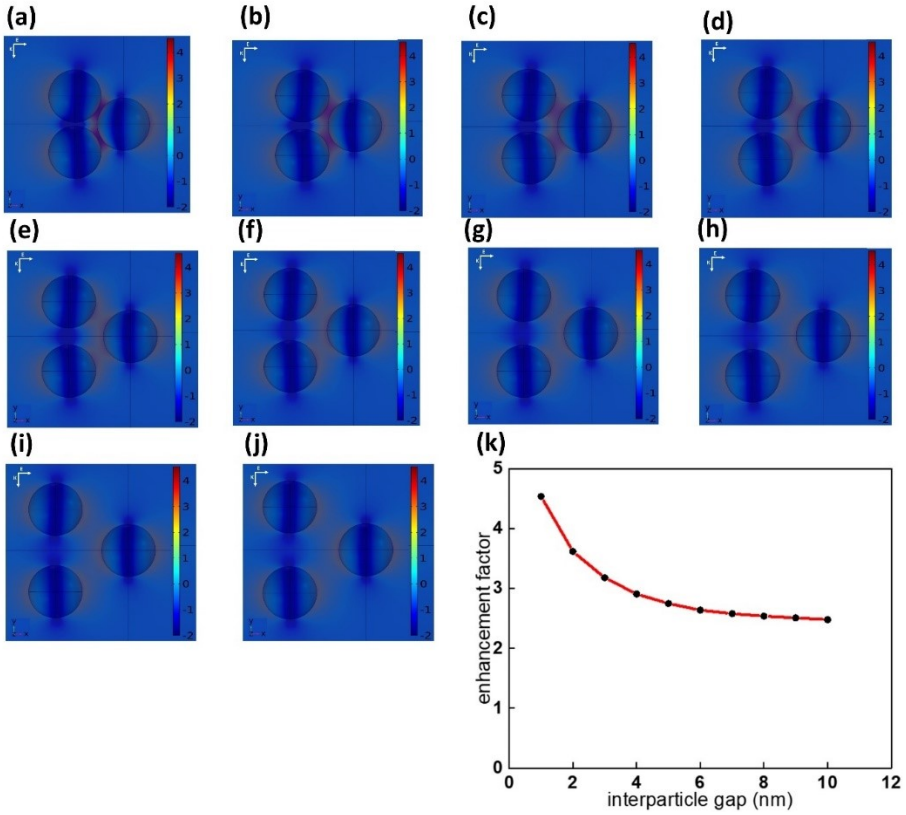

Figure 4.6: (a-j) Electromagnetic field enhancement for interparticle distance changing from 1 nm to 10 nm with a step size of 1 nm. (k) interparticle distance versus the enhancement factor showing an inverse relationship between the two parameters.

EF versus interparticle distance (Figure 4.6k) plotted with the interparticle distance varying from 1 nm to 10 nm clearly shows that with increasing interparticle distance the EF reduces. The inverse relationship between EF and interparticle distance has been explained by classical electromagnetics with the reason being the reduction in near-field interactions found between adjacent nanoparticles with increasing interparticle distance [185], [205].

4.4.2 Characterisation of ALF and ALF-HB

To validate the efficacy of a straightforward deposition technique for the incorporation of AuNPs on ALF as a SERS substrate, SEM analysis was conducted on ALF prior to the addition of AuNP (Figure 4.7a) and afterwards (Figure 4.7b) to compare morphologies.

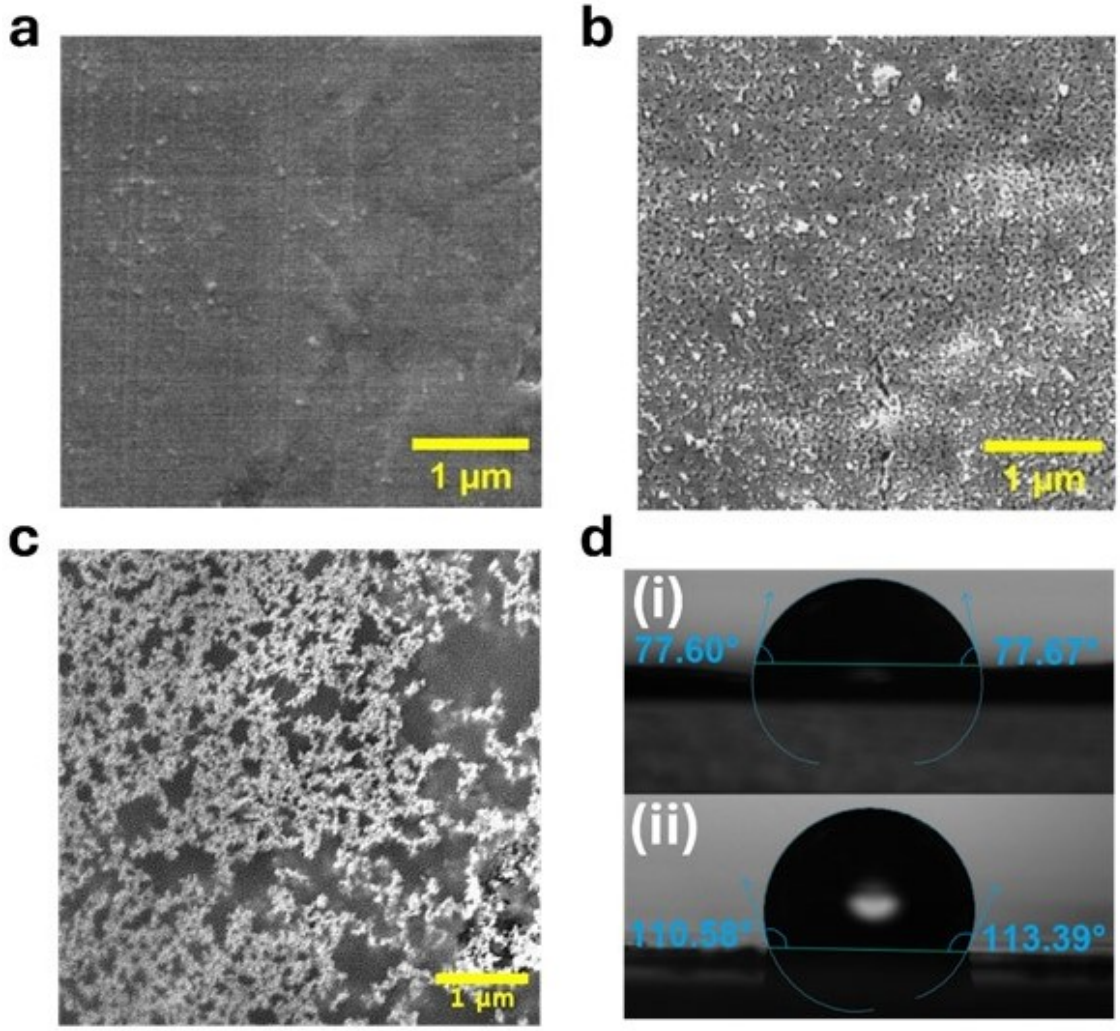

Figure 4.7: (a-c) shows SEM images of ALF, ALF@AuNPs and ALF-HB@AuNPs respectively at 1000x magnification. d (i-ii) Shows images from the optical tensiometer for a dH2O droplet on ALF and ALF-HB respectively and the subsequent contact angle.

The dense clusters of AuNPs on the ALF@AuNP surface clearly observed in Figure 4.7b confirms that the simple deposition method is indeed an effective and cost-efficient

approach to create a SERS active substrate. Subsequently, SEM analysis was completed on an AuNP enhanced ALF-HB surface which can be seen in Figure 4.7c. Denser AuNP clusters can be observed on the ALF-HB@AuNP surface when compared to the enhanced ALF@AuNP surface, likely attributable the hydrophobic effect of lauric acid on its surface. To measure the effect that lauric acid modification had on the hydrophobicity of ALF, the average contact angle of water was calculated (Figure 4.7d.).

The average contact angle of dH_2O deposited onto the non-modified foil (ALF) was determined to be 78.54°, with the hydrophilic nature of the ALF being attributable to the inherent high-energy hydroxyl groups present on such metal oxides. However, the foil modified with lauric acid (ALF-HB) exhibited an average static contact angle of 115.72° indicating that the lauric acid had hydrolysed onto the surface of ALF and was mitigating the pinning of dH_2O onto the underlying surface, for a hydrophobic surface. The failure to achieve a super hydrophobic surface (contact angle >150°) is hypothesized as being due to the KOH roughening process only expanding the nanopores, and thus a surface characterised by mono-valued topography, thereby failing to produce the necessary negative Laplace pressure for the induction of a Cassie-Baxter wetting state [428].

4.4.3 Comparing SERS performance for ALF@AuNP and ALF-HB@AuNP using R6G

Prior to doing the comparison of the SERS performance of ALF@AuNP and ALF-HB@AuNP, background measurements were carried out on the ALF-HB without any analyte (Figure 4.8).

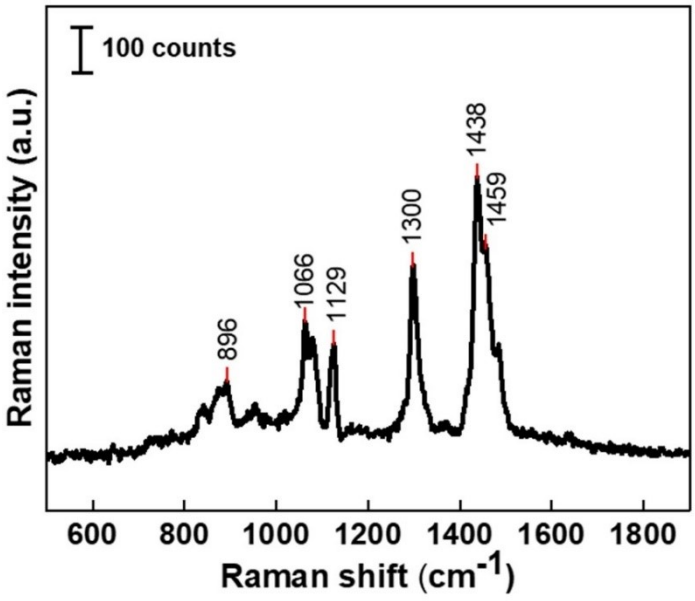

Figure 4.8: SERS spectrum for ALF-HB@AuNP showing the characteristic peaks of lauric acid found at 896 cm^{-1}, 1066 cm^{-1}, 1129 cm^{-1}, 1300 cm^{-1}, 1438 cm^{-1}, 1507 cm^{-1} and 1459 cm^{-1} clearly marked.

The background measurements showed peaks which were matched to those found in literature for lauric acid as shown in Table 4.2. However, fortunately the lauric acid peaks did not coincide with those of molecules of interest within this thesis (i.e. R6G or polystyrene). Furthermore, the peaks of lauric acid found in the SERS spectrum substantiate that lauric acid had been functionalised onto ALF-HB and accounts for the observed differences in wetting properties and subsequently the post drying AuNP density in Figure 4.7 d and c, respectively.

Tables 4.2 and 4.3 show the peak assignment for lauric acid and R6G, respectively, with comparison of the peak positions found in literature. The slight difference of few wavenumbers in the experimental and literature based peak positions (in Table 4.2, 4.3 and 4.4) is hypothesised to be due to variations in system and calibration protocols across different instruments [429], [430]. However such variations are also possible in measurements carried out on the same equipment due to time temporal variances, such as positional drift or thermal expansion which can occur over a period of time [431].

Table 4.2: Peak assignment done for the background signal from lauric acid with a comparison of the peak position found experimentally to those found within the literature.

Raman shift according to the experiment (cm^{-1})	Raman shift according to the literature (cm^{-1})	Band assignment	Ref
896	893	CH2 rocking	[432]
1066	1064	C-C stretch	[432]
1122	1127	C-C stretch	[432]
1300	1298	CH2 twisting	[432]
1438	1438	CH3 or CH2 deformations	[433], [434]
1459	1457	CH3 or CH2 deformations	[433], [434]

Following the background measurements, SERS spectrum of 10^{-5} M R6G on ALF@AuNP was taken to map out the characteristic peaks of R6G (Figure 4.9) and select a diagnostic peak for the comparative SERS study between ALF@AuNP and ALF-HB@AuNP.

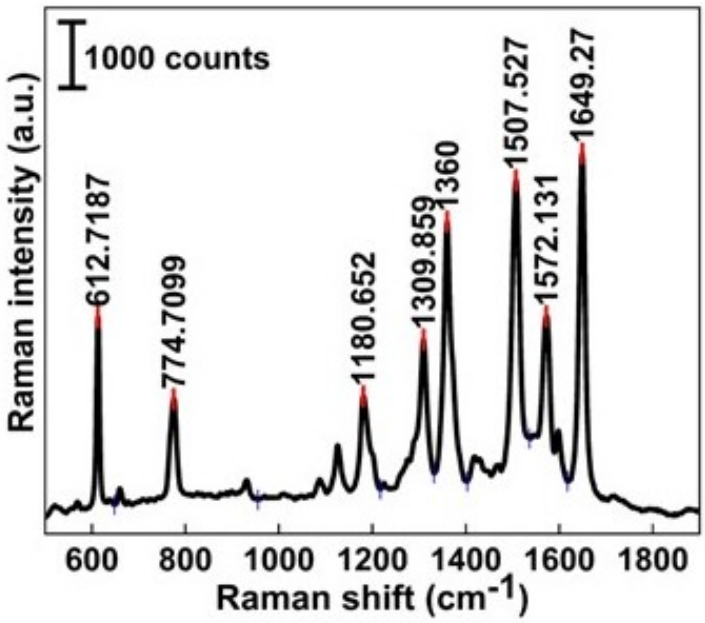

Figure 4.9: SERS spectrum for 10^{-5} M of R6G on ALF@AuNP with the characteristic peaks of R6G found at 612 cm^{-1}, 774 cm^{-1}, 1180 cm^{-1}, 1309 cm^{-1}, 1360 cm^{-1}, 1507 cm^{-1}, 1572 cm^{-1} and 1649 cm^{-1} clearly marked.

Furthermore, the peaks found in the SERS spectrum of the R6G were compared with those found in the literature and comprehensive band assignment for R6G characteristic peaks was carried out as seen in Table 4.3. Out of all the characteristic peaks of R6G (Figure 4.9 and Table 4.3) the most prominent peak at 1360 cm^{-1}, attributed to C-C stretching, was selected as the diagnostic peak for further analysis. The characterisation of ALF@AuNP and ALF-HB@AuNP done through a concentration study of R6G can be seen in Figure 4.10 a and b, c respectively.

Table 4.3: Peak assignment done for the R6G peaks with a comparison of the peak position found experimentally to those found within the literature.

Raman shift according to the experiment (cm^{-1})	Raman shift according to the literature (cm^{-1})	Band assignment	Ref
611.07	617	C-C-C ring in-plane bending	[435]
772.99	776	C-H out-of-plane bending	[435]
1123.97	1131	C-H in-plane bending	[435]
1182.79	1188	C-C stretching	[435]
1309.11	1318	C-C stretching	[435]
1360.17	1360	C-C stretching	[436]
1506.77	1512	C-C stretching	[435]
1575.23	1577	C-C stretching	[435]
1645.62	1652	C-C stretching	[435]

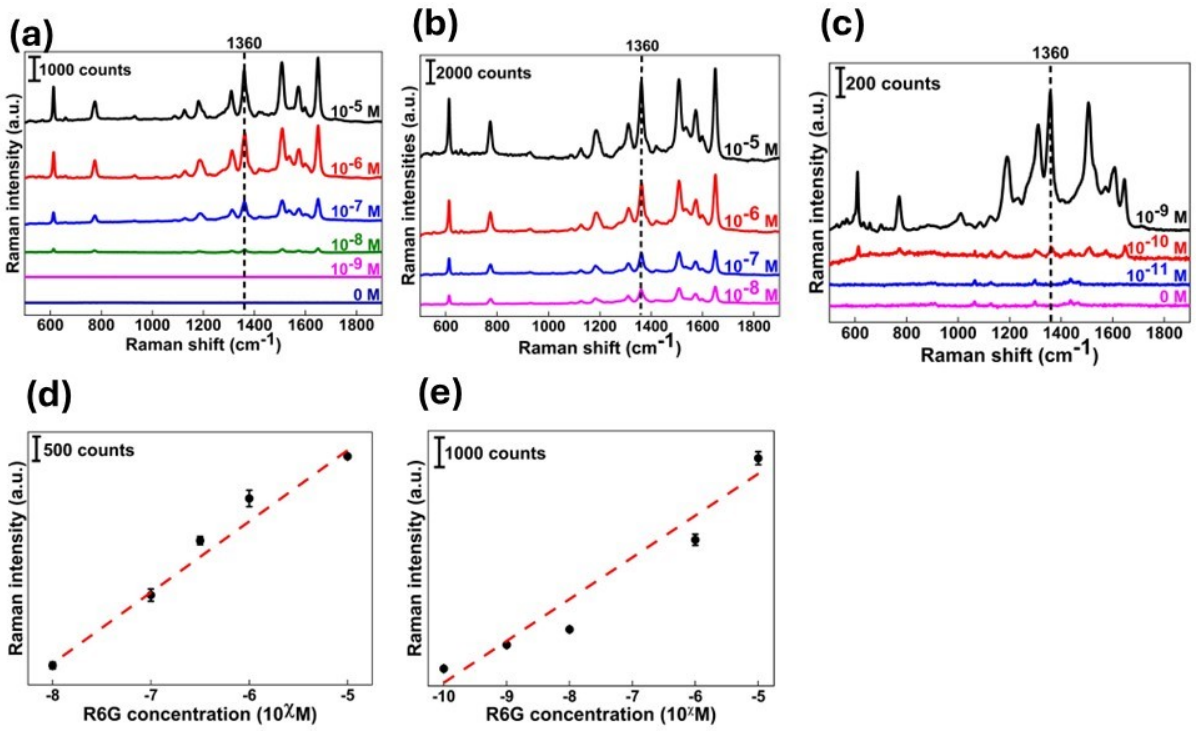

Figure 4.10: (a) SERS spectra of different concentrations of R6G measured on ALF@AuNP with the lowest concentration detected as 10^{-9} M. (b-c) SERS spectra of different concentrations of R6G measured on ALF-HB@AuNP with the lowest concentration detected as 10^{-11} M. (d) Linear regression fitting of Raman intensities at 1360 cm^{-1} for each concentration of R6G on ALF@AuNP, with y = 1461.3x + 12094 and R^2 = 0.98. (e) Linear regression fitting of Raman intensities at 1360 cm^{-1} for each concentration of R6G on ALF-HB@AuNP, with y = 1365.4x + 13133 and R^2 = 0.94.

Using ALF@AuNP, detection of R6G as low as 10^{-9} M was possible as compared to ALF-HB@AuNP which made detection of R6G concentration as low as 10^{-11} M possible, therefore the hydrophobic layer resulted from lauric acid led to an increase in two orders of magnitude for the detection limit of R6G. The calibration curve for the detection of R6G on ALF@AuNP (Figure 4.10d) plotted using the linear regression fitting for the signal intensity at the diagnostic peak of 1360 cm^{-1} for the various concentrations of R6G from 10^{-5} to 10^{-9} M resulted in R^2 value of 0.98. Similarly, R^2 value of 0.94 was obtained by plotting the SERS signal intensity of the diagnostic peak for various concentrations of R6G from 10^{-5} to 10^{-11} M on ALF-HB@AuNP with the linear fitting of the data (Figure 4.10e).

From the determination of the LoB the LoD were calculated using equation 4.6 and 4.7 [437] for R6G on both ALF@AuNP and ALF-HB@AuNP. The mean and standard deviation for the blank samples were calculated as explained in Section 4.3.9 with the values coming out to be 1.46 ($mean_{blank}$) and 1.036 (SD_{blank}) for ALF@AuNP; 17.0 ($mean_{blank}$) and 6.72 (SD_{blank}) for ALF-HB@AuNP. Therefore, the calculation of LoB for ALF@AuNP and ALF-HB@AuNP using Equation 4.6 are shown below:

$$LoB_{ALF@AuNP} = 1.46 + 1.645\ (1.036) = 3.17$$

$$LoB_{ALF\text{-}HB@AuNP} = 17.0 + 1.645\ (6.72) = 28.0$$

The standard deviation for the lowest concentration of 10^{-9} M for ALF@AuNP and 10^{-11} for ALF-HB@AuNP (as these are the lowest detected concentrations using the particular foil types as seen in Figure 4.10) were calculated by measuring the Raman intensities from the ten SERS spectra measured on ALF@AuNP and ALF-HB@AuNP respectively (seen in Figure 4.11 a and b) using R6G of 10^{-9} M and 10^{-11}, respectively. The SD comes out to be 69.23 and 14.35 for ALF@AuNP and ALF-HB@AuNP, respectively. Therefore, the calculation of LoD for ALF@AuNP and ALF-HB@AuNP using Equation 4.7 are shown below:

$$LoD_{ALF@AuNP} = 3.17 + 1.645\ (69.23) = 3.17$$

$$LoD_{ALF\text{-}HB@AuNP} = 28.0 + 1.645\ (14.35) = 28.0$$

The values of LoD achieved above were then plugged into the straight-line equations obtained from the calibration curve for ALF@AuNP (Figure 4.10d) and ALF-HB@AuNP (Figure 4.10e) as shown below:

Straight line equation for ALF@AuNP (Figure 4.10d):

$y = mx + c \Rightarrow y = 1461.3x + 12094$ (a)

(a) becomes $\frac{177.06 - 12094}{1461.3} = -8.198 \Rightarrow LoD_{ALF@AuNP} = 1.98 \times 10^{-8}$ M

Straight line equation for ALF-HB@AuNP (Figure 4.10e):

$y = mx + c \Rightarrow y = 1365.4x + 13133$ (b)

(b) becomes $\frac{51.6 - 13133}{1365.4} = -9.58 \Rightarrow LoD_{ALF\text{-}IL} = 5.8 \times 10^{-9}$ M

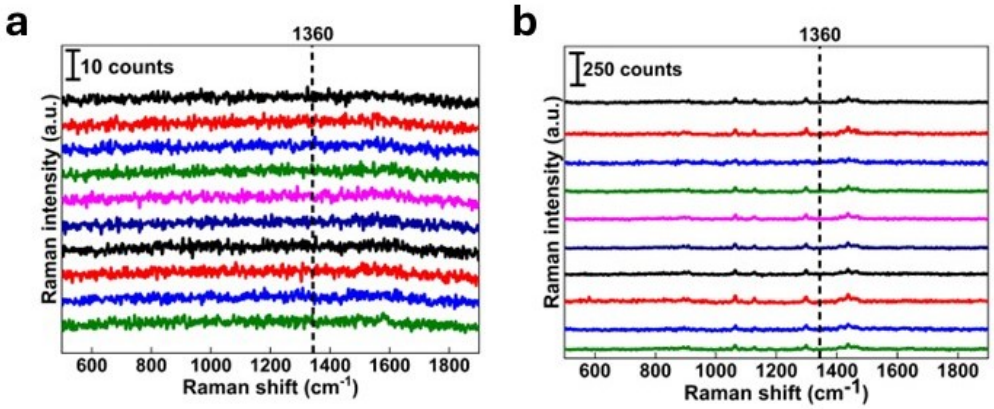

Figure 4.11: Ten SERS spectra measured for LoD calculations using lowest concentrations of R6G of (a) 10^{-9} M R6G on ALF@AuNP and (b) 10^{-11} M R6G on ALF-HB@AuNP.

4.4.4 Calculating the homogeneity of ALF-HB@AuNPs

Therefore, as a promising candidate as SERS substrate, the homogeneity of ALF-HB@AuNP was assessed through mapping the peak Raman intensity at 1360 cm^{-1} for

10^{-6} M (in dH_2O) R6G across its surface (Figure 4.12a) to determine percentage of coefficient of variation (CV%) (Figure 4.12b). The CV% was determined to be 14.5% (n = 100), indicating an acceptable homogeneity across the surface, and significantly better than that reported from previous studies, approximately 20%, based on the deposition of nanomaterials on ALF [438]. This improvement in homogeneity across the ALF-HB surface is hypothesised to be due to the reduced pinning of R6G to the surface, reducing uneven drying and thus the formation of a coffee ring [387].

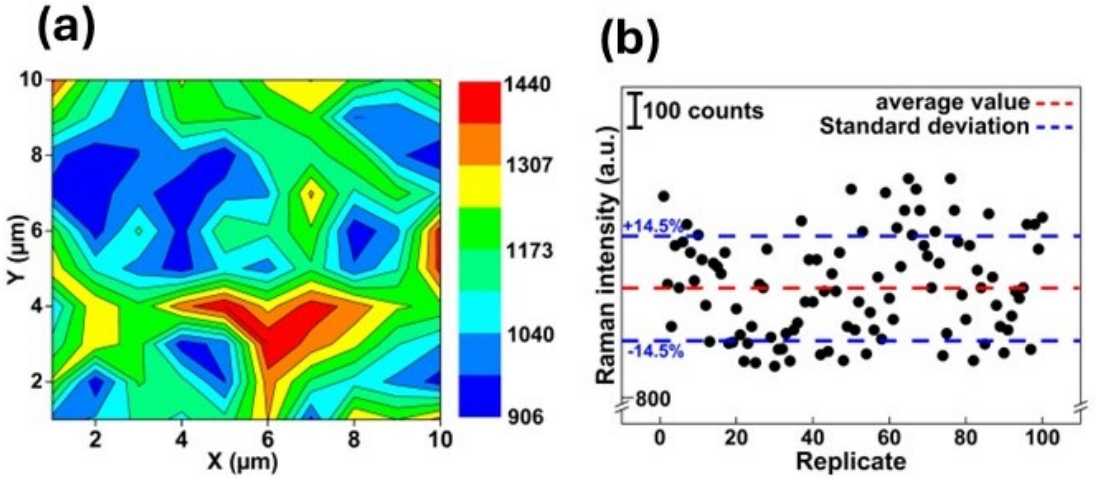

Figure 4.12: 10 × 10 μm^2 map collected with a 1 μm step size showing the variation of Raman intensity (a.u.) at 1360 cm^{-1} for 10^{-6} M R6G on ALF-HB@AuNPs. (f) A scatter plot generated from the mapping data, representing the Raman intensities at 1360 cm^{-1} for 10^{-6} M R6G on ALF-HB@AuNPs, with the average Raman intensity recorded (red line) and the coefficient of variation standard deviations (blue line) also represented.

4.4.5 SERS measurements of nanoplastics

Figure 4.13 shows the Raman spectrum obtained from a PS pellet, to experimentally recognise the characteristic peaks of PS and select an appropriate diagnostic peak for the concentration study done on 50 nm and 100 nm PS nanoplastics (Figure 4.14 a and b).

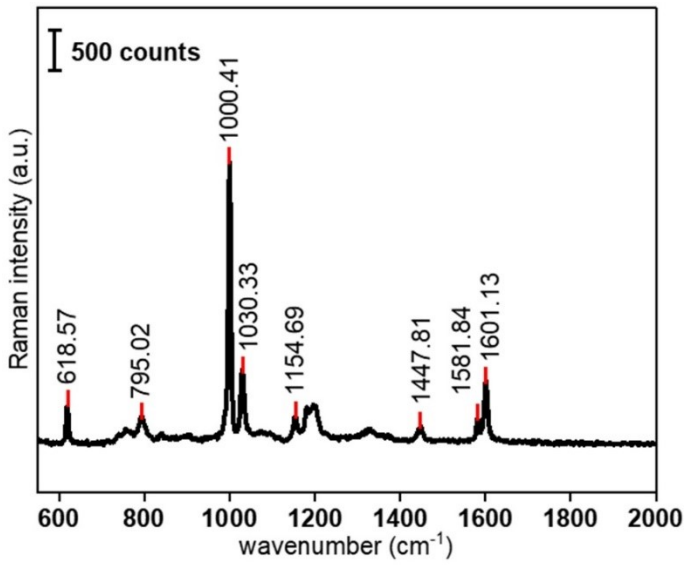

Figure 4.13: Raman spectra for a PS pellet with the characteristic peaks 618 cm^{-1}, 795 cm^{-1}, 1000 cm^{-1}, 1030 cm^{-1}, 1154 cm^{-1}, 1447 cm^{-1}, 1581 cm^{-1} and 1601 cm^{-1} marked.

The experimentally found characteristic peaks of the PS pellet were compared with those found in literature and corresponding bands were assigned to each peak as seen in Table 4.4. The most dominant peak at 1000 cm^{-1} attributed to ring breathing mode was selected as the diagnostic peak after confirming that lauric acid has no peak at that position to avoid any interference from background signal.

Table 4.4: Experimentally measured characteristic peaks for polystyrene listed against values found in the literature and their band assignment.

Raman shift according to the experiment (cm^{-1})	Raman shift according to the literature (cm^{-1})	Band assignment	Ref
619.54	621	Ring deformation mode	[366]
795.03	795	C-H out-of-plane deformation	[366]
1000.41	1001	Ring breathing mode	[366]
1030.30	1031	C-H in-plane deformation	[366]
1153.72	1155	C-C stretching	[366]
1447.82	1450	CH_2 scissoring	[366]
1581.84	1583	C=C stretching	[366]
1601.13	1602	Ring-skeletal stretching	[366]

The SERS spectra for all concentrations of both sizes of PS nanoplastics on ALF-HB@AuNPs (Figure 4.14 a-b) clearly demonstrate that the diagnostic peak is visible for concentrations down to 1µg/mL for both the sizes of nanoplastics. Furthermore, for both sizes of nanoplastics, and at all concentrations, the intensities for the diagnostic peak at 100 cm^{-1} (Figure 4.14 c and d) are relatively similar indicating that the SERS enhancement for the prepared substrates is nanoplastic size independent, as seen previously by others [439].

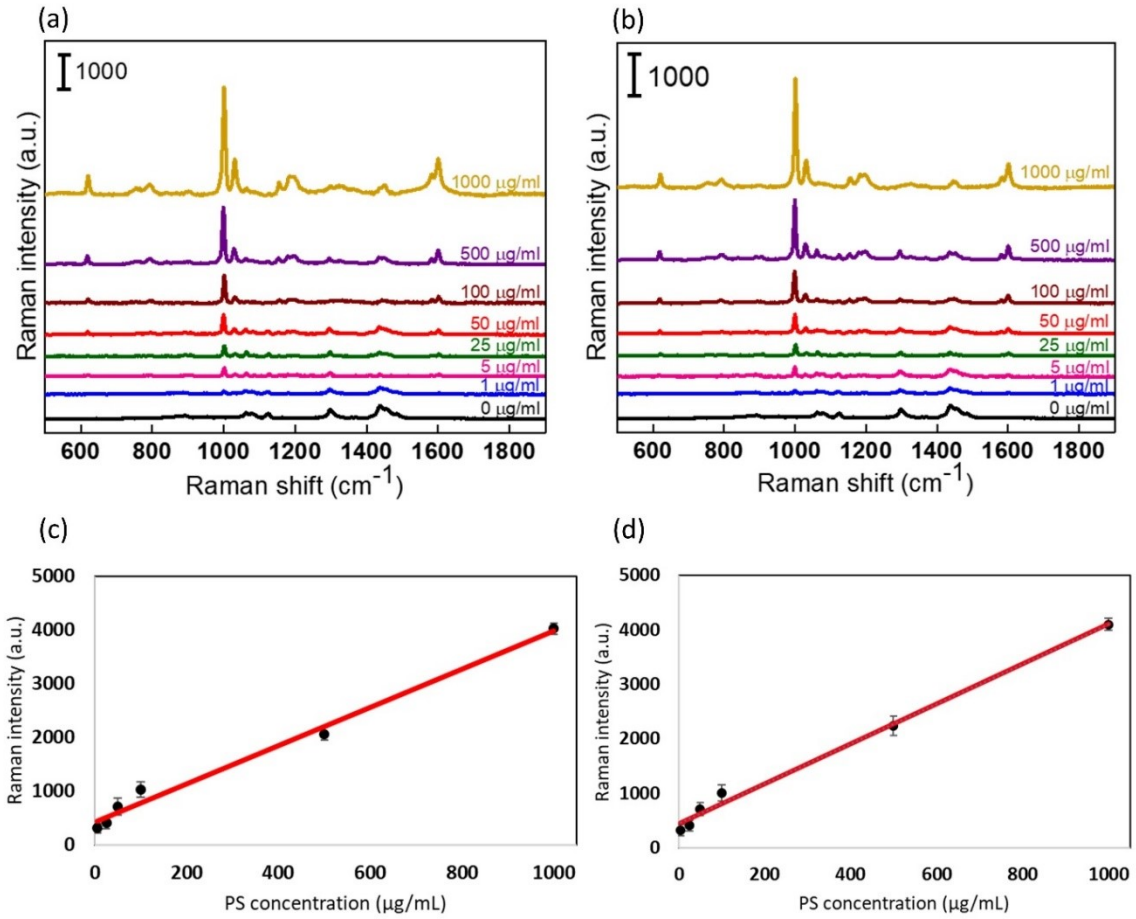

Figure 4.14: (a) SERS spectra for various concentrations of 50 nm PS nanoplastics (in dH_2O) on ALF-HB@AuNP (b) SERS spectra for various concentrations of 100 nm PS nanoplastics (in dH_2O) measured on ALF-HB@AuNP (c) Linear plots of 50 nm PS nanoplastic concentrations against SERS intensity at 1000 cm^{-1} having R^2 value of 0.98 (d) Linear plots of 100 nm PS nanoplastic concentrations against SERS intensity at 1000 cm^{-1} having R^2 value of 0.99.

This could, in part, be due to the manufacturer's amine modification of the 50 nm PS nanoplastics, as amine is the functional group with the highest affinity for gold after thiol [440], therefore leading to better sitting of the 50 nm PS within the hotspots as compared to the 100 nm PS nanoplastics. The linear regression fits through plots of SERS intensity at 1000 cm^{-1}, each measured three times and thus denoted by error bars, against nanoplastic concentrations for both 50 nm (Figure 4.14c) and 100 nm PS (Figure 4.14d) show very high R^2 values of 0.98 and 0.99, respectively. But despite the very high R^2 values for a linear fit, a non-linear trend is clearly visible in the lower concentration regime (Figure 4.14 c and d). Similar trend was noticed in the calibration curves for nanoplastics detected using the salt-assisted aggregation of AuNPs in Chapter 3 and that in another work on KI assisted-aggregation of AgNPs [269]. Considering the similar trend, it would be easy to say that the hypothesis that this is because of larger number of hotpots formed due to aggregation or clustering leads to a greater chance of all the nanoplastic particles in lower concentrations to be in hotspots resulting in greater SERS signal intensity for

these concentrations seems more likely as the reason behind this non-linear behaviour at lower concentration. Compared to previously published work [414], whilst nanoplastics have been detected at lower concentrations than the 1 µg/mL here, the smallest particle used was only 100nm, and the other 500nm. Furthermore, the overall methodology used was very time consuming, requiring 99 minutes of centrifugal enrichment of the nanoplastics and AgNPs to detect such low concentrations, and 14 hours to prepare the substrates as compared to the maximum two hours taken to prepare the ALF-HB, therefore, highlighting the potential of using ALF-HB@AuNP for SERS detection of nanoplastics.

4.4.6 Detection of micro- and nanoplastics (MNPs) released from hot cups

To demonstrate the suitability of the ALF-HB@AuNP for real world MNP, the substrates were used to detect the release of MNPs from insulated cups made of expanded PS used for drinking hot beverages. Figure 4.15a shows the nanoplastics released from a hot cup and detected on an ALF-HB@AuNP.

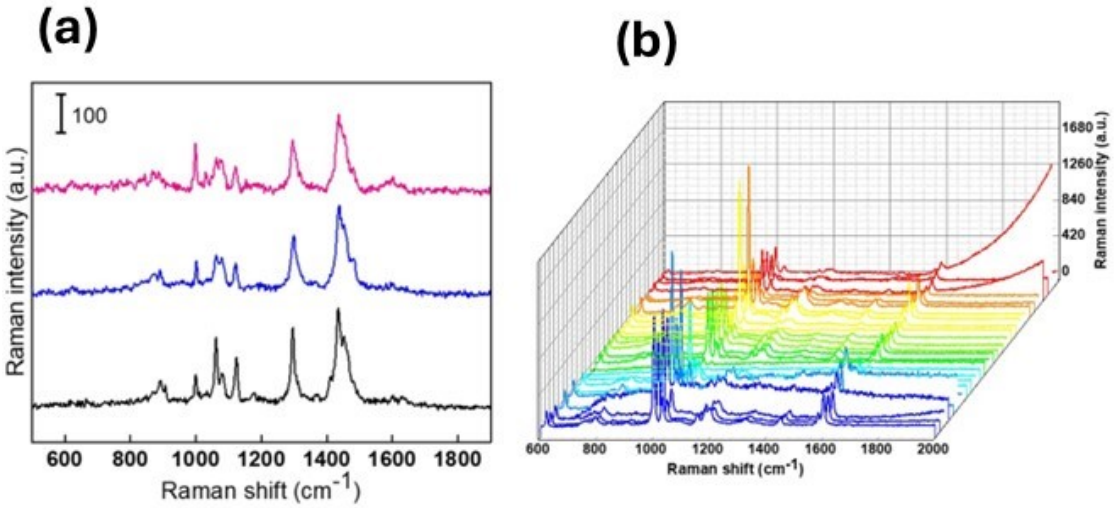

Figure 4.15: (a) SERS spectra of an ALF-HB with 1 µL of centrifugal enriched nanoplastic solution drop cast on to it. (b) Raman spectra of the microplastic particles detected on a 10x10 µm^2 area of the 1x1 cm^2 of the Si filter using particle analysis feature of the OMNIC software.

The particle analysis feature of the OMNIC software, was used to detect microplastics detected 28 PS microplastics on a 10x10 µm^2 area of the 1x1 cm^2 of the Si filter with their Raman spectra (shown in Figure 4.15b) matching with the reference spectrum in a range of 30.7% to 98.1%. If it is assumed that microplastics in similar amounts were present on the rest of the filter too, then by this approximation about 280,000 microplastic particles must have been released in one cup of hotwater added to such a PS cup.

4.5 Conclusion

This Chapter reported on the development of a methodology to cluster gold nanoparticles (AuNPs) for the reliable detection of lower concentrations of nanoplastics by utilising the wetting properties of aluminium foil to form a hydrophobic layer, rather than upsetting the stability of the AuNPs as was previously done through salt-assisted aggregation of AuNPs (in Chapter 3). The main findings are thus:

- Firstly, the increase in hydrophobicity of a surface i.e. enhancing its anti-wettability potentially decreases the pinning of droplets of AuNPs and R6G/nanoplastic suspension that are dropcast onto it, therefore clustering the AuNPs and R6G/nanoplastics upon drying which increases the SERS signal.
- Secondly, use of hydrophobic layers can increase the efficacy of straight-forward deposition of AuNPs (i.e. dropcasting), therefore introducing a very simple method for improving SERS detection.
- Thirdly, the use of low-cost materials and chemicals to develop a hydrophobic layer in a time-efficient methodology puts it at an advantage to other methodologies based on increasing the anti-wettability for SERS detection.
- The prepared hydrophobic SERS substrate demonstrated efficient detection of 50 nm and 100 nm PS nanoplastics with LoDs of 1 μg/mL for both the sizes of nanoplastics achieved.
- Finally, the release of micro and nanoplastics from insulated cups made of expanded PS used for hot drinks was found.

Whilst nanoplastics were successfully detected through the use of clusters of AuNPs through modification of the wetting properties of ALF, measurements were not so reliable, as like the substrates produced in Chapter 3, the hotspots were not always well defined nor had a fixed size.

The methodology presented in Chapter Five to realise well defined hot spots of a fixed size is based on surface modification through a combination of salinisation process to form a monolayer of AuNPs on ALF with further linking of AuNPs to that monolayer using a linking molecule as 3D nanostructures. The detailed explanation and methodology are presented in Chapter Five.

Chapter Five

The detection of nanoplastics through the use of surface enhanced Raman spectroscopy (SERS) substrates with islands of gold nanoparticles (AuNPs) formed through the use of cucurbit[5]uril (CB[5]).

5.1 Introduction

In contrast to the use of colloidal nanoparticles, the immobilisation of nanoparticles onto solid surfaces to form SERS substrates has gained a lot of interest as it also allows to take advantage of their unique properties whilst also increasing the stability of the nanoparticles, and enhancing the reusability and handling of the substrate [441]. That with said, as nanoparticle LSPR properties are affected by their surrounding environment and interparticle interactions, controlled and precise immobilisation of nanoparticles is essential to achieve desired surface properties [442] and therefore the properties of the SERS substrate they form.

The techniques for incorporating nanoparticles on solid substrates can be broadly classified into two primary methods: *in situ* formation of nanoparticles on substrates and *ex situ* immobilisation of pre-formed colloidal nanoparticles on substrates. The former involves the growth of nanoparticles directly on a surface through processes such as ion reduction [333], thermal evaporation [443], or electrodeposition [444]. These *in situ* methods typically require substrates pre-patterned via micro- or nano-fabrication techniques, such as electron beam lithography, to create precise periodic arrays of nanoparticles [445]. While these techniques are highly accurate, they necessitate specialized equipment, are costly and are confined to small-area applications. Conversely, the *ex situ* immobilisation of pre-synthesised colloidal nanoparticles is a cost-effective alternative that does not require specialized equipment, leveraging well-established synthesis techniques to produce colloidal nanoparticles of specific shapes and sizes, that can then be applied to large surface areas [446]. Furthermore, as it allows the variation of the size, shape, and immobilisation state of the nanoparticles its flexibility for modifying the surface properties enables the creation of diverse nanoparticle-enhanced surfaces [8]. Surface functionalisation, or the introduction of chemical moieties such as functional groups or other ligands on a surface to achieve desired properties [447], is an example of a developed method for the *ex situ* immobilisation of nanoparticles onto solid surfaces [448].

5.1.1 Surface functionalisation for the immobilization of gold nanoparticles

Surface functionalisation for the *ex situ* immobilisation of AuNPs onto solid surfaces is typically done through the use of an intermediary layer of molecular structures on the surface to generate either electrostatic or chemical interactions between the AuNPs and their functional groups [449]. For AuNPs salinisation is typically used, being based on the modification of surfaces terminated with a hydroxyl (–OH) group, such as glass, silicon and metals with an oxide layer, through the use of alkoxysilane compounds [450]. It forms either a covalent bond or electrostatic attachment between the AuNPs and molecules, depending on whether the latter contain a thiol or amine moiety, due to gold's strong affinity to those functional groups [368], [451], [452]. A covalent bond between the AuNPs and the functional group used to modify the solid surface is advantageous as it supports the immobilisation of charged, as well as uncharged, nanoparticles, eliminating the need for nanoparticle functionalisation [452]. However, as discussed in Chapter 4, the negative charge that surrounds citrate capped AuNPs is very convenient for the electrostatic attachment of nanoplastics with an amine modified surface, with no additional nanoparticle functionalisation required [453], [454], [455], [456]. Fundamentally, the choice of the chemical moiety used for the salinisation surface modification, either aminated, or thiolated, depends upon the solid surface used and the alkoxysilane compounds used to immobilise AuNPs, with Table 5.1 showing those typically used.

Table 5.1: A list of the amine and thiol alkoxysilanes typically used for surface modification through the salinisation process to immobilise AuNPs.

Amine-terminated alkoxysilane	Thiol-terminated alkoxysilane
3-aminopropyltrimethoxysilane (APTMS) [457]	3-mercaptopropyltrimethoxysilane (MPTMS) [458]
3-aminopropyltriethoxysilane (APTES) [453]	3-mercaptopropyltriethoxysilane (MPTES) [453]
p-aminophenyltrimethoxysilane (APhTMS) [459]	

APTES contains four reactive groups, being three functional ethoxy ($O–CH_3$) groups and one amine group ($–NH_3$) [450], and is the molecule most commonly used to functionalise oxide surfaces [460], [461], [462], [463], [464], [465], [466], doing so in two steps (Figure 5.1Figure 5.1A). First, hydrolysis, where an –OH group replaces the $O–CH_3$ groups within an acidic, alkaline or neutral medium; and second, condensation, through the formation of the Si–O–Si bonds.

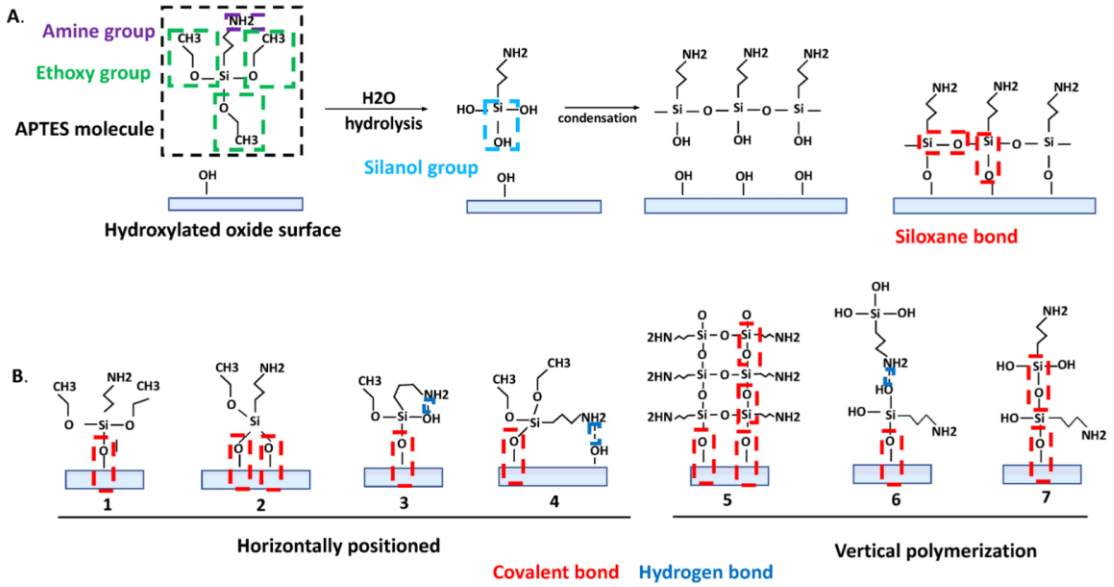

Figure 5.1: (A) Schematic representation of an APTES molecule, its activation through hydrolysis and condensation, and reaction with the hydroxylated oxide surface in an ideal situation. (B) Schematic representation of chemical interactions involved in the grafting of APTES on the hydroxylated oxide surface [450].

The four reactive groups (three O–CH_3 and one –NH_3) within APTES molecule and the complex kinetics of the in the reactions of the salinisation process necessitate the control of conditions such as humidity, solvent used, quantity of water, pH of the solution and concentration of APTES, to achieve a reproducible, stable and highly functionalised surface [463], [465], [467]. The first step of hydrolysis is particularly important in determining the quality of the functionalised surface obtained as it determines the how many of the three O–CH_3 per molecule will hydrolyse and form silanol groups [468]. There are two ways the condensation step can go; either between two APTES molecules and/or between an APTES molecule and the oxide surface being functionalised (Figure 5.1 A) [469]. The covalent bond between APTES and the surface being functionalised can form in various ways as seen in Figure 5.1 B. Furthermore, in presence of excess water molecules, the silanol groups of different APTES molecules form covalent bonds resulting in polymeric structures composed of polysiloxane due to uncontrolled polymerisation (Figure 5.1 B (5-7)) [470], [471], [472], [473]. However, if the water content is controlled, the moderate reactivity of APTES makes it easy to handle thanks and its O–CH_3 groups ensure a robust silanisation process), which leaves the amine group available for further reaction, in this particular case immobilisation of AuNPs [453].

Therefore, following the salinisation process, the modified or salinised solid surface is immersed into a colloidal AuNP solution, with the AuNPs attaching to the thiol or amine terminated molecule due to their strong affinity, to form a monolayer of immobilised AuNPs. As the –NH_3 group on an APTES salinsed surface is free and highly reactive the

electrostatically immobilised AuNPs (Figure 5.2) offer similar plasmonic properties to colloidal nanoparticles, albeit with greater stability.

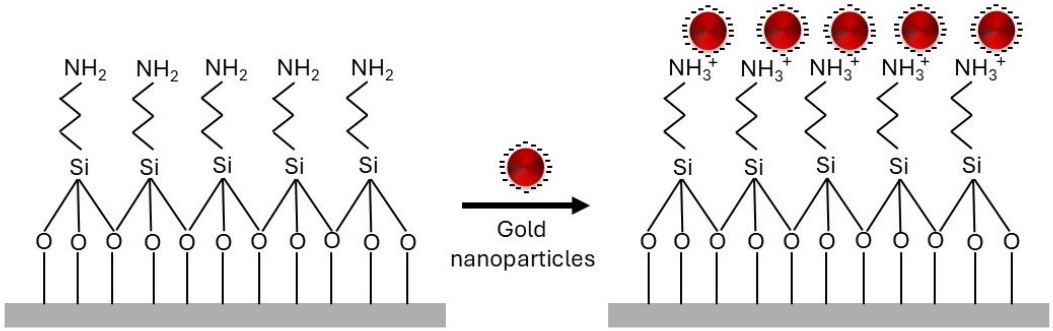

Figure 5.2: Surface functionalised using APTES and electrostatic attachment of AuNPs to the free and terminal amine group of the functionalised surface.

Functionalised solid surfaces covered in a monolayer of immobilised nanoparticles have thus been reported as being used as SERS substrates for the detection of many different analytes (Table 5.2).

Table 5.2: Summary of the SERS substrates (nanostructure and solid surface) formed through APTES based salinisation that have been used to detect various analytes and achieved LoDs.

Nano structure	Solid surface	Analyte	LoD	Ref
AuNP	Si	citrate	-	[453]
AuNS	Polydimethylsiloxane (PDMS)	Thiabendazole (pesticide on fruit skin)	20µg/L	[474]
AuNS	PDMS	4-aminothiophenol (4-ATP)	20 ppb	[475]
AuNS	Glass slip	Nile blue A R6G	$5x10^{-11}$ M $1x10^{-9}$ M	[476]
AuNP	Silica	4-mercaptobenzoic acid (4-MBA)	-	[477]
Au-Ag	Si	4-MBA	10^{-6} M	[478]

core shell nano partic les				
AuNP	capillary	R6G Thiram (pesticide) Aspartamae (food additive)	10^{-10} M 10^{-6} M 0.25 g/L	[479]
AuNP	capillary	4-ATP Ceratinine	10^{-9} M 0.9 mg/ dL	[480]
AuNP	optical fibrer	Methylene Blue Crystal Violet R6G	10^{-9} mol/L 10^{-8} mol/L 10^{-8} mol/L	[481]
AgNP and graph ene oxide	glass	Crystal Violet phosphorus triphenyl (PPh_3)	-	[482]

5.1.2 Binding of gold nanoparticles (AuNPs) to functionalized surfaces

5.1.2.1 Introduction

The use of linking molecules or molecular linkers/binders, such as DNA [483], biotin-streptavidin [484], polymers [485], biometric ligands [486], cucurbit[n]uril (CB[n]) [487], thiols [488] and amines [489], has been previously reported to form islands and/or chains of nanoparticles. Discussion on the various types of molecular binders is out of the scope of this thesis, therefore, the rest of the chapter will concentrate on CB[n] and their use as molecular binders to bind AuNPs. In 1905, Behrend et al. synthesised the first ever cucurbit uril, CB[6], however, its structure was not explained until much later when in 1981 Freeman et al. used various characterisation techniques and discovered that CB[6] contains six glycourils and twelve methylene bridges [490]. The work of these two groups

subsequently led to discoveries of CB[5], CB[7], CB[8] and CB[10] by other researchers in the following decades [491], [492], [493]. In terms of the general structure CB[n] (Figure 5.3i), where n is the number of glycoluril units (Figure 5.3iv), are a family of molecules that have well-defined, symmetric, barrel-shaped structures (Figure 5.3ii) of hydrophobic internal cavity surrounded by circularly repeating glycoluril units [487]. CB[n] that have been used to bind AuNPs through the polar carbonyl portals found at the top and bottom (the flat part of the barrel shape) of the molecule (Figure 5.3) [494]. CB[n] always binds AuNPs through the carbonyl portals, therefore independent of the number of glycoluril units present in the CB molecule, the distance between any two adjacent AuNPs bound through a CB molecule (Figure 5.4) is always precisely 9.1 Å (d in Figure 5.3 ii and iii) with no other binding configuration possible [494], [495], [496].The following section will concentrate on the novel approaches that have been employed to use CB[n] molecules for SERS detection of various analytes

(i)

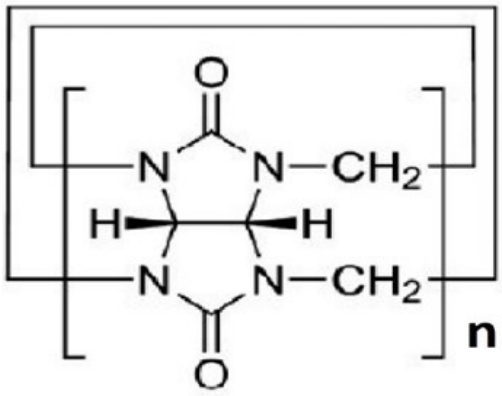

(ii)

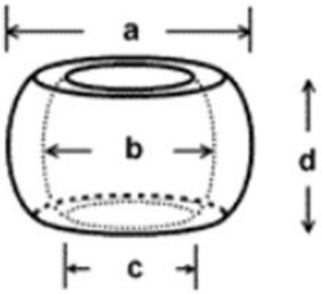

(iii)

		CB[5]	CB[6]	CB[7]	CB[8]	CB[10]
outer diameter (Å)	a	13.1	14.4	16.0	17.5	
cavity (Å)	b	4.4	5.8	7.3	8.8	11.3-12.4
	c	2.4	3.9	5.4	6.9	9.5-10.6
height (Å)	d	9.1	9.1	9.1	9.1	9.1
Cavity volume (Å^3)		82	164	279	479	

(iv)

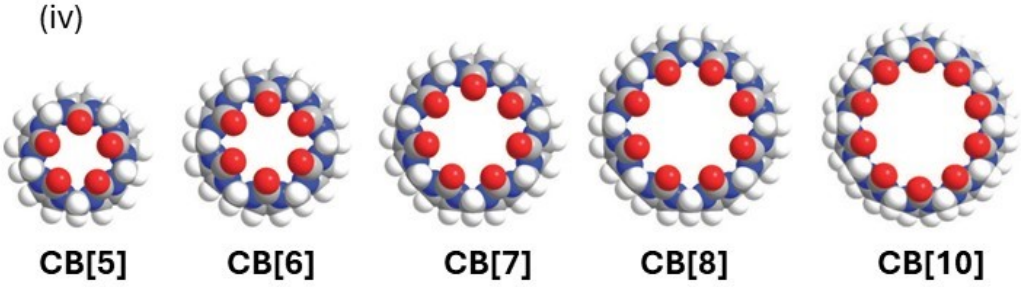

Figure 5.3: (i) The Cucurbit[n]uril structural formula; (ii) An image of the barrel shaped molecule of cucurbit[n] with all the dimension variables marked; (iii) A table of the dimensions for the barrel shaped cucurbit[5-10] in Angstroms; (iv) An image of Cucurbit[5-10] composed of five-ten circularly arranged glycouril units each having a hydrophobic central cavity and polar carbonyl portals that bind to the Au surface [497], [498], [499].

5.1.2.2 Novel approaches of using bound gold nanoparticles for SERS detection

In 2009 Scherman and Mahajan along with their coworkers pioneered the use of CB[n] in Raman spectroscopy, presenting it as the binding agent as well as the analyte for SERS measurements [496], [500]. The following year, the same group successfully developed

a self-calibrated and reliable SERS substrate based on the *in situ* immobilisation of AuNPs through the use of CB[n] as a binder. It was capable of selectively trapping analyte molecules at CB[*n*] binding sites between adjacently connected AuNPs with plasmonic enhancement provided from the AuNPs [494], thus demonstrating the triple functionality of CB[n] within SERS detection (Figure 5.4). First, the structurally well-defined CB[n] molecules can be used as binding molecules to provide fixed sized hotspots and thus homogeneous substrates for a stable SERS signal [494]. Second, the Raman-active nature of the CB[n] molecules makes self-calibration possible and so they can also be used as local reporters of the field confinement within the hotspots created by themselves [494], [500]. Finally, CB[n] molecules can be used as nanocontainers to house "guest" molecules within their hydrophobic cavity with their subsequent use as binders between AuNPs enabling the enhancement of the SERS signal from the "guest" molecule [494], [501], [502].

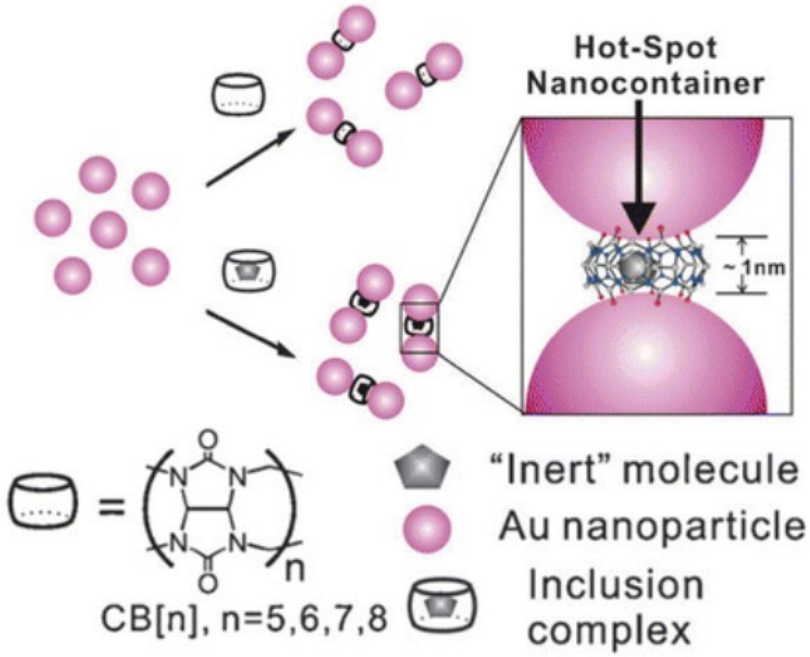

Figure 5.4: Schematic illustration of two out of the three functionality of CB[n] in the SERS process – as a rigid binding molecule providing a fixed size of hotspot and as a nanocontainer that can house molecules getting better detection capabilities [501].

A study by Baumberg and coworkers involving the use of CB[7] to assemble AuNPs on three different surfaces, gold (Au), silica (SiO_2) and silicon (Si), [503], showed that in addition to the SERS signal being dependent on the interparticle gaps, it is also influenced by the gap between nanoparticles and their underlying surface. Specifically, they showed that the SERS signal is 3 orders of magnitude greater for assemblies on the surface of SiO_2 as compared to that in solution, but only half of that for those formed on a Au surface.

The lowest SERS intensity from assemblies on Si was attributed to damping by the absorption in the semiconductor.

The majority of the work on utilising CB[n] as binders in the formation of SERS substrates had been done with AuNPs, until Jones et al. [504] reported the SERS detection of R6G through the use of gold nanorods (AuNRs) and both CB[5] and CB[7] simultaneously. In doing so achieving both the binding of AuNRs by CB[5] and the containing of R6G within CB[7], or the capture of R6G by CB[7] into a hotspot made by CB[5]. Additionally, this study explained how the use of cetyltrimethylammonium bromide (CTAB) to stabilise AuNRs helps in their end-to-end connection because the weaker binding of CTAB molecules along the curved ends than along the rods lead to an easier functionalisation there. Seo et al. also reported the use of CB[7] as a binding molecule between AuNRs, although scanning electron microscopy images showed a lack of preferential end-to-end linking between AuNRs and therefore more random binding of the AuNRs in contrast to those presented by Jones et al. [504]. The same study also discussed the stability and reproducibility of SERS signals for Raman probes encapsulated within CB[n], demonstrating up to 20 days of SERS enhancement and stability for R6G contained within CB[7] [505]. Later, in a unique approach, Baumberg et al. mixed CB[5] with AuNPs within a microfluidic device to form microdroplets, taking SERS measurements on a millisecond timescale, thereby laying the foundation for high-speed single molecule optical detection within microfluidic setups and their optimisation [506]. Table 5.3 presents a comprehensive summary of many of the SERS substrates that are based on the use of CB[n]uril as a binder, reporter and/or container, including those discussed within this section.

Table 5.3: A summary of some of the studies which utilise CB[n] molecules as either: binders (B) to link or bind metallic nanoparticles to each other into various assemblies, including chains and/or islands of metallic nanoparticles; local reporters (R) to measure the SERS enhancement offered by the assembled metallic nanoparticles; or as containers (C) when an analytes is housed within the hydrophobic cavity of the CB[n] molecule.

Nanostructure	CB[n]	Purpose (binder (B), reporter (R), container(C))	Analyte	Ref
AuNP	CB[5] CB[7]	B, R B, R, C	CB[5]; R6G CB[7]; R6G	[494]
AuNP	CB[5], CB[6], CB[7]	B, R	CB[5], CB[6], CB[7]	[500]
AuNP	CB[7]	B, R	CB[7]	[503]
AuNR	CB[5], CB[7]	B B, C	R6G	[504]
AuNR	CB[7]	B, C	R6G	[505]
AuNR	CB[8]	B, C	Methylene blue	[507]
AuNP	CB[5]	B, R	CB[5]; PDMS; citrate	[506]
AuNP	CB[7]	B, R	CB[7]; Pb^{2+}	[508]
AuNP	CB[7]	B, R, C	CB[7]; methyl viologen; 2,7 dimethyldiazapyrenium; 1-adamantylamine; *N*-methyl-1-adamantylamine;1-adamantane carboxylic acid; (dimethylamino methyl)ferrocene; 1,1 ferrocene dimethano and ferrocene.	[509]

AgNP	CB[6]	B, C	spermine	[510]
AgNP	CB[7]	B, C	fentanyl	[511]
AuNP	CB[7]	B, C	Dopamine; epinephrine and serotonin	[512]
AuNP	CB[5], CB[6]	B, R	ethanol; methanol	[513]
AuNP	CB[8]	B, C	Methyl viologen; naphthalene; 2-naphthol; phloroglucinol; and 2,3-naphthalenediol	[514]
AuNP	CB[7]	B	uric acid	[515]
AuNP	CB[8]	B	estrogen	[516]
AuNP	CB[6]	B, C	methyl viologen	[517]

5.1.3 Summary

Despite the advantages offered by the use of APTES to functionalise solid surfaces for the immobilisation of metallic nanoparticles (Table 5.2) and the use of CB[n] molecules to form well-defined hotspots between each connected interparticle (Table 5.3), neither have been used to their greatest potential, nor a combination of both used, for the formation of structured SERS substrates. In subsequent sections, the combined use of APTES functionalisation and CB[5] binding to form SERS substrates is demonstrated for the first time, whereby the binding functionality of CB[5] is used to form islands of AuNPs on to a monolayer of AuNPs already immobilised onto aluminium foil (ALF) using APTES. Thereafter the resultant SERS substrates are used to detect nanoplastics.

5.2 Aims & Objectives

The main aim of the chapter is to focus on developing a novel homogeneous 3D SERS substrate formed through having well-defined hotspots to achieve a more stable SERS signals as compared to that obtained in preceding chapters through the randomised aggregation of AuNPs based on salt-assisted aggregation approach (Chapter 3) and comparatively better controlled clustering of AuNPs based on used of hydrophobicity (Chapter 4). The homogeneous 3D SERS substrate was synthesised based on AuNP

islands formed on the monolayer of immobilised AuNPs achieved by functionalising ALF with APTES. The chapter will focus on achieving stability of SERS signal through the use of fixed sized hotspots by taking advantage of the rigid and structurally well-defined CB[5] molecules. To the best of our knowledge, this is the first ever work done on forming islands of AuNPs in a 3D morphology onto a framework of an already immobilised monolayer of AuNPs. Furthermore, the importance and additional novelty of this work lies in detecting release of real-world nanoplastics from gloves used for food preparation, thus contributing to the preservation of the environment and human health.

To fulfil the aims of the chapter the main objectives are:

1. To document the variations in SERS signal by carrying out complete characterisation of the synthesised SERS substrate through the use of Rhodamine 6G (R6G) dye.
2. To study the performance of the SERS substrate in nanoplastic detection, do a complete concentration study using pristine nanoplastics.
3. To study the potential release of nanoplastics from hot treatment of gloves used commonly by restaurants other food places during preparation of food in order to ensure hygiene conditions are followed.

5.3 Materials and methods

5.3.1 Chemicals and reagents

Gold (III) chloride trihydrate ($HAuCl_4 \cdot 3H_2O$, 99.9%), sodium citrate tribasic dehydrate ($HOC(COONa)(CH_2COONa)^2 \cdot aq$), ethanol ($C_2H_6O$), potassium hydroxide (KOH), acetic acid (CH_3COOH), 3-aminopropyltriethoxysilane (APTES), cucurbit[5]uril (CB[5]), red colour dye rhodamine 6G (R6G) and UV-transparent disposable cuvettes were all purchased from Sigma Aldrich (UK). Aqueous suspensions of 2.5% solids polystyrene nanoplastic latex beads of 50 nm diameter and 10% solids polystyrene nanoplastic latex beads of 100 nm with densities of 1.05 g/cm^3 were purchased from Sigma Aldrich (UK). 1x1 cm^2 silicon (Si) filters with pore size of 1 µm were purchased from Thermo Fisher Scientific (UK). Polyethylene gloves used for preparing food were acquired from a local food place (Belfast, UK). Kitchen aluminium foil was purchased from local store, Tesco Extra (Belfast, UK).

5.3.2 Analysis Instrumentation

The ultraviolet-visible spectroscopy (UV-vis) absorption measurements were performed using a Cary 60 spectrophotometer (Agilent Technologies, USA). The SERS substrates were visualised in high resolution scanning electron microscopy (SEM) images through the use of a JSM-6500F SEM microscope (JEOL, Japan) at 15 kV. All the SERS

measurements were carried out using a DXR2 Raman microscope (Thermo Fisher Scientific, UK) operating with a 532 nm laser and a 50x objective, having na umerical aperture (NA) of 0.5. Unless mentioned otherwise, all the SERS measurements presented in this chapter were carried out with an excitation power of 10 mW, with each spectra representing the average of 3 measurements and each measurement having an acquisition time of 3 seconds. The labelling of the peaks in the SERS spectra were done using OMNICTM Series software whilst the analysis of microplastics released from gloves was carried by Raman mapping by the inbuilt Atlμs function available in the OMNICTM series software (Thermo Fisher Scientific, UK). ImageJ software was used to determine the size of each individual nanoparticle from TEM images.

5.3.3 Numerical Simulations

The wave optics physics module of COMSOL Multiphysics was used to numerically simulate and quantify, with the the finite element method (FEM), the enhancement factor (EF) using equation 5.1, and thus SERS signal, that could be expected from a small section of the SERS substrates to be developed (Figure 5.5).

$$EF = |E_{loc}(\omega_0)/E_0(\omega_0)|^4 \qquad (5.1)$$

where:

EF – enhancement factor

$E_0(\omega_0)$ – incident electric field

$E_{loc}(\omega_0)$ – localised electric field

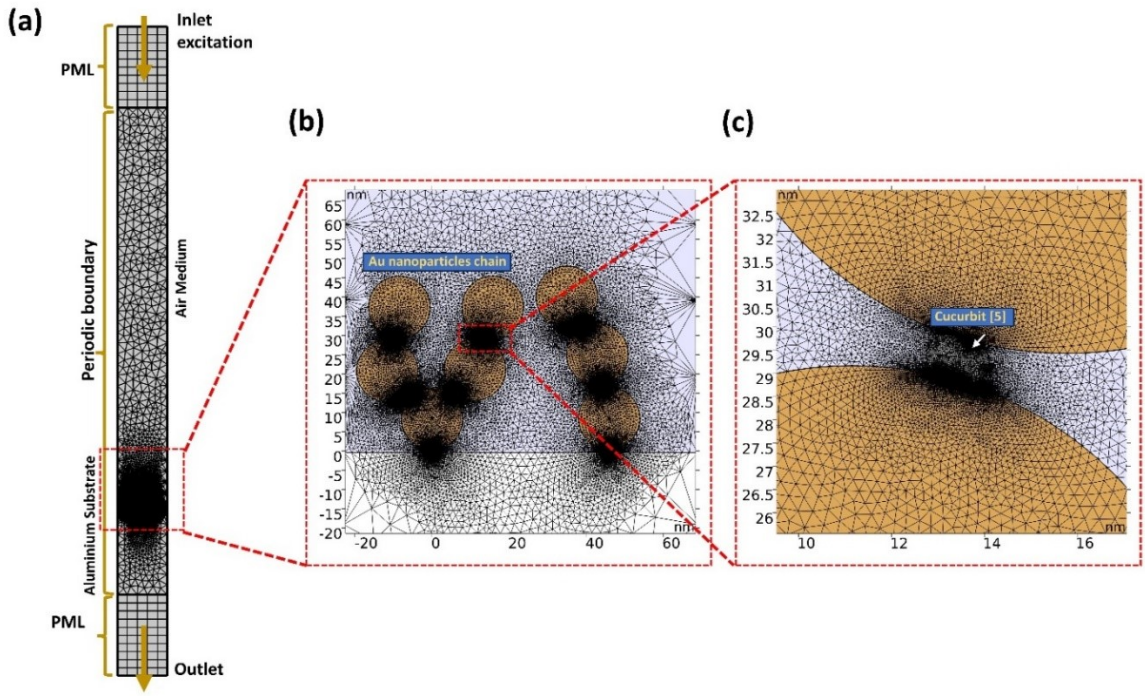

Figure 5.5: (a) Top view of the geometry in the numerical simulation to calculate the enhancement factor of 3D structures formed using cucurbit[5] for the SERS substrate. (b) The magnification of the inset area of (a) showing a geometry that consists of three strand-like features formed by eight interconnecting 15 nm diameter gold nanoparticles attached to two others that are immobilised on a functionalised aluminium base. (c) The magnification of an inset of (b) showing the interparticle geometry, including the cucurbit molecule that binds the AuNPs.

The model simulated consisted of eight AuNPs interconnected by CB[5] formed into three strands that are attached via CB[5] to two AuNPs that are immobilized on the functionalized ALF (Figure 5.5b). The eight 15 nm AuNPs are connected through barrel shaped features with a height of 9 nm (Figure 5.5c). Perfectly matched layer boundary conditions are used at the top and bottom of the simulation region as artificial absorbing layers to truncate the simulation region (Figure 5.5a) whilst a periodic boundary condition is used on the left and right to imitate it being just a small part of a larger physical domain (Figure 5.5b). Whilst a fine mesh is used in the area with the AuNPs, an even finer mesh is used in the areas between the AuNPs as those are the hotspot regions.

5.3.4 Gold nanoparticle synthesis

AuNPs were synthesised using the well-established Turkevich method, with minor modifications [518]. First, 500 µL of 100 mM $HauCl_4$ was added to 49.50 µL of deionised water (dH_2O) and then heated, whilst undergoing constant slow speed stirring, until boiling. Upon reflux 5 mL of 1% $HOC(COONa)(CH_2COONa)^2$ was quickly added whilst vigorously stirring, with the heat removed upon the citrate-meditated reduction of the gold ions, as indicated by the solution's colour changing from pale yellow to wine red. Whilst cooling to room temperature (approximately 30 minutes) the AuNPs were then subjected to continuous slow stirring whereafter the synthesised AuNPs were stored in a refrigerator until subsequent experiments.

5.3.5 Gold nanoparticle characterisation

UV-vis absorption measurements of the synthesised nanoparticles were performed to also confirm their successful synthesis as well as estimate their diameter and concentration from the use of equations 5.2 and 5.3 [360]. Specifically, entering the value of *r* from below within a data table found in Table S-2 of [360], provides the diameter of the AuNPs:

$$r = \frac{A_{max}}{A_{450}} \qquad (5.2)$$

where:

r – is the ratio of two specific absorbance values.

A_{max} – the highest absorbance value on the UV-vis absorption curve.

A_{450} – the value of absorbance at a wavelength of 450 nm on the UV-vis absorption curve.

Meanwhile, the concentration of the nanoparticles in solution formed in 5.3.4 is determined by the equation below through the use of a value of ε_{450} from Table S-3 of [360] that corresponds to the diameter calculated above:

$$c = \frac{A_{450}}{\varepsilon_{450}} \quad (5.3)$$

where:

c – the concentration (in M/L) of the nanoparticles in the solution formed in 5.3.4

ε_{450} – the molar decadic extinction coefficient in M^{-1} at a wavelength of 450 nm obtained from Table S-3 of [360] for the diameter calculated above

A_{450} – the value of absorbance at a wavelength of 450 nm on the UV-vis absorption curve.

Transmission electron microscopy (TEM) analysis was also used to calculate the size distribution of the colloidal AuNPs. The TEM grid was prepared for analysis by drop-casting on to it approximately 5 µL of the AuNP colloid before leaving it to dry overnight in ambient conditions. The size of each particle was measured with the image processing software ImageJ and a normal distribution curve fitted to a histogram of those values. The normal distribution was then translated to a log normal distribution from which the average and standard deviation for the diameters were calculated using equations 5.4 and 5.5:

$$d_{avg} = 2.718^{ln\,mean} \quad (5.4)$$

$$\sigma = 2.718^{ln\,sd} \quad (5.5)$$

where:

d_{avg} – average diameter of the synthesized colloidal AuNPs

ln mean – log normal of the mean diameter (obtained from the log normal distribution)

σ – standard deviation of the nanoparticle diameter

ln sd – log normal of the standard deviation of particle diameters (obtained from the log normal distribution)

5.3.6 Synthesis of SERS substrate

The synthesis of the SERS substrate was conducted through a five-step process (Figure 5.6): (i) annealing, (ii) etching, (iii) APTES, (iv) heating/submersion in AuNP colloid, and (v) drop casting of CB[5]. Whilst the annealing and etching steps are not strictly required for the subsequent salinisation and formation of a monolayer of AuNPs on ALF (S-ALF) or AuNP island formation on the S-ALF (ALF-IL), unless explicitly indicated otherwise,

those ‘pre-treatment’ steps were also undertaken as they were found to significantly enhance the efficiency of the salinisation process (see 5.4.3.1). To evaluate their enhancement additional ALF samples were prepared using just process steps iii-v.

The annealing step (i) involved heating the ALF to 350°C on a hotplate until the disappearance of mark previously made with a permanent marker, indicating sufficient annealing. Following annealing, the etching step (ii) consisted of immersing the ALF in 1 M potassium hydroxide (KOH) until the solution began to fizz, approximately 30 seconds. Step (iii) consisted of immersing the ALF into a 2% (3-Aminopropyl)triethoxysilane (APTES) solution at pH 5 for 30 minutes, with the 2% APTES solution having been prepared by adding 200 µL of APTES to 9.8 mL of dH_2O. Through monitoring with a pH meter the pH of the solution was carefully maintained by the dropwise addition of acetic acid (CH_3COOH) while continuously stirring, initially exhibiting minimal changes but then decreasing sharply requiring significant additions. In step (iv) the ALF was removed from the APTES solution, incubated at 40°C for an additional 30 minutes, rinsed with dH_2O to remove any unbound APTES and then small sections (each ~ 3 mm x 5 mm) of the now salinized ALF were submerged in aliquots of 2 mL synthesized 0.819 nM AuNP solution to immobilise a monolayer of AuNPs to the salinized surface, forming S-ALF. Finally in step (v) 10 µL of a 0.24 mM cucurbit[5]uril (CB[5]) solution prepared in dH_2O was added to each aliquot and left to incubate for 1 hour to facilitate molecular binding of three-dimensional islands of AuNPs to the AuNP monolayer, forming ALF-IL. The ALF-IL were then removed after one hour from the aliquots, and excess unbound AuNPs were rinsed off with dH_2O, before they were allowed to air dry.

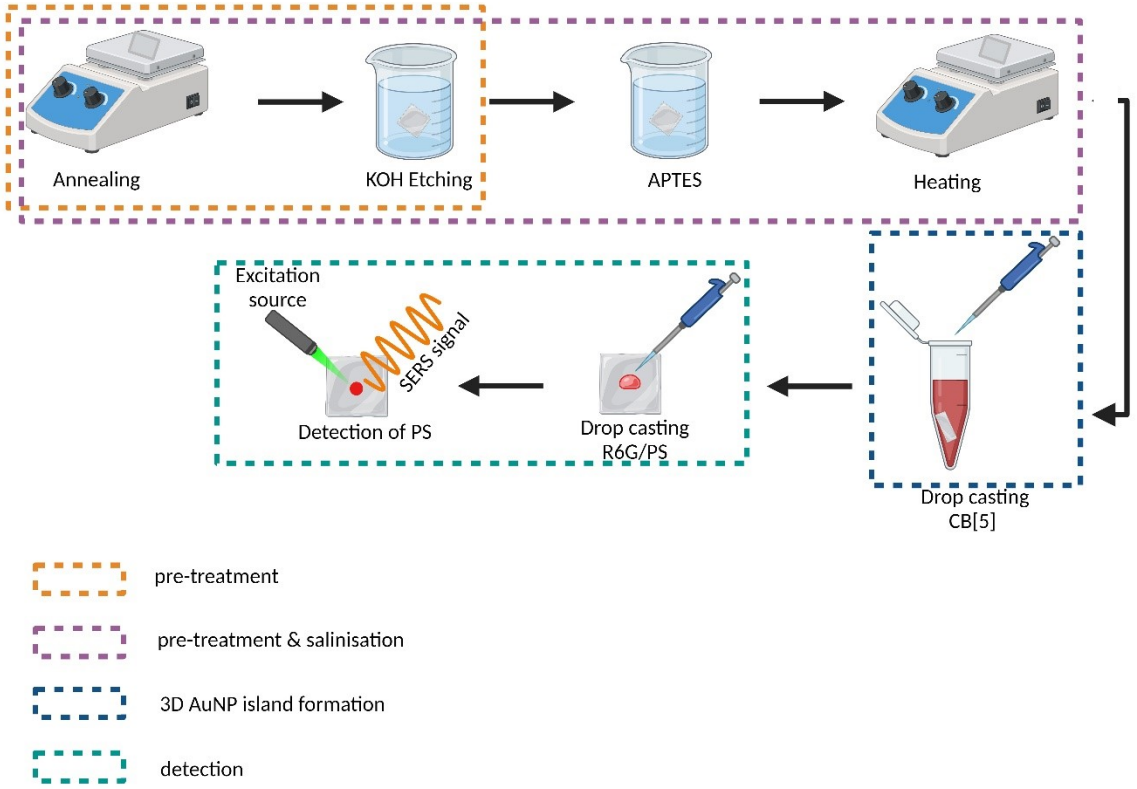

Figure 5.6: The synthesis processes for salinized ALF covered in a monolayer of AuNPs (S-ALF) and ALF with AuNP island formations (ALF-IL) consists of optional process steps (i) and (ii), as well as steps (iii-iv) and (iii-v), respectively.

5.3.7 Preparation of R6G solutions

The purchased R6G had a molecular weight of 479.02 g/mol and so a 1 mM stock solution (SS) of R6G was prepared by adding 239.51 mg of R6G to 5 mL of dH_2O with the graphpad molarity calculator used for calculations. The various concentrations of R6G (10^{-11} to 10^{-4} M) for subsequent experiments were prepared by diluting the 1 mM stock solution with the required quantity of dH_2O.

5.3.8 Characterisation of the SERS substrate

The immobilization of a layer of AuNPs onto the ALF and the binding of AuNPs to each other, and the immobilized AuNPs, in the presence of CB[5] was validated through a scanning electron microscopy (SEM) analysis of the S-ALF and the ALF-IL respectively. The efficacy of pre-treatment was also visualised through SEM imaging of the surface of the aluminum surfaces.

To measure the efficiency of AuNP binding through CB[5] a complete concentration study using the well characterized Raman dye of R6G [425] was undertaken, for both S-ALF and AFL-IL, having chosen an appropriate spectral peak by first analysing the prominent

peaks for R6G on ALF and comparing them to those published in the literature. SERS spectra were taken after 1 µL of each R6G concentration (10^{-11} to 10^{-3} M) was drop cast on each substrate and allowed to dry in air at room temperature. The efficacy of the pre-treatment steps was determined by comparing the SERS signal for 1 µL of 10^{-6} M R6G drop-cast and airdried on ALF-ILs prepared with, and without, the pretreatment steps.

5.3.9 Calculating the Limit of Detection (LoD)

Data from the R6G concentration studies was used to determine the lowest concentration that could be measured, or the limit of detection (LoD), using the following equations [426]:

$$LoD = LoB + 1.645\ (SD_{low\ concentration\ sample}) \quad (5.6)$$

$$LoB = mean_{blank} + 1.645\ (SD_{blank}) \quad (5.7)$$

where:

LoD - Limit of detection for R6G for the SERS substrate used.

$SD_{low\ concentration\ sample}$ – standard deviation of the SERS intensity for the lowest concentration of R6G at the diagnostic peak detected through the use of the SERS substrate.

SD_{blank} – standard deviation of the SERS intensity for the matrix blank at the diagnostic peak detected through the use of the SERS substrate.

LoB - Limit of the blank.

The matrix blank consisted of a SERS substrate having had 1µL of plain dH_2O drop-cast onto it before being allowed to air-dry.

5.3.10 Calculating the homogeneity of the ALF-IL

The homogeneity of ALF-IL was determined by first performing a SERS mapping over a 20 µm x 20 µm area, with a step size of 1 µm, in a randomly selected region where 1 µL of 10^{-6} M R6G had been drop cast and allowed to air dry. The SERS intensity at the diagnostic peak for each of the 400 points was represented as a contour map, from which the mean and coefficient of variation percentage (CV%) was calculated using the equations below:

$$mean_{400} = {\sum I_{400}}/{400}$$

$$CV\% = {mean_{400}}/{\sigma_{400}}\ x\ 100$$

where:

ΣI_{400} – the sum of the 400 intensities

σ_{400} – the standard deviation for the 400 intensities.

5.3.11 Preparation of nanoplastic solutions

The stock solutions for the 50nm and 100nm diameter PS nanoplastics purchased from the manufacturer were 10% solid, i.e. 100 mg/mL and 2.5% solid i.e. 25 mg/mL, respectively. Therefore, to prepare a 500 µg/mL solution of the 100 nm PS, 5 µL of the 10% solid stock solution was added to 995 µL of dH_2O. Similarly, a 500 µg/mL solution of the 50 nm PS was prepared by adding 20 µL of the 2.5% solid stock solution to 980 µL of dH_2O. PS solutions of both diameters, with concentrations of 250 µg/mL, 100 µg/mL, 50 µg/mL, 25 µg/mL, 5 µg/mL and 1 µg/mL, were prepared through diluting the 500 µg/mL solutions with appropriate amounts of dH_2O.

5.3.12 Concentration study of nanoplastics

SERS measurements at the diagnostic peak were taken of ALF-IL after 1 µL droplets of the prepared various concentrations of 50 nm and 100 nm nanoplastic solutions were drop cast onto them and allowed to air dry. A calibration curve for each solution was constructed by fitting a curve through a plot of average SERS signal intensities, with error bars comprising of their standard deviation, against concentration.

5.3.13 Study of micro and nanoplastics released from gloves

The release of nanoplastics from food preparation gloves whilst in use was studied using the synthesised ALF-IL. In an attempt to mimic the conditions the gloves undergo during use, two gloves underwent a heat treatment consisting of leaving them in a sonication bath containing 100 mL dH2O that had been heated to 40˚C before the heat source was removed. Following the sonication bath, the gloves were removed and the liquid vacuum filtered through Si filters, leaving behind any plastics larger than nanoplastics that might have been released from the gloves. The liquid was then centrifuged at 10˚C and 1200 relative centrifugal force (rcf) for 30 minutes to enrich the nanoplastic solution before 1 µL droplets were sequentially extracted and drop cast onto the ALF-IL for SERS measurements until nanoplastics were detected. Furthermore, a 10x10 µm2 area of the filter was scanned using the particle analysis feature of the OMNIC software to analyse any microplastics that might have been present in that area of the filter.

5.4 Results and discussion

5.4.1 Numerical Simulation

Figure 5.7a shows a region of the numerically simulated electric field (see Section 5.3.3) that contains AuNPs, each connected by a CB[5] molecule, with hotspots between them.

Figure 5.7b is a magnification of the inset area of Figure 5.7a, containing one such hotspot region between two AuNPs, showing a maximum enhancement of 7.50.

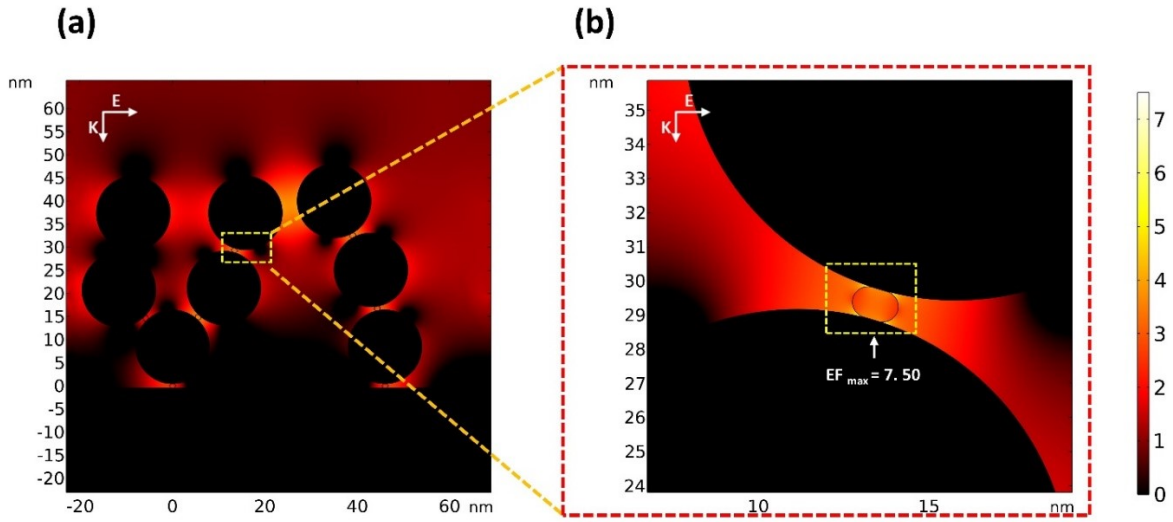

Figure 5.7: (a) A region of numerically simulated electric field that contains the strands of connected AuNPs (b) A magnification of the inset from (a) featuring the region between two AuNPs connected by a cucurbit molecule with a maximum enhancement factor of 7.50.

5.4.2 Gold nanoparticle characterization

The UV-vis absorbance spectrum (Figure 5.8a) of the synthesised AuNPs (see Section 5.3.4) indicates a maximum absorbance of 2.35 at 521 nm and an absorbance of 1.51 at 450nm (A_{450}), with the ratio of the two (r) being 1.56. Those values correspond to (see Section 5.3.5) their diameter being 12 nm, a molar decadic extinction coefficient of 1.09×10^8 M^{-1} and the concentration of the nanoparticle colloidal being 13.85 nM. The diameter is within one standard deviation range of the average diameter determined from a TEM image (Figure 5.8b) of the same AuNPs, appearing as spherical and of a uniform size, being calculated at 13.01±1.09 nm from a size distribution curve plotted using the log normal function (Figure 5.8c).

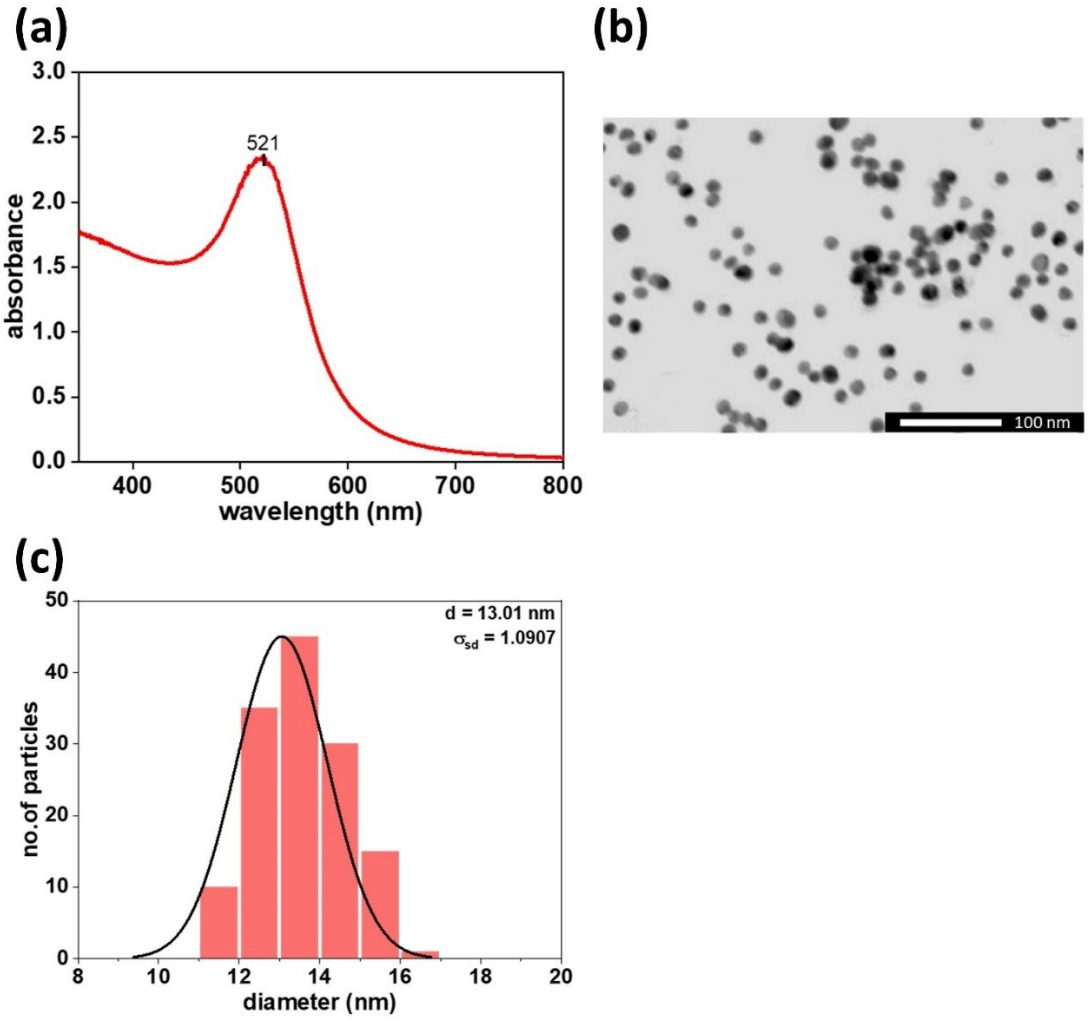

Figure 5.8: (a) A UV-vis absorption spectrum for the synthesised colloidal AuNPs with the greatest absorbance, at 2.35, seen at 521 nm (b) A TEM image of 136 representative AuNPs with a scale bar of 100 nm (c) A histogram of the size distribution for the 136 nanoparticles in TEM image indicating an average diameter of 13.01±1.09 nm.

5.4.3 Characterisation of the SERS substrate

5.4.3.1 SEM analysis

The interparticle interaction between AuNPs and their attachment to the solid surface of ALF was studied with SEM, both after the salinisation process, with (Figure 5.9a) and without pre-treatment (Figure 5.9b), and after CB[5] binding following pre-treatment and salinisation (Figure 5.9 c and d). A comparison of Figure 5.9 a and b (both have the same size scale for ease of comparison) indicates that the S-ALF prepared with the pre-treatment steps has a denser coverage of AuNPs than that prepared without. This would indicate that the S-ALF prepared through the additional pre-treatment steps has a greater number of sites for AuNP to attach, which would be consequential of greater salinisation, that in turn follows from a very rich (thick) layer of hydroxyl groups being present when the

ALF is immersed in APTES. The additional steps of annealing (heating in air) the intrinsic (thin) aluminium oxide on the surface of the ALF to grow a thicker layer [519], [520], [521] and then etching it in KOH to hydroxylate it, thereby dissociating the oxides, forms such a rich (thick) layer of hydroxyl groups which salinizes readily [453], [522].

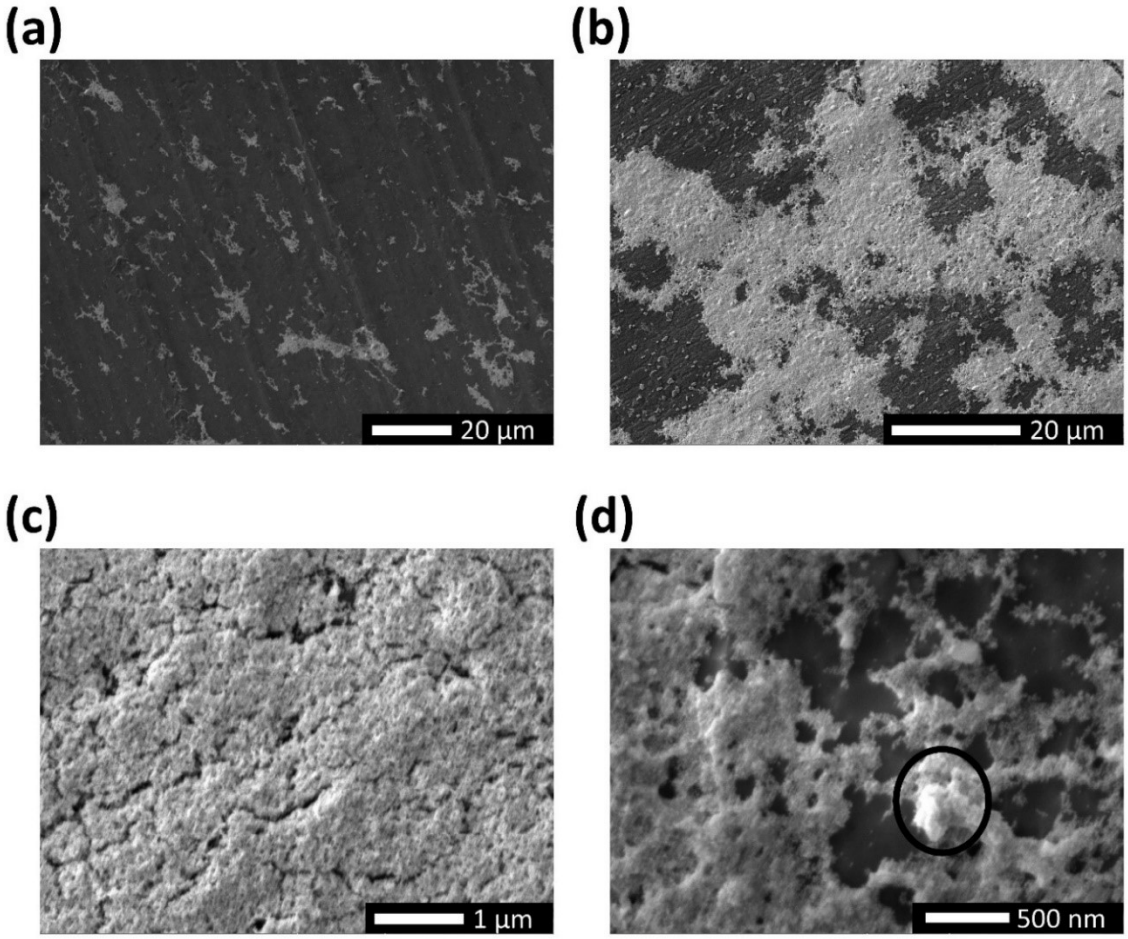

Figure 5.9: SEM images of: (a) S-ALF, that has not undergone pre-treatment steps prior to the salinisation process, with a scale bar of 20 µm; (b) S-ALF, that underwent pre-treatment steps prior to the salinisation process, with a scale bar of 20 µm; (c) ALF-IL showing the 3D deposition of AuNPs in different morphologies due to the inter-particle bindings provided by CB[5], with a scale bar of 1 µm; (d) the same ALF-IL at a higher magnification showing more clearly (particularly the encircled section) the formation of 3D AuNP islands due to the interparticle binding provided by the addition of CB[5], with a scale bar of 500 nm.

In contrast to Figure 5.9b, Figure 5.9c and Figure 5.9d show a significantly denser coverage of AuNPs and the formation of 3D nanostructures, due to inter-nanoparticle binding in the presence of CB[5], which are indicated by features with a lumpy morphology, one such example being clearly indicated within the circle of Figure 5.9d. Whilst both figures demonstrate a noticeable lack of symmetric 3D geometry the use of CB[5] ensures constant sized hotspots between each pair of adjacent linked AuNP.

5.4.3.2 Characterisation using R6G

To experimentally evaluate S-ALF and ALF-IL as SERS substrates a concentration study using rhodamine 6G (R6G) was conducted with Raman (see Section 5.3.7) at the wavenumber that corresponded to the most prominent representative peak identified from a Raman spectral analysis for R6G drop-cast on ALF. To determine the latter, prominent experimentally detected peaks at approximately 611 cm^{-1}, 772 cm^{-1}, 1124 cm^{-1}, 1182 cm^{-1}, 1309 cm^{-1}, 1361 cm^{-1}, 1506 cm^{-1}, 1575 cm^{-1}, and 1645 cm^{-1} (Figure 5.10) were compared to those reported in the literature for comprehensive band assignment (Table 5.4). Among those, the most prominent peak of R6G at 1361 cm^{-1}, attributed to C-C stretching, was selected as the diagnostic peak for further analysis.

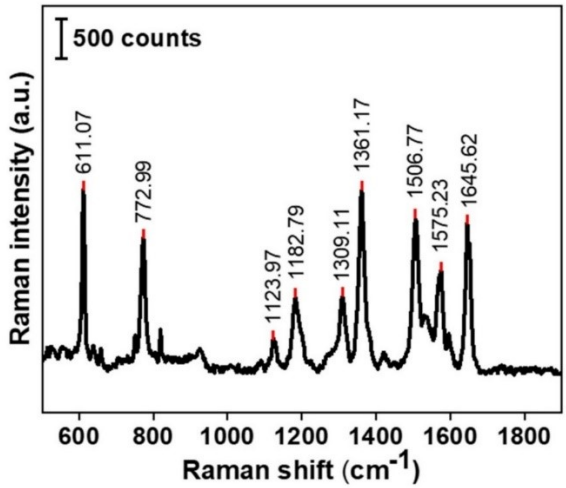

Figure 5.10: A Raman spectral analysis for R6G drop casted on ALF with the most prominent peaks indicated for subsequent comparison with those reported in the literature that are associated with characteristic bands and thus the selection of the most appropriate diagnostic peak for a concentration study of S-ALF and ALF-IL.

Table 5.4: Characteristic experimentally measured peaks for R6G on ALF listed against those seen in the literature that have been assigned to characteristic bands.

Raman shift according to the experiment (cm^{-1})	Raman shift according to the literature (cm^{-1})	Band assignment	Ref
611.07	617	C-C-C ring in-plane bending	[435]
772.99	776	C-H out-of-plane bending	[435]
1123.97	1131	C-H in-plane bending	[435]
1182.79	1188	C-C stretching	[435]
1309.11	1318	C-C stretching	[435]
1361.17	1360	C-C stretching	[436]
1506.77	1512	C-C stretching	[435]
1575.23	1577	C-C stretching	[435]
1645.62	1652	C-C stretching	[435]

It should be noted that the minor differences in Raman shift between the experimentally measured peaks and those reported in the literature are to be expected as cross-system variations in Raman shift and signal intensity for identical samples are well-documented, and present a significant challenge in inter-laboratory studies [523]. Same sample studies across various instruments have shown that these inconsistencies are due to variations in system and calibration protocols [429], [430]. That with said, Raman shift variations are also possible in each instrument due to inherent limitations such as resolution, or temporal variances, such as positional drift or thermal expansion [431] with regular calibration of wavenumber and signal intensity mitigating some of these issues. A detailed discussion of the issue is beyond the scope of this thesis.

In the concentration studies of S-ALF and ALF-IL with R6G, the lowest concentration detected with the former (Figure 5.11a) was 10^{-7} M whilst for the latter (Figure 5.11c and Figure 5.11d) it was 10^{-11} M. The four orders of magnitude improvement in the detection limit for R6G is attributed to the 3D islands of AuNPs resulting from the use of CB[5] binding. For both substrates, R^2 values for linear regression fits through plots of signal intensity at the diagnostic peak of 1361 cm^{-1} for each R6G concentration (Figure 5.11b and Figure 5.11e) are high, 0.996 and 0.984 respectively. Such high R^2 values for the calibration curves are evidence that the synthesised S-ALF and ALF-IL give a good linear response, and so unknown concentrations can be estimated from experimental measured intensities at that diagnostic wavenumber.

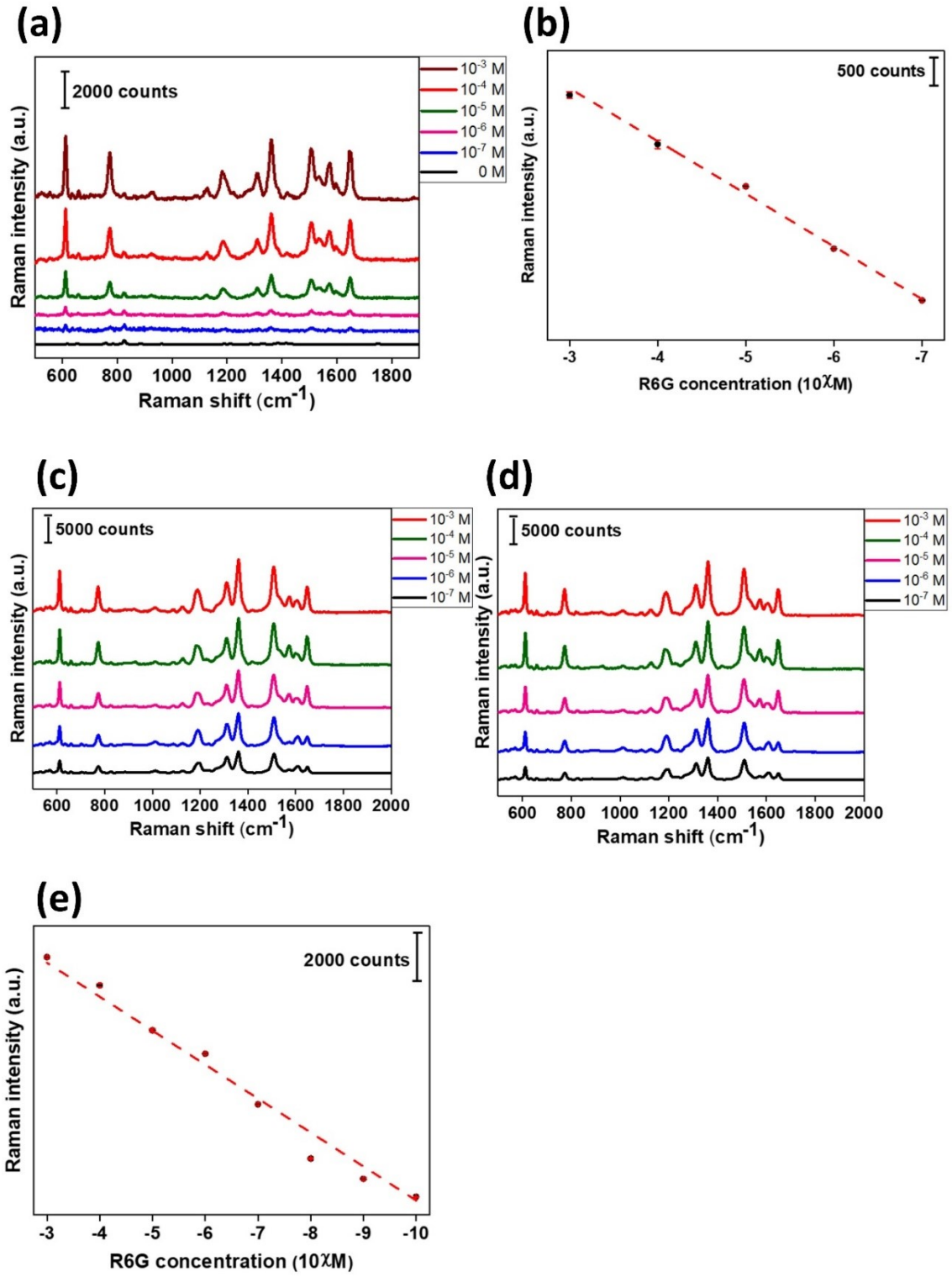

Figure 5.11: (a) Raman spectra for various concentrations of R6G (10^{-7} M to 10^{-3} M) on S-ALF, with 10^{-7} M being the lowest detectable. (b) Linear regression fitting of Raman intensities at 1361 cm^{-1} for each concentration of R6G on S-ALF, with y = 1000.91x + 7289.99 and R^2 = 0.996. (c-d) Raman spectra for various concentrations of R6G (10^{-11} M to 10^{-3} M) on ALF-IL, with 10^{-11} M being the lowest concentration detectable. (e) Linear regression fitting of Raman intensities at 1361 cm^{-1} for each concentration of R6G on ALF-IL, with y = 1468.92x + 14823.12 and R^2 = 0.984.

5.4.4 Calculating the Limit of Detection (LoD) of S-ALF and ALF-IL

SERS measurements of S-ALF and ALF-IL that had 1μL of plain dH_2O drop-cast onto them before being allowed to air-dry, Figure 5.12 a and b respectively, were used to determine SD_{blank} which through the use of equation 6 (Section 5.3.9) led to:

$LoB_{S\text{-}ALF}$ = 53.86 + 1.645 (7.17) = 65.65

$LoB_{ALF\text{-}IL}$ = 45.89 + 1.645 (3.24) = 51.22

Thereafter, from equation 7 (Section 5.3.9) using these values and the standard deviation of the SERS intensities for the lowest concentration of R6G at the diagnostic peak of 1261 cm^{-1} the Limits of Detection (LoDs) could be determined:

$LoD_{S\text{-}ALF}$ = 65.65 + 1.645 (24.19) = 105.44

$LoD_{ALF\text{-}IL}$ = 51.22 + 1.645 (8) = 64.38

The use of those values in the linear regression fits for S-ALF (Figure 5.11b) and ALF-IL (Figure 5.11e) lead to their LoD in Moles, respectively:

y = mx + c = 1000.91x + 7289.99 -> $\frac{105.44 - 7289.99}{1000.91}$ = -7.178

=> $LoD_{S\text{-}ALF}$ = 1.78 x 10^{-7} M

y = mx + c = 1468.92x + 14823.12 -> $\frac{64.38 - 14823.12}{1468.92}$ = -10.0473

=> $LoD_{ALF\text{-}IL}$ = 4.73 x 10^{-11} M

and thus in good agreement with the experimentally measured LoDs of 10^{-7} M and 10^{-11} M.

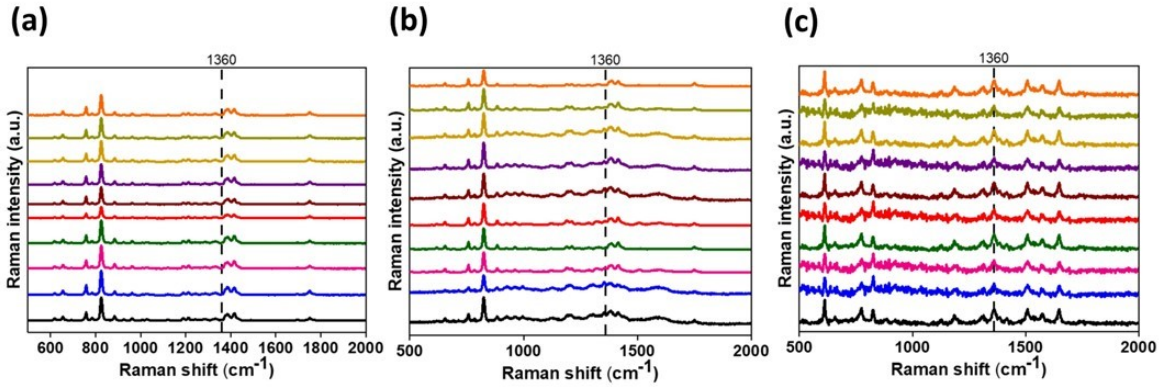

Figure 5.12: Ten SERS spectra taken for the (a) matrix blank (b) lowest concentration of R6G on S-ALF with the measurements taken for diagnostic peak (c) lowest concentration of R6G on S-ALF with the measurements taken for diagnostic peak.

5.4.5 Comparison of the performance of untreated S-ALF, pretreated S-ALF and pre-treated ALF-IL.

Figure 5.13a indicates Raman signal intensities at 1361 cm^{-1} for 10^{-6} M R6G on non-pre-treated S-ALF, pre-treated S-ALF and pre-treated ALF-IL, with that for the latter being four and thirteen times greater than for pre-treated S-ALF and non-pre-treated S-ALF,

respectively. The greater signal on pre-treated S-ALF compared to the non-pre-treated S-ALF is attributed to the increase in the oxide, and consequently the number of hydroxyl groups, and thus binding sites for AuNPs (see Section 5.4.3.1).

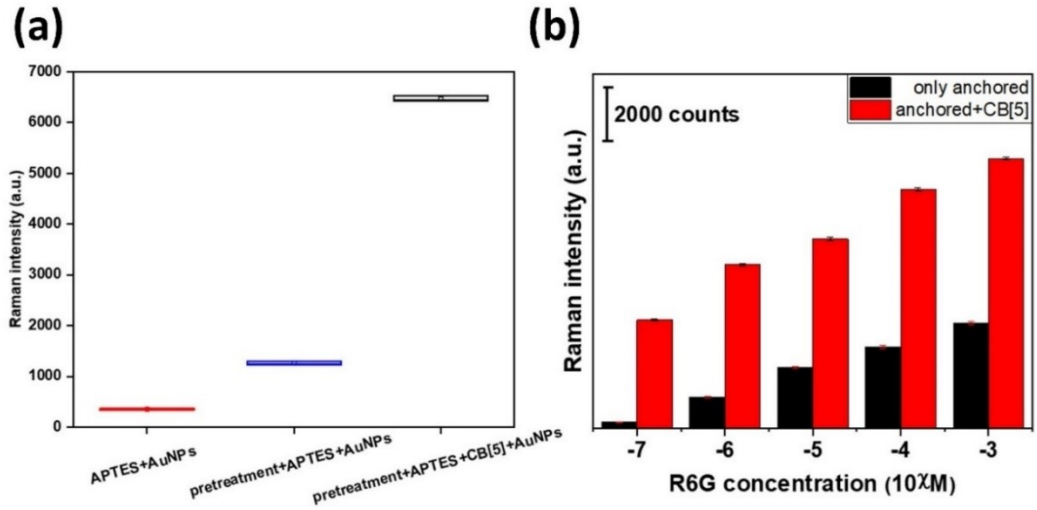

Figure 5.13: (a) Raman signal intensities at 1361 cm^{-1} for 10^{-6} M R6G drop cast and air dried on non-pre-treated S-ALF (red), pre-treated S-ALF (blue) and pre-treated ALF-IL (black). (b) Raman signal intensities at 1361 cm^{-1} for various concentrations of R6G drop cast and air dried on pre-treated S-ALF and pre-treated ALF-IL.

The comparison of the signal intensities at 1361 cm^{-1} for various concentrations of R6G drop cast and air dried on pre-treated ALF-IL and pre-treated S-ALF (Figure 5.13b) clearly show those for the former are at least double that for the latter at every concentration. The difference being attributed to the 3D AuNPs islands formed from the use of CB[5] in producing ALF-IL, resulting in a greater number of hotspot sites as compared to those within the monolayer formed by the salinisation process on S-ALF (see Section 5.4.3.1).

Given the significantly higher performance, or efficacy, of ALF-IL over the other two foils as a SERS substrate reported above, it was selected for the detection of nanoplastics, pending a confirmation of its homogeneity.

5.4.6 Calculating the homogeneity of the ALF-IL

SERS intensities measured at the diagnostic peak of 1361 cm^{-1} 400 times across a randomly selected region where 10^{-6} M R6G had been drop cast and dried on ALF-IL (plotted as a contour map in Figure 5.14a) have a variation from 5585 to 7320 counts, indicating a very well distribution and drying of the droplet.

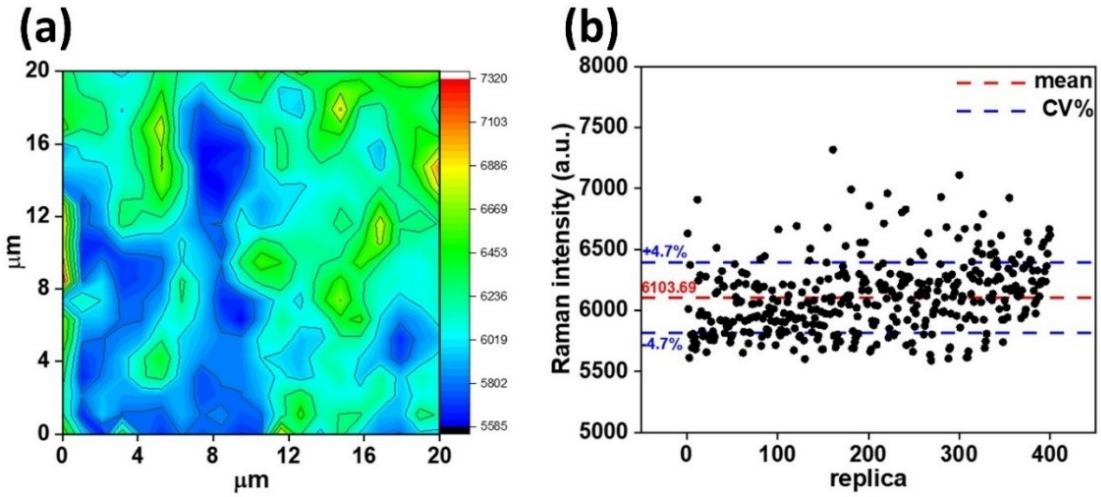

Figure 5.14: (a) A contour map for 400 measurements over a 20 μm × 20 μm area, with a 1 μm step, for the SERS intensity at 1361 cm^{-1} of 10^{-6} M R6G on ALF-IL (b) A scatter plot of 400 measurements from (a) along with their average and the CV percentage.

5.4.7 Detection of nanoplastics

In order to use AlF-IL as a SERS substrate for the detection of various concentrations of 50 nm and 100 nm diameter polystyrene (PS) spherical nanoplastics in suspension, the characteristic peaks for PS had to be first determined. To do so Raman measurements of a PS pellet was made (Figure 5.15) and the experimentally detected peaks, at approximately 619 cm^{-1}, 795 cm^{-1}, 1000 cm^{-1}, 1030 cm^{-1}, 1153 cm^{-1}, 1447 cm^{-1}, 1581 cm^{-1}, and 1601 cm^{-1}, were compared with those reported in the literature for comprehensive band assignment (Table 5.5). Slight differences between the two are caused by using different instruments that have been calibrated separately, most likely using different protocols as explained in section 5.4.3.2, The most prominent peak for PS was at 1000 cm^{-1} and is attributed to ring breathing mode and was selected as the diagnostic peak of interest for the subsequent concentration study.

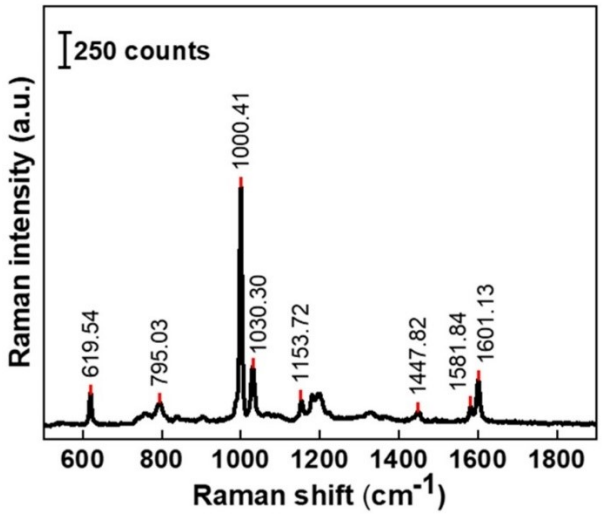

Figure 5.15: Raman spectra for a PS pellet with band assignment of the characteristic peaks included.

Table 5.5: Experimentally measured characteristic peaks for polystyrene listed against values found in the literature and their band assignment.

Raman shift according to the experiment (cm^{-1})	Raman shift according to the literature (cm^{-1})	Band assignment	Ref
619.54	621	Ring deformation mode	[366]
795.03	795	C-H out-of-plane deformation	[366]
1000.41	1001	Ring breathing mode	[366]
1030.30	1031	C-H in-plane deformation	[366]
1153.72	1155	C-C stretching	[366]
1447.82	1450	CH_2 scissoring	[366]
1581.84	1583	C=C stretching	[366]
1601.13	1602	Ring-skeletal stretching	[366]

The AIF-IL based SERS study for 50 nm and 100 nm PS particles revealed (Figure 5.16a and Figure 5.16c) clear characteristic peaks at 1000 cm^{-1} and 1030 cm^{-1} for all the concentrations used: 250 µg/mL, 100 µg/mL, 50 µg/mL, 25 µg/mL, 5 µg/mL and 1 µg/mL. Moreover, for both sizes the lowest concentration detected was 1 µg/mL, which is much lower than that reported elsewhere for the SERS detection of nanoplastics [160], [281], [524], and their calibration curves for intensities measured at 1000 cm^{-1} show significant linearity with R^2 values of 0.969 and 0.995 from 1 µg/mL to 500 µg/mL (Figure 5.16 b and d). Finally, a comparison of intensities at the diagnostic peak for both sizes at all concentrations (Figure 5.16e) shows them being greater for the larger particle, although with a lower than expected difference which is hypothesised as being due to the hotspot size being much smaller than the nanoplastics themselves.

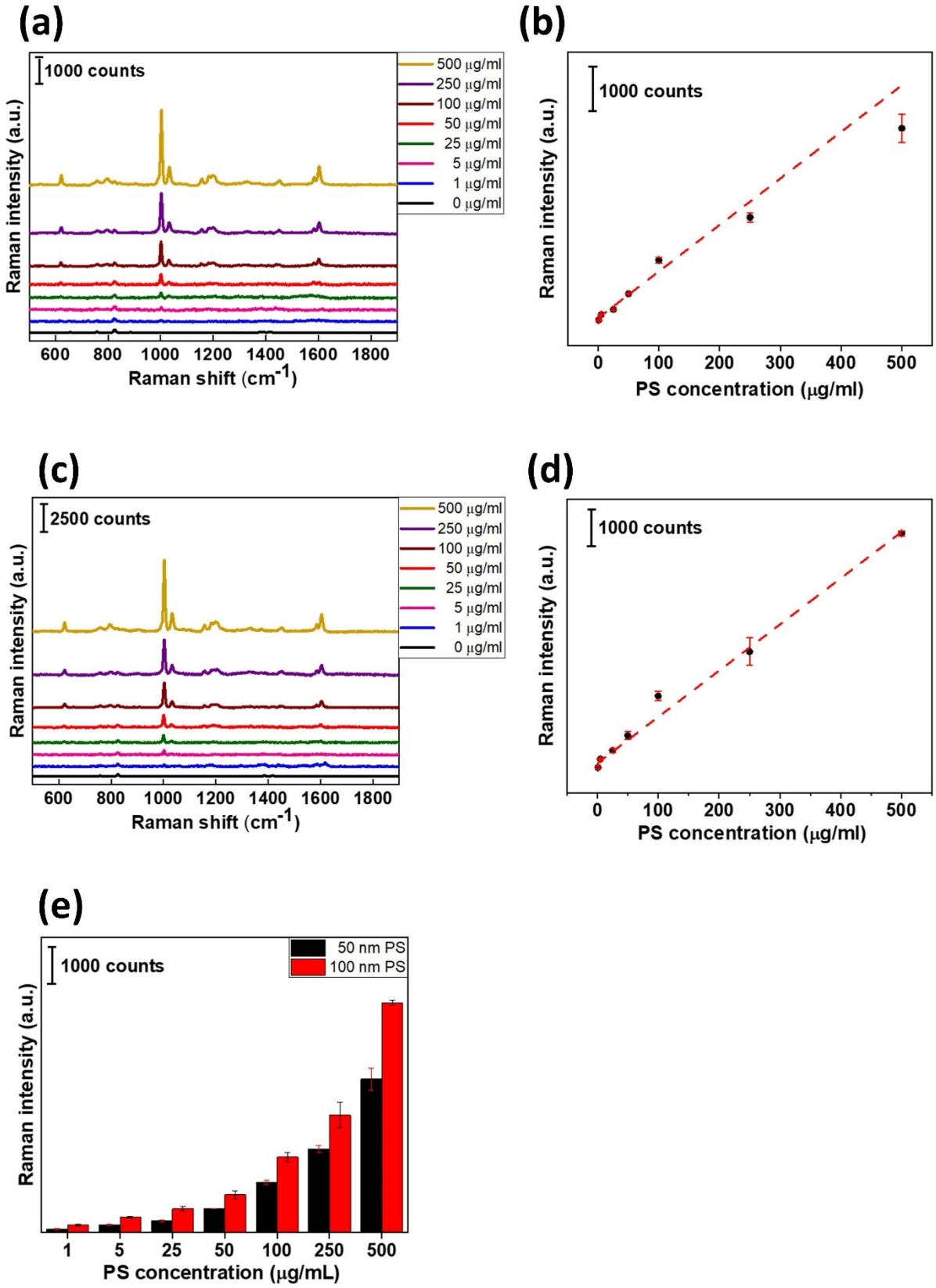

Figure 5.16: (a) SERS spectra for 50 nm polystyrene (PS) spherical nanoplastics on ALF-IL for concentrations ranging from 1 µg/mL to 500 µg/mL (b) A scatter plot of Raman intensity at 1000 cm^{-1} against concentration for 50 nm PS nanoplastic plotted with a calibration curve fitted of y = 11.09x + 156.99 with R^2 = 0.969 (c) SERS spectra for 100 nm polystyrene (PS) spherical nanoplastics on ALF-IL for concentrations ranging from 1 µg/mL to 500 µg/mL (d) A scatter plot of

Raman intensity at 1000 cm^{-1} against concentration for 100 nm PS nanoplastic plotted with a calibration curve fitted of y = 13.38x + 357.93 with R^2 = 0.995. (e) A histogram of intensities at the diagnostic peak for both sizes of PS nanoplastics and at all concentrations.

5.4.8 Study of micro and nanoplastics released from gloves

Food preparation gloves made of polyethylene underwent heat treatment in a sonication bath containing dH_2O, to mimic their conditions when in use, and the 1 µm pore size Si filter used to vaccum filter the liquid was examined for microplastics whilst the strained liquid for examined for nanoplastics. Raman spectra for the thirty microplastic particles found within a small section (10x10 $µm^2$ area) of the 1x1 cm^2 filter (Figure 5.17a), when compared to a reference spectrum for polyethylene, were identified as being of polyethylene using the particle analysis feature of the OMNIC software. Given the number detected here and assuming a similar density of microplastics across the rest of the filter, some 300,000 microplastic particles could have been released from the gloves during the heat treatment. Figure 17b shows the SERS spectra for the nanoplastics detected from the 1 µL of centrifugally enriched filtered solution dropcasted onto ALF-IL.

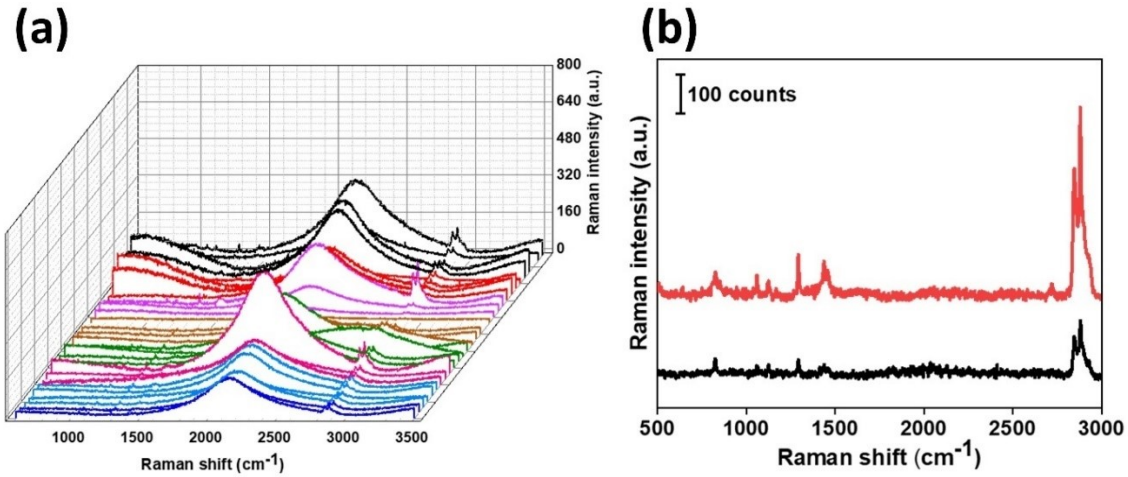

Figure 5.17: (a) Raman spectra for 30 particles detected on a small 10x10 $µm^2$ region of the Si filter with 1 µm sized pores that are indicative of polyethylene microplastics. (b) Spectra of nanoplastics detected from 1µL of the filtered (microplastic removed) and centrifugally enriched water containing only nanoplastics drop casted and air dried onto ALF-IL.

5.5 Conclusions

In summary, a methodology to form assemblies of gold nanoparticle (AuNP) fixed on solid surface as a homogeneous 3D SERS substrate with well-defined hotspots, that has not been reported elsewhere previously, i.e. the combination of salinisation and CB[n] binding, to successfully demonstrate very efficient SERS detection of R6G and nanoplastics.

The main findings are the following:

1 A pre-treatment step, consisting of annealing and etching, prior to the salinisation of aluminium foil and immersion in a colloid of gold nanoparticles for use as a SERS substrate, results in greater salinisation and thus a denser coverage of AuNPs.

2 As the distance between any two adjacent AuNPs linked by a cucurbit[n] (CB[n]) molecule is equidistant, salinisation and cucurbit binding have been novely used together to form solid surface immobilsed AuNP 3D nanostructures resulting in well-defined hotspots of a fixed size, and thus a homogenous SERS substrate for very stable and reproducible SERS signal.

3 The AuNP 3D nanostructure based SERS substrate efficiently detects low concentrations of 1 μg/mL of 50 nm and 100 nm PS nanoplastics.

4 The novel 3D SERS substate was used to demonstrate the release of micro and nanoplastics from food preparation polyethylene gloves within a study that mimicked the heat treatment they would receive in use.

Chapter Six

Summary and Future work

6.1 Summary

Within this monograph, Chapter 1 identified that little is known about NPs, and the significant risk to humanity that they are expected to have, due to limitations in analytical technologies, of which SERS is the most promising. Thereafter, in Chapter 2, after introducing SERS, and the principle of Raman scattering upon which it is based, the importance of well-designed substrates for SERS was presented before the state of art in their application in SERS for the low cost and reliable detection of low concentrations of nanoplastics in water concluded the chapter. Subsequently, the following three chapters reported the development and application of various novel SERS substrates, based on the ordered assemblies of (closely packed) AuNPs, through three different methodologies to overcome the state of art.

6.1.1 A comparison of the novel SERS substrates and their performance for NP detection

With a demand for substrates that produce reliable SERS signals, thereby negating the use of colloidal AuNPs with their freely moving nanoparticles, Chapter 3 presented a novel methodology based on the NaCl assisted aggregation of AuNPs around nanoplastics in suspension to immobilise them within the hotspots formed between the aggregated metal nanoparticles. After filtering the material to ensure a stable SERS signal, an ultra-low concentration (0.5 μg/mL) of 50 nm and 100 nm PS nanoplastics was. The applicability of the methodology for the detection of nanoplastics in real world samples was demonstrated through the achievement of very high recovery rates of >94% for nanoplastic 'spiked' drinking water. That with said, repeatability could not be demonstrated over large areas due to inhomogeneities in the AuNPs assemblies over long scale lengths due to uncontrolled aggregation caused by the NaCl.

Chapter 4 thus showed, in a previously unexplored approach, how a more controlled assembly of AuNPs over large areas could be achieved through the clustering that they undergo on contact with a hydrophobic surface, namely aluminium foil (ALF) that had been modified to form hydrophobic aluminium foil (ALF-HB). A comparison of rhodamine 6G (R6G) detection on SERS substrates of AuNP drop cast onto ALF (ALF@AuNP) versus those of AuNPs drop cast onto ALF-HB (ALF-HB@AuNP) showed a two orders of magnitude better limit of detection (LoD) of 10^{-11} M for the latter due to the clustering caused by its hydrophobicity. Mapping and scatter plots for the R6G data show high

reliability with CV% of 14.5%. Whilst the ALF-HB@AuNP could only demonstrate a LoD for 50 nm and 100 nm PS nanoplastics down to twice that for the salt assisted aggregation of AuNPs, i.e. 1 µg/mL, the latter was done with 475 and 25-times greater volumes of AuNPs and nanoplastic suspensions, respectively. Intuitively, higher volumes of AuNPs means more hotspots and greater volumes of nanoplastics means relatively higher chances of detection, therefore, the performance of ALF-HB@AuNPs can be considered as good as the aggregated nanopasticles. A ALF-HB substrate was then used to demonstrate the release/leaching of micro- and nanoplastics from insulated polystyrene cups into hot beverages.

Chapter 5 presented a unique approach for even greater control over the assembly of AuNPs based on the combined use of salinisation, to anchor a monolayer of AuNPs onto ALF, and CB[5] linking, to attach groups of AuNPs 0.91nm apart (the height of the CB[5] linker) to the monolayer of AuNPs to form a novel substrate of 3D islands of AuNPs on ALF forming ALF-IL. Subsequently hotspots are formed that are significantly better defined compared to those for the substrates reported in Chapters 3 and 4. Whilst both the LoD for R6G detection and 50 nm and 100 nm PS nanoplastics was identical to that for ALF-HB, a much better CV% of 4.7% was achieved demonstrating a more homogeneous behaviour from the ALF-IL. Substrates were then used to demonstrate the release of real-world nanoplastics from gloves used for food preparation.

Table 6.1: A comprehensive comparison for SERS substrates prepared from all three methodologies developed and presented in Chapters 3, 4 and 5 of this thesis: salt-assisted aggregation of AuNPs, AuNPs drop casted onto hydrophobic aluminium foil (ALF-HB) and aluminium foil with 3D gold nanoparticle geometry formed with the combination of salinisation and CB[5] linking (ALF-IL).

	Salt Aggregated AuNPs	**ALF-HB with AuNPs drop cast**	**ALF-IL**
LoD (R6G)	-	10^{-11} M	10^{-11} M
LoD (nanoplastics)	0.5 µg/mL	1 µg/mL	1 µg/mL
CV% (R6G)	-	14.5%	4.7%
Pristine nanoplastics detected	50 nm PS 100 nm PS	50 nm PS 100 nm PS	50 nm PS 100 nm PS
Real world nanoplastics detected	Spiked drinking water	Nanoplastics released from insulated hot cups	Nanoplastics released from gloves used for food preparation

Whilst Table 6.1 summarises the above, it should be noted that SERS signals were size independent for all nanoplastic measurements, that is hypothesised as being due to the amine modification by the manufacturer of the 50 nm, and not 100nm, PS which assists these smaller nanoplastics to attach better to the AuNPs.

6.1.2 A comparison of the novel SERS substrates and their performance for NP detection to others that have used the similar methodologies

Table 6.2 compiles details of the various substrates used for the SERS detection of nanoplastics, as reported in the literature, with detailed discussion in this subsection on the ones that have used similar methodologies to those presented in this monograph, for their comparison.

In contrast to the detection of 0.5 µg/mL of 50nm nanoplastics with NaCl aggregated AuNPs in Chapter 3, the first nanoplastic detection through salt-assisted aggregation of nanoparticles [160] used AgNPs aggregated through NaCl, but only down to 40 µg/mL and for 100nm NPs. Thereafter, whilst 50nm NPs were detected in other studies through the aggregation of AgNPs, using different aggregating agents such as magnesium sulphate (MgSO4) [268] and potassium iodide (KI) [269], the concentrations were at least hundred times higher than those from our work (see Table 6.2). Similarly, whilst smaller NPs have been detected, Mikac et al. [525] demonstrated the detection of 20 nm PS via sodium iodide (NaI) assisted aggregation of AgNPs, it was at LoD hundred times greater than that reported in Chapter 3. Other approaches, such as through the aggregation of AuNPs using three different salts, sodium nitrate (NaNO3), potassium chloride (KCl) and NaCl [269] could only demonstrate the detection of 350 nm PS nanoplastics, whilst non-spherical metal nanoparticles have also been used to detect nanoplastics, such as the aggregation of gold nanourchins (AuNUs) with NaCl, that could detect 600 nm nanoplastics [285].

Whilst hydrophobic SERS substrates have been employed previously for nanoplastic detection with LoD of 0.5 and 1 µg/mL achieved for 100 nm and 500 nm and PS, respectively [414]. Although the substrates in [414] achieved half the LoD for 100 nm nanoplastic, but the performance of the hydrophobic, ALF-HB@AuNP, substrate presented in Chapter 4 is also at par with demonstration of detection of 50 nm nanoplastics with the same LoD of 1 µg/mL achieved by [414] for nanoplastics 10 times bigger i.e. 500 nm. Moreover, the methodology adopted in [414] is a lengthy process taking around 12 hours more than that presented in Chapter 4.

Finally, the SERS substrate developed in Chapter 5, ALF-IL, is based on a novel methodology of combining salinisation and CB[5] that has not been reported before, and so a comparison is not possible. However, this in itself is what sets the ALF-IL apart from the rest of the substrates found in the field of nanoplastic detection.

In conclusion, compared to the state of art the SERS substrates presented in this thesis demonstrate better performance for the detection of low concentrations of 50 nm and 100 nm PS. Furthermore, the processes used to produce them are simple and cost-effective

that result in homogeneous SERS substrates that are suitable for detecting both pristine and real-world nanoplastics alike.

Table 6.2: A comprehensive comparison of the various substrates used for the SERS detection of nanoplastics as reported in the literature, including the type and size of detected nanoplastics, the matrix the detection was carried out in, the sample preparation method and the limit of detection (LoD) achieved.

SERS substrate	Plastic Type	Size	Matrix	Preparation Method	LoD	Ref
AgNP	PS, PE, PP	100 nm, 500 nm	Pure Water & Spiked seawater	Aggregation of AgNPs using NaCl; Detection in a liquid environment	40µg/mL	[160]
AgNP	PS	50 nm	Pure Water & Spiked river water	Aggregation of AgNPs using $MgSO_4$; Detection on silicon wafer	5µg/mL	[268]
AgNP	PS	50 – 500 nm	Pure Water & Spiked seawater	Aggregation of AgNPs using KI; Detection in a liquid environment	6.2µg/mL -	[269]
AuNP	PS	350 nm	Pure water	Aggregation of AuNPs using KCl/$NaNO_3$/NaCl; Detection in a liquid environment	6.5µg/ml	[182]
AuNU	PS	600 nm	Pure water	Aggregation of AuNUs using NaCl; Drying on aluminum foil	7×10^8 particle/mL	[285]
AgNP	PS	20 nm	Pure water & expanded PS box	Aggregation using NaI	5µg/mL	[525]
AgNP	PS	100 nm 500 nm	Pure water	Centrifugal enrichment combined with hydrophobic substrate	1µg/mL 0.5µg/mL	[414]
Klarite	PS, PMMA PMMA, PET	PS 360, 500 nm >360 nm >360 nm	Pure water & Atmospheric Aerosols	Drying on substrate Fiber filters for sampling; H_2O_2: for removal of organics; Drying on substrate	-	[264]
Self-assembled SiO sputtered with Ag	PS	100-1000 nm	Pure water & spiked bottled, tap, and river water	Drying on substrate	0.005µg/mL 5µg/mL	[286]
AAO-MoS_2-AgNP	PS	100-300 nm	Pure Water	Drying on substrate	-	[526]
AgNP	PS PMMA	500 nm 300 nm	Pure water	Mixed with Ag NPs Detection on silicon wafer	-	[527]
AuNP	PS	20 nm	Pure water	Mixed with AuNPs; Filter to filter paper	10µg/mL	[524]
Ag coated Au nanostars inside AAO	PS	400 nm	Pure water & spiked tap, river and sea water	Drying on substrate	50µg/mL	[528]
AuNP on glass slide	PS PET	161, 33 nm 62 nm	Pure Water	Drying on substrate	10µg/mL	[277]
AuNR on RC	PS	84, 630 nm	Pure Water	Filter onto RC	500µg/mL	[281]
AgNW on RC	PS	84, 630 nm	Pure Water	Filter onto RC	100µg/mL	[281]
AgNW on AAO cellulose	PS	50 nm	Pure water & expanded PS containers	Filter onto AAO cellulose	10^{-7} g/L	[284]

6.2 Future Work

Whilst Section 6.1 highlights the promising results achieved for AuNP based SERS substrates for the detection of low concentrations of 50 nm and 100 nm PS nanoplastics, several areas of interest remain unexplored for future work, broadly categorised within: (i) Nanoplastic type diversity, (ii) Substrate development and (ii) Instrumentation.

(i) **Nanoplastic type diversity**: Until recently, there was a dearth in the availability of commercial pristine nanoplastics with regards to types and sizes, limiting proof of concept work for the developed methodologies to the detection of 50 nm and 100 nm PS nanoplastics. Pristine nanoplastics of various sizes and plastic types are now much easier to find, therefore future work should continue by expanding the use of the developed methodologies on different nanoplastic types of much smaller sizes than 50 nm.

(ii) **Substrate development:** Whilst all work presented in this monograph was undertaken using spherical gold nanoparticles (AuNPs), the literature suggests that nanoparticles with sharp edges such as nanostars and nanourchins, can provide much lower LoDs. Therefore, it will be of interest to replace AuNPs within the developed methodologies with different sharp-edged nanostructures.

(iii) **Instrumentation:** The plasmon resonance peak wavelength depends on the size and shape of the metallic nanostructures providing the SERS enhancement and so the SERS signal can be maximized by matching the excitation source wavelength to that (Chapter 2). To that end a variable excitation wavelength is required and so a multiwavelength Raman spectrometer, with 532 nm, 785 nm and 1064 nm laser lines, has been designed (Figure 6.1) and is under construction (Table 6.3). Figure 6.2 shows preliminary Raman spectroscopy results at 532nm for random shaped polystyrene (PS), polyethylene terephthalate (PET), and polypropylene (PP) microplastic sheets.

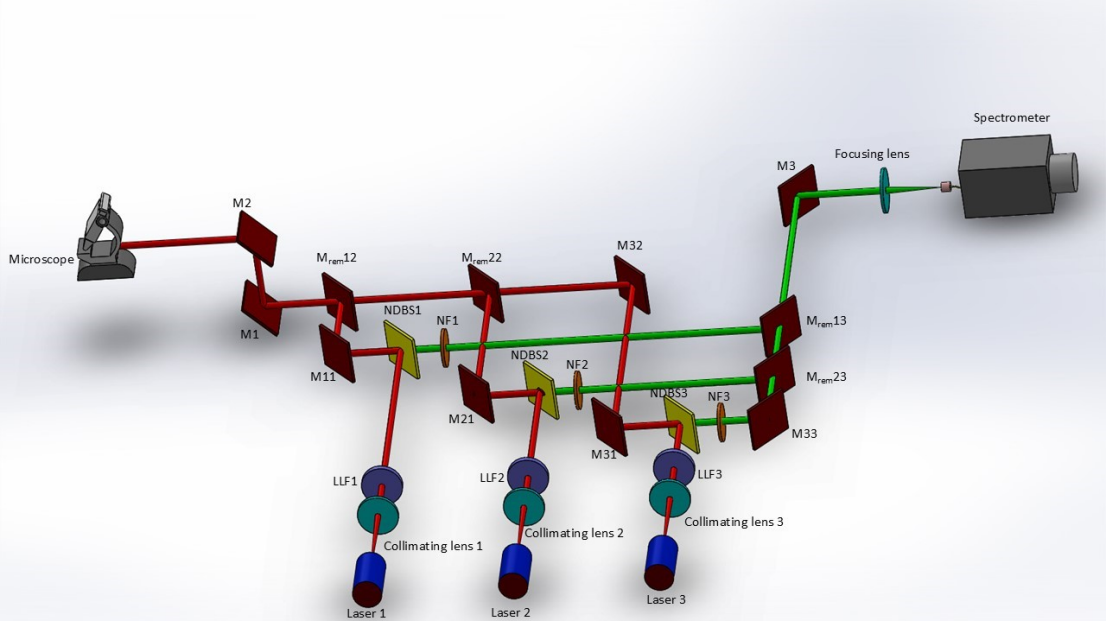

Figure 6.118: Illustration for the planned multi-wavelength Raman spectrometer with three laser lines.

Table 6.3: List of the components shown in the illustration (Figure 6.1) of the planned multi-wavelength Raman spectrometer with short description of the function of each component.

Component	Function
Laser 1, 2, 3	Excitation sources.
LLF 1,2,3	Laser line filters to remove lines apart from for the laser wavelength.
M 1, 2, 3, 11, 21, 31, 33	Fixed mirrors to direct the beam.
NDBS 1, 2, 3	Notch dichroic beam splitters to remove Rayleigh scattered signal and let only Raman scattered signal pass through.
NF 1, 2 ,3	Notch filters to remove any remaining Rayleigh scattering.
M_{rem} 12, 13, 22, 23 32	Removable mirrors which are removed or put in place according to the laser line in operation.

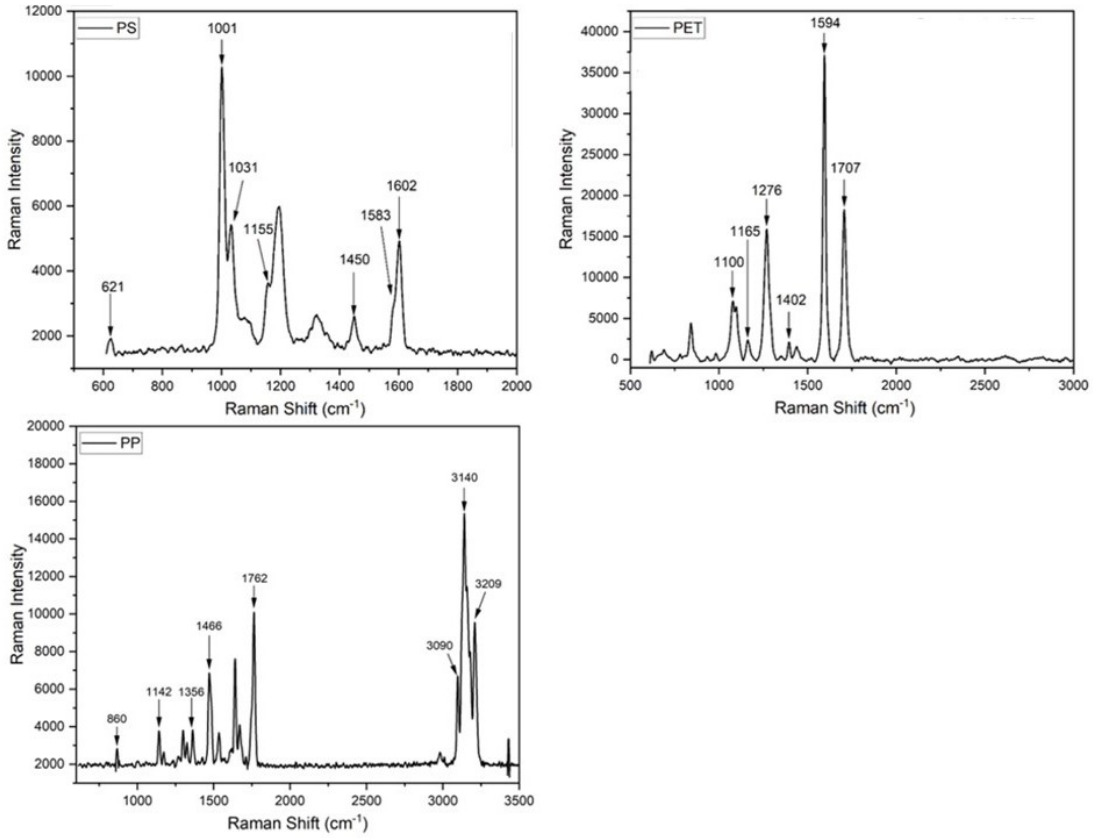

Figure 6.2: Raman spectrum detected using a 532 nm excitation laser source within a custom-built Raman spectrometer according to the illustration shown in Figure 6.1.

List of Publications

A. Bibi et al., “A review on state-of-the-art detection techniques for micro- and nano-plastics with prospective use in point-of-site detection,” in Comprehensive Analytical Chemistry, Elsevier, 2023. doi: 10.1016/bs.coac.2022.11.003. (Book Chapter)

A. Bibi, U. Pant, J. Tate, D. Hill, C. Cao, “SERS detection of nanoplastics in drinking water through the use of controlled agglomeration of gold nanoparticles,” in Sensors and Actuator B: Chemical (under review)

A. Bibi, J. Tate, U. Pant, D. Hill, C. Cao, Improving detection of nanoplastics in water through the use of a highly sensitive and cost-effective hydrophobic SERS substrate,” in Nanoscale (under review)

A. Iqrar, **A. Bibi**, C.M. Raghavan, D. Hill, A.G. Rozhin, Excitation-Emission Fluorescence Mapping Analysis of Microplastic that are typically pollutants,” in Heliyon (under review)

A. Bibi, C. Krafft, D. Hill, Polarised Raman spectroscopy of microplastic fibres,” in preparation for submission in 2024

A. Bibi, J. Tate, U. Pant, D. Hill, C. Cao, Cost-effective detection of nanoplastics through the use of reproducible SERS substrates, based on 3D islands of aggregated gold nanoparticle pairs,” in preparation for submission in 2024

J. Tate, **A. Bibi**, D. Hill, C. Cao, Reliable detection across a wide range of applications through the use of SERS substrates based on gold nanoparticles on an omniphobic aluminium foil,” in preparation for submission in 2024

U. Pant, **A. Bibi**, J. Tate, D. Hill, C. Cao, Low-cost, flexible, and highly sensitive SERS-based detection platform for nanoplastics, in preparation for submission in 2024

A. Iqrar, A. Bibi, C.M. Raghavan, D. Hill, A.G. Rozhin, Intrinsic fluorescence analysis of ‘doped’ micro and nanoplastics in food samples valid through Raman spectroscopy, in preparation for submission in 2024

Conference Proceedings

A. Bibi, U. Pant, J. Tate, D. Hill, and C. Cao, "Salt-induced aggregation of gold nanoparticles for sensitive SERS-based detection of nanoplastics in water," in *Proc.SPIE*, Mar. 2023, p. 1243012. doi: 10.1117/12.2650251.

Oral Presentations

A. Bibi, D. Hill, C. Krafft, "A step towards the identification of non-pristine microplastics and their origins in environmental analysis through the novel application of polarised Raman spectroscopy," (Abstract submitted to SPIE Photonics West 2025)

A. Bibi, J. Tate, D. Hill, C. Cao, "Detection of nanoplastics through low-cost SERS substrates, based on 3D islands of aggregated gold nanoparticles on aluminum foil, for wide ranging applications," in Proceedings Volume PC12835, Optical Fibers and Sensors for Medical Diagnostics, Treatment, and Environmental Applications XXIV; PC128350P (2024) https://doi.org/10.1117/12.3011294] at SPIE Photonics West 2024

A. Bibi, J. Tate, D. Hill, C. Cao, "A highly sensitive SERS substrate for detection of nanoplastics in water," CLEO Europe: IR & Raman sensing, ISBN: 979-8-3503-4599-5] at CLEO Europe 2023

A. Bibi, D. Hill, "High throughput SERS measurements for detection of MNPs," at ICCE 2023

A. Bibi, U. Pant, J. Tate, D. Hill, C. Cao, "SERS based detection of nanoplastics in drinking water through the use of salt induced nanoparticle aggregation," at Micro2022, 2022

S. Atif Iqrar, **A. Bibi**, C-M. Raghavan, D. Hill, A. Rozhin, "Exploring the potential of photoluminescence spectroscopy for the detection of microplastics," at Micro2022, 2022

Poster Presentations

A. Bibi, J. Tate, D. Hill, C. Cao, "Hydrophobic SERS surface enabling sensitive detection of nanoplastics in water," at 33rd Anniversary World Congress on Biosensors, 2023

A. Bibi, U. Pant, J. Tate, D. Hill, C. Cao, "Salt-induced aggregation of gold nanoparticles for sensitive SERS-based detection of nanoplastics in water," at SPIE Photonics West 2023

References

[1] H. Millet, P. Vangheluwe, C. Block, A. Sevenster, L. Garcia, and R. Antonopoulos, “The Nature of Plastics and Their Societal Usage,” Nov. 2018, doi: 10.1039/9781788013314-00001.

[2] D. Hosler, S. L. Burkett, and M. J. Tarkanian, “Prehistoric polymers: Rubber processing in ancient Mesoamerica,” *Science*, vol. 284, no. 5422, pp. 1988–1991, Jun. 1999, doi: 10.1126/science.284.5422.1988.

[3] “A Brief History of the Invention of Plastics.” Accessed: Dec. 17, 2020. [Online]. Available: https://www.thoughtco.com/history-of-plastics-1992322

[4] N. Bacon, “Vulcanization of rubber,” *Journal of Physical Chemistry*, vol. 32, no. 6, pp. 801–828, 1928, doi: 10.1021/J150288A001/ASSET/J150288A001.FP.PNG_V03.

[5] “Alexander Parkes | British chemist | Britannica.” Accessed: Dec. 17, 2020. [Online]. Available: https://www.britannica.com/biography/Alexander-Parkes

[6] “The Age of Plastic: From Parkesine to pollution | Science Museum.” Accessed: Aug. 18, 2023. [Online]. Available: https://www.sciencemuseum.org.uk/objects-and-stories/chemistry/age-plastic-parkesine-pollution

[7] L. H. Baekeland, “Method of making insoluble products of phenol and formaldehyde,” *United States Patent Office*, p. 3, 1909.

[8] “A Brief History of PVC - Piper Plastics Corp.” Accessed: Dec. 14, 2020. [Online]. Available: https://www.piper-plastics.com/2017/03/27/a-brief-history-of-pvc/

[9] J. R. Wagner and S. B. Marks, “Introduction,” in *Multilayer Flexible Packaging*, Elsevier Inc., 2010, pp. 3–11. doi: 10.1016/B978-0-8155-2021-4.10001-2.

[10] R. Geyer, “A Brief History of Plastics,” in *Mare Plasticum - The Plastic Sea: Combatting Plastic Pollution Through Science and Art*, M. Streit-Bianchi, M. Cimadevila, and W. Trettnak, Eds., Cham: Springer International Publishing, 2020, pp. 31–47. doi: 10.1007/978-3-030-38945-1_2.

[11] J. N. Hahladakis, C. A. Velis, R. Weber, E. Iacovidou, and P. Purnell, “An overview of chemical additives present in plastics: Migration, release, fate and environmental impact during their use, disposal and recycling,” *Journal of Hazardous Materials*, vol. 344, pp. 179–199, Feb. 2018, doi: 10.1016/J.JHAZMAT.2017.10.014.

[12] B. P. Federation, “How Is Plastic Made? A Simple Step-By-Step Explanation,” British Plastics Federation. Accessed: Aug. 20, 2023. [Online]. Available: https://www.bpf.co.uk/plastipedia/how-is-plastic-made.aspx

[13] T. Keshavarz and I. Roy, “Polyhydroxyalkanoates: bioplastics with a green agenda,” *Current Opinion in Microbiology*, vol. 13, no. 3, pp. 321–326, Jun. 2010, doi: 10.1016/j.mib.2010.02.006.

[14] R. Geyer, “Chapter 2 - Production, use, and fate of synthetic polymers,” in *Plastic Waste and Recycling*, T. M. Letcher, Ed., Academic Press, 2020, pp. 13–32. doi: 10.1016/B978-0-12-817880-5.00002-5.

[15] “Global plastics production,” Our World in Data. Accessed: Aug. 28, 2023. [Online]. Available: https://ourworldindata.org/grapher/global-plastics-production

[16] Joseph Edward Alegado *et al.*, *Plastic Atlas Asia Edition: Facts and figures about the world of synthetic polymers*. Heinrich Boell Stiftung Hong Kong Office, Break Free From Pacific Asia Pacific, Institute for Global Environmental Strategies, 2021, p. 54 pages. Accessed: Aug. 28, 2023. [Online]. Available: https://www.iges.or.jp/en/pub/plastic-atlas-asia-edition-2021/en

[17] "Primary plastic production by polymer type, 2015." Accessed: Dec. 19, 2020. [Online]. Available: https://ourworldindata.org/grapher/plastic-production-polymer

[18] S. Freinkel, "A Brief History of Plastic's Conquest of the World," Scientific American. Accessed: Aug. 28, 2023. [Online]. Available: https://www.scientificamerican.com/article/a-brief-history-of-plastic-world-conquest/

[19] "Cumulative global production of plastics," Our World in Data. Accessed: Aug. 28, 2023. [Online]. Available: https://ourworldindata.org/grapher/cumulative-global-plastics

[20] "Plastics - the Facts 2021 • Plastics Europe," Plastics Europe. Accessed: Aug. 28, 2023. [Online]. Available: https://plasticseurope.org/knowledge-hub/plastics-the-facts-2021/

[21] Y. Sun, S. Liu, P. Wang, X. Jian, X. Liao, and W.-Q. Chen, "China's roadmap to plastic waste management and associated economic costs," *Journal of Environmental Management*, vol. 309, p. 114686, May 2022, doi: 10.1016/j.jenvman.2022.114686.

[22] "Plastics - the Facts 2022 • Plastics Europe," Plastics Europe. Accessed: Sep. 07, 2023. [Online]. Available: https://plasticseurope.org/knowledge-hub/plastics-the-facts-2022/

[23] L. T. Peiró, G. V. Méndez, and R. U. Ayres, "Material Flow Analysis of Scarce Metals: Sources, Functions, End-Uses and Aspects for Future Supply," *Environ. Sci. Technol.*, vol. 47, no. 6, pp. 2939–2947, Mar. 2013, doi: 10.1021/es301519c.

[24] A. L. Andrady and M. A. Neal, "Applications and societal benefits of plastics," *Philosophical Transactions of the Royal Society B: Biological Sciences*, vol. 364, no. 1526, pp. 1977–1984, Jul. 2009, doi: 10.1098/rstb.2008.0304.

[25] "Primary plastic production by industrial sector," Our World in Data. Accessed: Sep. 08, 2023. [Online]. Available: https://ourworldindata.org/grapher/plastic-production-by-sector

[26] R. Geyer, J. R. Jambeck, and K. L. Law, "Production, use, and fate of all plastics ever made," *Science Advances*, vol. 3, no. 7, p. e1700782, Jul. 2017, doi: 10.1126/sciadv.1700782.

[27] J. Kaushal, M. Khatri, and S. K. Arya, "Recent insight into enzymatic degradation of plastics prevalent in the environment: A mini - review," *Cleaner Engineering and Technology*, vol. 2, p. 100083, Jun. 2021, doi: 10.1016/j.clet.2021.100083.

[28] "Sustainability | Free Full-Text | Regenerative Textiles: A Framework for Future Materials Circularity in the Textile Value Chain." Accessed: Sep. 17, 2023. [Online]. Available: https://www.mdpi.com/2071-1050/13/24/13910

[29] "Mean product lifetime of plastic uses," Our World in Data. Accessed: Sep. 17, 2023. [Online]. Available: https://ourworldindata.org/grapher/mean-product-lifetime-plastic

[30] "Packaging waste statistics." Accessed: Sep. 17, 2023. [Online]. Available: https://ec.europa.eu/eurostat/statistics-explained/index.php?title=Packaging_waste_statistics

[31]“Plastic Atlas 2019 ✓ Download or order for free!” Accessed: Sep. 17, 2023. [Online]. Available: https://www.boell.de/en/plasticatlas

[32]“Plastic Plastic Facts & Figures,” Plastic Soup Foundation. Accessed: Sep. 18, 2023. [Online]. Available: https://www.plasticsoupfoundation.org/en/plastic-facts-and-figures/

[33]“Brand Audit 2020 | Brand Audit.” Accessed: Sep. 23, 2024. [Online]. Available: https://brandaudit.breakfreefromplastic.org/brand-audit-2020/

[34]“Visual Feature | Beat Plastic Pollution.” Accessed: Sep. 17, 2023. [Online]. Available: http://unep.org/interactive/beat-plastic-pollution/

[35]“Global plastic waste by disposal,” Our World in Data. Accessed: Aug. 28, 2023. [Online]. Available: https://ourworldindata.org/grapher/global-plastic-fate

[36]R. Geyer, B. Kuczenski, T. Zink, and A. Henderson, “Common Misconceptions about Recycling,” *Journal of Industrial Ecology*, vol. 20, no. 5, pp. 1010–1017, 2016, doi: 10.1111/jiec.12355.

[37]T. Zink and R. Geyer, “Material Recycling and the Myth of Landfill Diversion,” *Journal of Industrial Ecology*, vol. 23, no. 3, pp. 541–548, 2019, doi: 10.1111/jiec.12808.

[38]A. Bibi, U. Pant, J. Tate, D. Hill, and C. Cao, “Salt-induced aggregation of gold nanoparticles for sensitive SERS-based detection of nanoplastics in water,” in *Proc.SPIE*, Mar. 2023, p. 1243012. doi: 10.1117/12.2650251.

[39]E. J. Carpenter and K. L. Smith, “Plastics on the Sargasso sea surface,” *Science*, vol. 175, no. 4027, pp. 1240–1241, 1972, doi: 10.1126/science.175.4027.1240.

[40]D. Tamburini *et al.*, “A multi-scalar investigation of the colouring materials used in textile wrappings of Egyptian votive animal mummies,” *Heritage Science*, vol. 9, no. 1, pp. 1–26, Dec. 2021, doi: 10.1186/S40494-021-00585-2/FIGURES/9.

[41]J. B. Colton, B. R. Burns, and F. D. Knapp, “Plastic Particles in Surface Waters of the Northwestern Atlantic: The abundance, distribution, source, and significance of various types of plastics are discussed.,” *Science*, vol. 185, no. 4150, pp. 491–497, Aug. 1974, doi: 10.1126/science.185.4150.491.

[42]W. R. P. Bourne and M. J. Imber, “Plastic pellets collected by a prion on Gough Island, central South Atlantic ocean,” *Marine Pollution Bulletin*, vol. 13, no. 1, pp. 20–21, Jan. 1982, doi: 10.1016/0025-326X(82)90491-X.

[43]L. K. Blight and A. E. Burger, “Occurrence of plastic particles in seabirds from the eastern North Pacific,” *Marine Pollution Bulletin*, vol. 34, no. 5, pp. 323–325, May 1997, doi: 10.1016/S0025-326X(96)00095-1.

[44]A. Ragusa *et al.*, “Plasticenta: First evidence of microplastics in human placenta,” *Environment International*, vol. 146, p. 106274, 2021.

[45]A. A. Shah, F. Hasan, A. Hameed, and S. Ahmed, “Biological degradation of plastics: A comprehensive review,” *Biotechnology Advances*, vol. 26, no. 3, pp. 246–265, May 2008, doi: 10.1016/j.biotechadv.2007.12.005.

[46]T. RC *et al.*, “Lost at sea: where is all the plastic?,” *Science (New York, N.Y.)*, vol. 304, no. 5672, p. 838, May 2004, doi: 10.1126/SCIENCE.1094559.

[47] L. Lebreton *et al.*, “Evidence that the Great Pacific Garbage Patch is rapidly accumulating plastic,” *Scientific reports*, vol. 8, no. 1, pp. 1–15, 2018.

[48] A. A. Horton, A. Walton, D. J. Spurgeon, E. Lahive, and C. Svendsen, “Microplastics in freshwater and terrestrial environments: Evaluating the current understanding to identify the knowledge gaps and future research priorities,” *Science of the total environment*, vol. 586, pp. 127–141, 2017.

[49] M. Claessens, S. De Meester, L. Van Landuyt, K. De Clerck, and C. R. Janssen, “Occurrence and distribution of microplastics in marine sediments along the Belgian coast,” *Marine pollution bulletin*, vol. 62, no. 10, pp. 2199–2204, 2011.

[50] A. L. Andrady, “Microplastics in the marine environment,” *Marine pollution bulletin*, vol. 62, no. 8, pp. 1596–1605, 2011.

[51] M. Mahmoudi, I. Lynch, M. R. Ejtehadi, M. P. Monopoli, F. B. Bombelli, and S. Laurent, “Protein-nanoparticle interactions: Opportunities and challenges,” *Chemical Reviews*, vol. 111, no. 9, pp. 5610–5637, Sep. 2011, doi: 10.1021/CR100440G/ASSET/IMAGES/MEDIUM/CR-2010-00440G_0006.GIF.

[52] M. Cole, P. Lindeque, E. Fileman, C. Halsband, and T. S. Galloway, “The impact of polystyrene microplastics on feeding, function and fecundity in the marine copepod Calanus helgolandicus,” *Environmental Science and Technology*, vol. 49, no. 2, pp. 1130–1137, Jan. 2015, doi: 10.1021/ES504525U/ASSET/IMAGES/LARGE/ES-2014-04525U_0005.JPEG.

[53] “Small is different: a science perspective on the regulatory challenges of the nanoscale.,” Expert Panel on Nanotechnology., Council of Canadian Academies, 2008.

[54] I. S. O. Nanotechnologies—Terminology, “definitions for nano-objects—Nanoparticle, nanofibre and nanoplate,” *International Organization for Standardization*, 2008.

[55] S. C. on C. Products, “Opinion on safety of nanomaterials in cosmetic products,” *European Commission*, 2007.

[56] J. Coombs Obrien, L. Torrente-Murciano, D. Mattia, and J. L. Scott, “Continuous Production of Cellulose Microbeads via Membrane Emulsification,” *ACS Sustainable Chemistry and Engineering*, vol. 5, no. 7, pp. 5931–5939, Jul. 2017, doi: 10.1021/acssuschemeng.7b00662.

[57] “US9636845B2 - Method of manufacturing pet nurdles - Google Patents.” Accessed: Feb. 17, 2021. [Online]. Available: https://patents.google.com/patent/US9636845B2/en

[58] P. Wu *et al.*, “Environmental occurrences, fate, and impacts of microplastics,” *Ecotoxicology and environmental safety*, vol. 184, p. 109612, 2019.

[59] “Microplastics: sources, effects and solutions,” Topics | European Parliament. Accessed: Sep. 24, 2024. [Online]. Available: https://www.europarl.europa.eu/topics/en/article/20181116STO19217/microplastics-sources-effects-and-solutions

[60] “Microplastics - ECHA.” Accessed: Sep. 24, 2024. [Online]. Available: https://echa.europa.eu/hot-topics/microplastics

[61] A. Bibi *et al.*, “A review on state-of-the-art detection techniques for micro- and nano-plastics with prospective use in point-of-site detection,” in *Comprehensive Analytical Chemistry*, Elsevier, 2023. doi: 10.1016/bs.coac.2022.11.003.

[62] D. E. ; W. D. ; S. R. M. MacArthur, “The New Plastics Economy: Rethinking the future of plastics.” World Economic Forum, 2016. Accessed: Jul. 03, 2022. [Online]. Available: https://ellenmacarthurfoundation.org/the-new-plastics-economy-rethinking-the-future-of-plastics

[63] K. A. V. Zubris and B. K. Richards, “Synthetic fibers as an indicator of land application of sludge,” *Environmental pollution (Barking, Essex : 1987)*, vol. 138, no. 2, pp. 201–211, Nov. 2005, doi: 10.1016/J.ENVPOL.2005.04.013.

[64] M. C. Samolada and A. A. Zabaniotou, “Comparative assessment of municipal sewage sludge incineration, gasification and pyrolysis for a sustainable sludge-to-energy management in Greece,” *Waste management (New York, N.Y.)*, vol. 34, no. 2, pp. 411–420, Feb. 2014, doi: 10.1016/J.WASMAN.2013.11.003.

[65] M. Malinconico, Ed., “Soil Degradable Bioplastics for a Sustainable Modern Agriculture,” 2017, doi: 10.1007/978-3-662-54130-2.

[66] C. M. Rochman *et al.*, “Scientific Evidence Supports a Ban on Microbeads,” *Environmental science & technology*, vol. 49, no. 18, pp. 10759–10761, Sep. 2015, doi: 10.1021/ACS.EST.5B03909.

[67] L. M. Hernandez, N. Yousefi, and N. Tufenkji, “Are There Nanoplastics in Your Personal Care Products?,” *Environ. Sci. Technol. Lett.*, vol. 4, no. 7, pp. 280–285, Jul. 2017, doi: 10.1021/acs.estlett.7b00187.

[68] M. Liu *et al.*, “Microplastic and mesoplastic pollution in farmland soils in suburbs of Shanghai, China,” *Environmental Pollution*, vol. 242, pp. 855–862, Nov. 2018, doi: 10.1016/J.ENVPOL.2018.07.051.

[69] W. SL and K. FJ, “Plastic and Human Health: A Micro Issue?,” *Environmental science & technology*, vol. 51, no. 12, pp. 6634–6647, Jun. 2017, doi: 10.1021/ACS.EST.7B00423.

[70] M. A. Browne, A. Dissanayake, T. S. Galloway, D. M. Lowe, and R. C. Thompson, “Ingested microscopic plastic translocates to the circulatory system of the mussel, Mytilus edulis (L.),” *Environmental Science and Technology*, vol. 42, no. 13, pp. 5026–5031, Jul. 2008, doi: 10.1021/ES800249A.

[71] H. A. Leslie, M. J. M. van Velzen, S. H. Brandsma, A. D. Vethaak, J. J. Garcia-Vallejo, and M. H. Lamoree, “Discovery and quantification of plastic particle pollution in human blood,” *Environment International*, vol. 163, p. 107199, May 2022, doi: 10.1016/J.ENVINT.2022.107199.

[72] M. Pirsaheb, H. Hossini, and P. Makhdoumi, “Review of microplastic occurrence and toxicological effects in marine environment: Experimental evidence of inflammation,” *Process Safety and Environmental Protection*, vol. 142, pp. 1–14, 2020, doi: 10.1016/j.psep.2020.05.050.

[73] L. G and L. E, “Non-pollen particulates in honey and sugar,” *Food additives & contaminants. Part A, Chemistry, analysis, control, exposure & risk assessment*, vol. 30, no. 12, pp. 2136–2140, 2013, doi: 10.1080/19440049.2013.843025.

[74] G. Liebezeit and E. Liebezeit, “Synthetic particles as contaminants in German beers,” *Food Additives & Contaminants: Part A*, vol. 31, no. 9, pp. 1574–1578, Sep. 2014, doi: 10.1080/19440049.2014.945099.

[75] A. Karami, A. Golieskardi, C. K. Choo, V. Larat, T. S. Galloway, and B. Salamatinia, “The presence of microplastics in commercial salts from different countries,” *SCIENTIFIC REPORTS*, vol. 7, Apr. 2017, doi: 10.1038/srep46173.

[76] E. B. Jadhav, M. S. Sankhla, R. A. Bhat, and D. S. Bhagat, “Microplastics from food packaging: An overview of human consumption, health threats, and alternative solutions,” *Environmental Nanotechnology, Monitoring & Management*, vol. 16, p. 100608, Dec. 2021, doi: 10.1016/j.enmm.2021.100608.

[77] J. Gasperi *et al.*, “Microplastics in air: Are we breathing it in?,” *Current Opinion in Environmental Science and Health*, vol. 1, pp. 1–5, Feb. 2018, doi: 10.1016/j.coesh.2017.10.002.

[78] A. Alfaro-Núñez *et al.*, “Microplastic pollution in seawater and marine organisms across the Tropical Eastern Pacific and Galápagos,” *Sci Rep*, vol. 11, no. 1, Art. no. 1, Mar. 2021, doi: 10.1038/s41598-021-85939-3.

[79] I. Peeken *et al.*, “Arctic sea ice is an important temporal sink and means of transport for microplastic,” *Nat Commun*, vol. 9, no. 1, Art. no. 1, Apr. 2018, doi: 10.1038/s41467-018-03825-5.

[80] M. Sajjad *et al.*, “Microplastics in the soil environment: A critical review,” *Environmental Technology & Innovation*, vol. 27, p. 102408, Aug. 2022, doi: 10.1016/j.eti.2022.102408.

[81] F. Wang, X. Feng, Y. Liu, C. A. Adams, Y. Sun, and S. Zhang, “Micro(nano)plastics and terrestrial plants: Up-to-date knowledge on uptake, translocation, and phytotoxicity,” *Resources, Conservation and Recycling*, vol. 185, p. 106503, Oct. 2022, doi: 10.1016/j.resconrec.2022.106503.

[82] K. Nanthini devi, P. Raju, P. Santhanam, and P. Perumal, “Impacts of microplastics on marine organisms: Present perspectives and the way forward,” *The Egyptian Journal of Aquatic Research*, vol. 48, no. 3, pp. 205–209, Sep. 2022, doi: 10.1016/j.ejar.2022.03.001.

[83] Y. Deng, Y. Zhang, B. Lemos, and H. Ren, “Tissue accumulation of microplastics in mice and biomarker responses suggest widespread health risks of exposure,” *Scientific Reports*, vol. 7, 2017, doi: 10.1038/srep46687.

[84] Y. Jin, L. Lu, W. Tu, T. Luo, and Z. Fu, “Impacts of polystyrene microplastic on the gut barrier, microbiota and metabolism of mice,” *Science of the Total Environment*, vol. 649, pp. 308–317, 2019, doi: 10.1016/j.scitotenv.2018.08.353.

[85] L. Lu, Z. Wan, T. Luo, Z. Fu, and Y. Jin, “Polystyrene microplastics induce gut microbiota dysbiosis and hepatic lipid metabolism disorder in mice,” *Science of the Total Environment*, vol. 631–632, pp. 449–458, 2018, doi: 10.1016/j.scitotenv.2018.03.051.

[86] A. P. Walczak *et al.*, “Bioavailability and biodistribution of differently charged polystyrene nanoparticles upon oral exposure in rats,” *Journal of Nanoparticle Research*, vol. 17, no. 5, pp. 1–13, May 2015, doi: 10.1007/S11051-015-3029-Y/TABLES/3.

[87] S. Jeon *et al.*, “The reactive oxygen species as pathogenic factors of fragmented microplastics to macrophages,” *Environmental Pollution*, vol. 281, p. 117006, Jul. 2021, doi: 10.1016/j.envpol.2021.117006.

[88] S. S *et al.*, “Nanoplastics Cause Neurobehavioral Impairments, Reproductive and Oxidative Damages, and Biomarker Responses in Zebrafish: Throwing up Alarms of Wide Spread Health Risk of Exposure,” *International journal of molecular sciences*, vol. 21, no. 4, Feb. 2020, doi: 10.3390/IJMS21041410.

[89] A. T. B. Guimarães *et al.*, “Toxicity of polystyrene nanoplastics in Ctenopharyngodon idella juveniles: A genotoxic, mutagenic and cytotoxic perspective,” *Science of The Total Environment*, vol. 752, p. 141937, Jan. 2021, doi: 10.1016/j.scitotenv.2020.141937.

[90] S. GF, P.-P. I, S. J, R. C, F. M, and B. D, “Cytotoxic effects of commonly used nanomaterials and microplastics on cerebral and epithelial human cells,” *Environmental research*, vol. 159, pp. 579–587, 2017, doi: 10.1016/J.ENVRES.2017.08.043.

[91] S. Liu, X. Wu, W. Gu, J. Yu, and B. Wu, “Influence of the digestive process on intestinal toxicity of polystyrene microplastics as determined by in vitro Caco-2 models,” *Chemosphere*, vol. 256, p. 127204, Oct. 2020, doi: 10.1016/j.chemosphere.2020.127204.

[92] S. Ballesteros, J. Domenech, I. Barguilla, C. Cortés, R. Marcos, and A. Hernández, “Genotoxic and immunomodulatory effects in human white blood cells after: Ex vivo exposure to polystyrene nanoplastics,” *Environmental Science: Nano*, vol. 7, no. 11, pp. 3431–3446, 2020, doi: 10.1039/d0en00748j.

[93] J. H *et al.*, “Polystyrene microplastics induced male reproductive toxicity in mice,” *Journal of hazardous materials*, vol. 401, Jan. 2021, doi: 10.1016/J.JHAZMAT.2020.123430.

[94] S. Chen *et al.*, “Interaction of particles with mucosae and cell membranes,” *Colloids and Surfaces B: Biointerfaces*, vol. 186, p. 110657, Feb. 2020, doi: 10.1016/J.COLSURFB.2019.110657.

[95] C. Q. Y. Yong, S. Valiyaveetill, and B. L. Tang, “Toxicity of microplastics and nanoplastics in Mammalian systems,” *International Journal of Environmental Research and Public Health*, vol. 17, no. 5, 2020, doi: 10.3390/ijerph17051509.

[96] Y.-F. Yang, C.-Y. Chen, T.-H. Lu, and C.-M. Liao, “Toxicity-based toxicokinetic/toxicodynamic assessment for bioaccumulation of polystyrene microplastics in mice,” *Journal of Hazardous Materials*, vol. 366, pp. 703–713, 2019, doi: 10.1016/j.jhazmat.2018.12.048.

[97] S. Liu *et al.*, “Size-dependent neurotoxicity of micro- and nanoplastics in flowing condition based on an in vitro microfluidic study,” *Chemosphere*, vol. 303, p. 135280, Sep. 2022, doi: 10.1016/J.CHEMOSPHERE.2022.135280.

[98] M. T. Ekvall, I. Gimskog, J. Hua, E. Kelpsiene, M. Lundqvist, and T. Cedervall, “Size fractionation of high-density polyethylene breakdown nanoplastics reveals different toxic response in Daphnia magna,” *Scientific Reports*, vol. 12, no. 1, Dec. 2022, doi: 10.1038/S41598-022-06991-1.

[99] O. Hollóczki and S. Gehrke, “Can Nanoplastics Alter Cell Membranes?,” *ChemPhysChem*, vol. 21, no. 1, pp. 9–12, 2020, doi: 10.1002/cphc.201900481.

[100] I. Velzeboer, C. J. A. F. Kwadijk, and A. A. Koelmans, “Strong Sorption of PCBs to Nanoplastics, Microplastics, Carbon Nanotubes, and Fullerenes,” *Environ. Sci. Technol.*, vol. 48, no. 9, pp. 4869–4876, May 2014, doi: 10.1021/es405721v.

[101] D. Brennecke, B. Duarte, F. Paiva, I. Caçador, and J. Canning-Clode, “Microplastics as vector for heavy metal contamination from the marine environment,” *Estuarine, Coastal and Shelf Science*, vol. 178, pp. 189–195, Sep. 2016, doi: 10.1016/j.ecss.2015.12.003.

[102] C.-B. Jeong *et al.*, “Nanoplastic Ingestion Enhances Toxicity of Persistent Organic Pollutants (POPs) in the Monogonont Rotifer Brachionus koreanus via Multixenobiotic Resistance (MXR) Disruption,” *Environ. Sci. Technol.*, vol. 52, no. 19, pp. 11411–11418, Oct. 2018, doi: 10.1021/acs.est.8b03211.

[103] L. Bradney *et al.*, “Particulate plastics as a vector for toxic trace-element uptake by aquatic and terrestrial organisms and human health risk,” *Environment International*, vol. 131, p. 104937, Oct. 2019, doi: 10.1016/j.envint.2019.104937.

[104] F. G. Torres, D. C. Dioses-Salinas, C. I. Pizarro-Ortega, and G. E. De-la-Torre, “Sorption of chemical contaminants on degradable and non-degradable microplastics: Recent progress and research trends,” *Science of The Total Environment*, vol. 757, p. 143875, Feb. 2021, doi: 10.1016/j.scitotenv.2020.143875.

[105] C. J. Pestana *et al.*, “Potentially Poisonous Plastic Particles: Microplastics as a Vector for Cyanobacterial Toxins Microcystin-LR and Microcystin-LF,” *Environ. Sci. Technol.*, vol. 55, no. 23, pp. 15940–15949, Dec. 2021, doi: 10.1021/acs.est.1c05796.

[106] J. R. Rochester, “Bisphenol A and human health: A review of the literature,” *Reproductive Toxicology*, vol. 42, pp. 132–155, Dec. 2013, doi: 10.1016/J.REPROTOX.2013.08.008.

[107] E. Molina and S. Benedé, “Is There Evidence of Health Risks From Exposure to Micro- and Nanoplastics in Foods?,” *Frontiers in Nutrition*, vol. 9, 2022, Accessed: Nov. 24, 2023. [Online]. Available: https://www.frontiersin.org/articles/10.3389/fnut.2022.910094

[108] J. P. da Costa, “Micro- and nanoplastics in the environment: Research and policymaking,” *Current Opinion in Environmental Science & Health*, vol. 1, pp. 12–16, Feb. 2018, doi: 10.1016/j.coesh.2017.11.002.

[109] C. Guerranti, T. Martellini, G. Perra, C. Scopetani, and A. Cincinelli, “Microplastics in cosmetics: Environmental issues and needs for global bans,” *Environmental Toxicology and Pharmacology*, vol. 68, pp. 75–79, 2019, doi: 10.1016/j.etap.2019.03.007.

[110] “California SB1422 | 2017-2018 | Regular Session,” LegiScan. Accessed: Sep. 24, 2024. [Online]. Available: https://legiscan.com/CA/text/SB1422/id/1821771

[111] “California SB1263 | 2017-2018 | Regular Session,” LegiScan. Accessed: Sep. 24, 2024. [Online]. Available: https://legiscan.com/CA/text/SB1263/id/1820639

[112] “Commission Regulation (EU) 2023/2055 - Restriction of microplastics intentionally added to products - European Commission.” Accessed: Sep. 24, 2024. [Online]. Available: https://single-market-economy.ec.europa.eu/commission-regulation-eu-20232055-restriction-microplastics-intentionally-added-products_en

[113] W. J. Shim, S. H. Hong, and S. E. Eo, “Identification methods in microplastic analysis: a review,” *Anal. Methods*, vol. 9, no. 9, pp. 1384–1391, Mar. 2017, doi: 10.1039/C6AY02558G.

[114] Y. K. Song *et al.*, “A comparison of microscopic and spectroscopic identification methods for analysis of microplastics in environmental samples,” *Mar Pollut Bull*, vol. 93, no. 1–2, pp. 202–209, Apr. 2015, doi: 10.1016/j.marpolbul.2015.01.015.

[115] R. Dris, J. Gasperi, M. Saad, C. Mirande, and B. Tassin, “Synthetic fibers in atmospheric fallout: A source of microplastics in the environment?,” *Marine Pollution Bulletin*, vol. 104, no. 1, pp. 290–293, Mar. 2016, doi: 10.1016/j.marpolbul.2016.01.006.

[116] J. Běhal *et al.*, “Toward an All-Optical Fingerprint of Synthetic and Natural Microplastic Fibers by Polarization-Sensitive Holographic Microscopy,” *ACS Photonics*, vol. 9, no. 2, pp. 694–705, Feb. 2022, doi: 10.1021/acsphotonics.1c01781.

[117] R. Molenaar, S. Chatterjee, B. Kamphuis, I. M. J. Segers-Nolten, M. M. A. E. Claessens, and C. Blum, “Nanoplastic sizes and numbers: quantification by single particle tracking,” *Environ. Sci.: Nano*, vol. 8, no. 3, pp. 723–730, Mar. 2021, doi: 10.1039/D0EN00951B.

[118] S. Dehghani, F. Moore, and R. Akhbarizadeh, “Microplastic pollution in deposited urban dust, Tehran metropolis, Iran,” *Environ Sci Pollut Res*, vol. 24, no. 25, pp. 20360–20371, Sep. 2017, doi: 10.1007/s11356-017-9674-1.

[119] W. Li, Y. Luo, and X. Pan, “Identification and Characterization Methods for Microplastics Basing on Spatial Imaging in Micro-/Nanoscales,” in *Microplastics in Terrestrial Environments: Emerging Contaminants and Major Challenges*, D. He and Y. Luo, Eds., in The Handbook of Environmental Chemistry. , Cham: Springer International Publishing, 2020, pp. 25–37. doi: 10.1007/698_2020_446.

[120] D. Li *et al.*, “Microplastic release from the degradation of polypropylene feeding bottles during infant formula preparation,” *Nat Food*, vol. 1, no. 11, Art. no. 11, Nov. 2020, doi: 10.1038/s43016-020-00171-y.

[121] C. Schwaferts, R. Niessner, M. Elsner, and N. P. Ivleva, “Methods for the analysis of submicrometer- and nanoplastic particles in the environment,” *TrAC Trends in Analytical Chemistry*, vol. 112, pp. 52–65, Mar. 2019, doi: 10.1016/j.trac.2018.12.014.

[122] A. Baruah, A. Sharma, S. Sharma, and R. Nagraik, “An insight into different microplastic detection methods,” *Int. J. Environ. Sci. Technol.*, vol. 19, no. 6, pp. 5721–5730, Jun. 2022, doi: 10.1007/s13762-021-03384-1.

[123] S. Morgana, B. Casentini, V. Tirelli, F. Grasso, and S. Amalfitano, “Fluorescence-based detection: A review of current and emerging techniques to unveil micro/ nanoplastics in environmental samples,” *TrAC Trends in Analytical Chemistry*, vol. 172, p. 117559, Mar. 2024, doi: 10.1016/j.trac.2024.117559.

[124] M. Majewsky, H. Bitter, E. Eiche, and H. Horn, “Determination of microplastic polyethylene (PE) and polypropylene (PP) in environmental samples using thermal analysis (TGA-DSC),” *Sci Total Environ*, vol. 568, pp. 507–511, Oct. 2016, doi: 10.1016/j.scitotenv.2016.06.017.

[125] S. Mariano, S. Tacconi, M. Fidaleo, M. Rossi, and L. Dini, “Micro and Nanoplastics Identification: Classic Methods and Innovative Detection Techniques,” *Frontiers in*

Toxicology, vol. 3, 2021, Accessed: Jun. 27, 2022. [Online]. Available: https://www.frontiersin.org/article/10.3389/ftox.2021.636640

[126] E. Duemichen, P. Eisentraut, C. G. Bannick, A.-K. Barthel, R. Senz, and U. Braun, "Fast identification of microplastics in complex environmental samples by a thermal degradation method," *CHEMOSPHERE*, vol. 174, pp. 572–584, May 2017, doi: 10.1016/j.chemosphere.2017.02.010.

[127] J. La Nasa, G. Biale, D. Fabbri, and F. Modugno, "A review on challenges and developments of analytical pyrolysis and other thermoanalytical techniques for the quali-quantitative determination of microplastics," *Journal of Analytical and Applied Pyrolysis*, vol. 149, p. 104841, Aug. 2020, doi: 10.1016/j.jaap.2020.104841.

[128] J. Caldwell *et al.*, "The micro-, submicron-, and nanoplastic hunt: A review of detection methods for plastic particles," *Chemosphere*, vol. 293, p. 133514, Apr. 2022, doi: 10.1016/j.chemosphere.2022.133514.

[129] M.-T. Nuelle, J. H. Dekiff, D. Remy, and E. Fries, "A new analytical approach for monitoring microplastics in marine sediments," *Environmental Pollution*, vol. 184, pp. 161–169, Jan. 2014, doi: 10.1016/j.envpol.2013.07.027.

[130] A. T. Halle *et al.*, "Nanoplastic in the {North} {Atlantic} {Subtropical} {Gyre}," *Environ. Sci. Technol.*, vol. 51, no. 23, pp. 13689–13697, Dec. 2017, doi: 10.1021/acs.est.7b03667.

[131] C. Goedecke *et al.*, "Evaluation of thermoanalytical methods equipped with evolved gas analysis for the detection of microplastic in environmental samples," *Journal of Analytical and Applied Pyrolysis*, vol. 152, p. 104961, Nov. 2020, doi: 10.1016/j.jaap.2020.104961.

[132] R. Becker, K. Altmann, T. Sommerfeld, and U. Braun, "Quantification of microplastics in a freshwater suspended organic matter using different thermoanalytical methods – outcome of an interlaboratory comparison," *Journal of Analytical and Applied Pyrolysis*, vol. 148, p. 104829, Jun. 2020, doi: 10.1016/j.jaap.2020.104829.

[133] L. K. Ncube, A. U. Ude, E. N. Ogunmuyiwa, R. Zulkifli, and I. N. Beas, "An Overview of Plastic Waste Generation and Management in Food Packaging Industries," *Recycling 2021, Vol. 6, Page 12*, vol. 6, no. 1, p. 12, Feb. 2021, doi: 10.3390/RECYCLING6010012.

[134] T. Hammond and R. S. Lehrle, "Pyrolysis-GLC applied to composition analysis, general characterisation and the detailed specification of polymers," *British Polymer Journal*, vol. 21, no. 1, pp. 23–30, 1989, doi: 10.1002/pi.4980210105.

[135] A. S. Tagg, M. Sapp, J. P. Harrison, and J. J. Ojeda, "Identification and Quantification of Microplastics in Wastewater Using Focal Plane Array-Based Reflectance Micro-FT-IR Imaging," *Anal. Chem.*, vol. 87, no. 12, pp. 6032–6040, Jun. 2015, doi: 10.1021/acs.analchem.5b00495.

[136] S. M. Mintenig, M. G. J. Löder, S. Primpke, and G. Gerdts, "Low numbers of microplastics detected in drinking water from ground water sources," *Science of The Total Environment*, vol. 648, pp. 631–635, Jan. 2019, doi: 10.1016/j.scitotenv.2018.08.178.

[137] D. Schymanski, C. Goldbeck, H.-U. Humpf, and P. Fürst, "Analysis of microplastics in water by micro-Raman spectroscopy: Release of plastic particles from different

packaging into mineral water," *Water Research*, vol. 129, pp. 154–162, Feb. 2018, doi: 10.1016/j.watres.2017.11.011.

[138] A.-K. Kniggendorf, C. Wetzel, and B. Roth, "Microplastics Detection in Streaming Tap Water with Raman Spectroscopy," *Sensors*, vol. 19, no. 8, Art. no. 8, Jan. 2019, doi: 10.3390/s19081839.

[139] L. M. Hernandez, E. G. Xu, H. C. E. Larsson, R. Tahara, V. B. Maisuria, and N. Tufenkji, "Plastic Teabags Release Billions of Microparticles and Nanoparticles into Tea," *Environ. Sci. Technol.*, vol. 53, no. 21, pp. 12300–12310, Nov. 2019, doi: 10.1021/acs.est.9b02540.

[140] M. Gniadek and A. Dąbrowska, "The marine nano- and microplastics characterisation by SEM-EDX: The potential of the method in comparison with various physical and chemical approaches," *Marine Pollution Bulletin*, vol. 148, pp. 210–216, Nov. 2019, doi: 10.1016/j.marpolbul.2019.07.067.

[141] J. Ornik *et al.*, "Could photoluminescence spectroscopy be an alternative technique for the detection of microplastics? First experiments using a 405 nm laser for excitation," *Appl. Phys. B*, vol. 126, no. 1, p. 15, Dec. 2019, doi: 10.1007/s00340-019-7360-3.

[142] S. Konde, J. Ornik, J. A. Prume, J. Taiber, and M. Koch, "Exploring the potential of photoluminescence spectroscopy in combination with Nile Red staining for microplastic detection," *Marine Pollution Bulletin*, vol. 159, p. 111475, Oct. 2020, doi: 10.1016/j.marpolbul.2020.111475.

[143] J. S. Hanvey, P. J. Lewis, J. L. Lavers, N. D. Crosbie, K. Pozo, and B. O. Clarke, "A review of analytical techniques for quantifying microplastics in sediments," *ANALYTICAL METHODS*, vol. 9, no. 9, pp. 1369–1383, Mar. 2017, doi: 10.1039/c6ay02707e.

[144] S. Veerasingam *et al.*, "Contributions of Fourier transform infrared spectroscopy in microplastic pollution research: A review," *Critical Reviews in Environmental Science and Technology*, vol. 0, no. 0, pp. 1–63, Aug. 2020, doi: 10.1080/10643389.2020.1807450.

[145] B. C. Smith, *Fundamentals of Fourier Transform Infrared Spectroscopy*. CRC Press, 2011.

[146] X. Wang, C. Li, K. Liu, L. Zhu, Z. Song, and D. Li, "Atmospheric microplastic over the South China Sea and East Indian Ocean: abundance, distribution and source," *Journal of Hazardous Materials*, vol. 389, p. 121846, May 2020, doi: 10.1016/j.jhazmat.2019.121846.

[147] M. Bergmann, S. Mützel, S. Primpke, M. B. Tekman, J. Trachsel, and G. Gerdts, "White and wonderful? Microplastics prevail in snow from the Alps to the Arctic," *Science Advances*, vol. 5, no. 8, p. eaax1157, Aug. 2019, doi: 10.1126/sciadv.aax1157.

[148] K. Szewc, B. Graca, and A. Dołęga, "Atmospheric deposition of microplastics in the coastal zone: Characteristics and relationship with meteorological factors," *Science of The Total Environment*, vol. 761, p. 143272, Mar. 2021, doi: 10.1016/j.scitotenv.2020.143272.

[149] "Plastic rain in protected areas of the United States." Accessed: Jun. 28, 2022. [Online]. Available: https://www.science.org/doi/10.1126/science.aaz5819

[150] S. Yukioka *et al.*, “Occurrence and characteristics of microplastics in surface road dust in Kusatsu (Japan), Da Nang (Vietnam), and Kathmandu (Nepal),” *Environmental Pollution*, vol. 256, p. 113447, Jan. 2020, doi: 10.1016/j.envpol.2019.113447.

[151] Q. Zhou, C. Tian, and Y. Luo, “Various forms and deposition fluxes of microplastics identified in the coastal urban atmosphere,” 2017, doi: 10.1360/N972017-00956.

[152] “Applications of ATR-FTIR spectroscopic imaging to biomedical samples - ScienceDirect.” Accessed: Sep. 25, 2024. [Online]. Available: https://www.sciencedirect.com/science/article/pii/S0005273606000630

[153] M. G. J. Löder and G. Gerdts, “Methodology Used for the Detection and Identification of Microplastics—A Critical Appraisal,” in *Marine Anthropogenic Litter*, M. Bergmann, L. Gutow, and M. Klages, Eds., Cham: Springer International Publishing, 2015, pp. 201–227. doi: 10.1007/978-3-319-16510-3_8.

[154] M. Cole *et al.*, “Microplastic Ingestion by Zooplankton,” *Environ. Sci. Technol.*, vol. 47, no. 12, pp. 6646–6655, Jun. 2013, doi: 10.1021/es400663f.

[155] R. Kiselev, I. W. Schie, S. Aškrabić, C. Krafft, and J. Popp, “Design and first applications of a flexible Raman micro-spectroscopic system for biological imaging,” *Biomedical Spectroscopy and Imaging*, vol. 5, no. 2, pp. 115–127, Jan. 2016, doi: 10.3233/BSI-160141.

[156] S. K. Majumder, M. D. Keller, F. I. Boulos, M. C. Kelley, and A. Mahadevan-Jansen, “Comparison of autofluorescence, diffuse reflectance, and Raman spectroscopy for breast tissue discrimination,” *JBO*, vol. 13, no. 5, p. 054009, Sep. 2008, doi: 10.1117/1.2975962.

[157] R. L. McCreery, M. Fleischmann, and P. Hendra, “Fiber optic probe for remote Raman spectrometry,” p. 3.

[158] B. Zhao, S. Feng, Y. Hu, S. Wang, and X. Lu, “Rapid determination of atrazine in apple juice using molecularly imprinted polymers coupled with gold nanoparticles-colorimetric/SERS dual chemosensor,” *Food Chemistry*, vol. 276, pp. 366–375, Mar. 2019, doi: 10.1016/j.foodchem.2018.10.036.

[159] P. K. Rai, V. Kumar, C. Sonne, S. S. Lee, R. J. C. Brown, and K.-H. Kim, “Progress, prospects, and challenges in standardization of sampling and analysis of micro- and nano-plastics in the environment,” *Journal of Cleaner Production*, vol. 325, p. 129321, Nov. 2021, doi: 10.1016/j.jclepro.2021.129321.

[160] L. Lv *et al.*, “In situ surface-enhanced Raman spectroscopy for detecting microplastics and nanoplastics in aquatic environments,” *Science of The Total Environment*, vol. 728, p. 138449, Aug. 2020, doi: 10.1016/j.scitotenv.2020.138449.

[161] W. T. Mason, *Fluorescent and luminescent probes for biological activity: a practical guide to technology for quantitative real-time analysis*. Elsevier, 1999.

[162] “Introduction to Raman Spectroscopy techniques,” Oxford Instruments. Accessed: May 21, 2021. [Online]. Available: https://andor.oxinst.com/learning/view/article/raman-spectroscopy

[163] C. Marcott, M. Padalkar, and N. Pleshko, “3.23 Infrared and Raman Microscopy and Imaging of Biomaterials at the Micro and Nano Scale☆,” in *Comprehensive Biomaterials*

II, P. Ducheyne, Ed., Oxford: Elsevier, 2017, pp. 498–518. doi: 10.1016/B978-0-12-803581-8.10183-3.

[164] "Micro Raman Spectroscopy - Scientific Explanations." Accessed: Jan. 07, 2024. [Online]. Available: https://smacgigworld.com/blog/science-of-micro-raman-spectroscopy.php

[165] I. Chakraborty, S. Banik, R. Biswas, T. Yamamoto, H. Noothalapati, and N. Mazumder, "Raman spectroscopy for microplastic detection in water sources: a systematic review," *Int. J. Environ. Sci. Technol.*, vol. 20, no. 9, pp. 10435–10448, Sep. 2023, doi: 10.1007/s13762-022-04505-0.

[166] Granite, "Confocal Raman Microscopy | Confocal Microscope," Edinburgh Instruments. Accessed: Jan. 07, 2024. [Online]. Available: https://www.edinst.com/us/blog/what-is-confocal-raman-microscopy/

[167] G. Giridhar, R. R. K. N. Manepalli, and G. Apparao, "Chapter 7 - Confocal Raman Spectroscopy," in *Spectroscopic Methods for Nanomaterials Characterization*, S. Thomas, R. Thomas, A. K. Zachariah, and R. K. Mishra, Eds., in Micro and Nano Technologies. , Elsevier, 2017, pp. 141–161. doi: 10.1016/B978-0-323-46140-5.00007-8.

[168] E. B. Barros *et al.*, "Raman spectroscopy of graphitic foams," *Phys. Rev. B*, vol. 71, no. 16, p. 165422, Apr. 2005, doi: 10.1103/PhysRevB.71.165422.

[169] M. V. Schulmerich *et al.*, "Noninvasive Raman tomographic imaging of canine bone tissue," *JBO*, vol. 13, no. 2, p. 020506, Mar. 2008, doi: 10.1117/1.2904940.

[170] B. Schrader, A. Hoffmann, and S. Keller, "Near-infrared Fourier transform Raman spectroscopy: Facing absorption and background," *Spectrochimica Acta Part A: Molecular Spectroscopy*, vol. 47, no. 9, pp. 1135–1148, Jan. 1991, doi: 10.1016/0584-8539(91)80201-S.

[171] J. Johansson, A. Sparén, O. Svensson, S. Folestad, and M. Claybourn, "Quantitative Transmission Raman Spectroscopy of Pharmaceutical Tablets and Capsules," *Appl. Spectrosc., AS*, vol. 61, no. 11, pp. 1211–1218, Nov. 2007.

[172] P. Matousek *et al.*, "Subsurface Probing in Diffusely Scattering Media Using Spatially Offset Raman Spectroscopy," *Appl. Spectrosc., AS*, vol. 59, no. 4, pp. 393–400, Apr. 2005.

[173] "Noninvasive Raman Spectroscopy of Human Tissue in vivo - Pavel Matousek, Edward R. C. Draper, Allen E. Goodship, Ian P. Clark, Kate L. Ronayne, Anthony W. Parker, 2006." Accessed: Jul. 06, 2021. [Online]. Available: https://journals.sagepub.com/doi/abs/10.1366/000370206777886955?casa_token=EQpVY6Q_-xQAAAAA:cKzcDjUS2r2EMpbsjU93RJq17bSCBrSdZMRi1GPB48pCM8YOTshSxCOm9Xz5dd3WDFLEK5lZyH8rGQ

[174] N. Stone, R. Baker, K. Rogers, A. William Parker, and P. Matousek, "Subsurface probing of calcifications with spatially offset Raman spectroscopy (SORS): future possibilities for the diagnosis of breast cancer," *Analyst*, vol. 132, no. 9, pp. 899–905, 2007, doi: 10.1039/B705029A.

[175] S. Sil and S. Umapathy, “Raman spectroscopy explores molecular structural signatures of hidden materials in depth: Universal Multiple Angle Raman Spectroscopy,” *Sci Rep*, vol. 4, no. 1, p. 5308, Jun. 2014, doi: 10.1038/srep05308.

[176] N. Kuhar, S. Sil, T. Verma, and S. Umapathy, “Challenges in application of Raman spectroscopy to biology and materials,” *RSC Advances*, vol. 8, no. 46, pp. 25888–25908, 2018, doi: 10.1039/C8RA04491K.

[177] S. Sil, R. Gautam, and S. Umapathy, “Space-Resolved Raman Spectroscopy Applications: From Single Cells to Tissues,” in *Encyclopedia of Analytical Chemistry*, American Cancer Society, 2018, pp. 1–25. doi: 10.1002/9780470027318.a9650.

[178] “Transmission Raman Spectroscopy (TRS) | Agilent.” Accessed: Jul. 06, 2021. [Online]. Available: https://www.agilent.com/en/product/molecular-spectroscopy/raman-spectroscopy/transmission-raman-spectroscopy

[179] P. Fredericks, “Forensic analysis of fibres by vibrational spectroscopy,” in *Infrared and Raman Spectroscopy in Forensic Science*, H. G. M. Edwards, J. M. Chalmers, and M. D. Hargreaves, Eds., United Kingdom: John Wiley & Sons, 2012, pp. 153–169. Accessed: Jul. 07, 2021. [Online]. Available: http://au.wiley.com/WileyCDA/WileyTitle/productCd-0470749067.html

[180] G. J. Puppels, J. H. F. Olminkhof, G. M. J. Segers-Nolten, C. Otto, F. F. M. de Mul, and J. Greve, “Laser irradiation and Raman spectroscopy of single living cells and chromosomes: Sample degradation occurs with 514.5 nm but not with 660 nm laser light,” *Experimental Cell Research*, vol. 195, no. 2, pp. 361–367, Aug. 1991, doi: 10.1016/0014-4827(91)90385-8.

[181] L. Zada *et al.*, “Fast microplastics identification with stimulated Raman scattering microscopy,” *JOURNAL OF RAMAN SPECTROSCOPY*, vol. 49, no. 7, SI, pp. 1136–1144, Jul. 2018, doi: 10.1002/jrs.5367.

[182] L. Mikac, I. Rigó, L. Himics, A. Tolić, M. Ivanda, and M. Veres, “Surface-enhanced Raman spectroscopy for the detection of microplastics,” *Applied Surface Science*, vol. 608, p. 155239, Jan. 2023, doi: 10.1016/j.apsusc.2022.155239.

[183] C. Grand, C. Scotté, É. Prado, M. El Rakwe, O. Fauvarque, and H. Rigneault, “Fast compressive Raman micro-spectroscopy to image and classify microplastics from natural marine environment,” *Environmental Technology & Innovation*, vol. 34, p. 103622, May 2024, doi: 10.1016/j.eti.2024.103622.

[184] M. Fleischmann, P. J. Hendra, and A. J. McQuillan, “Raman spectra of pyridine adsorbed at a silver electrode,” *Chemical Physics Letters*, vol. 26, no. 2, pp. 163–166, May 1974, doi: 10.1016/0009-2614(74)85388-1.

[185] J. Langer *et al.*, “Present and future of surface-enhanced Raman scattering,” *ACS Nano*, vol. 14, no. 1, pp. 28–117, Jan. 2020, doi: 10.1021/ACSNANO.9B04224/ASSET/IMAGES/LARGE/NN9B04224_0044.JPEG.

[186] D. L. Jeanmaire and R. P. Van Duyne, “Surface raman spectroelectrochemistry: Part I. Heterocyclic, aromatic, and aliphatic amines adsorbed on the anodized silver electrode,” *Journal of Electroanalytical Chemistry and Interfacial Electrochemistry*, vol. 84, no. 1, pp. 1–20, Nov. 1977, doi: 10.1016/S0022-0728(77)80224-6.

[187] M. G. Albrecht and J. A. Creighton, “Anomalously intense Raman spectra of pyridine at a silver electrode,” p. 3.

[188] “Probing Single Molecules and Single Nanoparticles by Surface-Enhanced Raman Scattering | Science.” Accessed: Jun. 25, 2021. [Online]. Available: https://science.sciencemag.org/content/275/5303/1102.abstract?casa_token=XjWrS83FnGoAAAAA:TTmFXP98zXSVLl86SVNz8OrRlKxc8Qsxx4T3DY5mUTlf3DHan43x0pPAyeKYqcMaQZN9Bv4JvfhkDj4

[189] K. Kneipp *et al.*, “Single Molecule Detection Using Surface-Enhanced Raman Scattering (SERS),” *Phys. Rev. Lett.*, vol. 78, no. 9, pp. 1667–1670, Mar. 1997, doi: 10.1103/PhysRevLett.78.1667.

[190] E. L. Ru and P. Etchegoin, *Principles of Surface-Enhanced Raman Spectroscopy: and Related Plasmonic Effects*. Elsevier, 2008.

[191] R. Shi, X. Liu, and Y. Ying, “Facing Challenges in Real-Life Application of Surface-Enhanced Raman Scattering (SERS): Design and Nanofabrication of SERS Substrates for Rapid Field Test of Food Contaminants,” *Journal of Agricultural and Food Chemistry*, vol. 66, Sep. 2017, doi: 10.1021/acs.jafc.7b03075.

[192] M. Moskovits, “Surface roughness and the enhanced intensity of Raman scattering by molecules adsorbed on metals,” *J. Chem. Phys.*, vol. 69, no. 9, pp. 4159–4161, Nov. 1978, doi: 10.1063/1.437095.

[193] “Localized Surface Plasmon Resonance Sensors | Chemical Reviews.” Accessed: Sep. 25, 2024. [Online]. Available: https://pubs.acs.org/doi/abs/10.1021/cr100313v

[194] K. Y. Kim, *Plasmonics: Principles and Applications*. BoD – Books on Demand, 2012.

[195] H. Xu, E. J. Bjerneld, M. Käll, and L. Börjesson, “Spectroscopy of Single Hemoglobin Molecules by Surface Enhanced Raman Scattering,” *Phys. Rev. Lett.*, vol. 83, no. 21, pp. 4357–4360, Nov. 1999, doi: 10.1103/PhysRevLett.83.4357.

[196] K. Li, M. I. Stockman, and D. J. Bergman, “Self-Similar Chain of Metal Nanospheres as an Efficient Nanolens,” *Phys. Rev. Lett.*, vol. 91, no. 22, p. 227402, Nov. 2003, doi: 10.1103/PhysRevLett.91.227402.

[197] “Light Concentration at the Nanometer Scale | The Journal of Physical Chemistry Letters.” Accessed: Jun. 30, 2021. [Online]. Available: https://pubs.acs.org/doi/abs/10.1021/jz100820m

[198] F. J. García-Vidal and J. B. Pendry, “Collective Theory for Surface Enhanced Raman Scattering,” *Phys. Rev. Lett.*, vol. 77, no. 6, pp. 1163–1166, Aug. 1996, doi: 10.1103/PhysRevLett.77.1163.

[199] S. Schiavi, M. Parmigiani, P. Galinetto, B. Albini, A. Taglietti, and G. Dacarro, “Plasmonic Nanomaterials for Micro- and Nanoplastics Detection,” *Applied Sciences*, vol. 13, no. 16, Art. no. 16, Jan. 2023, doi: 10.3390/app13169291.

[200] E. C. Le Ru, E. Blackie, M. Meyer, and P. G. Etchegoint, “Surface enhanced raman scattering enhancement factors: A comprehensive study,” *Journal of Physical Chemistry C*, vol. 111, no. 37, pp. 13794–13803, Sep. 2007, doi: 10.1021/jp0687908.

[201] S. Schlücker, *Surface Enhanced Raman Spectroscopy: Analytical, Biophysical and Life Science Applications*. John Wiley & Sons, 2011.

[202] X.-F. Zhang, Z.-G. Liu, W. Shen, and S. Gurunathan, “Silver Nanoparticles: Synthesis, Characterization, Properties, Applications, and Therapeutic Approaches,”

International Journal of Molecular Sciences, vol. 17, no. 9, Art. no. 9, Sep. 2016, doi: 10.3390/ijms17091534.

[203] C. Zhang, K. Lin, Y. Huang, and J. Zhang, “Graphene-Ag Hybrids on Laser-Textured Si Surface for SERS Detection,” *Sensors*, vol. 17, no. 7, Art. no. 7, Jul. 2017, doi: 10.3390/s17071462.

[204] “Highly Raman-Enhancing Substrates Based on Silver Nanoparticle Arrays with Tunable Sub-10 nm Gaps - Wang - 2006 - Advanced Materials - Wiley Online Library.” Accessed: Jul. 08, 2021. [Online]. Available: https://onlinelibrary.wiley.com/doi/abs/10.1002/adma.200501875

[205] J. M. McMahon, S. Li, L. K. Ausman, and G. C. Schatz, “Modeling the Effect of Small Gaps in Surface-Enhanced Raman Spectroscopy,” *J. Phys. Chem. C*, vol. 116, no. 2, pp. 1627–1637, Jan. 2012, doi: 10.1021/jp207661y.

[206] S. Abalde-Cela, P. Aldeanueva-Potel, C. Mateo-Mateo, L. Rodríguez-Lorenzo, R. A. Alvarez-Puebla, and L. M. Liz-Marzán, “Surface-enhanced Raman scattering biomedical applications of plasmonic colloidal particles,” *Journal of The Royal Society Interface*, vol. 7, no. suppl_4, pp. S435–S450, Aug. 2010, doi: 10.1098/rsif.2010.0125.focus.

[207] M. Moskovits, “Surface-enhanced Raman spectroscopy: a brief retrospective,” *Journal of Raman Spectroscopy*, vol. 36, no. 6–7, pp. 485–496, 2005, doi: 10.1002/jrs.1362.

[208] P. Pal *et al.*, “A generalized exponential relationship between the surface-enhanced Raman scattering (SERS) efficiency of gold/silver nanoisland arrangements and their non-dimensional interparticle distance/particle diameter ratio,” *Sensors and Actuators A: Physical*, vol. 314, p. 112225, Oct. 2020, doi: 10.1016/j.sna.2020.112225.

[209] “CMOS Technology.” Accessed: Sep. 25, 2024. [Online]. Available: https://www.nanowerk.com/The-Different-Types-of-Lithography-in-Nanotechnology.php

[210] A. Shiohara, Y. Wang, and L. M. Liz-Marzán, “Recent approaches toward creation of hot spots for SERS detection,” *Journal of Photochemistry and Photobiology C: Photochemistry Reviews*, vol. 21, pp. 2–25, 2014, doi: 10.1016/j.jphotochemrev.2014.09.001.

[211] Z. Ye, C. Li, Q. Chen, Y. Xu, and S. E. J. Bell, “Self-assembly of colloidal nanoparticles into 2D arrays at water–oil interfaces: rational construction of stable SERS substrates with accessible enhancing surfaces and tailored plasmonic response,” *Nanoscale*, vol. 13, no. 12, pp. 5937–5953, Apr. 2021, doi: 10.1039/D0NR08803J.

[212] P. A. Mosier-Boss, “Review of SERS Substrates for Chemical Sensing,” *Nanomaterials (Basel)*, vol. 7, no. 6, p. 142, Jun. 2017, doi: 10.3390/nano7060142.

[213] P. Šimáková, M. Procházka, and E. Kočišová, “SERS Microspectroscopy of Biomolecules on Dried Ag Colloidal Drops,” *Spectroscopy: An International Journal*, vol. 27, no. 5–6, pp. 449–453, Jul. 2012, doi: 10.1155/2012/393847.

[214] R. Pilot, R. Signorini, C. Durante, L. Orian, M. Bhamidipati, and L. Fabris, “A Review on Surface-Enhanced Raman Scattering,” *Biosensors*, vol. 9, no. 2, Art. no. 2, Jun. 2019, doi: 10.3390/bios9020057.

[215] H. Ko and V. V. Tsukruk, “Nanoparticle-Decorated Nanocanals for Surface-Enhanced Raman Scattering,” *Small*, vol. 4, no. 11, pp. 1980–1984, 2008, doi: 10.1002/smll.200800301.

[216] X. Zhao, M. Li, and Z. Xu, “Detection of Foodborne Pathogens by Surface Enhanced Raman Spectroscopy,” *Frontiers in Microbiology*, vol. 9, 2018, Accessed: Jan. 14, 2024. [Online]. Available: https://www.frontiersin.org/articles/10.3389/fmicb.2018.01236

[217] Y. Liu, H. Zhou, Z. Hu, G. Yu, D. Yang, and J. Zhao, “Label and label-free based surface-enhanced Raman scattering for pathogen bacteria detection: A review,” *Biosensors and Bioelectronics*, vol. 94, pp. 131–140, Aug. 2017, doi: 10.1016/j.bios.2017.02.032.

[218] “Enhancement of the Raman Signal,” in *Practical Raman Spectroscopy – An Introduction*, John Wiley & Sons, Ltd, 2013, pp. 47–60. doi: 10.1002/9781119961284.ch3.

[219] Z. Sobhani, X. Zhang, C. Gibson, R. Naidu, M. Megharaj, and C. Fang, “Identification and visualisation of microplastics/nanoplastics by Raman imaging (i): Down to 100 nm,” *WATER RESEARCH*, vol. 174, May 2020, doi: 10.1016/j.watres.2020.115658.

[220] L. Y. Vélez-Escamilla and F. F. Contreras-Torres, “Latest Advances and Developments to Detection of Micro- and Nanoplastics Using Surface-Enhanced Raman Spectroscopy,” *Particle & Particle Systems Characterization*, vol. 39, no. 3, p. 2100217, 2022, doi: 10.1002/ppsc.202100217.

[221] W. Fu, J. Min, W. Jiang, Y. Li, and W. Zhang, “Separation, characterization and identification of microplastics and nanoplastics in the environment,” *Science of The Total Environment*, vol. 721, p. 137561, Jun. 2020, doi: 10.1016/j.scitotenv.2020.137561.

[222] A. Cózar *et al.*, “Plastic debris in the open ocean,” *Proceedings of the National Academy of Sciences of the United States of America*, vol. 111, no. 28, pp. 10239–10244, Jul. 2014, doi: 10.1073/PNAS.1314705111/SUPPL_FILE/PNAS.1314705111.SAPP.PDF.

[223] Z. Salehi, S. H. Hashemi, and M. Flury, “Micro- and Mesoplastics in Farmlands with Different Irrigation Water Sources,” *Water Air Soil Pollut*, vol. 234, no. 4, p. 267, Apr. 2023, doi: 10.1007/s11270-023-06289-6.

[224] R. Pashaei *et al.*, “Assessing the Occurrence and Distribution of Microplastics in Surface Freshwater and Wastewaters of Latvia and Lithuania,” *Toxics*, vol. 11, no. 4, Art. no. 4, Apr. 2023, doi: 10.3390/toxics11040292.

[225] T. M. Karlsson *et al.*, “Screening for microplastics in sediment, water, marine invertebrates and fish: Method development and microplastic accumulation,” *MARINE POLLUTION BULLETIN*, vol. 122, no. 1–2, pp. 403–408, Sep. 2017, doi: 10.1016/j.marpolbul.2017.06.081.

[226] K. Chandrakanthan, M. P. Fraser, and P. Herckes, “Microplastics are ubiquitous and increasing in soil of a sprawling urban area, Phoenix (Arizona),” *Science of The Total Environment*, vol. 906, p. 167617, Jan. 2024, doi: 10.1016/j.scitotenv.2023.167617.

[227] L.-E. Tympa, K. Katsara, P. N. Moschou, G. Kenanakis, and V. M. Papadakis, “Do Microplastics Enter Our Food Chain Via Root Vegetables? A Raman Based Spectroscopic Study on Raphanus sativus,” *Materials*, vol. 14, no. 9, p. 2329, 2021.

[228] S. Ghosal, M. Chen, J. Wagner, Z.-M. Wang, and S. Wall, “Molecular identification of polymers and anthropogenic particles extracted from oceanic water and fish stomach - A Raman micro-spectroscopy study,” *ENVIRONMENTAL POLLUTION*, vol. 233, pp. 1113–1124, Feb. 2018, doi: 10.1016/j.envpol.2017.10.014.

[229] K. Katsara, G. Kenanakis, E. Alissandrakis, and V. M. Papadakis, “Honey Quality and Microplastic Migration from Food Packaging: A Potential Threat for Consumer Health?,” *Microplastics*, vol. 1, no. 3, Art. no. 3, Sep. 2022, doi: 10.3390/microplastics1030030.

[230] D. Mazumder, Md. F. B. Quader, S. Saha, Md. A. Islam, R. H. Sarker, and A. M. Chowdhury, “An investigation on the prevalence of microplastic in commercial and open pan salts obtained from Cox’s Bazar and Maheshkhali region of Bay of Bengal (Bangladesh),” *Food Science & Nutrition*, vol. 11, no. 9, pp. 5283–5295, 2023, doi: 10.1002/fsn3.3486.

[231] B. E. Oßmann, G. Sarau, S. W. Schmitt, H. Holtmannspötter, S. H. Christiansen, and W. Dicke, “Development of an optimal filter substrate for the identification of small microplastic particles in food by micro-Raman spectroscopy,” *Analytical and Bioanalytical Chemistry*, vol. 409, no. 16, pp. 4099–4109, 2017, doi: 10.1007/s00216-017-0358-y.

[232] J. C. Prata *et al.*, “Identification of microplastics in white wines capped with polyethylene stoppers using micro-Raman spectroscopy,” *FOOD CHEMISTRY*, vol. 331, Nov. 2020, doi: 10.1016/j.foodchem.2020.127323.

[233] A. Dąbrowska, M. Mielańczuk, and M. Syczewski, “The Raman spectroscopy and SEM/EDS investigation of the primary sources of microplastics from cosmetics available in Poland,” *Chemosphere*, vol. 308, p. 136407, Dec. 2022, doi: 10.1016/j.chemosphere.2022.136407.

[234] L. Montano *et al.*, “Raman Microspectroscopy evidence of microplastics in human semen,” *Science of The Total Environment*, vol. 901, p. 165922, Nov. 2023, doi: 10.1016/j.scitotenv.2023.165922.

[235] A. Ragusa *et al.*, “Raman Microspectroscopy Detection and Characterisation of Microplastics in Human Breastmilk,” *Polymers 2022, Vol. 14, Page 2700*, vol. 14, no. 13, p. 2700, Jun. 2022, doi: 10.3390/POLYM14132700.

[236] D. Wu *et al.*, “Pigment microparticles and microplastics found in human thrombi based on Raman spectral evidence,” *Journal of Advanced Research*, vol. 49, pp. 141–150, Jul. 2023, doi: 10.1016/j.jare.2022.09.004.

[237] R. Schmidt *et al.*, “Correlative SEM-Raman microscopy to reveal nanoplastics in complex environments,” *MICRON*, vol. 144, May 2021, doi: 10.1016/j.micron.2021.103034.

[238] C. F. Araujo, M. M. Nolasco, A. M. P. Ribeiro, and P. J. A. Ribeiro-Claro, “Identification of microplastics using Raman spectroscopy: Latest developments and future prospects,” *Water Research*, vol. 142, pp. 426–440, Oct. 2018, doi: 10.1016/j.watres.2018.05.060.

[239] H. K. Imhof, N. P. Ivleva, J. Schmid, R. Niessner, and C. Laforsch, “Contamination of beach sediments of a subalpine lake with microplastic particles,” *Current Biology*, vol. 23, no. 19, pp. R867–R868, Oct. 2013, doi: 10.1016/j.cub.2013.09.001.

[240] A. Dehaut *et al.*, “Microplastics in seafood: Benchmark protocol for their extraction and characterization,” *Environmental Pollution*, vol. 215, pp. 223–233, Aug. 2016, doi: 10.1016/j.envpol.2016.05.018.

[241] M. Cole, H. Webb, P. K. Lindeque, E. S. Fileman, C. Halsband, and T. S. Galloway, “Isolation of microplastics in biota-rich seawater samples and marine organisms,” *Sci Rep*, vol. 4, no. 1, Art. no. 1, Mar. 2014, doi: 10.1038/srep04528.

[242] K. Enders, R. Lenz, S. Beer, and C. A. Stedmon, “Extraction of microplastic from biota: recommended acidic digestion destroys common plastic polymers,” *ICES JOURNAL OF MARINE SCIENCE*, vol. 74, no. 1, pp. 326–331, 2017, doi: 10.1093/icesjms/fsw173.

[243] J. Zhao, H. Lui, D. I. McLean, and H. Zeng, “Automated Autofluorescence Background Subtraction Algorithm for Biomedical Raman Spectroscopy,” *Appl Spectrosc*, vol. 61, no. 11, pp. 1225–1232, Nov. 2007, doi: 10.1366/000370207782597003.

[244] “Automated Method for Subtraction of Fluorescence from Biological Raman Spectra - Chad A. Lieber, Anita Mahadevan-Jansen, 2003.” Accessed: Jan. 10, 2024. [Online]. Available: https://journals.sagepub.com/doi/abs/10.1366/00037020332255451 8?casa_token=BcbPgWP_HRQAAAAA:mwD7g9n1KhNOh234tFVy00s9reA4ULO_8dBgcld9xMk9OsSNp_uCufMr1GLi-LfREeuIDcs60UniVw&casa_token=ynkClhUZvNUAAAAA:k34ySdD5oKMH74KsaxBuz_y47JFvLrgYpq9A1sSZwJhOt3qjYZPdjgoRmzDJJ6BobIm7d7gR-0s7mQ

[245] M. T. Technology Andor, “Optimizing an EMCCD for Spectroscopy.” Accessed: Jan. 10, 2024. [Online]. Available: https://www.photonics.com/Articles/Optimizing_an_EMCCD_for_Spectroscopy/a31367

[246] P. R. Griffiths and E. V. Miseo, “Infrared and Raman Instrumentation for Mapping and Imaging,” in *Infrared and Raman Spectroscopic Imaging*, John Wiley & Sons, Ltd, 2014, pp. 1–56. doi: 10.1002/9783527678136.ch1.

[247] T. Dieing and O. Hollricher, “High-resolution, high-speed confocal Raman imaging,” *Vibrational Spectroscopy*, vol. 48, no. 1, pp. 22–27, Sep. 2008, doi: 10.1016/j.vibspec.2008.03.004.

[248] T. S. Galloway *et al.*, “Ecotoxicological assessment of nanoparticle-containing acrylic copolymer dispersions in fairy shrimp and zebrafish embryos,” *Environmental Science: Nano*, vol. 4, no. 10, pp. 1981–1997, 2017, doi: 10.1039/C7EN00385D.

[249] A. J. R. Watts, M. A. Urbina, R. Goodhead, J. Moger, C. Lewis, and T. S. Galloway, “Effect of Microplastic on the Gills of the Shore Crab Carcinus maenas,” *ENVIRONMENTAL SCIENCE \& TECHNOLOGY*, vol. 50, no. 10, pp. 5364–5369, May 2016, doi: 10.1021/acs.est.6b01187.

[250] W. J. Shim, Y. K. Song, S. H. Hong, and M. Jang, “Identification and quantification of microplastics using Nile Red staining,” *Marine Pollution Bulletin*, vol. 113, no. 1, pp. 469–476, Dec. 2016, doi: 10.1016/j.marpolbul.2016.10.049.

[251] T. Maes, R. Jessop, N. Wellner, K. Haupt, and A. G. Mayes, “A rapid-screening approach to detect and quantify microplastics based on fluorescent tagging with Nile Red,” *Sci Rep*, vol. 7, no. 1, Art. no. 1, Mar. 2017, doi: 10.1038/srep44501.

[252] G. Erni-Cassola, M. I. Gibson, R. C. Thompson, and J. A. Christie-Oleza, “Lost, but Found with Nile Red: A Novel Method for Detecting and Quantifying Small Microplastics (1 mm to 20 μm) in Environmental Samples,” *Environ. Sci. Technol.*, vol. 51, no. 23, pp. 13641–13648, Dec. 2017, doi: 10.1021/acs.est.7b04512.

[253] H. Kang, S. Park, B. Lee, J. Ahn, and S. Kim, “Modification of a Nile Red Staining Method for Microplastics Analysis: A Nile Red Plate Method,” *Water*, vol. 12, no. 11, Art. no. 11, Nov. 2020, doi: 10.3390/w12113251.

[254] G. Sancataldo *et al.*, “Identification of microplastics using 4-dimethylamino-4′-nitrostilbene solvatochromic fluorescence,” *Microscopy Research and Technique*, vol. 84, no. 12, pp. 2820–2831, 2021, doi: 10.1002/jemt.23841.

[255] A. M. Elert *et al.*, “Comparison of different methods for MP detection: What can we learn from them, and why asking the right question before measurements matters?,” *ENVIRONMENTAL POLLUTION*, vol. 231, no. 2, pp. 1256–1264, Dec. 2017, doi: 10.1016/j.envpol.2017.08.074.

[256] L. Frere *et al.*, “A semi-automated Raman micro-spectroscopy method for morphological and chemical characterizations of microplastic litter,” *MARINE POLLUTION BULLETIN*, vol. 113, no. 1–2, pp. 461–468, Dec. 2016, doi: 10.1016/j.marpolbul.2016.10.051.

[257] R. Lenz, K. Enders, C. A. Stedmon, D. M. A. Mackenzie, and T. G. Nielsen, “A critical assessment of visual identification of marine microplastic using Raman spectroscopy for analysis improvement,” *MARINE POLLUTION BULLETIN*, vol. 100, no. 1, pp. 82–91, Nov. 2015, doi: 10.1016/j.marpolbul.2015.09.026.

[258] S.-J. Yang *et al.*, “Rapid Identification of Microplastic Using Portable Raman System and Extra Trees Algorithm,” in *REAL-TIME PHOTONIC MEASUREMENTS, DATA MANAGEMENT, AND PROCESSING V*, Li, M and Jalali, B and Asghari, MH, Ed., in Proceedings of SPIE, vol. 11555. 1000 20TH ST, PO BOX 10, BELLINGHAM, WA 98227-0010 USA: SPIE; Chinese Opt Soc, 2020. doi: 10.1117/12.2573364.

[259] Y. Luo, R. Naidu, X. Zhang, and C. Fang, “Microplastics and nanoplastics released from a PPE mask under a simulated bushfire condition,” *Journal of Hazardous Materials*, vol. 439, p. 129621, Oct. 2022, doi: 10.1016/j.jhazmat.2022.129621.

[260] C. Fang, Z. Sobhani, X. Zhang, C. T. Gibson, Y. Tang, and R. Naidu, “Identification and visualisation of microplastics/ nanoplastics by Raman imaging (ii): Smaller than the diffraction limit of laser?,” *Water Research*, vol. 183, p. 116046, Sep. 2020, doi: 10.1016/j.watres.2020.116046.

[261] C. Fang *et al.*, “Identification and visualisation of microplastics / nanoplastics by Raman imaging (iii): algorithm to cross-check multi-images,” *Water Research*, vol. 194, p. 116913, Apr. 2021, doi: 10.1016/j.watres.2021.116913.

[262] N. H. Ly *et al.*, “Advanced microplastic monitoring using Raman spectroscopy with a combination of nanostructure-based substrates,” *Journal of Nanostructure in Chemistry 2022*, pp. 1–24, Jun. 2022, doi: 10.1007/S40097-022-00506-0.

[263] W. Pei, R. Hu, H. Liu, L. Wang, and Y. Lai, “Advanced Raman spectroscopy for nanoplastics analysis: Progress and perspective,” *TrAC Trends in Analytical Chemistry*, vol. 166, p. 117188, Sep. 2023, doi: 10.1016/j.trac.2023.117188.

[264] M. A. Tahir *et al.*, “Klarite as a label-free SERS-based assay: A promising approach for atmospheric bioaerosol detection,” *Analyst*, vol. 145, no. 1, pp. 277–285, Jan. 2020, doi: 10.1039/c9an01715a.

[265] G. Xu *et al.*, “Surface-Enhanced Raman Spectroscopy Facilitates the Detection of Microplastics <1 μm in the Environment,” *Environmental Science and Technology*, 2020, doi: 10.1021/acs.est.0c02317.

[266] D. Xu *et al.*, “A gold nanoparticle doped flexible substrate for microplastics SERS detection,” *Physical Chemistry Chemical Physics*, vol. 24, no. 19, pp. 12036–12042, May 2022, doi: 10.1039/D1CP05870C.

[267] J. Liu, G. Xu, X. Ruan, K. Li, and L. Zhang, “V-shaped substrate for surface and volume enhanced Raman spectroscopic analysis of microplastics,” *Front. Environ. Sci. Eng.*, vol. 16, no. 11, p. 143, Jun. 2022, doi: 10.1007/s11783-022-1578-8.

[268] X.-X. Zhou, R. Liu, L.-T. Hao, and J.-F. Liu, “Identification of polystyrene nanoplastics using surface enhanced Raman spectroscopy,” *Talanta*, vol. 221, p. 121552, Jan. 2021, doi: 10.1016/j.talanta.2020.121552.

[269] R. Hu, K. Zhang, W. Wang, L. Wei, and Y. Lai, “Quantitative and sensitive analysis of polystyrene nanoplastics down to 50 nm by surface-enhanced Raman spectroscopy in water,” *Journal of Hazardous Materials*, vol. 429, p. 128388, May 2022, doi: 10.1016/J.JHAZMAT.2022.128388.

[270] X. Sun *et al.*, “Toxicities of polystyrene nano- and microplastics toward marine bacterium Halomonas alkaliphila,” *Science of The Total Environment*, vol. 642, pp. 1378–1385, Nov. 2018, doi: 10.1016/j.scitotenv.2018.06.141.

[271] A. Bellingeri *et al.*, “Combined effects of nanoplastics and copper on the freshwater alga Raphidocelis subcapitata,” *Aquatic Toxicology*, vol. 210, pp. 179–187, May 2019, doi: 10.1016/j.aquatox.2019.02.022.

[272] R. Yin *et al.*, “Sensitive and rapid detection of trace microplastics concentrated through Au-nanoparticle-decorated sponge on the basis of surface-enhanced Raman spectroscopy,” *Environmental Advances*, vol. 5, p. 100096, Oct. 2021, doi: 10.1016/j.envadv.2021.100096.

[273] L. Liu *et al.*, “Highly Scalable, Wearable Surface-Enhanced Raman Spectroscopy,” *Advanced Optical Materials*, vol. 10, no. 17, p. 2200054, 2022, doi: 10.1002/adom.202200054.

[274] X. Lin *et al.*, “Rapid and simple detection of sodium thiocyanate in milk using surface-enhanced Raman spectroscopy based on silver aggregates,” *Journal of Raman Spectroscopy*, vol. 45, no. 2, pp. 162–167, 2014, doi: 10.1002/jrs.4436.

[275] “Fabrication and Application of Noble Metal Nanocomposites-Based Surface-Enhanced Raman Scattering Active Substrate - CNKI.” Accessed: Jan. 15, 2024. [Online]. Available: http://kns.cnki.net/kcms/detail/detail.aspx?doi=10.19756/j.issn.0253-3820.210897

[276] A. B. D. Nandiyanto, A. Suhendi, T. Ogi, T. Iwaki, and K. Okuyama, “Synthesis of additive-free cationic polystyrene particles with controllable size for hollow template applications,” *Colloids and Surfaces A: Physicochemical and Engineering Aspects*, vol. 396, pp. 96–105, Feb. 2012, doi: 10.1016/j.colsurfa.2011.12.048.

[277] J. Caldwell, P. Taladriz-Blanco, B. Rothen-Rutishauser, and A. Petri-Fink, “Detection of Sub-Micro- and Nanoplastic Particles on Gold Nanoparticle-Based Substrates through Surface-Enhanced Raman Scattering (SERS) Spectroscopy,” *Nanomaterials*, vol. 11, no. 5, Art. no. 5, May 2021, doi: 10.3390/nano11051149.

[278] J. Turkevich, P. C. Stevenson, and J. Hillier, “A study of the nucleation and growth processes in the synthesis of colloidal gold,” *Discuss. Faraday Soc.*, vol. 11, no. 0, pp. 55–75, Jan. 1951, doi: 10.1039/DF9511100055.

[279] K. R. Brown and M. J. Natan, “Hydroxylamine Seeding of Colloidal Au Nanoparticles in Solution and on Surfaces,” *Langmuir*, vol. 14, no. 4, pp. 726–728, Feb. 1998, doi: 10.1021/la970982u.

[280] N. D. Israelsen, C. Hanson, and E. Vargis, “Nanoparticle Properties and Synthesis Effects on Surface-Enhanced Raman Scattering Enhancement Factor: An Introduction,” *ScientificWorldJournal*, vol. 2015, p. 124582, 2015, doi: 10.1155/2015/124582.

[281] Y. Jeon *et al.*, “Detection of nanoplastics based on surface-enhanced Raman scattering with silver nanowire arrays on regenerated cellulose films,” *Carbohydrate Polymers*, vol. 272, p. 118470, Nov. 2021, doi: 10.1016/j.carbpol.2021.118470.

[282] M. Fan, F.-J. Lai, H.-L. Chou, W.-T. Lu, B.-J. Hwang, and A. G. Brolo, “Surface-enhanced Raman scattering (SERS) from Au:Ag bimetallic nanoparticles: the effect of the molecular probe,” *Chem. Sci.*, vol. 4, no. 1, pp. 509–515, Nov. 2012, doi: 10.1039/C2SC21191B.

[283] Z. Starowicz, R. Wojnarowska-Nowak, P. Ozga, and E. M. Sheregii, “The tuning of the plasmon resonance of the metal nanoparticles in terms of the SERS effect,” *Colloid Polym Sci*, vol. 296, no. 6, pp. 1029–1037, Jun. 2018, doi: 10.1007/s00396-018-4308-9.

[284] Q. Yang *et al.*, “Identification of Trace Polystyrene Nanoplastics Down to 50 nm by the Hyphenated Method of Filtration and Surface-Enhanced Raman Spectroscopy Based on Silver Nanowire Membranes,” *Environ. Sci. Technol.*, vol. 56, no. 15, pp. 10818–10828, Aug. 2022, doi: 10.1021/acs.est.2c02584.

[285] C.-H. Lee and J. K.-H. Fang, “The onset of surface-enhanced Raman scattering for single-particle detection of submicroplastics,” *Journal of Environmental Sciences*, vol. 121, pp. 58–64, Nov. 2022, doi: 10.1016/j.jes.2021.08.044.

[286] L. Chang *et al.*, “Environmental Science Nanowell-enhanced Raman spectroscopy enables the visualization and quantification of nanoplastics in the environment †,” 2022, doi: 10.1039/d1en00945a.

[287] V. Petrikaitė *et al.*, “Stability and SERS signal strength of laser-generated gold, silver, and bimetallic nanoparticles at different KCl concentrations,” *Heliyon*, vol. 10, no. 15, p. e34815, Aug. 2024, doi: 10.1016/j.heliyon.2024.e34815.

[288] T. Bora, “Recent Developments on Metal Nanoparticles for SERS Applications,” in *Noble and Precious Metals - Properties, Nanoscale Effects and Applications*, IntechOpen, 2017. doi: 10.5772/intechopen.71573.

[289] “Surface Plasmons and Surface Enhanced Raman Spectra of Aggregated and Alloyed Gold-Silver Nanoparticles - Fleger - 2009 - International Journal of Optics - Wiley Online Library.” Accessed: Sep. 19, 2024. [Online]. Available: https://onlinelibrary.wiley.com/doi/10.1155/2009/475941

[290] M. Wei, Q. Xiang, P. Wang, L. Chen, and M. Ren, “Ambivalent effects of dissolved organic matter on silver nanoparticles/silver ions transformation: A review,” *Journal of Hazardous Materials*, vol. 445, p. 130533, Mar. 2023, doi: 10.1016/j.jhazmat.2022.130533.

[291] C. M. Muntean *et al.*, “Gold vs. Silver Colloidal Nanoparticle Films for Optimized SERS Detection of Propranolol and Electrochemical-SERS Analyses,” *Biosensors (Basel)*, vol. 13, no. 5, p. 530, May 2023, doi: 10.3390/bios13050530.

[292] M. R. Kumalasari, R. Alfanaar, and A. S. Andreani, “Gold nanoparticles (AuNPs): A versatile material for biosensor application,” *Talanta Open*, vol. 9, p. 100327, Aug. 2024, doi: 10.1016/j.talo.2024.100327.

[293] M. R. Ivanov, H. R. Bednar, and A. J. Haes, “Investigations of the Mechanism of Gold Nanoparticle Stability and Surface Functionalization in Capillary Electrophoresis,” *ACS Nano*, vol. 3, no. 2, pp. 386–394, Feb. 2009, doi: 10.1021/nn8005619.

[294] “A Multidentate Peptide for Stabilization and Facile Bioconjugation of Gold Nanoparticles | Bioconjugate Chemistry.” Accessed: Sep. 18, 2024. [Online]. Available: https://pubs.acs.org/doi/full/10.1021/bc8003028?casa_token=wbqnXKEbeMkAAAAA%3ANQ2AMRMXHx2Qp3acAeVsUShX8TWsmLB-KyG0r3Emv2GPuIJlrgqOr7BApRyNlDweDGx7pDC2s96vbPVO

[295] W. C. W. Chan, *Bio-Applications of Nanoparticles*. Springer Science & Business Media, 2009.

[296] “Bionanoconjugation via Click Chemistry: The Creation of Functional Hybrids of Lipases and Gold Nanoparticles | Bioconjugate Chemistry.” Accessed: Sep. 18, 2024. [Online]. Available: https://pubs.acs.org/doi/full/10.1021/bc0601018?casa_token=b2Q1D_7EhO0AAAAA%3A4e3u33h4s5stA7kpJ_g4Y5kvkhwvTeZUamqxwjUXU8fIHfoBsIHJRwS06dSqsq4TyFgE-N9Z7hBUX0Fk

[297] “Synthesis, Characterization and Biocompatibility of a Multifunctional Gold Nanoparticle System for the Delivery of Single-Stranded RNA to Lymphocytes.” Accessed: Sep. 19, 2024. [Online]. Available: https://www.scielo.org.za/scielo.php?script=sci_arttext&pid=S0379-43502018000100001

[298] “Gold nanoparticles: Optical properties and implementations in cancer diagnosis and photothermal therapy - ScienceDirect.” Accessed: Sep. 16, 2024. [Online]. Available: https://www.sciencedirect.com/science/article/pii/S2090123210000056

[299] Y. Wu, M. R. K. Ali, K. Chen, N. Fang, and M. A. El-Sayed, “Gold nanoparticles in biological optical imaging,” *Nano Today*, vol. 24, pp. 120–140, Feb. 2019, doi: 10.1016/j.nantod.2018.12.006.

[300] K. Saha, S. S. Agasti, C. Kim, X. Li, and V. M. Rotello, “Gold Nanoparticles in Chemical and Biological Sensing,” *Chem. Rev.*, vol. 112, no. 5, pp. 2739–2779, May 2012, doi: 10.1021/cr2001178.

[301] F.-Y. Kong, J.-W. Zhang, R.-F. Li, Z.-X. Wang, W.-J. Wang, and W. Wang, “Unique Roles of Gold Nanoparticles in Drug Delivery, Targeting and Imaging Applications,” *Molecules*, vol. 22, no. 9, p. 1445, Aug. 2017, doi: 10.3390/molecules22091445.

[302] R. Wilson, “The use of gold nanoparticles in diagnostics and detection,” *Chem. Soc. Rev.*, vol. 37, no. 9, pp. 2028–2045, Aug. 2008, doi: 10.1039/B712179M.

[303] L. A. Austin, M. A. Mackey, E. C. Dreaden, and M. A. El-Sayed, “The optical, photothermal, and facile surface chemical properties of gold and silver nanoparticles in biodiagnostics, therapy, and drug delivery,” *Arch Toxicol*, vol. 88, no. 7, pp. 1391–1417, Jul. 2014, doi: 10.1007/s00204-014-1245-3.

[304] W. Chansuvarn, T. Tuntulani, and A. Imyim, “Colorimetric detection of mercury(II) based on gold nanoparticles, fluorescent gold nanoclusters and other gold-based nanomaterials,” *TrAC Trends in Analytical Chemistry*, vol. 65, pp. 83–96, Feb. 2015, doi: 10.1016/j.trac.2014.10.013.

[305] Y. Zhang, I. D. McKelvie, R. W. Cattrall, and S. D. Kolev, “Colorimetric detection based on localised surface plasmon resonance of gold nanoparticles: Merits, inherent shortcomings and future prospects,” *Talanta*, vol. 152, pp. 410–422, May 2016, doi: 10.1016/j.talanta.2016.02.015.

[306] G. FRENS, “Controlled Nucleation for the Regulation of the Particle Size in Monodisperse Gold Suspensions,” *Nature Physical Science 1973 241:105*, vol. 241, no. 105, pp. 20–22, Jan. 1973, doi: 10.1038/physci241020a0.

[307] Y.-C. Yeh, B. Creran, and V. M. Rotello, “Gold Nanoparticles: Preparation, Properties, and Applications in Bionanotechnology,” *Nanoscale*, vol. 4, no. 6, pp. 1871–1880, Mar. 2012, doi: 10.1039/c1nr11188d.

[308] M. Brust, M. Walker, D. Bethell, D. J. Schiffrin, and R. Whyman, “Synthesis of thiol-derivatised gold nanoparticles in a two-phase Liquid–Liquid system,” *Journal of the Chemical Society, Chemical Communications*, vol. 0, no. 7, pp. 801–802, 1994, doi: 10.1039/C39940000801.

[309] D. V. Leff, P. C. Ohara, J. R. Heath, and W. M. Gelbart, “Thermodynamic Control of Gold Nanocrystal Size: Experiment and Theory,” *J. Phys. Chem.*, vol. 99, no. 18, pp. 7036–7041, May 1995, doi: 10.1021/j100018a041.

[310] M. J. Hostetler *et al.*, “Alkanethiolate Gold Cluster Molecules with Core Diameters from 1.5 to 5.2 nm: Core and Monolayer Properties as a Function of Core Size,” *Langmuir*, vol. 14, no. 1, pp. 17–30, Jan. 1998, doi: 10.1021/la970588w.

[311] “Kinetic Stabilization of Growing Gold Clusters by Passivation with Thiolates | The Journal of Physical Chemistry B.” Accessed: Sep. 17, 2024. [Online]. Available: https://pubs.acs.org/doi/full/10.1021/jp062140m?casa_token=-RQ743QBvGEAAAAA%3AYFwdNUm3wtCqQDabyxgUxhq6YK8_hG2ghs7fLOGQxcIUJ2QKCg4qqAvjNHzq3md56b8GIPkgmYiVdmb-

[312] S. R. K. Perala and S. Kumar, “On the Mechanism of Metal Nanoparticle Synthesis in the Brust–Schiffrin Method,” *Langmuir*, vol. 29, no. 31, pp. 9863–9873, Aug. 2013, doi: 10.1021/la401604q.

[313] S. J. Amina and B. Guo, “A Review on the Synthesis and Functionalization of Gold Nanoparticles as a Drug Delivery Vehicle,” *International Journal of Nanomedicine*, Dec. 2020, Accessed: Sep. 19, 2024. [Online]. Available: https://www.tandfonline.com/doi/abs/10.2147/IJN.S279094

[314] P. Raveendran, J. Fu, and S. L. Wallen, “Completely ‘Green’ Synthesis and Stabilization of Metal Nanoparticles,” *J. Am. Chem. Soc.*, vol. 125, no. 46, pp. 13940–13941, Nov. 2003, doi: 10.1021/ja029267j.

[315] M. Navlani-García, D. Salinas-Torres, K. Mori, Y. Kuwahara, and H. Yamashita, “Tailoring the Size and Shape of Colloidal Noble Metal Nanocrystals as a Valuable Tool in Catalysis,” *Catal Surv Asia*, vol. 23, no. 3, pp. 127–148, Sep. 2019, doi: 10.1007/s10563-019-09271-7.

[316] “Full article: A Review on the Synthesis and Functionalization of Gold Nanoparticles as a Drug Delivery Vehicle.” Accessed: Sep. 19, 2024. [Online]. Available: https://www.tandfonline.com/doi/full/10.2147/IJN.S279094#d1e1170

[317] C. Lourenco, M. Teixeira, S. Simões, and R. Gaspar, “Steric stabilization of nanoparticles: Size and surface properties,” *International Journal of Pharmaceutics*, vol. 138, no. 1, pp. 1–12, Jul. 1996, doi: 10.1016/0378-5173(96)04486-9.

[318] L. Johnson, D. M. Gray, E. Niezabitowska, and T. O. McDonald, “Multi-stimuli-responsive aggregation of nanoparticles driven by the manipulation of colloidal stability,” *Nanoscale*, vol. 13, no. 17, pp. 7879–7896, 2021, doi: 10.1039/D1NR01190A.

[319] M. Zubair Iqbal, I. Ali, W. S. Khan, X. Kong, and E. Dempsey, “Reversible self-assembly of gold nanoparticles in response to external stimuli,” *Materials & Design*, vol. 205, p. 109694, Jul. 2021, doi: 10.1016/j.matdes.2021.109694.

[320] G. Sobczak, I. Misztalewska-Turkowicz, and V. Sashuk, “Photoswitching, Colloidal Stability, and Reversible Self-Assembly of Gold Nanoparticles Covered with Thiolated Donor–Acceptor Stenhouse Adducts,” *J. Phys. Chem. C*, vol. 125, no. 9, pp. 5306–5314, Mar. 2021, doi: 10.1021/acs.jpcc.0c10595.

[321] “Interactions between Natural Organic Matter and Gold Nanoparticles Stabilized with Different Organic Capping Agents | Environmental Science & Technology.” Accessed: Sep. 19, 2024. [Online]. Available: https://pubs.acs.org/doi/10.1021/es102603p

[322] “Gold nanoparticle-based colorimetric biosensors - Nanoscale (RSC Publishing) DOI:10.1039/C7NR06367A.” Accessed: Sep. 17, 2024. [Online]. Available: https://pubs.rsc.org/en/content/articlehtml/2017/sc/c7nr06367a?casa_token=WVM3oxLSeNMAAAAA:1JfBpYCf8o_jMdQBUnv5BGKisd5wiXPvaDDLED5bXJda8qWCMjECL4aYhPrjyvUmKpqI5O-5-izvZ0Q

[323] W. Zhao, M. A. Brook, and Y. Li, “Design of Gold Nanoparticle-Based Colorimetric Biosensing Assays,” *ChemBioChem*, vol. 9, no. 15, pp. 2363–2371, 2008, doi: 10.1002/cbic.200800282.

[324] K. Xing, H. Bao, N. Ding, Y. Xiong, J. Peng, and W. Lai, “Plasmonic gold nanoparticles aggregate based on charge neutralization for the convenient detection of fumonisin B1 by colorimetry and SERS,” *Food Control*, vol. 147, p. 109610, May 2023, doi: 10.1016/j.foodcont.2023.109610.

[325] Z. Shen, W. Baker, H. Ye, and Y. Li, “pH-Dependent aggregation and pH-independent cell membrane adhesion of monolayer-protected mixed charged gold nanoparticles,” *Nanoscale*, vol. 11, no. 15, pp. 7371–7385, Apr. 2019, doi: 10.1039/C8NR09617A.

[326] S. M. Louie, E. R. Spielman-Sun, M. J. Small, R. D. Tilton, and G. V. Lowry, “Correlation of the Physicochemical Properties of Natural Organic Matter Samples from Different Sources to Their Effects on Gold Nanoparticle Aggregation in Monovalent Electrolyte,” *Environ. Sci. Technol.*, vol. 49, no. 4, pp. 2188–2198, Feb. 2015, doi: 10.1021/es505003d.

[327] S. Christau, T. Moeller, J. Genzer, R. Koehler, and R. von Klitzing, “Salt-Induced Aggregation of Negatively Charged Gold Nanoparticles Confined in a Polymer Brush Matrix,” *Macromolecules*, vol. 50, no. 18, pp. 7333–7343, Sep. 2017, doi: 10.1021/acs.macromol.7b00866.

[328] I. Lázár and H. J. Szabó, “Prevention of the Aggregation of Nanoparticles during the Synthesis of Nanogold-Containing Silica Aerogels,” *Gels*, vol. 4, no. 2, p. 55, Jun. 2018, doi: 10.3390/gels4020055.

[329] Y. Yang, S. Matsubara, M. Nogami, and J. Shi, “Controlling the aggregation behavior of gold nanoparticles,” *Materials Science and Engineering: B*, vol. 140, no. 3, pp. 172–176, Jun. 2007, doi: 10.1016/j.mseb.2007.03.021.

[330] S. Schlücker, “SERS Microscopy: Nanoparticle Probes and Biomedical Applications,” *ChemPhysChem*, vol. 10, no. 9–10, pp. 1344–1354, 2009, doi: 10.1002/cphc.200900119.

[331] G. P. Szekeres and J. Kneipp, “SERS Probing of Proteins in Gold Nanoparticle Agglomerates,” *Frontiers in Chemistry*, vol. 7, 2019, Accessed: May 30, 2023. [Online]. Available: https://www.frontiersin.org/articles/10.3389/fchem.2019.00030

[332] “Unique Gold Nanoparticle Aggregates as a Highly Active Surface-Enhanced Raman Scattering Substrate | The Journal of Physical Chemistry B.” Accessed: Sep. 18, 2024. [Online]. Available: https://pubs.acs.org/doi/full/10.1021/jp048430p?casa_token=m_TTxdikNb4AAAAA%3ACarL1pRvquL7ylSpe-4_lllo5D3BHZbnf7AvV8HQ_hjFYo30Aadhj-VcPUb-ojCwdRY7fOtjL5Uv4aJK

[333] S. Hadano, H. Handa, K. Nagai, T. Iyoda, J. Li, and S. Watanabe, “Surface-enhanced Raman Scattering (SERS) Effect of Hexagonally Arranged Gold Nanoparticle Array with 29-nm Particles and 23-nm Gaps Using Liquid-crystalline Block-copolymer Template,” *Chemistry Letters*, vol. 42, no. 1, pp. 71–73, Jan. 2013, doi: 10.1246/cl.2013.71.

[334] “Materials | Free Full-Text | Optical Aggregation of Gold Nanoparticles for SERS Detection of Proteins and Toxins in Liquid Environment: Towards Ultrasensitive and Selective Detection.” Accessed: Sep. 18, 2024. [Online]. Available: https://www.mdpi.com/1996-1944/11/3/440

[335] K. Wang *et al.*, “SERS detection of thiram using polyacrylamide hydrogel-enclosed gold nanoparticle aggregates,” *Science of The Total Environment*, vol. 856, p. 159108, Jan. 2023, doi: 10.1016/j.scitotenv.2022.159108.

[336] M. J. Tan *et al.*, “Metal carbonyl-gold nanoparticle conjugates for highly sensitive SERS detection of organophosphorus pesticides,” *Biosensors and Bioelectronics*, vol. 96, pp. 167–172, Oct. 2017, doi: 10.1016/j.bios.2017.05.005.

[337] S. S. R. Dasary, A. K. Singh, D. Senapati, H. Yu, and P. C. Ray, “Gold Nanoparticle Based Label-Free SERS Probe for Ultrasensitive and Selective Detection of Trinitrotoluene,” *J. Am. Chem. Soc.*, vol. 131, no. 38, pp. 13806–13812, Sep. 2009, doi: 10.1021/ja905134d.

[338] “Integrating Deoxyribozymes into Colorimetric Sensing Platforms.” Accessed: Sep. 20, 2024. [Online]. Available: https://www.mdpi.com/1424-8220/16/12/2061

[339] L. Shen, J. A. Hagen, and I. Papautsky, “Point-of-care colorimetric detection with a smartphone,” *Lab on a Chip*, vol. 12, no. 21, pp. 4240–4243, 2012, doi: 10.1039/C2LC40741H.

[340] “Gold Nanoparticle-Based Colorimetric Strategies for Chemical and Biological Sensing Applications - PMC.” Accessed: Sep. 20, 2024. [Online]. Available: https://www.ncbi.nlm.nih.gov/pmc/articles/PMC6631916/

[341] K. Abels *et al.*, “Quantitative Point-of-Care Colorimetric Assay Modeling Using a Handheld Colorimeter,” *ACS Omega*, vol. 6, no. 34, pp. 22439–22446, Aug. 2021, doi: 10.1021/acsomega.1c03460.

[342] “A DNA-based method for rationally assembling nanoparticles into macroscopic materials | Nature.” Accessed: Sep. 18, 2024. [Online]. Available: https://www.nature.com/articles/382607a0

[343] “Colorimetric detection of DNA, small molecules, proteins, and ions using unmodified gold nanoparticles and conjugated polyelectrolytes | PNAS.” Accessed: Sep. 18, 2024. [Online]. Available: https://www.pnas.org/doi/full/10.1073/pnas.1005632107

[344] L. Liu, S. Li, L. Liu, D. Deng, and N. Xia, “Simple, sensitive and selective detection of dopamine using dithiobis(succinimidylpropionate)-modified gold nanoparticles as colorimetric probes,” *Analyst*, vol. 137, no. 16, pp. 3794–3799, Jul. 2012, doi: 10.1039/C2AN35734H.

[345] J. Liu and Y. Lu, “Fast Colorimetric Sensing of Adenosine and Cocaine Based on a General Sensor Design Involving Aptamers and Nanoparticles,” *Angewandte Chemie*, vol. 118, no. 1, pp. 96–100, 2006, doi: 10.1002/ange.200502589.

[346] “Amalgamated gold-nanoalloys with enhanced catalytic activity for the detection of mercury ions (Hg2+) in seawater samples | Nano Research.” Accessed: Sep. 18, 2024. [Online]. Available: https://link.springer.com/article/10.1007/s12274-020-2731-y

[347] J. Liu and Y. Lu, “A Colorimetric Lead Biosensor Using DNAzyme-Directed Assembly of Gold Nanoparticles,” *J. Am. Chem. Soc.*, vol. 125, no. 22, pp. 6642–6643, Jun. 2003, doi: 10.1021/ja034775u.

[348] “Enhancement the detection of Ni2+ and Zn2+ ions using nanostructure of synthesized dithiol surfactants with gold nanoparticles - ScienceDirect.” Accessed: Sep. 18, 2024. [Online]. Available: https://www.sciencedirect.com/science/article/pii/S1226086X14000239?casa_token=SfYUq0znDtwAAAAA:xZ5rTMX8y44kuIMgD7Vdo7dUNWYPNK23TLZ1k4vYhBsKIqEbgsJByWWpTWbSfhEpsif6uLbbuGY

[349] “Colorimetric Sensing of Silver(I) and Mercury(II) Ions Based on an Assembly of Tween 20-Stabilized Gold Nanoparticles | Analytical Chemistry.” Accessed: Sep. 18, 2024. [Online]. Available: https://pubs.acs.org/doi/10.1021/ac1007909

[350] N. Logan, C. Cao, S. Freitag, S. A. Haughey, R. Krska, and C. T. Elliott, “Advancing Mycotoxin Detection in Food and Feed: Novel Insights from Surface-Enhanced Raman Spectroscopy (SERS),” *Advanced Materials*, vol. 36, no. 15, p. 2309625, 2024, doi: 10.1002/adma.202309625.

[351] J. Li, B. Zheng, Z. Zheng, Y. Li, and J. Wang, “Highly sensitive and selective colorimetric and SERS dual-mode detection of arsenic (III) based on glutathione

functionalized gold nanoparticles," *Sensors and Actuators Reports*, vol. 2, no. 1, p. 100013, Nov. 2020, doi: 10.1016/j.snr.2020.100013.

[352] M. Li *et al.*, "A sensitive and simple competitive nanozyme-linked apta-sorbent assay for the dual-mode detection of ochratoxin A," *Analyst*, vol. 147, no. 10, pp. 2215–2222, 2022, doi: 10.1039/D1AN02335G.

[353] X. Liu *et al.*, "Non-linear responses via agglomeration and aggregation of gold nanoparticles for surface-enhanced Raman spectroscopy (SERS) coupled with chemometric analysis for chlorpyrifos detection," *Food Chemistry*, vol. 455, p. 139944, Oct. 2024, doi: 10.1016/j.foodchem.2024.139944.

[354] "Importance of Nanoparticle Size in Colorimetric and SERS-Based Multimodal Trace Detection of Ni(II) Ions with Functional Gold Nanoparticles - Krpetić - 2012 - Small - Wiley Online Library." Accessed: Sep. 18, 2024. [Online]. Available: https://onlinelibrary.wiley.com/doi/full/10.1002/smll.201101980

[355] B. Amanulla, K. N. Perumal, and S. K. Ramaraj, "Chitosan functionalized gold nanoparticles assembled on sulphur doped graphitic carbon nitride as a new platform for colorimetric detection of trace Hg2+," *Sensors and Actuators B: Chemical*, vol. 281, pp. 281–287, Feb. 2019, doi: 10.1016/j.snb.2018.10.039.

[356] "Two-step aggregation of gold nanoparticles based on charge neutralization for detection of melamine by colorimetric and surface-enhanced Raman spectroscopy platform - ScienceDirect." Accessed: Sep. 18, 2024. [Online]. Available: https://www.sciencedirect.com/science/article/pii/S0022030222003988

[357] R. Asapu *et al.*, "Plasmonic Near-Field Localization of Silver Core-Shell Nanoparticle Assemblies via Wet Chemistry Nanogap Engineering," *ACS Applied Materials and Interfaces*, vol. 9, no. 47, pp. 41577–41585, Nov. 2017, doi: 10.1021/ACSAMI.7B13965/SUPPL_FILE/AM7B13965_SI_001.PDF.

[358] X. Yang, Z. Zhou, J. Qi, S. Zhang, K. Guo, and S. Zhao, "Modeling and Theoretical Analysis of the SERS Enhancement Factor Considering the Electronic Structural Energy," *IEEE Access*, vol. 9, pp. 121279–121287, 2021, doi: 10.1109/ACCESS.2021.3107507.

[359] R. Chen and L. Jensen, "Interpreting chemical enhancements of surface-enhanced Raman scattering," *Chemical Physics Reviews*, vol. 4, no. 2, p. 021305, May 2023, doi: 10.1063/5.0138501.

[360] W. Haiss, N. T. K. Thanh, J. Aveyard, and D. G. Fernig, "Determination of size and concentration of gold nanoparticles from UV-Vis spectra," *Analytical Chemistry*, vol. 79, no. 11, pp. 4215–4221, Jun. 2007, doi: 10.1021/AC0702084/SUPPL_FILE/AC0702084SI20070321_014144.PDF.

[361] J.-A. Gu, Y.-J. Lin, Y.-M. Chia, H.-Y. Lin, and S.-T. Huang, "Colorimetric and bare-eye determination of fluoride using gold nanoparticle agglomeration probes," *Microchim Acta*, vol. 180, no. 9, pp. 801–806, Jul. 2013, doi: 10.1007/s00604-013-0972-0.

[362] W. Haiss, N. T. K. Thanh, J. Aveyard, and D. G. Fernig, "Determination of Size and Concentration of Gold Nanoparticles from UV−Vis Spectra," *Anal. Chem.*, vol. 79, no. 11, pp. 4215–4221, Jun. 2007, doi: 10.1021/ac0702084.

[363] J. M. Zook, R. I. MacCuspie, L. E. Locascio, M. D. Halter, and J. T. Elliott, "Stable nanoparticle aggregates/agglomerates of different sizes and the effect of their size on

hemolytic cytotoxicity," *Nanotoxicology*, vol. 5, no. 4, pp. 517–530, Dec. 2011, doi: 10.3109/17435390.2010.536615.

[364] A. P. Herrera, O. Resto, J. G. Briano, and C. Rinaldi, "Synthesis and agglomeration of gold nanoparticles in reverse micelles," *Nanotechnology*, vol. 16, no. 7, p. S618, Jun. 2005, doi: 10.1088/0957-4484/16/7/040.

[365] S. Yu *et al.*, "Aggregation kinetics of different surface-modified polystyrene nanoparticles in monovalent and divalent electrolytes," *Environmental Pollution*, vol. 255, p. 113302, Dec. 2019, doi: 10.1016/j.envpol.2019.113302.

[366] T. E. Bridges, M. P. Houlne, and J. M. Harris, "Spatially Resolved Analysis of Small Particles by Confocal Raman Microscopy: Depth Profiling and Optical Trapping," *Anal. Chem.*, vol. 76, no. 3, pp. 576–584, Feb. 2004, doi: 10.1021/ac034969s.

[367] "Polystyrene 50 nm latex beads | Sigma-Aldrich." Accessed: Jul. 04, 2024. [Online]. Available: https://www.sigmaaldrich.com/GB/en/search/polystyrene-50-nm-latex-beads?focus=products&page=1&perpage=30&sort=relevance&term=polystyrene%2050%20nm%20latex%20beads&type=product

[368] A. M. Donia, A. A. Atia, and K. Z. Elwakeel, "Gold(III) recovery using synthetic chelating resins with amine, thio and amine/mercaptan functionalities," *Separation and Purification Technology*, vol. 42, no. 2, pp. 111–116, Mar. 2005, doi: 10.1016/j.seppur.2004.06.009.

[369] Q. Hu, C. Sellers, J. S.-I. Kwon, and H.-J. Wu, "Integration of surface-enhanced Raman spectroscopy (SERS) and machine learning tools for coffee beverage classification," *Digital Chemical Engineering*, vol. 3, p. 100020, Jun. 2022, doi: 10.1016/j.dche.2022.100020.

[370] "Contact Angle Measurements and Wettability | Nanoscience Instruments." Accessed: Sep. 05, 2024. [Online]. Available: https://www.nanoscience.com/techniques/tensiometry/contact-angle-measurements-and-wettability/

[371] T. Huhtamäki, X. Tian, J. T. Korhonen, and R. H. A. Ras, "Surface-wetting characterization using contact-angle measurements," *Nat Protoc*, vol. 13, no. 7, pp. 1521–1538, Jul. 2018, doi: 10.1038/s41596-018-0003-z.

[372] Y. Guo and H. Zhao, "Femtosecond laser processed superhydrophobic surface," *Journal of Manufacturing Processes*, vol. 109, pp. 250–287, Jan. 2024, doi: 10.1016/j.jmapro.2023.12.005.

[373] S. Ghaffari, M. Aliofkhazraei, Gh. Barati Darband, A. Zakeri, and E. Ahmadi, "Review of superoleophobic surfaces: Evaluation, fabrication methods, and industrial applications," *Surfaces and Interfaces*, vol. 17, p. 100340, Dec. 2019, doi: 10.1016/j.surfin.2019.100340.

[374] I. M. Hauner, A. Deblais, J. K. Beattie, H. Kellay, and D. Bonn, "The Dynamic Surface Tension of Water," *J. Phys. Chem. Lett.*, vol. 8, no. 7, pp. 1599–1603, Apr. 2017, doi: 10.1021/acs.jpclett.7b00267.

[375] K.-Y. Law, "Definitions for Hydrophilicity, Hydrophobicity, and Superhydrophobicity: Getting the Basics Right," *J. Phys. Chem. Lett.*, vol. 5, no. 4, pp. 686–688, Feb. 2014, doi: 10.1021/jz402762h.

[376] C. Li, J. Zhang, J. Han, and B. Yao, “A numerical solution to the effects of surface roughness on water–coal contact angle,” *Sci Rep*, vol. 11, no. 1, p. 459, Jan. 2021, doi: 10.1038/s41598-020-80729-9.

[377] B. Majhy, R. Iqbal, and A. K. Sen, “Facile fabrication and mechanistic understanding of a transparent reversible superhydrophobic – superhydrophilic surface,” *Sci Rep*, vol. 8, no. 1, p. 18018, Dec. 2018, doi: 10.1038/s41598-018-37016-5.

[378] C. W. Extrand, “Criteria for ultralyophobic surfaces,” *Langmuir*, vol. 20, no. 12, pp. 5013–5018, Jun. 2004, doi: 10.1021/la036481s.

[379] K.-Y. Law, “Water–surface interactions and definitions for hydrophilicity, hydrophobicity and superhydrophobicity,” *Pure and Applied Chemistry*, vol. 87, no. 8, pp. 759–765, Aug. 2015, doi: 10.1515/pac-2014-1206.

[380] “Fabrication, Surface Properties, and Origin of Superoleophobicity for a Model Textured Surface | Langmuir.” Accessed: Sep. 11, 2024. [Online]. Available: https://pubs.acs.org/doi/10.1021/la104872q

[381] T. Darmanin and F. Guittard, “Superhydrophobic and superoleophobic properties in nature,” *Materials Today*, vol. 18, no. 5, pp. 273–285, Jun. 2015, doi: 10.1016/j.mattod.2015.01.001.

[382] S. Parvate, P. Dixit, and S. Chattopadhyay, “Superhydrophobic Surfaces: Insights from Theory and Experiment,” *J. Phys. Chem. B*, vol. 124, no. 8, pp. 1323–1360, Feb. 2020, doi: 10.1021/acs.jpcb.9b08567.

[383] I. J. Gresham and C. Neto, “Advances and challenges in slippery covalently-attached liquid surfaces,” *Advances in Colloid and Interface Science*, vol. 315, p. 102906, May 2023, doi: 10.1016/j.cis.2023.102906.

[384] C. Wang, R. Shao, G. Wang, and S. Sun, “Hierarchical hydrophobic surfaces with controlled dual transition between rose petal effect and lotus effect via structure tailoring or chemical modification,” *Colloids and Surfaces A: Physicochemical and Engineering Aspects*, vol. 622, p. 126661, Aug. 2021, doi: 10.1016/j.colsurfa.2021.126661.

[385] F. Peng, D. Zhang, X. Liu, and Y. Zhang, “Recent progress in superhydrophobic coating on Mg alloys: A general review,” *Journal of Magnesium and Alloys*, vol. 9, no. 5, pp. 1471–1486, Sep. 2021, doi: 10.1016/j.jma.2020.08.024.

[386] U. U. Ghosh, S. Nair, A. Das, R. Mukherjee, and S. DasGupta, “Replicating and resolving wetting and adhesion characteristics of a Rose petal,” *Colloids and Surfaces A: Physicochemical and Engineering Aspects*, vol. 561, pp. 9–17, Jan. 2019, doi: 10.1016/j.colsurfa.2018.10.028.

[387] M. Yang, “The application of coffee-ring effect in analytical chemistry - ScienceDirect.” Accessed: Jul. 30, 2024. [Online]. Available: https://www.sciencedirect.com/science/article/pii/S0165993622002357?casa_token=Gz1dhU9rBUAAAAAA:a-bbEOC9crHmGPI_lXSI2P6fZra0T8t3rPy4N_TlAUY8Xze5Zw1F5bKY9iPQ1P42pzN-92vSZiU

[388] C. Sun, S. Zhang, J. Wang, and F. Ge, “Enhancement of SERS performance using hydrophobic or superhydrophobic cotton fabrics,” *Surfaces and Interfaces*, vol. 28, p. 101616, Feb. 2022, doi: 10.1016/j.surfin.2021.101616.

[389] X. Ma *et al.*, “Hybrid superhydrophilic–superhydrophobic micro/nanostructures fabricated by femtosecond laser-induced forward transfer for sub-femtomolar Raman detection,” *Microsyst Nanoeng*, vol. 5, no. 1, pp. 1–10, Sep. 2019, doi: 10.1038/s41378-019-0090-1.

[390] T. Wang, L. Chang, S. Yang, Y. Jia, and C. Wong, “Hydrophobic properties of biomorphic carbon surfaces prepared by sintering lotus leaves,” *Ceramics International*, vol. 39, no. 7, pp. 8165–8172, Sep. 2013, doi: 10.1016/j.ceramint.2013.03.092.

[391] S. S. Latthe, C. Terashima, K. Nakata, and A. Fujishima, “Superhydrophobic Surfaces Developed by Mimicking Hierarchical Surface Morphology of Lotus Leaf,” *Molecules*, vol. 19, no. 4, pp. 4256–4283, Apr. 2014, doi: 10.3390/molecules19044256.

[392] H. J. Ensikat, P. Ditsche-Kuru, C. Neinhuis, and W. Barthlott, “Superhydrophobicity in perfection: the outstanding properties of the lotus leaf,” *Beilstein J Nanotechnol*, vol. 2, pp. 152–161, Mar. 2011, doi: 10.3762/bjnano.2.19.

[393] S. Agarwal, M. Gogoi, S. Talukdar, P. Bora, T. K. Basumatary, and N. N. Devi, “Green synthesis of silver nanoplates using the special category of plant leaves showing the lotus effect,” *RSC Adv*, vol. 10, no. 60, pp. 36686–36694, doi: 10.1039/d0ra06533a.

[394] L. Yao, P. Dai, L. Ouyang, and L. Zhu, “A sensitive and reproducible SERS sensor based on natural lotus leaf for paraquat detection,” *Microchemical Journal*, vol. 160, p. 105728, Jan. 2021, doi: 10.1016/J.MICROC.2020.105728.

[395] J. A. Huang, Y. L. Zhang, Y. Zhao, X. L. Zhang, M. L. Sun, and W. Zhang, “Superhydrophobic SERS chip based on a Ag coated natural taro-leaf,” *Nanoscale*, vol. 8, no. 22, pp. 11487–11493, Jun. 2016, doi: 10.1039/C6NR03285K.

[396] Y. Ebihara, R. Ota, T. Noriki, M. Shimojo, and K. Kajikawa, “Biometamaterials: Black Ultrathin Gold Film Fabricated on Lotus Leaf,” *Sci Rep*, vol. 5, no. 1, p. 15992, Nov. 2015, doi: 10.1038/srep15992.

[397] “Silver-Coated Rose Petal: Green, Facile, Low-Cost and Sustainable Fabrication of a SERS Substrate with Unique Superhydrophobicity and High Efficiency - Xu - 2013 - Advanced Optical Materials - Wiley Online Library.” Accessed: Sep. 10, 2024. [Online]. Available: https://onlinelibrary.wiley.com/doi/epdf/10.1002/adom.201200019

[398] D. Thanh Nguyen *et al.*, “Surface-enhanced Raman scattering (SERS) from low-cost silver nanoparticle-decorated cicada wing substrates for rapid detection of difenoconazole in potato,” *Spectrochimica Acta Part A: Molecular and Biomolecular Spectroscopy*, vol. 275, p. 121117, Jul. 2022, doi: 10.1016/j.saa.2022.121117.

[399] F. Yang, H. Zhang, H. Feng, J. Dong, C. Wang, and Q. Liu, “Bionic SERS chip with super-hydrophobic and plasmonic micro/nano dual structure,” *Photon. Res., PRJ*, vol. 6, no. 2, pp. 77–83, Feb. 2018, doi: 10.1364/PRJ.6.000077.

[400] V. Sharma and V. Krishnan, “Fabrication of highly sensitive biomimetic SERS substrates for detection of herbicides in trace concentration,” *Sensors and Actuators B: Chemical*, vol. 262, pp. 710–719, Jun. 2018, doi: 10.1016/j.snb.2018.01.230.

[401] H. Sun *et al.*, “Bioinspired surface-enhanced Raman scattering substrate with intrinsic Raman signal for the interactive SERS detection of pesticides residues,” *Spectrochimica Acta Part A: Molecular and Biomolecular Spectroscopy*, vol. 270, p. 120800, Apr. 2022, doi: 10.1016/j.saa.2021.120800.

[402] G. Shi, M. Wang, Y. Zhu, Y. Wang, and H. Xu, “A novel natural SERS system for crystal violet detection based on graphene oxide wrapped Ag micro-islands substrate fabricated from Lotus leaf as a template,” *Applied Surface Science*, vol. 459, pp. 802–811, Nov. 2018, doi: 10.1016/j.apsusc.2018.08.065.

[403] P. Kumar, R. Khosla, M. Soni, D. Deva, and S. K. Sharma, “A highly sensitive, flexible SERS sensor for malachite green detection based on Ag decorated microstructured PDMS substrate fabricated from Taro leaf as template,” *Sensors and Actuators B: Chemical*, vol. 246, pp. 477–486, Jul. 2017, doi: 10.1016/j.snb.2017.01.202.

[404] A. H. Chiou, C. W. Chang, and C. J. Ting, “Spectrally selective antireflection of nanoimprint lithography-formed 3D spherical structures on film coated with a silver layer,” *Sci Rep*, vol. 12, no. 1, p. 19505, Nov. 2022, doi: 10.1038/s41598-022-23348-w.

[405] E. Sharma *et al.*, “Evolution in Lithography Techniques: Microlithography to Nanolithography,” *Nanomaterials (Basel)*, vol. 12, no. 16, p. 2754, Aug. 2022, doi: 10.3390/nano12162754.

[406] H. Wu *et al.*, “A Simple SERS-Based Trace Sensing Platform Enabled by AuNPs-Analyte/AuNPs Double-Decker Structure on Wax-Coated Hydrophobic Surface,” *Front. Chem.*, vol. 6, Oct. 2018, doi: 10.3389/fchem.2018.00482.

[407] D.-J. Lee and D. Y. Kim, “Hydrophobic Paper-Based SERS Sensor Using Gold Nanoparticles Arranged on Graphene Oxide Flakes,” *Sensors*, vol. 19, no. 24, Art. no. 24, Jan. 2019, doi: 10.3390/s19245471.

[408] H. Yang *et al.*, “Femtosecond laser patterned superhydrophobic/hydrophobic SERS sensors for rapid positioning ultratrace detection,” *Opt. Express, OE*, vol. 29, no. 11, pp. 16904–16913, May 2021, doi: 10.1364/OE.423789.

[409] “Hydrophobic Slippery Surface-Based Surface-Enhanced Raman Spectroscopy Platform for Ultrasensitive Detection in Food Safety Applications | Analytical Chemistry.” Accessed: Sep. 10, 2024. [Online]. Available: https://pubs.acs.org/doi/10.1021/acs.analchem.9b00085

[410] M. Usman *et al.*, “Facile silicone oil-coated hydrophobic surface for surface enhanced Raman spectroscopy of antibiotics,” *RSC Adv.*, vol. 9, no. 25, pp. 14109–14115, May 2019, doi: 10.1039/C9RA00817A.

[411] M. Lee *et al.*, “Subnanomolar Sensitivity of Filter Paper-Based SERS Sensor for Pesticide Detection by Hydrophobicity Change of Paper Surface,” *ACS Sens.*, vol. 3, no. 1, pp. 151–159, Jan. 2018, doi: 10.1021/acssensors.7b00782.

[412] M. Sakir, E. Yilmaz, and M. S. Onses, “SERS-active hydrophobic substrates fabricated by surface growth of Cu nanostructures,” *Microchemical Journal*, vol. 154, p. 104628, May 2020, doi: 10.1016/j.microc.2020.104628.

[413] S. Zhuang *et al.*, “Lotus leaf-inspired biomimetic SERS substrate for detection of thiram on apple,” *Food Bioscience*, vol. 58, p. 103818, Apr. 2024, doi: 10.1016/j.fbio.2024.103818.

[414] D. Li, X. Tian, W. Yang, X. Wang, Y. Liu, and J. Shan, “Hydrophobicity-driven self-assembly of nanoplastics and silver nanoparticles for the detection of polystyrene microspheres using surface enhanced Raman spectroscopy,” *Chemosphere*, vol. 339, p. 139775, Oct. 2023, doi: 10.1016/j.chemosphere.2023.139775.

[415] Y.-M. Chen *et al.*, “Production of natural chitin film from pupal shell of moth: Fabrication of plasmonic surfaces for SERS-based sensing applications,” *Carbohydrate Polymers*, vol. 262, p. 117909, Jun. 2021, doi: 10.1016/j.carbpol.2021.117909.

[416] S. Nair, J. Gomez-Cruz, G. Ascanio, A. Docoslis, R. G. Sabat, and C. Escobedo, “Cicada Wing Inspired Template-Stripped SERS Active 3D Metallic Nanostructures for the Detection of Toxic Substances,” *Sensors*, vol. 21, no. 5, Art. no. 5, Jan. 2021, doi: 10.3390/s21051699.

[417] G. Shi *et al.*, “Biomimetic synthesis of Ag-coated glasswing butterfly arrays as ultra-sensitive SERS substrates for efficient trace detection of pesticides,” *Beilstein J. Nanotechnol.*, vol. 10, no. 1, pp. 578–588, Feb. 2019, doi: 10.3762/bjnano.10.59.

[418] N. Kumari, N. Sood, and V. Krishnan, “Beetle wing inspired fabrication of nanojunction based biomimetic SERS substrates for sensitive detection of analytes,” *Materials Technology*, Jan. 2022, Accessed: Sep. 10, 2024. [Online]. Available: https://www.tandfonline.com/doi/abs/10.1080/10667857.2020.1816382

[419] K.-S. Wang *et al.*, “Novel strategy for flexible and super-hydrophobic SERS substrate fabricated by deposited gold nanoislands on organic semiconductor nanostructures for bio-detection,” *Surface and Coatings Technology*, vol. 435, p. 128251, Apr. 2022, doi: 10.1016/j.surfcoat.2022.128251.

[420] Q. Peng *et al.*, “Hydrophobic AgNPs: one-step synthesis in aqueous solution and their greatly enhanced performance for SERS detection,” *Journal of Materials Chemistry C*, vol. 7, no. 34, pp. 10465–10470, 2019, doi: 10.1039/C9TC03143J.

[421] Z.-Q. Geng *et al.*, “A disposable paper-based hydrophobic substrate for highly sensitive surface-enhanced Raman scattering detection,” *Talanta*, vol. 220, p. 121340, Dec. 2020, doi: 10.1016/j.talanta.2020.121340.

[422] “Investigation of the Hydrophobic Nature of Metal Oxide Surfaces Created by Atomic Layer Deposition | Langmuir.” Accessed: Sep. 11, 2024. [Online]. Available: https://pubs.acs.org/doi/10.1021/acs.langmuir.9b00577

[423] “Nanoengineered Superhydrophobic Surfaces of Aluminum with Extremely Low Bacterial Adhesivity | ACS Applied Materials & Interfaces.” Accessed: Sep. 11, 2024. [Online]. Available: https://pubs.acs.org/doi/10.1021/acsami.7b01322

[424] P. Varshney, “Full article: Superhydrophobic coatings for aluminium surfaces synthesized by chemical etching process.” Accessed: Jul. 30, 2024. [Online]. Available: https://www.tandfonline.com/doi/full/10.1080/19475411.2016.1272502

[425] M. Aydemir, V. Jankus, F. B. Dias, and A. Monkman, “The key role of geminate electron–hole pair recombination in the delayed fluorescence in rhodamine 6G and ATTO-532,” *Physical Chemistry Chemical Physics*, vol. 16, no. 39, pp. 21543–21549, 2014, doi: 10.1039/C4CP01675K.

[426] T. Wenzl *et al.*, “Guidance Document on the Estimation of LOD and LOQ for Measurements in the Field of Contaminants in Food and Feed,” Jun. 2016, Accessed: Jul. 30, 2024. [Online]. Available: https://orbi.uliege.be/handle/2268/199914

[427] P. Agarwal, S. Prakash, and G. Saini, “Quantification and size classification of Microplastics leached from disposable beverage cups,” Feb. 23, 2024. doi: 10.21203/rs.3.rs-3962261/v1.

[428] Y. Cho and C. Hee Park, “Objective quantification of surface roughness parameters affecting superhydrophobicity,” *RSC Advances*, vol. 10, no. 52, pp. 31251–31260, 2020, doi: 10.1039/D0RA03137B.

[429] “Baseline Assessment for the Consistency of Raman Shifts Acquired with 26 Different Raman Systems and Necessity of a Standardized Calibration Protocol.” Accessed: Aug. 30, 2024. [Online]. Available: https://www.jstage.jst.go.jp/article/analsci/35/5/35_18P501/_article/-char/ja/

[430] “Comparability of Raman Spectroscopic Configurations: A Large Scale Cross-Laboratory Study | Analytical Chemistry.” Accessed: Aug. 30, 2024. [Online]. Available: https://pubs.acs.org/doi/full/10.1021/acs.analchem.0c02696

[431] D. Liu and B. M. Hennelly, “Wavenumber Calibration Protocol for Raman Spectrometers Using Physical Modelling and a Fast Search Algorithm,” *Appl Spectrosc*, vol. 78, no. 8, pp. 790–805, Aug. 2024, doi: 10.1177/00037028241254847.

[432] M. Saggu, J. Liu, and A. Patel, “Identification of Subvisible Particles in Biopharmaceutical Formulations Using Raman Spectroscopy Provides Insight into Polysorbate 20 Degradation Pathway,” *Pharm Res*, vol. 32, no. 9, pp. 2877–2888, Sep. 2015, doi: 10.1007/s11095-015-1670-x.

[433] J. De Gelder, K. De Gussem, P. Vandenabeele, and L. Moens, “Reference database of Raman spectra of biological molecules,” *Journal of Raman Spectroscopy*, vol. 38, no. 9, pp. 1133–1147, 2007, doi: 10.1002/jrs.1734.

[434] “Lauric acid(143-07-7) Raman spectrum.” Accessed: Jul. 24, 2024. [Online]. Available: https://www.chemicalbook.com/SpectrumEN_143-07-7_Raman.htm

[435] O. Kulakovich, “Nanoplasmonic Raman detection of bromate in water.” Accessed: Jul. 30, 2024. [Online]. Available: https://opg.optica.org/oe/fulltext.cfm?uri=oe-24-2-A174&id=333585

[436] X. He *et al.*, “Surface-enhanced Raman spectroscopy using gold-coated horizontally aligned carbon nanotubes,” *Nanotechnology*, vol. 23, p. 205702, May 2012, doi: 10.1088/0957-4484/23/20/205702.

[437] D. A. Armbruster and T. Pry, “Limit of Blank, Limit of Detection and Limit of Quantitation,” *Clin Biochem Rev*, vol. 29, no. Suppl 1, pp. S49–S52, Aug. 2008.

[438] P. G. Martínez-Torres, M. M. Martínez-García, P. E. Cardoso-Ávila, and J. L. Pichardo-Molina, “Facile Nanostructured Substrate Preparation Using Gold Nanocuboids for SERS,” *Nanomaterials and Nanotechnology*, vol. 5, p. 12, Jan. 2015, doi: 10.5772/60500.

[439] B. Chaisrikhwun, S. Ekgasit, and P. Pienpinijtham, “Size-independent quantification of nanoplastics in various aqueous media using surfaced-enhanced Raman scattering,” *Journal of Hazardous Materials*, vol. 442, p. 130046, Jan. 2023, doi: 10.1016/J.JHAZMAT.2022.130046.

[440] Y. Lyu *et al.*, “The Interaction of Amines with Gold Nanoparticles,” *Adv Mater*, vol. 36, no. 10, p. e2211624, Mar. 2024, doi: 10.1002/adma.202211624.

[441] C. Boukoufi, A. Boudier, S. Lahouari, J. Vigneron, and I. Clarot, “Activity and reusability of immobilized gold nanoparticles for the catalysis of both oxidation and

reduction reactions," *Results in Chemistry*, vol. 5, p. 100979, Jan. 2023, doi: 10.1016/j.rechem.2023.100979.

[442] M. Matsumoto, K. Kaneko, M. Hara, M. Matsui, K. Morita, and T. Maruyama, "Covalent immobilization of gold nanoparticles on a plastic substrate and subsequent immobilization of biomolecules," *RSC Advances*, vol. 11, no. 38, pp. 23409–23417, 2021, doi: 10.1039/D1RA03902D.

[443] C. D. Rosa *et al.*, "Toward hyperuniform disordered plasmonic nanostructures for reproducible surface-enhanced Raman spectroscopy," *Phys. Chem. Chem. Phys.*, vol. 17, no. 12, pp. 8061–8069, Mar. 2015, doi: 10.1039/C4CP06024E.

[444] B.-W. Park, D.-S. Kim, and D.-Y. Yoon, "Surface modification of gold electrode with gold nanoparticles and mixed self-assembled monolayers for enzyme biosensors," *Korean J. Chem. Eng.*, vol. 28, no. 1, pp. 64–70, Jan. 2011, doi: 10.1007/s11814-010-0349-6.

[445] M. Kahl, E. Voges, S. Kostrewa, C. Viets, and W. Hill, "Periodically structured metallic substrates for SERS," *Sensors and Actuators B: Chemical*, vol. 51, no. 1, pp. 285–291, Aug. 1998, doi: 10.1016/S0925-4005(98)00219-6.

[446] S. Karabel Ocal, J. Patarroyo, N. B. Kiremitler, S. Pekdemir, V. F. Puntes, and M. S. Onses, "Plasmonic assemblies of gold nanorods on nanoscale patterns of poly(ethylene glycol): Application in surface-enhanced Raman spectroscopy," *Journal of Colloid and Interface Science*, vol. 532, pp. 449–455, Dec. 2018, doi: 10.1016/j.jcis.2018.07.124.

[447] A. P. Alekhin *et al.*, "Synthesis of biocompatible surfaces by nanotechnology methods," *Nanotechnol Russia*, vol. 5, no. 9, pp. 696–708, Oct. 2010, doi: 10.1134/S1995078010090144.

[448] D. H. Jariwala, D. Patel, and S. Wairkar, "Surface functionalization of nanodiamonds for biomedical applications," *Materials Science and Engineering: C*, vol. 113, p. 110996, Aug. 2020, doi: 10.1016/j.msec.2020.110996.

[449] J. Klug, L. A. Pérez, E. A. Coronado, and G. I. Lacconi, "Chemical and Electrochemical Oxidation of Silicon Surfaces Functionalized with APTES: The Role of Surface Roughness in the AuNPs Anchoring Kinetics," *J. Phys. Chem. C*, vol. 117, no. 21, pp. 11317–11327, May 2013, doi: 10.1021/jp212613f.

[450] "Biosensors | Free Full-Text | Review: 3-Aminopropyltriethoxysilane (APTES) Deposition Methods on Oxide Surfaces in Solution and Vapor Phases for Biosensing Applications." Accessed: Aug. 04, 2024. [Online]. Available: https://www.mdpi.com/2079-6374/13/1/36

[451] F. Ahangaran and A. H. Navarchian, "Recent advances in chemical surface modification of metal oxide nanoparticles with silane coupling agents: A review," *Advances in Colloid and Interface Science*, vol. 286, p. 102298, Dec. 2020, doi: 10.1016/j.cis.2020.102298.

[452] Y. Han, D. Mayer, A. Offenhäusser, and S. Ingebrandt, "Surface activation of thin silicon oxides by wet cleaning and silanization," *Thin Solid Films*, vol. 510, no. 1, pp. 175–180, Jul. 2006, doi: 10.1016/j.tsf.2005.11.048.

[453] M. Ben Haddada *et al.*, "Optimizing the immobilization of gold nanoparticles on functionalized silicon surfaces: amine- vs thiol-terminated silane," *Gold Bull*, vol. 46, no. 4, pp. 335–341, Dec. 2013, doi: 10.1007/s13404-013-0120-y.

[454] J. Zheng, Z. Zhu, H. Chen, and Z. Liu, “Nanopatterned Assembling of Colloidal Gold Nanoparticles on Silicon,” *Langmuir*, vol. 16, no. 10, pp. 4409–4412, May 2000, doi: 10.1021/la991332o.

[455] A.-L. Morel, S. Boujday, C. Méthivier, J.-M. Krafft, and C.-M. Pradier, “Biosensors elaborated on gold nanoparticles, a PM-IRRAS characterisation of the IgG binding efficiency,” *Talanta*, vol. 85, no. 1, pp. 35–42, Jul. 2011, doi: 10.1016/j.talanta.2011.02.028.

[456] D. Aureau, Y. Varin, K. Roodenko, O. Seitz, O. Pluchery, and Y. J. Chabal, “Controlled Deposition of Gold Nanoparticles on Well-Defined Organic Monolayer Grafted on Silicon Surfaces,” *J. Phys. Chem. C*, vol. 114, no. 33, pp. 14180–14186, Aug. 2010, doi: 10.1021/jp104183m.

[457] T. Okamoto, I. Yamaguchi, and T. Kobayashi, “Local plasmon sensor with gold colloid monolayers deposited upon glass substrates,” *Opt. Lett., OL*, vol. 25, no. 6, pp. 372–374, Mar. 2000, doi: 10.1364/OL.25.000372.

[458] C.-D. Chen, S.-F. Cheng, L.-K. Chau, and C. R. C. Wang, “Sensing capability of the localized surface plasmon resonance of gold nanorods,” *Biosensors and Bioelectronics*, vol. 22, no. 6, pp. 926–932, Jan. 2007, doi: 10.1016/j.bios.2006.03.021.

[459] K. M. Hurst, N. Ansari, C. B. Roberts, and W. R. Ashurst, “Self-Assembled Monolayer-Immobilized Gold Nanoparticles as Durable, Anti-Stiction Coatings for MEMS,” *Journal of Microelectromechanical Systems*, vol. 20, no. 2, pp. 424–435, Apr. 2011, doi: 10.1109/JMEMS.2011.2112334.

[460] E. Asenath Smith and W. Chen, “How To Prevent the Loss of Surface Functionality Derived from Aminosilanes,” *Langmuir*, vol. 24, no. 21, pp. 12405–12409, Nov. 2008, doi: 10.1021/la802234x.

[461] M. Hijazi *et al.*, “Synthesis and characterization of tin dioxide thick film modified by APTES in vapor and liquid phases,” *J Mater Sci*, vol. 53, no. 1, pp. 727–738, Jan. 2018, doi: 10.1007/s10853-017-1541-4.

[462] A. Miranda, L. Martínez, and P. A. A. De Beule, “Facile synthesis of an aminopropylsilane layer on Si/SiO2 substrates using ethanol as APTES solvent,” *MethodsX*, vol. 7, p. 100931, Jan. 2020, doi: 10.1016/j.mex.2020.100931.

[463] A. A. Issa and A. S. Luyt, “Kinetics of Alkoxysilanes and Organoalkoxysilanes Polymerization: A Review,” *Polymers*, vol. 11, no. 3, Art. no. 3, Mar. 2019, doi: 10.3390/polym11030537.

[464] “Functionalization of silicon dioxide and silicon nitride surfaces with aminosilanes for optical biosensing applications - Antoniou - 2020 - MEDICAL DEVICES & SENSORS - Wiley Online Library.” Accessed: Aug. 06, 2024. [Online]. Available: https://onlinelibrary.wiley.com/doi/full/10.1002/mds3.10072

[465] N. S. K. Gunda, M. Singh, L. Norman, K. Kaur, and S. K. Mitra, “Optimization and characterization of biomolecule immobilization on silicon substrates using (3-aminopropyl)triethoxysilane (APTES) and glutaraldehyde linker,” *Applied Surface Science*, vol. 305, pp. 522–530, Jun. 2014, doi: 10.1016/j.apsusc.2014.03.130.

[466] F. Bauer *et al.*, “Water-based functionalization of mesoporous siliceous materials, Part 1: Morphology and stability of grafted 3-aminopropyltriethoxysilane,” *Microporous*

and Mesoporous Materials, vol. 250, pp. 221–231, Sep. 2017, doi: 10.1016/j.micromeso.2016.01.046.

[467] N. Aissaoui, L. Bergaoui, J. Landoulsi, J.-F. Lambert, and S. Boujday, “Silane Layers on Silicon Surfaces: Mechanism of Interaction, Stability, and Influence on Protein Adsorption,” *Langmuir*, vol. 28, no. 1, pp. 656–665, Jan. 2012, doi: 10.1021/la2036778.

[468] C.-P. Klages, V. Raev, D. Murugan, and V. V. R. Sai, “Argon–water DBD pretreatment and vapor-phase silanization of silica: Comparison with wet-chemical processes,” *Plasma Processes and Polymers*, vol. 17, no. 7, p. 1900265, 2020, doi: 10.1002/ppap.201900265.

[469] A. A. Issa, M. S. Elazazy, and A. S. Luyt, “Polymerization of 3-cyanopropyl (triethoxy) silane: A kinetic study using gas chromatography,” *International Journal of Chemical Kinetics*, vol. 50, no. 12, pp. 846–855, 2018, doi: 10.1002/kin.21219.

[470] “Effect of Solvents and Concentration on the Formation of a Self-Assembled Monolayer of Octadecylsiloxane on Silicon (001) | Langmuir.” Accessed: Aug. 07, 2024. [Online]. Available: https://pubs.acs.org/doi/full/10.1021/la025906s?casa_token=KKVh985x5IoAAAAA%3AAUCCoBVBFnsQzUB-I65g3jrCvHfKveSGsOIp4WD3HDO3udCQI7qQVsaFFOhKwVM_Z-oCYjYStTOyPb8c

[471] “Self-Assembly Is Not the Only Reaction Possible between Alkyltrichlorosilanes and Surfaces: Monomolecular and Oligomeric Covalently Attached Layers of Dichloro- and Trichloroalkylsilanes on Silicon | Langmuir.” Accessed: Aug. 07, 2024. [Online]. Available: https://pubs.acs.org/doi/full/10.1021/la000471z?casa_token=rDRbPddeM9YAAAAA%3AeSW8BwnXwl-V1gQm9LOt-AhrSsaUoucYoQO56WaeIRs-XLMdkTdrbsUwnZ4iSxwh_Jmuq3k2iDbiD8jL

[472] K. Wen *et al.*, “Postassembly Chemical Modification of a Highly Ordered Organosilane Multilayer: New Insights into the Structure, Bonding, and Dynamics of Self-Assembling Silane Monolayers,” *ACS Nano*, vol. 2, no. 3, pp. 579–599, Mar. 2008, doi: 10.1021/nn800011t.

[473] T. Manifar, A. Rezaee, M. Sheikhzadeh, and S. Mittler, “Formation of uniform self-assembly monolayers by choosing the right solvent: OTS on silicon wafer, a case study,” *Applied Surface Science*, vol. 254, no. 15, pp. 4611–4619, May 2008, doi: 10.1016/j.apsusc.2008.01.100.

[474] A. Y. F. Mahmoud, C. J. Rusin, and M. T. McDermott, “Gold nanostars as a colloidal substrate for in-solution SERS measurements using a handheld Raman spectrometer,” *Analyst*, vol. 145, no. 4, pp. 1396–1407, 2020, doi: 10.1039/C9AN02439E.

[475] A. Shiohara, J. Langer, L. Polavarapu, and L. M. Liz-Marzán, “Solution processed polydimethylsiloxane/gold nanostar flexible substrates for plasmonic sensing,” *Nanoscale*, vol. 6, no. 16, pp. 9817–9823, 2014, doi: 10.1039/C4NR02648A.

[476] Q. Su, X. Ma, J. Dong, C. Jiang, and W. Qian, “A reproducible SERS substrate based on electrostatically assisted aptes-functionalized surface-assembly of gold nanostars,” *ACS Applied Materials and Interfaces*, vol. 3, no. 6, pp. 1873–1879, Jun. 2011, doi: 10.1021/AM200057F.

[477] “Enhancing gold nanoparticle immobilization on thiolated silica: utilizing neutral ligands to achieve maximum surface coverage for improved SERS substrates - Journal of Materials Chemistry C (RSC Publishing).” Accessed: Aug. 07, 2024. [Online]. Available: https://pubs.rsc.org/en/content/articlelanding/2024/tc/d3tc04577c

[478] “DNA-embedded Au–Ag core–shell nanoparticles assembled on silicon slides as a reliable SERS substrate - Analyst (RSC Publishing).” Accessed: Aug. 07, 2024. [Online]. Available: https://pubs.rsc.org/en/content/articlelanding/2014/an/c3an02116e

[479] “Capillary-force-assisted self-assembly of gold nanoparticles into highly ordered plasmonic thin films for ultrasensitive SERS - Physical Chemistry Chemical Physics (RSC Publishing).” Accessed: Aug. 07, 2024. [Online]. Available: https://pubs.rsc.org/en/content/articlelanding/2023/cp/d2cp05158c

[480] “Gold nanoparticle incorporated inverse opal photonic crystal capillaries for optofluidic surface enhanced Raman spectroscopy - ScienceDirect.” Accessed: Aug. 07, 2024. [Online]. Available: https://www.sciencedirect.com/science/article/pii/S0956566315301329?via%3Dihub

[481] “Development of monolayer AuNPs decorated on an optical fiber facet for SERS analysis.” Accessed: Aug. 07, 2024. [Online]. Available: https://opg.optica.org/ao/fulltext.cfm?uri=ao-60-3-792&id=446698

[482] “Functionalizing Metal Nanostructured Film with Graphene Oxide for Ultrasensitive Detection of Aromatic Molecules by Surface-Enhanced Raman Spectroscopy | ACS Applied Materials & Interfaces.” Accessed: Aug. 07, 2024. [Online]. Available: https://pubs.acs.org/doi/full/10.1021/am200737b?casa_token=Q1BKVcyby1cAAAAA%3AQosAzw3ILHxhf18FwRhh_sCmkr7oPyCzcMDAkmz8hE5cgsIZwZsjfhf5cgRulKRlcaKeHMXYB-e8BqoK

[483] “Structures of DNA-Linked Nanoparticle Aggregates | The Journal of Physical Chemistry B.” Accessed: Aug. 08, 2024. [Online]. Available: https://pubs.acs.org/doi/10.1021/jp062212%2B

[484] “Organization of Inorganic Nanoparticles Using Biotin−Streptavidin Connectors | Chemistry of Materials.” Accessed: Aug. 08, 2024. [Online]. Available: https://pubs.acs.org/doi/10.1021/cm980610m

[485] “Hyperbranched Polymer–Gold Nanoparticle Assemblies: Role of Polymer Architecture in Hybrid Assembly Formation and SERS Activity | Langmuir.” Accessed: Aug. 08, 2024. [Online]. Available: https://pubs.acs.org/doi/full/10.1021/la4047462?casa_token=5_FjMFd5P4AAAAAA%3AoN6bGxIhhLBIo7IVby5WCkR2RLPrBQ3DfdopdTC3nVSSfCkjeqJfLqS9H8kJlSRgMUpojEe4jTWpAt9r

[486] M. Sethi, G. Joung, and M. R. Knecht, “Linear Assembly of Au Nanorods Using Biomimetic Ligands,” *Langmuir*, vol. 25, no. 3, pp. 1572–1581, Feb. 2009, doi: 10.1021/la802845b.

[487] “Emerging sensing platforms based on Cucurbit[n]uril functionalized gold nanoparticles and electrodes - Chemical Communications (RSC Publishing) DOI:10.1039/D3CC04851A.” Accessed: Aug. 08, 2024. [Online]. Available: https://pubs.rsc.org/en/content/articlehtml/2024/cc/d3cc04851a

[488] “Assembly of Metal Nanoparticle Arrays Using Molecular Bridges - IOPscience.” Accessed: Aug. 08, 2024. [Online]. Available: https://iopscience.iop.org/article/10.1149/2.F05013IF

[489] B. Vlčková, M. Moskovits, I. Pavel, K. Šišková, M. Sládková, and M. Šlouf, “Single-molecule surface-enhanced Raman spectroscopy from a molecularly-bridged silver nanoparticle dimer,” *Chemical Physics Letters*, vol. 455, no. 4–6, pp. 131–134, Apr. 2008, doi: 10.1016/j.cplett.2008.02.078.

[490] W. A. Freeman, W. L. Mock, and N. Y. Shih, “Cucurbituril,” *J. Am. Chem. Soc.*, vol. 103, no. 24, pp. 7367–7368, Dec. 1981, doi: 10.1021/ja00414a070.

[491] S. Sasmal, M. K. Sinha, and E. Keinan, “Facile purification of rare cucurbiturils by affinity chromatography,” *Org Lett*, vol. 6, no. 8, pp. 1225–1228, Apr. 2004, doi: 10.1021/ol0499755.

[492] A. Day, A. P. Arnold, R. J. Blanch, and B. Snushall, “Controlling factors in the synthesis of cucurbituril and its homologues,” *J Org Chem*, vol. 66, no. 24, pp. 8094–8100, Nov. 2001, doi: 10.1021/jo015897c.

[493] H.-J. Kim, W. S. Jeon, Y. H. Ko, and K. Kim, “Inclusion of methylviologen in cucurbit[7]uril,” *Proceedings of the National Academy of Sciences*, vol. 99, no. 8, pp. 5007–5011, Apr. 2002, doi: 10.1073/pnas.062656699.

[494] “Precise Subnanometer Plasmonic Junctions for SERS within Gold Nanoparticle Assemblies Using Cucurbit[n]uril ‘Glue’ | ACS Nano.” Accessed: Aug. 08, 2024. [Online]. Available: https://pubs.acs.org/doi/full/10.1021/nn200250v

[495] Q. An, G. Li, C. Tao, Y. Li, Y. Wu, and W. Zhang, “A general and efficient method to form self-assembled cucurbit[n]uril monolayers on gold surfaces,” *Chem. Commun.*, no. 17, pp. 1989–1991, Apr. 2008, doi: 10.1039/B719927A.

[496] T.-C. Lee and O. A. Scherman, “Formation of dynamic aggregates in water by cucurbit[5]uril capped with gold nanoparticles,” *Chem. Commun.*, vol. 46, no. 14, pp. 2438–2440, Mar. 2010, doi: 10.1039/B925051D.

[497] J. Lagona, P. Mukhopadhyay, S. Chakrabarti, and L. Isaacs, “The Cucurbit[n]uril Family,” *Angewandte Chemie International Edition*, vol. 44, no. 31, pp. 4844–4870, 2005, doi: 10.1002/anie.200460675.

[498] L. Isaacs, “Cucurbit[n]urils: from mechanism to structure and function,” *Chem Commun (Camb)*, no. 6, pp. 619–629, Feb. 2009, doi: 10.1039/b814897j.

[499] “Cucurbituril Homologues and Derivatives: New Opportunities in Supramolecular Chemistry | Accounts of Chemical Research.” Accessed: Aug. 08, 2024. [Online]. Available: https://pubs.acs.org/doi/10.1021/ar020254k

[500] S. Mahajan, T.-C. Lee, F. Biedermann, J. T. Hugall, J. J. Baumberg, and O. A. Scherman, “Raman and SERS spectroscopy of cucurbit[n]urils,” *Physical Chemistry Chemical Physics*, vol. 12, no. 35, pp. 10429–10433, 2010, doi: 10.1039/C0CP00071J.

[501] C. Tao *et al.*, “Cucurbit[n]urils as a SERS hot-spot nanocontainer through bridging gold nanoparticles,” *Chem. Commun.*, vol. 47, no. 35, pp. 9867–9869, Aug. 2011, doi: 10.1039/C1CC12474A.

[502] W.-I. K. Chio, H. Xie, Y. Zhang, Y. Lan, and T.-C. Lee, “SERS biosensors based on cucurbituril-mediated nanoaggregates for wastewater-based epidemiology,” *TrAC Trends in Analytical Chemistry*, vol. 146, p. 116485, Jan. 2022, doi: 10.1016/j.trac.2021.116485.

[503] C. Carnegie *et al.*, “Mapping SERS in CB:Au Plasmonic Nanoaggregates,” *ACS Photonics*, vol. 4, no. 11, pp. 2681–2686, Nov. 2017, doi: 10.1021/acsphotonics.7b00902.

[504] S. T. Jones *et al.*, “Gold Nanorods with Sub-Nanometer Separation using Cucurbit[n]uril for SERS Applications,” *Small*, vol. 10, no. 21, pp. 4298–4303, 2014, doi: 10.1002/smll.201401063.

[505] M. J. Seo, K. Baek, and J. W. Ha, “Indirect Interactions between Raman Probes Encapsulated within Cucurbit[7]urils and Gold Nanorods to Enhance Long-term Stability and Signal,” *ANAL. SCI.*, vol. 35, no. 9, pp. 1009–1013, Sep. 2019, doi: 10.2116/analsci.19P144.

[506] A. R. Salmon *et al.*, “Monitoring Early-Stage Nanoparticle Assembly in Microdroplets by Optical Spectroscopy and SERS,” *Small*, vol. 12, no. 13, pp. 1788–1796, 2016, doi: 10.1002/smll.201503513.

[507] N. Narayanan *et al.*, “Nanotheranostic Probe Built on Methylene Blue Loaded Cucurbituril [8] and Gold Nanorod: Targeted Phototherapy in Combination with SERS Imaging on Breast Cancer Cells,” *J. Phys. Chem. B*, vol. 125, no. 49, pp. 13415–13424, Dec. 2021, doi: 10.1021/acs.jpcb.1c08609.

[508] X. Shi *et al.*, “Construction of a Graphene/Au-Nanoparticles/Cucurbit[7]uril-Based Sensor for Pb2+ Sensing,” *Chemistry – A European Journal*, vol. 22, no. 16, pp. 5643–5648, 2016, doi: 10.1002/chem.201505034.

[509] D. O. Sigle *et al.*, “Observing Single Molecules Complexing with Cucurbit[7]uril through Nanogap Surface-Enhanced Raman Spectroscopy,” *Journal of Physical Chemistry Letters*, vol. 7, no. 4, pp. 704–710, Feb. 2016, doi: 10.1021/ACS.JPCLETT.5B02535/ASSET/IMAGES/LARGE/JZ-2015-02535Y_0005.JPEG.

[510] N. H. Kim *et al.*, “Smart SERS Hot Spots: Single Molecules Can Be Positioned in a Plasmonic Nanojunction Using Host–Guest Chemistry,” *J. Am. Chem. Soc.*, vol. 140, no. 13, pp. 4705–4711, Apr. 2018, doi: 10.1021/jacs.8b01501.

[511] A. S. Braegelman *et al.*, “Capture and Detection of Fentanyl with Thiolated Cucurbit[7]uril Macrocycles on Silver Nanoparticles,” *ACS Appl. Nano Mater.*, vol. 7, no. 9, pp. 10879–10885, May 2024, doi: 10.1021/acsanm.4c01444.

[512] S. Kasera, L. O. Herrmann, J. del Barrio, J. J. Baumberg, and O. A. Scherman, “Quantitative multiplexing with nano-self-assemblies in SERS,” *Sci Rep*, vol. 4, no. 1, p. 6785, Oct. 2014, doi: 10.1038/srep06785.

[513] B. de Nijs *et al.*, “Smart supramolecular sensing with cucurbit[n]urils: probing hydrogen bonding with SERS,” *Faraday Discuss.*, vol. 205, no. 0, pp. 505–515, Nov. 2017, doi: 10.1039/C7FD00147A.

[514] S. Kasera, F. Biedermann, J. J. Baumberg, O. A. Scherman, and S. Mahajan, “Quantitative SERS Using the Sequestration of Small Molecules Inside Precise

Plasmonic Nanoconstructs," *Nano Lett.*, vol. 12, no. 11, pp. 5924–5928, Nov. 2012, doi: 10.1021/nl303345z.

[515] "Quantitative SERS Detection of Uric Acid via Formation of Precise Plasmonic Nanojunctions within Aggregates of Gold Nanoparticles and Cucurbit[n]uril." Accessed: Aug. 12, 2024. [Online]. Available: https://app.jove.com/t/61682

[516] Y. Teng *et al.*, "Cucurbit[8]uril-mediated SERS plasmonic nanostructures with sub-nanometer gap for the identification and determination of estrogens," *Microchim Acta*, vol. 190, no. 5, p. 185, Apr. 2023, doi: 10.1007/s00604-023-05765-4.

[517] J. C. Fraire, V. N. Sueldo Ocello, L. G. Allende, A. V. Veglia, and E. A. Coronado, "Toward the Design of Highly Stable Small Colloidal SERS Substrates with Supramolecular Host–Guest Interactions for Ultrasensitive Detection," *J. Phys. Chem. C*, vol. 119, no. 16, pp. 8876–8888, Apr. 2015, doi: 10.1021/acs.jpcc.5b01647.

[518] N. Logan, J. Lou-Franco, C. Elliott, and C. Cao, "Catalytic gold nanostars for SERS-based detection of mercury ions (Hg 2+) with inverse sensitivity," *Environmental Science: Nano*, vol. 8, no. 9, pp. 2718–2730, Sep. 2021, doi: 10.1039/D1EN00548K.

[519] A. J. Brock and M. J. Pryor, "The kinetics of the oxidation of aluminum—copper alloys in oxygen at high temperature," *Corrosion Science*, vol. 13, no. 3, pp. 199–227, Jan. 1973, doi: 10.1016/0010-938X(73)90015-2.

[520] M. J. Pryor, "The defect structure of thin oxide films on aluminum," *Oxid Met*, vol. 3, no. 6, pp. 523–527, Nov. 1971, doi: 10.1007/BF00604998.

[521] K. Wefers, "Properties and Characterization of Surface Oxides on Aluminum Alloys," in *Advances in Materials Characterization*, D. R. Rossington, R. A. Condrate, and R. L. Snyder, Eds., Boston, MA: Springer US, 1983, pp. 321–321. doi: 10.1007/978-1-4615-8339-4_20.

[522] Z. Vít, J. Vala, and J. Málek, "Acid-base properties of aluminium oxide," *Applied Catalysis*, vol. 7, no. 2, pp. 159–168, Aug. 1983, doi: 10.1016/0166-9834(83)80004-9.

[523] D. Liu, B. Hennelly, L. O'Neill, and H. J. Byrne, "Investigation of wavenumber calibration for Raman spectroscopy using a polymer standard," in *Optical Sensing and Detection V*, F. Berghmans and A. G. Mignani, Eds., Strasbourg, France: SPIE, May 2018, p. 79. doi: 10.1117/12.2307574.

[524] S. Kihara *et al.*, "Detecting polystyrene nanoplastics using filter paper-based surface-enhanced Raman spectroscopy," *RSC Advances*, vol. 12, no. 32, pp. 20519–20522, 2022, doi: 10.1039/D2RA03395J.

[525] X. Ruan *et al.*, "Rapid detection of nanoplastics down to 20 nm in water by surface-enhanced raman spectroscopy," *Journal of Hazardous Materials*, vol. 462, p. 132702, Jan. 2024, doi: 10.1016/j.jhazmat.2023.132702.

[526] J. Li *et al.*, "Particle-in-Molybdenum Disulfide-Coated Cavity Structure with a Raman Internal Standard for Sensitive Raman Detection of Water Contaminants from Ions to <300 nm Nanoplastics," *Journal of Physical Chemistry Letters*, vol. 13, no. 25, pp. 5815–5823, Jun. 2022, doi: 10.1021/ACS.JPCLETT.2C01534/ASSET/IMAGES/LARGE/JZ2C01534_0005.JPEG.

[527] G. Li *et al.*, "Single-particle analysis of micro/nanoplastics by SEM-Raman technique," *Talanta*, vol. 249, p. 123701, Nov. 2022, doi: 10.1016/j.talanta.2022.123701.

[528] Q. T. Lê *et al.*, “Nanostructured Raman substrates for the sensitive detection of submicrometer-sized plastic pollutants in water,” *Journal of Hazardous Materials*, vol. 402, p. 123499, Jan. 2021, doi: 10.1016/j.jhazmat.2020.123499.